ROYAUME DU MAROC
Université Mohammed V - RABAT -
جامعة محمد الخامس – الرباط –
Faculté des sciences
كلية العلوم
CENTRE D'ÉTUDES DOCTORALES - SCIENCES ET TECHNOLOGIES

N° d'ordre : 4019

THÈSE DE DOCTORAT

En Vue de l'obtention du : **DOCTORAT**

Structure de Recherche : **Equipe de semi-conducteurs et technologie des capteurs pour l'environnement -STCE- centre de recherche en énergie**

Discipline : **Physique**

Spécialité : **Physique des matériaux-Optoélectronique, Génie électrique et Energie renouvelable**

Présentée et Soutenue le : **le 07/12/2024**

Par:

Mohamed ALLA

Complete study of perovskite-based prospective light harvesters for optoelectronics and photovoltaic applications

Devant le JURY :

Mohammed BENAISSA	PES	Faculté des Sciences, Université Mohammed V, Rabat	Président
Hamid EZ-ZAHRAOUY	PES	Faculté des Sciences, Université Mohammed V, Rabat	Examinateur/Rapporteur
Rachid MASROUR	PES	FSDM, Université Sidi Mohamed Ben Abdellah, Fès	Examinateur/Rapporteur
Lahoucine ATOURKI	PH	Faculté des Sciences, Université Mohammed V, Rabat	Examinateur/Rapporteur
Mustapha ROUCHDI	PH	Faculté des Sciences, Université Mohammed V, Rabat	Co-Directeur de thèse
Boubker FARES	PES	Faculté des Sciences, Université Mohammed V, Rabat	Directeur de thèse

Année Universitaire : 2023 - 24

✉ Faculté des Sciences, avenue Ibn Battouta, BP. 1014 RP, Rabat –Maroc
☎ 00212 (05) 37 77 18 76 🖷 00212(05) 37 77 42 61; http://www. fsr.um5.ac.ma

Dedicate

"This work is dedicated to my sisters, **Malika and Fatima Zahrae**, whose unfailing support and encouragement have meant the world to me, and to my loving brother, **Abderrahim**. I am incredibly appreciative to God for granting me your presence in my life.

I also dedicate this work to my father**, Lhanafi,** and my mother, **Fatima,** who have shown me the virtue of perseverance, taught me the value of hard labor, and shown me unconditional love.

My friends **OUALID ABDELAOUI, NOREDDINE ELHOUR, FATIMA ELFATOUKI, and OMAR ELOMARI** deserve special recognition for their unwavering support and help in finishing this work."

REMERCIEMENTS

Ce travail a été mené au sein de la structure de recherché STCE-Equipe de semi-conducteurs et technologie des capteurs pour l'environnement de la Faculté des Sciences de Rabat-Maroc, sous la direction de Monsieur le Professeur **Boubker FARES**, avec Monsieur **Mustapha ROUCHDI** en tant que co-encadrant.

Je tiens tout d'abord à exprimer ma profonde gratitude au Professeur **Boubker FARES**, Professeur de l'Enseignement Supérieur à la Faculté des Sciences de Rabat, pour avoir accepté de superviser ma thèse et pour ses efforts soutenus tout au long de mon travail. Ainsi que pour ses qualités professionnelles et humaines.

Un sincère remerciement est également adressé au Professeur **Mustapha ROUCHDI** pour ses précieux conseils et orientations qui ont contribué au développement de ce travail.

Je suis très honoré que Monsieur **Mohammed BENAISSA**, Professeur de l'Enseignement Supérieur à la Faculté des Sciences, Université Mohammed V, Rabat, ait accepté de présider le jury de ma thèse.

Je souhaite exprimer ma reconnaissance à Monsieur **Hamid EZ-ZAHRAOUY**, Professeur de l'Enseignement Supérieur à la Faculté des Sciences, Université Mohammed V, Rabat, pour l'intérêt qu'il a manifesté envers ce travail, ainsi que pour avoir consacré une partie de son temps à l'analyse de ma thèse en tant que rapporteur et examinateur.

Un grand merci également à Monsieur **Rachid MASROUR**, Professeur de l'Enseignement Supérieur à la Faculté des Sciences Dhar El Mahraz, université Sidi Mohamed Ben Abdellah de Fès, pour avoir accepté de participer au jury en tant que rapporteur et examinateur.

Je remercie chaleureusement Monsieur **Lahoucine ATOURKI**, Professeur de l'Enseignement Supérieur à la Faculté des Sciences, Université Mohammed V, Rabat, pour avoir accepté la lourde tâche de rapporter ce travail de recherche.

Je tiens aussi à exprimer ma reconnaissance envers le Professeur Rupesh S DEVAN et le Dr. Vishesh MANJUNATH de l'Institut de Technologie en Inde, pour leurs conseils précieux et leurs remarques constructives qui ont enrichi mon travail.

Enfin, je souhaite exprimer ma gratitude à mes collègues de la structure de recherché STCE ainsi qu'à ceux de l'Institut de Technologie en Inde.

Je désire également remercier ma famille pour leur soutien indéfectible tout au long de ces années. Un immense merci à tous ceux qui m'ont aidé et soutenu, même si je ne peux tous les nommer ici.

Mohamed ALLA

ACKNOWLEDGEMENTS

This work was conducted within the STCE research structure Semiconductors and Sensor Technology for the Environment Team at the Faculty of Sciences in Rabat, Morocco, under the supervision of Prof. **Boubker FARES**, with Prof. **Mustapha ROUCHDI** as a co-supervisor. I would first like to express my deep gratitude to Prof. **Boubker FARES**, Higher Education at the Faculty of Sciences in Rabat, for agreeing to supervise my thesis and for his sustained efforts throughout my work, as well as for his professional and personal qualities.

A sincere thank you is also extended to Prof. **Mustapha ROUCHDI**, for his valuable advice and guidance, which have contributed to the development of this work.

I am very honored that Prof. **Mohammed BENAISSA**, Higher Education at the Faculty of Sciences, Mohammed V University, Rabat, has agreed to chair the thesis jury.

I wish to express my gratitude to Prof. **Hamid EZ-ZAHRAOUY**, for the interest he has shown in this work and for dedicating part of his time to reviewing my thesis as a rapporteur and examiner.

A big thank you also goes to Prof. **Rachid MASROUR**, at the Faculty of Sciences DHAR EL MAHRAZ university Sidi Mohamed Ben Abdellah, FEZ-MOROCCO., for agreeing to participate in the jury as a rapporteur and examiner.

I warmly thank Prof. **Lahoucine ATOURKI**, Higher Education at the Faculty of Sciences, Mohammed V University, Rabat, for accepting the important task of reviewing my thesis as a rapporteur and examiner.

I also wish to express my gratitude to Prof. Rupesh S DEVAN and Dr. Vishesh Manjunath, from the Indian Institute of Technology, for their valuable advice and constructive feedback that enriched my work.

Finally, I would like to extend my gratitude to my colleagues in the STCE research structure as well as those at the Indian Institute of Technology.

I also wish to thank my family for their unwavering support throughout these years. A huge thank you to all who have helped and supported me, even if I cannot name everyone here.

Mohamed ALLA

RÉSUMÉ

La quantité d'énergie mondiale devrait augmenter d'environ 30 TW d'ici 2050 à 46 TW d'ici 2100. Parmi les différents types de solutions d'énergie verte facilement accessibles, les cellules photovoltaïques (PV) pour la conversion de l'énergie solaire présentent un intérêt particulier pour les secteurs scientifiques et industriels. Parmi les technologies de cellules solaires développées, les cellules solaires pérovskites de troisième génération ont récemment attiré l'attention. Actuellement, l'efficacité des cellules solaires pérovskites à jonction unique est comparable à celle de la technologie du silicium cristallin de première génération. Toutefois, leur toxicité et leur stabilité à long terme restent la principale source d'inquiétude. Par conséquent, l'étude des matériaux pérovskites avec l'objectif d'adapter leur structure cristalline à la non-toxicité et à la haute efficacité est essentielle pour améliorer et évaluer le potentiel des cellules solaires.

Ainsi, la première partie de la thèse se concentre sur l'optimisation des pérovskites à base d'halogénures mixtes $CH_3NH_3PbI_{3-X}Cl_X$ avec différentes couches de transport à l'aide du programme SCAPS-1D. La deuxième partie se consacre d'une part à l'effet du remplacement des ions de plomb toxique dans la pérovskite $FAPbI_3$ afin d'obtenir le pérovskite $FASnI_3$ à haute performance. Et d'autre part, à l'effet de remplacement de la partie organique FA^+ par Cs^+. Leurs optimisations conduit à un rendement élevé avec différentes couches de transport. Pour améliorer les propriétés optoélectroniques et photovoltaïques, la thèse s'oriente ensuite vers l'étude par DFT et SCAPS des cellules solaires à doubles pérovskites Cs_2BiAgI_6, Cs_2CuSbX_6, Cs_2AgSbX_6 non-toxiques et thermodynamiquement stables avec différentes couches de transport.

Mots-clés : SCAPS-1D, DFT, CASTEP, Cellules solaires à pérovskite, Double pérovskite.

ABSTRACT

The The global energy demand is expected to increase by about 30 TW by 2050, reaching 46 TW by 2100. Among the various types of readily accessible green energy solutions, photovoltaic (PV) cells for solar energy conversion hold particular interest for both scientific and industrial sectors. Among the solar cell technologies developed, third-generation perovskite solar cells have recently gained attention. Currently, the efficiency of single-junction perovskite solar cells is comparable to that of first-generation crystalline silicon technology. However, their toxicity and long-term stability remain the main concerns. Therefore, studying perovskite materials with the aim of adapting their crystal structure for non-toxicity and high efficiency is essential to improve and assess the potential of solar cells.

Thus, the first part of the thesis focuses on optimizing mixed halide perovskites $CH_3NH_3PbI_{3-x}Cl_X$ with different transport layers using the SCAPS-1D program. The second part addresses, on the one hand, the effect of replacing toxic lead ions in the perovskite $FAPbI_3$ to obtain high-performance $FASnI_3$ perovskite, and on the other hand, the effect of replacing the organic FA^+ part with Cs^+. Their optimization leads to high efficiency with different transport layers. To improve the optoelectronic and photovoltaic properties, the thesis then focuses on the study by DFT and SCAPS of non-toxic and thermodynamically stable double perovskite solar cells $Cs2BiAgI_6$, $Cs2CuSbX_6$, $Cs2AgSbX_6$ with different transport layers.

Keywords : SCAPS-1D, DFT, Perovskite Solar Cells, double perovskite, CASTEP.

Résumé détaillé

La quantité d'énergie dans le monde devrait augmenter d'environ 30 TW d'ici 2050 à 46 TW d'ici 2100. Les sources d'énergies conventionnelles comme le charbon, le pétrole, le gaz naturel, etc., ne peuvent pas suivre les projections en raison de la demande toujours croissante. Par conséquent, une évaluation approfondie des sources d'énergies durables et renouvelables doit être menée pour répondre à la demande croissante en énergie. Parmi les diverses solutions d'énergies vertes facilement accessibles, les cellules photovoltaïques (PV) pour la conversion de l'énergie solaire suscitent un intérêt notable dans les secteurs scientifiques et industriels. Les cellules photovoltaïques peuvent gérer des demandes énergétiques importantes et leur puissance peut être intégrée dans les réseaux électriques. Par conséquent, il existe plusieurs technologies photovoltaïques en fonction du type de matériaux utilisés et du coût de fabrication associé. Cependant, le coût est également lié à l'abondance et à la facilité de traitement. Dans l'ensemble, de nombreuses activités de recherches visent à développer de nouveaux matériaux de bon marché permettant d'optimiser la structure des dispositifs photovoltaïques et optoélectroniques pour améliorer leur efficacité et diminuer leur prix de revient. Néanmoins, il est de la plus haute importance de trouver des absorbeurs de lumière respectueux de l'environnement avec des propriétés optoélectroniques idéales pour lutter contre les défis modernes qui incluent le réchauffement climatique. En général, les panneaux photovoltaïques seront des moyens efficaces de répondre aux besoins énergétiques futurs de manière durable.

Parmi les technologies de cellules solaires développées, les cellules solaires à pérovskite de troisième génération ont récemment attiré l'attention. Actuellement, l'efficacité des cellules solaires à pérovskite à jonction unique est comparable à la technologie établie du silicium cristallin de première génération. De plus, la solidité de la structure cristalline de la pérovskite rend la fabrication rentable avec des simples techniques de dépôt en couche mince à des températures relativement basses. Ainsi, les pérovskites modernes font actuellement preuve d'une grande assurance. Mais les lacunes de leur toxicité et de leur stabilité à long terme restent la plus grande préoccupation. Cependant, la structure cristalline des absorbeurs offre une accordabilité qui peut être modulée vers des cellules solaires à pérovskite non toxiques, stables et très efficaces. En fonction des rayons ioniques et des états d'oxydation, plusieurs substitutions dans les structures

cristallines de pérovskite sont recherchées pour remplacer les ions toxiques et instables dans les conditions de fonctionnement.

Par conséquent, l'étude des absorbeurs à pérovskite avec l'adaptation de sa structure cristalline à la non-toxicité et à un rendement élevé est essentielle pour évaluer le potentiel des cellules solaires à pérovskite (CSP). Cependant, l'influence de l'épaisseur, du dopage et des densités de défauts sur les performances des cellules solaires à pérovskite n'est pas bien comprise. Ainsi, les optimisations nécessaires pour améliorer le rendement (PCE) des CSP basées sur le logiciel SCAPS-1D sont évaluées. L'effet du remplacement des ions Pb toxiques par des ions Sn dans la structure cristalline de la pérovskite et les changements concomitants dans les performances doivent être évalués. Les performances théoriques en tenant compte des paramètres physiques sont discutées et optimisées avec le programme SCAPS-1D. Les performances des doubles pérovskites inorganiques et non toxiques sont optimisées et évaluées. De plus, les calculs DFT basés sur le logiciel CASTEP sont effectués sur les doubles pérovskites pour comprendre leurs propriétés optoélectroniques intrinsèques.

Ce travail de thèse présente une étude détaillée de l'effet des paramètres de divers couches constituées la cellule solaire à base des pérovskites (épaisseur, défauts, densité de dopage, conductivité, température, résistances R_S et R_P, coefficient d'absorption, réflexion, indice de réfraction…) sur ses performances. Le remplacement éventuel des ions toxiques Pb^{2+} dans ces pérovskites est examinées pour atténuer la toxicité. Aussi, le potentiel de diverses double pérovskites thermodynamiquement stables est étudié avec différentes couches expérimentalement réalisables.

L’objectif détaillé de ce travail de recherche est :

- Étudier l'effet de l'épaisseur, les défauts, la température et de la densité de dopage des couches constituant la cellule solaire à base de pérovskite $CH_3NH_3PbI_{3-X}Cl_X$.
- Vérifier les performances de la cellule solaire à base de matériau pérovskite $FAPbI_3$ en remplaçant le Pb^{2+} toxique par des ions métalliques Sn^{2+} ($FASnI_3$) pour obtenir à la fois un rendement élevé et une stabilité à long terme.
- Examiner les cellules solaires à base des matériaux doubles pérovskites par transmutation d'ions Pb^{2+} avec des cations monovalents et trivalents.
- Évaluer le potentiel de la double pérovskite Cs_2BiAgI_6 sans plomb, non toxique et stable avec diverses couches de transport de charge à savoir des électrons et des trous.
- Étudier le double pérovskite Cs_2CuSbX_6 thermodynamiquement stable (où X = I, Cl et Br) avec différentes couches de transport de charge.
- Remplacer les ions Cu^+ dans le double pérovskite Cs_2CuSbX_6 par des ions Ag^+ et étudier les propriétés optoélectroniques et photovoltaïques avec des études DFT et SCAPS.
- Utiliser les résultats obtenus à partir des calculs DFT comme paramètres d’entrés pour évaluer la capacité de la double pérovskite Cs_2AgSbX_6.

Initialement, le logiciel SCAPS-1D est utilisé pour effectuer une étude sur l'absorbeur pérovskite $CH_3NH_3PbI_3$-XClX avec :

- L'oxyde d'étain dopé au fluor (FTO) comme oxyde conducteur transparent.
- TiO_2 comme ETL.
- Spiro-OMeTAD organique coûteux et du thiocyanate de cuivre inorganique bon marché (CuSCN) comme HTL.
- Diverses contre-électrodes pour construire expérimentalement une structure CSP haute performance.

Le rendement de la cellule à base de cette pérovskite dépasse 30% qui est simulé avec des matériaux à faible coût connus pour leur traitement simple et efficace (Figure 1).

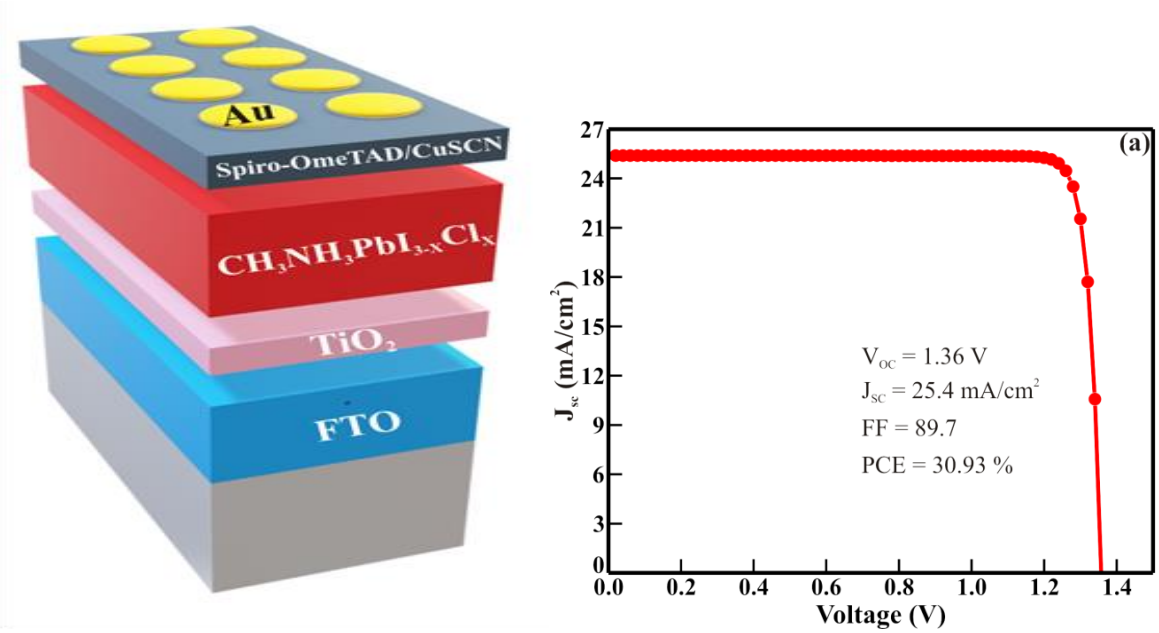

Figure 1. Optimisation de la structure de la cellule solaire à base de pérovskite $CH_3NH_3PbI_3$-XClX et la courbe *J-V* associée démontrant un PCE de ~30%.

La plupart des matériaux pérovskites à haute performance contiennent du plomb cancérigène (Pb). Ce qui facilite l'absorption directe intense de la lumière visible provenant des 6s remplis au maximum de la bande de valence et de l'orbitale 6p vide au minimum de la bande de conduction du cation Pb divalent. Par conséquent, le Pb a été remplacé par des cations divalents d'étain (Sn^{2+}) ou de germanium (Ge^{2+}) pour atténuer la toxicité. Expérimentalement, l'iodure de plomb α-formamidinium (α-$FAPbI_3$) a montré un PCE plus élevé de 25,2 %, mais l'inclusion de Pb peut entraver son utilité. Ainsi, lorsque le Pb^{2+} est remplacé par le Sn^{2+} pour former de l'iodure de formamidinium et d'étain ($FASnI_3$), le PCE décroit à ~14%. Cependant, l'inclusion de FA réduit la stabilité à long terme des cellules solaires à pérovskite (CSP). Par conséquent, après plusieurs études, tous les pérovskites inorganiques sans Pb, à savoir l'iodure de césium et d'étain ($CsSnI_3$) sont avérés être les plus appropriés en raison des propriétés intrinsèques supérieures de $CsSnI_3$ (telles que la bande interdite étroite (1,3 eV) et la plus grande mobilité des porteuses). Expérimentalement, l'efficacité des CSP à base de $CsSnI_3$ diminue encore à ~10 %. D'autre part, les couches de transport (électrons et trous) jouent un rôle important dans la délivrance de PCE élevés dans les CSP. Cependant, l'alignement de bande et la mobilité des porteurs sont essentiels à l'interface de la couche de transport pour le transfert des charges photogénérées. Par conséquent, il est nécessaire d'évaluer le potentiel des CSP basées sur $CsSnI_3$ par rapport aux CSP basées sur

$FAPbI_3$ et $FASnI_3$. Le logiciel SCAPS-1D est utilisé pour déterminer le potentiel des absorbeurs $FAPbI_3$, $FASnI_3$ et $CsSnI_3$. Leurs examinations avec divers ETL (à savoir le dioxyde de titane (TiO_2), l'oxyde d'étain (SnO_2), le stannate de baryum ($BaSnO_3$/BSO) et le BSO dopé au lanthane (La-BSO) avec du thiocyanate de cuivre (CuSCN) comme couche de transport de trous standard), permettent de fabriquer expérimentalement des CSP de haute performance. De plus, les paramètres physiques (l'épaisseur, le dopage et les densités de défauts) sont modifiés pour que les couches de CSP produisent des performances élevées. Les pérovskites $FAPbI_3$ et $FASnI_3$ sont hautement compatibles avec l'ETL SnO_2 et fournissent davantage un PCE optimisé supérieur à 25 % et 27 %, respectivement. Tandis que le $CsSnI_3$ affiche un PCE le plus élevé (~23 %) avec l'ETL La-BSO. Sachant que le PCE de $FAPbI_3$ ait dépassé 25 %. Donc, il est impératif de développer des techniques pour améliorer les performances de $CsSnI_3$, qui est entravé par sa faible solubilité dans les solvants précurseurs standards. Ainsi, des stratégies telles que la synthèse assistée par vapeur et les solvants mixtes peuvent être utilisées pour uniformiser les films $CsSnI_3$ avec une faible densité de défauts apparents (Figure 2).

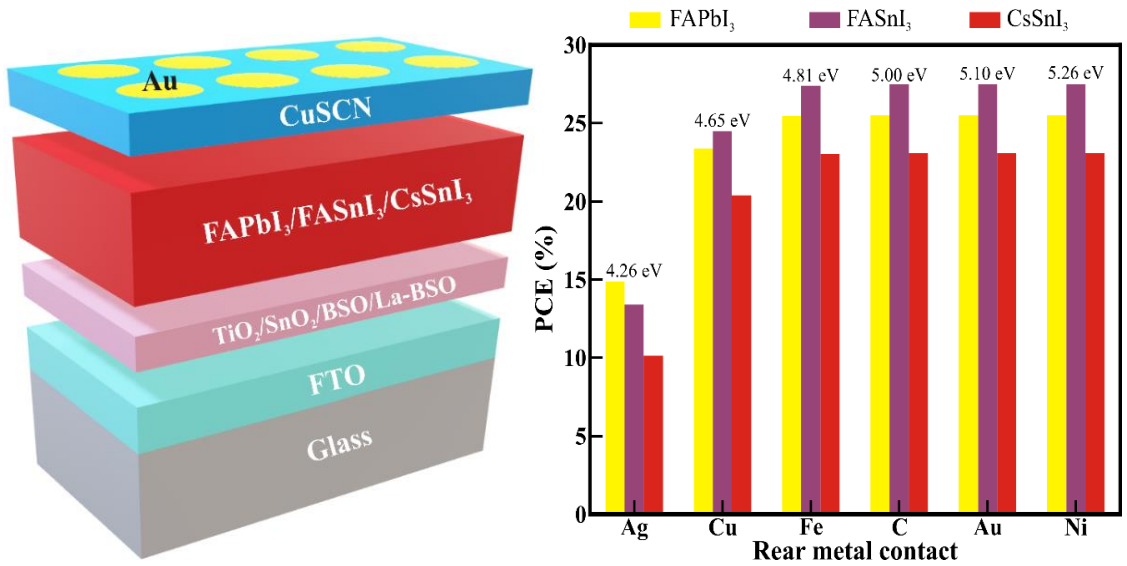

Figure 2. Schéma du dispositif envisagé pour remplacer les ions plomb toxiques par des ions Sn et le rendement de chaque pérovskite avec différents métaux.

Outre la substitution directe des ions Pb, plusieurs pérovskites non toxiques de plus faible dimension sans plomb (0D et 2D) obtenues par substitution hétérovalente de Pb^{2+} par Bi^{3+} ou Sb^{3+}. Les doubles pérovskites (3D) sont étudiées pour leur aptitude à absorber la lumière. Parmi toutes

les alternatives des pérovskites sans plomb obtenues par transmutation du cation M^{2+} avec une combinaison de cations monovalents et trivalents donnent une double pérovskite (3D) de formule chimique $A_2M'M''X_6$ (où A, M′, M" et X sont respectivement un cation monovalent, un ion métallique monovalent, un ion métallique trivalent et un halogène). La structure à double pérovskite (3D), qui cristallise dans le système cristallin cubique avec groupe d'espace $Fm\bar{3}m$. Selon les combinaisons M′ et M", la double pérovskite aux halogénures sans plomb peut être classée comme :

(i) Azote/métaux alcalins (M′ = Sb^{3+}, Bi^{3+} et M" = N^+, K^+).

(ii) Famille de l'azote/métaux de transition (M′ = Sb^{3+} et Bi^{3+} et M" = Tl^+, In^+).

(iii) Métaux post-transitionnels/nobles (M′ = In^{3+}, Ga^{3+} et M" = Cu^+, Ag^+).

(iv) Famille de l'azote/métaux nobles (M′ = Sb^{3+}, Bi^{3+} et M" = Cu^+, Ag^+).

Dans les doubles pérovskites, Les conditions théoriques d'une structure stable sont $\mu > 0{,}41$(facteur octaédrique) et $0{,}75 < t < 1$ (facteur de tolérance). Ainsi, l'atome de Pb peut être remplacé par une substitution hétérovalente Bi et Ag pour former des structures cristallines de double pérovskite Cs_2BiAgI_6. De plus, les doubles pérovskites $Cs_2BiAgCl_6$ et $Cs_2BiAgBr_6$ sont synthétisées expérimentalement via des réactions à l'état solide et un traitement en solution chimique et physique. De telles doubles pérovskites cristallisent en structure elpasolite (double pérovskite cubique symétrique centrée sur la face, avec des octaèdres occupant les sommets), avec des Cs au milieu de la cavité cubique-octaédrique. Les centres des octaèdres sont occupés par Bi ou Ag, alternant dans une configuration (rock-salt) rendant les propriétés de transport des porteurs isotropes. Le logiciel SCAPS-1D est utilisé pour modéliser et examiner les cellules solaires à doubles pérovskite avec trois couches de transport de trous (HTL) distinctes (c'est-à-dire MoO_3, CuSCN et spiro-OMeTAD). La structure modélisée du dispositif est FTO/AZnO (ETL)/Cs_2BiAgI_6/HTLs (MoO_3, CuSCN, spiro-OMeTAD) /contact arrière métallique (Au, C, Ag, Fe, Ni, Cu) (Figure 3). Les cellules solaires à double pérovskite à base de Cs_2BiAgI_6 sont optimisées en termes d'épaisseur, de volume et de densités de dopage, avec trois HTL distincts et AZnO comme ETL.

Par rapport à tous les paramètres physiques modifiés lors de l'optimisation, l'épaisseur et la densité des défauts de Cs_2BiAgI_6 avaient la plus grande influence sur ses performances. Les

électrodes de carbone bon marché et économiques pourraient fournir un PCE de ~29 % dans la cellule solaire à double pérovskite à base de Cs_2BiAgI_6. De plus, même lorsque la température de fonctionnement atteint 400 K, notre cellule fourni un PCE de ~26 %.

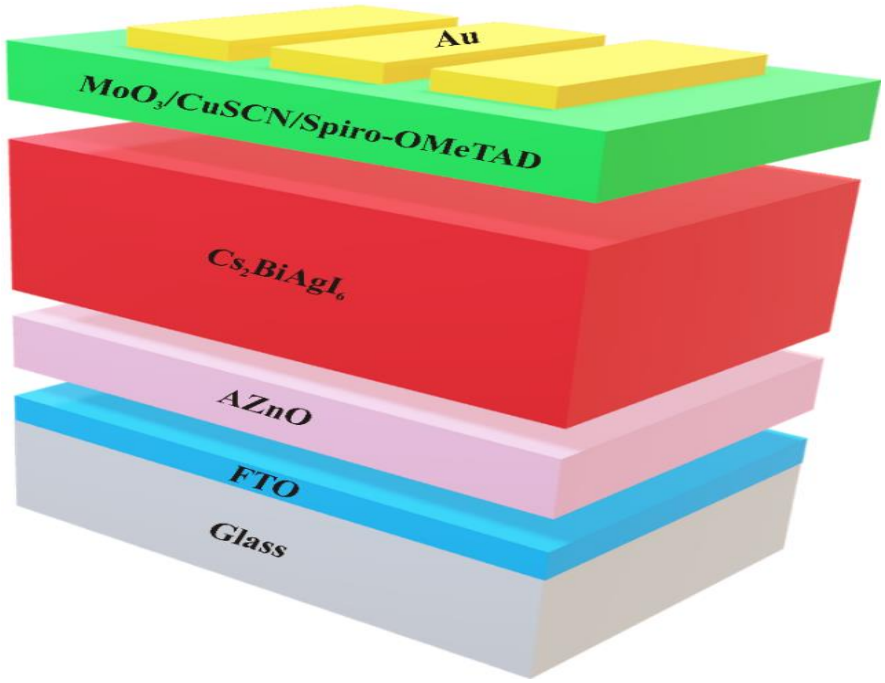

Figure 3. Schéma du dispositif de la cellule solaire à base de matériaux double pérovskite Cs_2BiAgI_6.

Parmi les permutations possibles, la majorité des matériaux à double pérovskite sont thermodynamiquement instables ou ont une large bande interdite. Cependant, plusieurs méthodes, y compris l'alliage dilué, le dopage sur le *site* M″ et le réglage assisté par pression, sont exploitées pour adapter la bande interdite à l'absorption de la lumière visible. La double pérovskite Cs_2CuSbX_6 (où X = Cl, Br et I) a potentiellement une faible bande interdite et offrent d'excellentes caractéristiques optoélectroniques. L'évaluation computationnelle de notre cellule est effectuée à l'aide du logiciel SCAPS-1D. Le potentiel des différentes doubles pérovskites, à savoir $Cs_2CuSbCl_6$, $Cs_2CuSbBr_6$ et Cs_2CuSbI_6, est évalué avec de l'oxyde de zinc dopé Aluminium (AZnO) comme couche de transport d'électrons (ETL), MoO_3/Cu_2O comme HTL et divers contacts arrière (Figure 4). De plus, en raison d'un meilleur alignement des bandes et d'un protocole de synthèse industriellement réalisable, MoO_3 et Cu_2O ont été largement étudiés pour extraire des trous vers la bonde externe. De plus, la nature inorganique de ces derniers peut améliorer la stabilité

à long terme de notre cellule par rapport au spiro-OMeTAD organique traditionnellement utilisé. Expérimentalement, ils sont connus pour améliorer l'extraction de charge dans les cellules solaires à pérovskite.

Les cellules solaires à double pérovskites Cs_2CuSbX_6 sont évaluées en ajustant l'épaisseur et la densité des défauts des couches suivantes pour extraire un PCE plus élevé (Figure 4). Pour l'évaluation, la température de fonctionnement est variée et les fluctuations de performance concernées sont également étudiées. Le dispositif simulé avec le double pérovskite Cs_2CuSbI_6 démontre un PCE de ~27%.

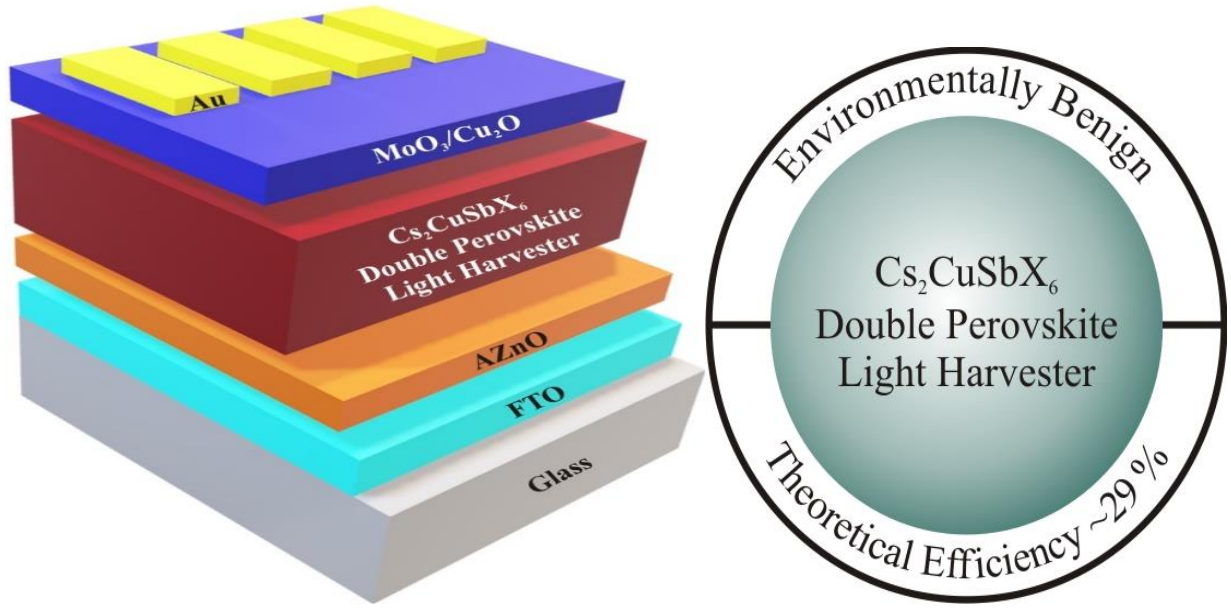

Figure 4. Schéma de la cellule solaire à double pérovskite Cs_2CuSbX_6 optimisée produisant un PCE de ~29%.

De même, les doubles pérovskites Cs_2AgSbX_6 ont été examinées pour leur efficacité à capter la lumière. En raison de la faisabilité industrielle (protocole de synthèse), les propriétés optoélectroniques et l'alignement de bande approprié avec l'oxyde de zinc dopé à l'aluminium (AZO) comme couches de transport d'électrons (ETL) et l'oxyde de molybdène (MoO_3) comme couches de transport de trous (HTL) ont été déterminés. La compréhension fondamentale des propriétés optoélectroniques intrinsèques de Cs_2AgSbX_6 a été initialement comprise sur la base des calculs DFT (par le biais du Cambridge Serial Total Energy Package). Ainsi que sa structure électronique et ses caractéristiques physiques ont été examinée avec le SCAPS-1D. Les performances de Cs_2AgSbX_6 ont été estimées avec une structure de dispositif comprenant de

l'oxyde d'étain dopé au fluor (FTO)/AZnO/ Cs_2AgSbX_6 /MoO_3/contact arrière (Figure 5). L'analyse DFT a montré l'accordabilité de la bande interdite avec d'autres propriétés optoélectroniques bénéfiques de la double pérovskite Cs_2AgSbX_6. Le rendement le plus élevé est de ~29,9 %, ~28,2 % et ~27,2 % a été estimé pour les doubles pérovskites Cs_2AgSbI_6, $Cs_2AgSbBr_6$ et $Cs_2AgSbCl_6$, respectivement.

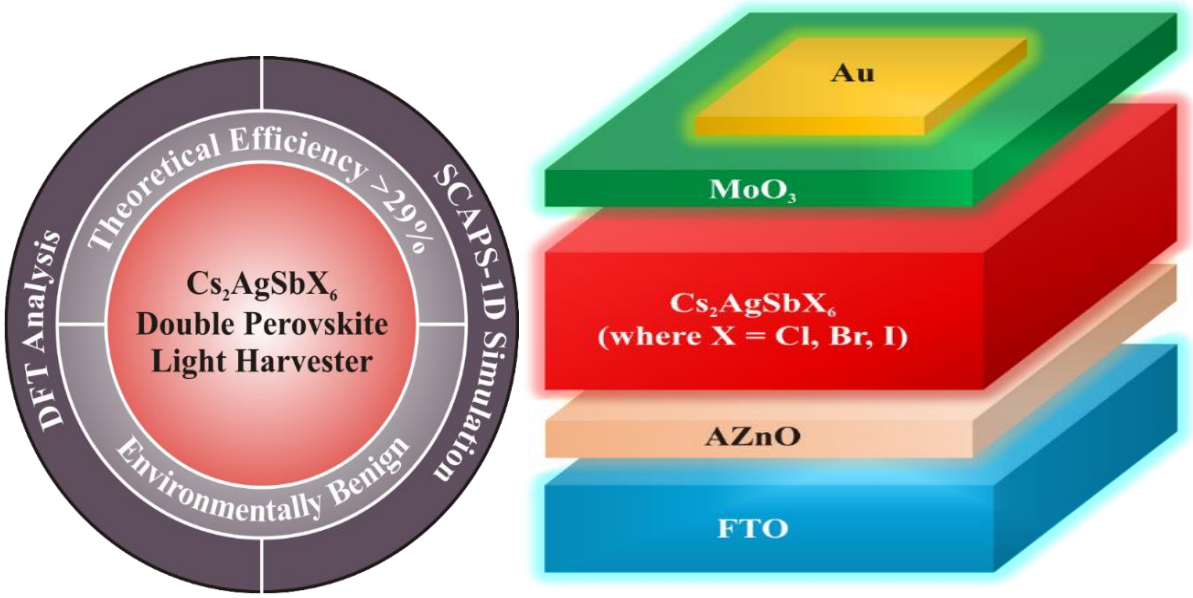

Figure 5. Schéma de la cellule solaire à double pérovskite Cs_2AgSbX_6 optimisée par les calculs DFT et SCAPS produisant un PCE de ~29%

La thèse a empilé un total de huit chapitres.

La vue d'ensemble de l'énergie solaire et l'évolution des différentes générations de technologie des cellules solaires sont brièvement abordées au **chapitre 1**. L'importance des cellules solaires à pérovskite, leurs architectures réalisables et leurs mécanismes de fonctionnement sont discutés en détail. La motivation et les objectifs du travail de recherche sont exposés à la fin de ce chapitre.

Le chapitre 2 est axé sur les techniques de simulation, qui sont utilisées pour réaliser le travail de thèse. Le logiciel SCAPS-1D développé à l'Université de Gand a été largement utilisé pour la simulation de cellules solaires à hétérojonction. L'algorithme de fonctionnement du logiciel SCAPS-1D est également décrit. Le logiciel CASTEP a été utilisé pour étudier les propriétés optoélectroniques des pérovskites.

Le chapitre 3 est consacré à l'optimisation et à l'étude de pérovskite aux halogénures mixtes à base de CH3NH3PbI3-XClX avec différentes couches de transport à l'aide du programme SCAPS-1D.

Le chapitre 4 se concentre d'une part sur l'effet du remplacement des ions de plomb toxiques dans la pérovskite $FAPbI_3$ et d'autre part sur son optimisation pour obtenir un rendement élevé avec diverses couches de transport des électrons et des trous.

Le chapitre 5 se consacre aux doubles pérovskites pour leurs applications photovoltaïques. Le logiciel SCAPS-1D est utilisé pour atteindre une efficacité théorique élevée.

Le chapitre 6 développe l'optimisation des cellules solaires à double pérovskite thermodynamiquement stables et non toxiques avec différentes couches de transport. L'effet des paramètres physiques sur les performances du dispositif est présenté en détail.

Le chapitre 7 décrit l'étude des propriétés optoélectroniques des doubles pérovskites par le calcul DFT à l'aide du logiciel CASTEP. Les résultats obtenus sont validés et utilisés pour estimer le potentiel des cellules solaires.

Le chapitre 8 comprend la conclusion générale et les perspectives.

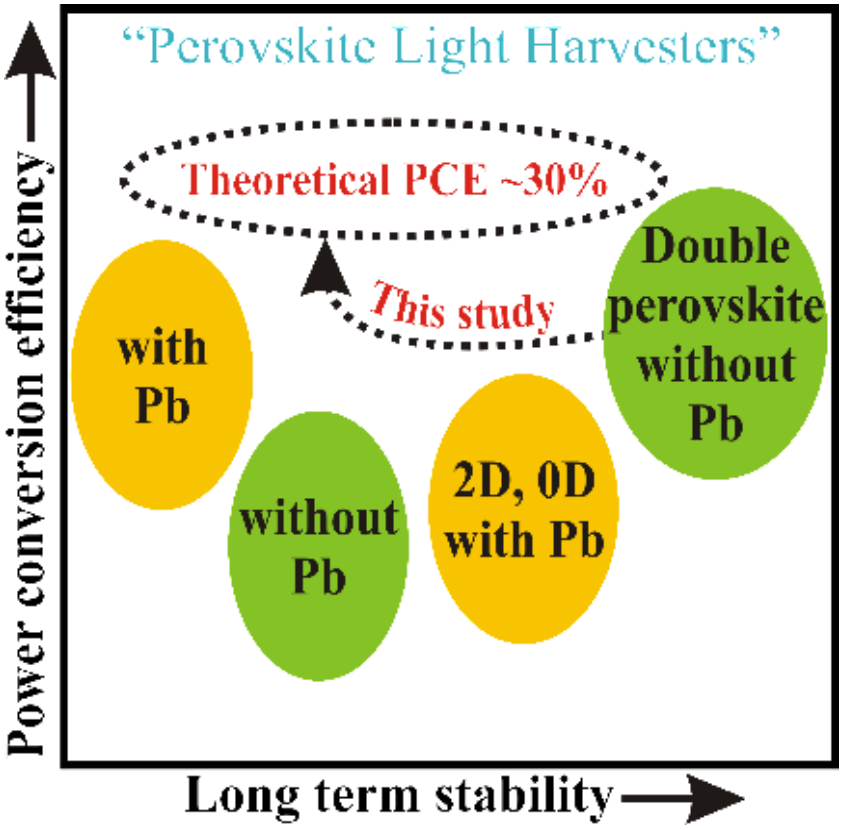

Les conclusions de ce travail de recherche sont :

Dans l'ensemble, l'approche actuelle consistant à utiliser le logiciel SCAPS-1D pour optimiser les cellules solaires à pérovskite avec un rendement élevé et aussi pour leurs applications dans les dispositifs optoélectroniques. Les pérovskites organiques-inorganiques ont fait d'énormes progrès au cours de la dernière décennie. Les cellules solaires à jonction unique avec des absorbeurs en pérovskite ont atteint des rendements supérieurs à 25 %. Une optimisation des couches minces dans les cellules solaires à pérovskite est essentielle pour atteindre des rendements de conversion plus élevés atteignant la limite de Shockley-Queisser.

Nous présentons les études sur la façon dont l'épaisseur et les propriétés du film mince peuvent être ajustées pour atteindre des rendements supérieurs à 30 %. Nous avons utilisé le logiciel SCAPS-1D pour optimiser l'épaisseur, les densités des donneurs, les défauts et les densités d'accepteurs de chaque film mince des cellules solaires à pérovskite. L'épaisseur et les densités de défauts de l'absorbeur $CH_3NH_3PbI_3$-XClX avaient le plus grand effet sur les rendements. Ainsi que, l'épaisseur et les densités d'accepteur de trous (couches HTL) avaient le moindre effet sur l'efficacité énergétique. Nous avons également étudié la variation de rendement en fonction de la température et d'autres paramètres de la cellule solaire. Pour combler l'effet de l'électrode en or coûteuse, nous avons comparé la variation de ce rendement avec des métaux (Au, C, Pt, Fe, Ni, Ag…) (Figure 6).

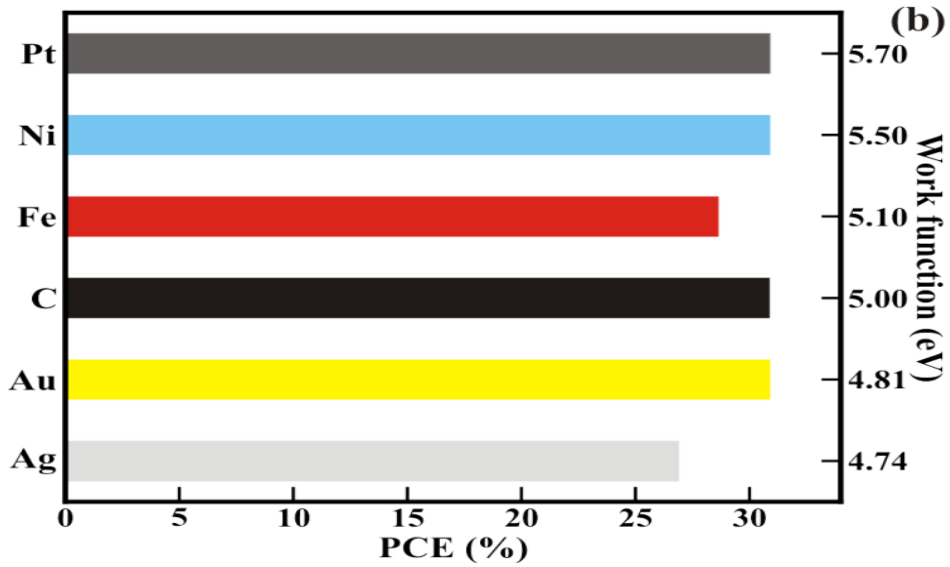

Figure 6. Variation de PCE en fonction des différentes électrodes.

Aussi, une étude comparative des trois pérovskites $FAPbI_3$, $FASnI_3$ et $CsSnI_3$ avec le logiciel SCPAS-1D est envisagée avec une approche vers des pérovskites stables et sans danger pour l'environnement. De plus, pour extraire les meilleures performances, chaque pérovskite est analysée avec quatre couches de transport d'électrons (TiO_2, SnO_2, $BaSnO_3$ et $BaSnO_3$ dopé au La) (Figure 7). Les paramètres physiques tels que l'épaisseur, le dopage et la densité des défauts sont optimisés afin d'offrir des performances élevées. En outre, la variation de l'efficacité en fonction de la température et d'autres paramètres des cellules solaires est également analysée.

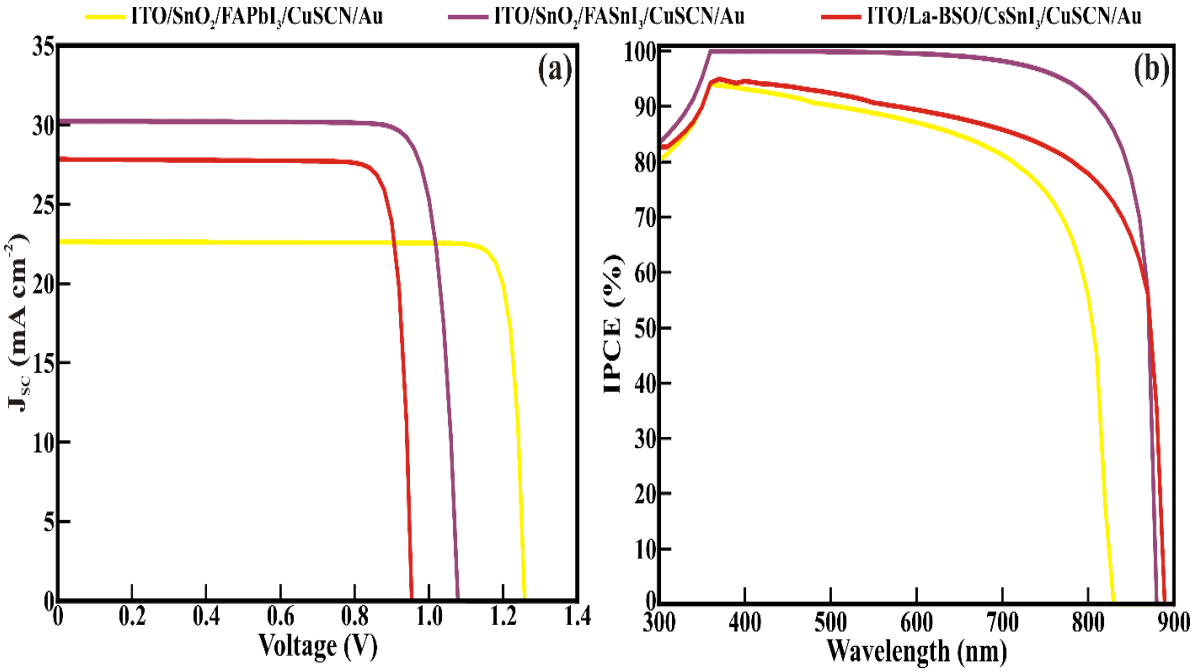

Figure 7. a. Courbe J-V, **b.** Courbe de PCE des CSP avec ITO/SnO_2FAPbI3/CuSCN/Au, ITO/SnO_2/$FASnI_3$/CuSCN/Au et ITO/La-BSO/$CsSnI_3$/CuSCN/Au.

Récemment, l'efficacité des cellules solaires à pérovskite à jonction unique a été en concurrence avec les cellules solaires cristallines Si. Cependant, les pérovskites sont toxiques et sensibles à l'humidité. Les cellules solaires à double pérovskite optimisées à base de Cs_2BiAgI_6 avec trois couches de transport de trous (HTL) distinctes (MoO_3, CuSCN et spiro-OMeTAD) et avec AZnO comme couche de transport d'électrons (ETL) offrent un rendement de conversion de puissance supérieur à 29 % (Figure 8). De plus, une variété d'électrodes arrière est explorée et leur effet sur les performances est estimé. La variation de PCE en fonction la température de

fonctionnement est étudiée. L'épaisseur de ce dernier et la densité des défauts apparents sont les clés pour atteindre des rendements élevés.

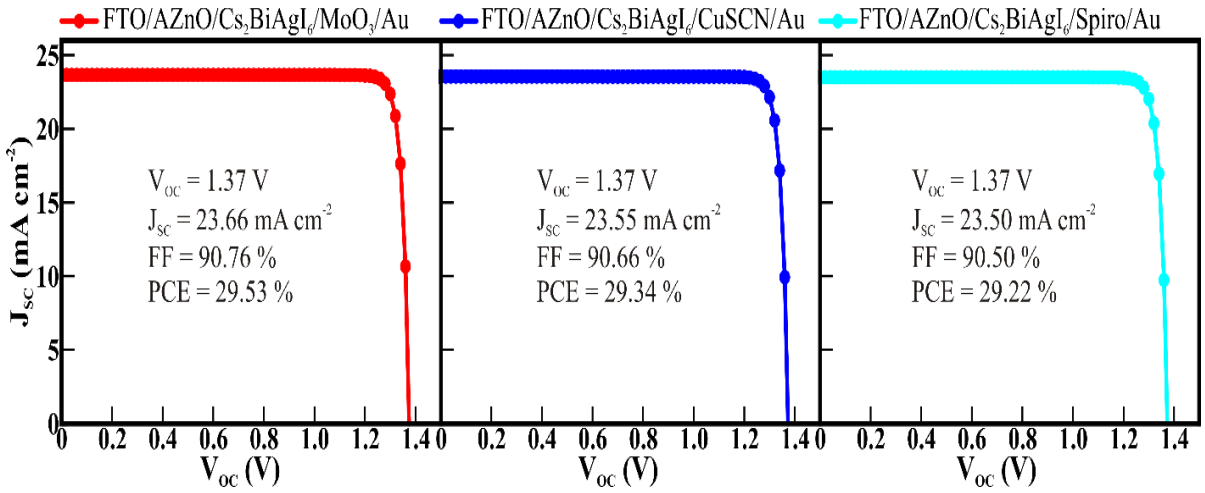

Figure 8. Courbe de J-V de Cs_2BiAgI_6-avec différentes couches de transport HTL (MoO_3/CuSCN/Spiro-OMeTAD).

Les principaux problèmes entravant la commercialisation des cellules solaires à pérovskite nous oblige à trouver un absorbeur fiable, respectueux de l'environnement et offrant une stabilité durable. Nous présentons dans ce travail des doubles pérovskites Cs_2CuSbX_6 stables et sans plomb (où X = Cl, Br et I) dans le but d'avoir une excellente efficacité et une bonne stabilité thermodynamique. Les densités des défauts des dopants ainsi que l'épaisseur des couches des cellules solaires à double pérovskite Cs_2CuSbX_6, sont modifiées pour extraire un rendement élevé d'environ 29 % (avec ZnO dopé à l'aluminium comme couche de transport d'électrons et MoO_3 et Cu_2O comme couches de transport de trous) (Figure 9). Plusieurs électrodes (contact-arrière) ainsi que la résistance série et parallèle sont également étudiées et leur impact sur les performances est évalué.

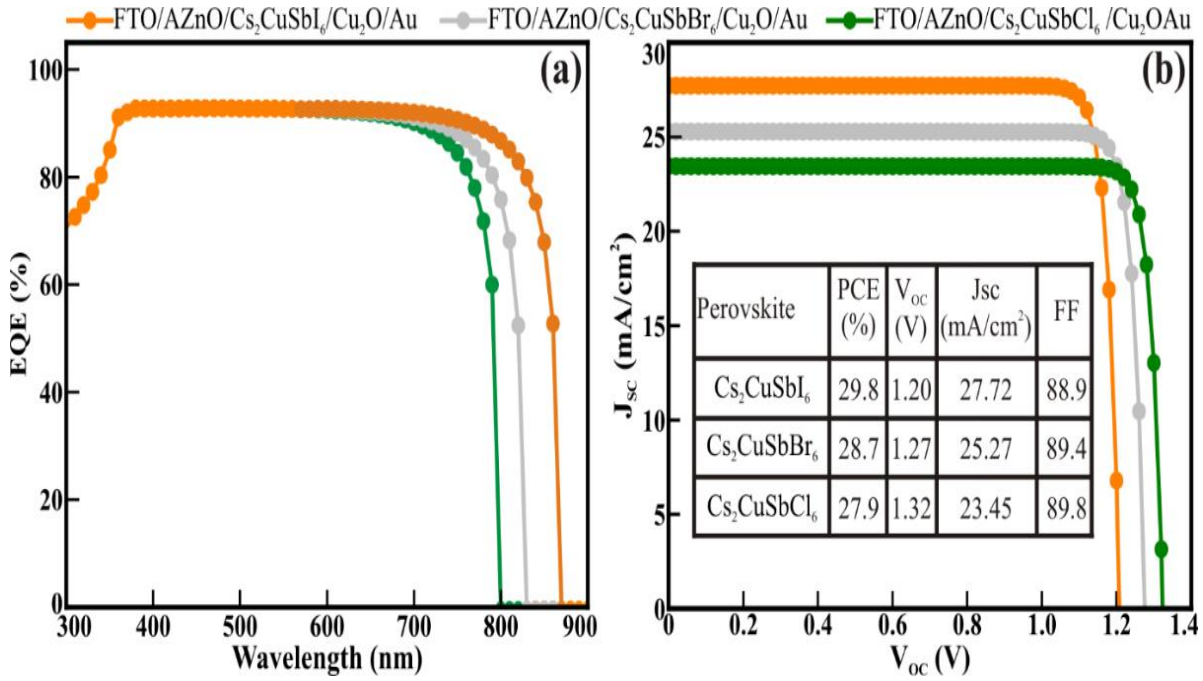

Figure 9. a. Rendement quantique (EQE) de la cellule solaire à base de double pérovskite Cs_2CuSbX_6. **b.** Courbe J-V avec Cu_2O comme HTL.

Par la suite, Nous étudions le double pérovskite Cs_2AgSbX_6 (où X = Cl, Br et I) stable et non toxique avec le logiciel CASTEP (DFT). La bande interdite (indirecte), les changements associés dans la densité d'états (DOS) et les propriétés optiques et électriques ont été explorés. Les résultats obtenus ont ensuite été introduits dans SCAPS-1D afin d'évaluer le potentiel de la cellule solaire. Avec la structure FTO/AZnO/Cs_2AgSbX_6/MoO_3/Au, l'épaisseur et la densité des défauts apparents de Cs_2AgSbX_6 avaient un impact élevé sur les performances de la cellule solaire. Le rendement le plus élevé de ~29,9 % a été estimé pour les couches de transport de trous MoO_3 et Cu_2O (Figure 10). De plus, l'efficacité de plusieurs électrodes arrière a été examinée (Figure 11).

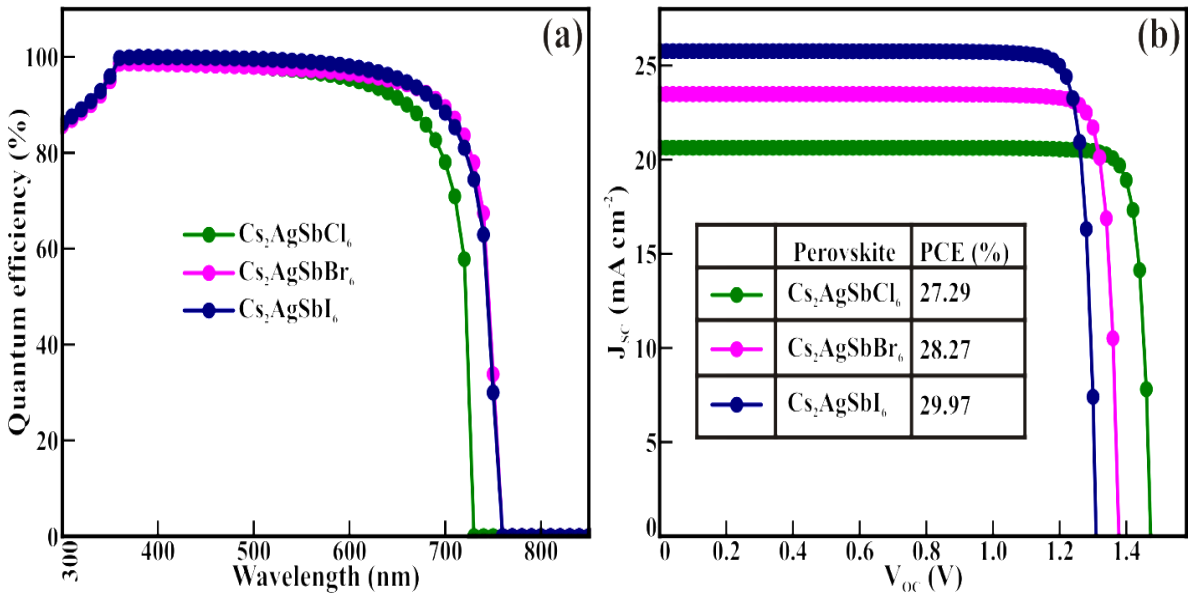

Figure 10. a. Rendement quantique (EQE) de la cellule solaire à base de double pérovskite Cs_2AgSbX_6. **b.** Courbe J-V avec MoO_3 comme HTL.

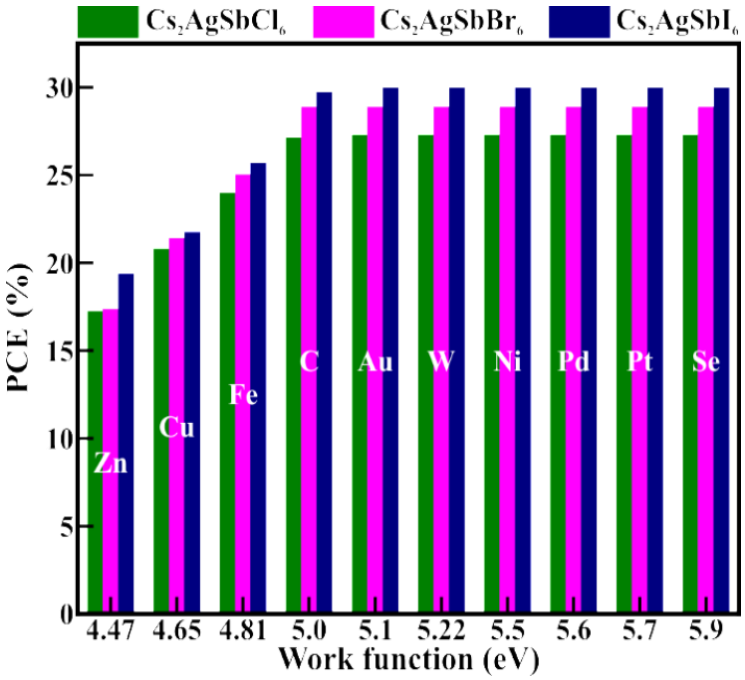

Figure 11. Variation de PCE en fonction des différentes électrodes

LIST OF PUBLICATIONS

PAPER-1

Alla, M., Manjunath, V., Chawki, N., Singh, D., Yadav, S. C., Rouchdi, M., & Boubker, F. (2022). Optimized $CH_3NH_3PbI_{3-X}Cl_X$-based perovskite solar cell with theoretical efficiency exceeding 30%. ***Optical Materials, 124,* 112044.**

PAPER-2

Alla, M., Bimli, S., Manjunath, V., Samtham, M., Kasaudhan, A., Choudhary, E., Rouchdi, M., & Boubker, F. (2022). Towards lead-free all-inorganic perovskite solar cell with theoretical efficiency approaching 23%. ***Materials Technology, 37,* 2963-2969.**

PAPER-3

Alla, M., Manjunath, V., Choudhary, E., Samtham, M., Sharma, S., Shaikh, P. A., Rouchdi, M., & Fares, B. (2023). Evaluating the potential of lead-free nontoxic Cs_2BiAgI_6-based double perovskite solar cell. ***physica status solidi (a), 220,* 2200642.**

PAPER-4

Alla, M., Bimli, S., Manjunath, V., Choudhary, E., Sharma, S., Wakale, G. R., Miglani, A., Rouchdi, M., & Fares, B. (2023). Examining the potential of non-toxic stable double perovskite solar cells based on Cs_2CuSbX_6. ***Materials Today Communications, 36,* 106608.**

PAPER-5

Alla, M., Mishra, O. P, Wakale, G. R., Choudhary, E., Manjunath, V., Hossain, M. K., Rouchdi, M., & Fares, B. (2023). Non-toxic and stable double perovskite solar cells based on Cs2AgSbX6 light harvester First principle calculations-aided theoretical estimation. ***Advanced Theory and Simulations,* 7, 2300605.**

PAPER -6

Alla, M., Choudhary, E., Sharma, R., Koppala, S., Manjunath, V., Rouchdi, M., & Boubker, F. (2024). DFT studies abided numerical assessment of stable ternary Al_2CdX_4 (where X = S, Se, Te) chalcogenides for thin film photovoltaics. ***Materials Today Communications***, 39, 108648.

PAPER-7

N Chawki, M Rouchdi, **M Alla,** B Fares. (2023) Simulation and analysis of high-performance hole transport material SrZrS3-based perovskite solar cells with a theoretical efficiency approaching 26% software. ***Solar Energy***, 262, 111913.

PAPER-8

N Chawki, M Rouchdi, **M Alla,** B Fares. (2024) Numerical Modelling of a novel solar cell system consisting of electron Transport material (ETM)/CaZrS3-based chalcogenide perovskites using SCAPS-1D software. ***Solar Energy***, 274, 112592.

PAPER-9

F ELFATOUAKI, R Takassa, M **Alla**, O Farkad, A EL Mouncharih, S Hassine, S Giusepponi, El Ibnouelghazi, A Outzourhit, D Abouelaoualim. (2024) Enhancing Perovskite Solar Cells Performance through investigation of Ruddlesden-Popper (2D) Cs2GeI2Br2 and (3D) CsGeI2Br absorbers ***The Journal of Physical Chemistry ACS*, *(in peer-reviewed process).***

PAPER-10

S Dar, **M Alla,** B Sengar. (2024) Breakthrough in Sustainable Photovoltaics: Achieving 30.86% Efficiency with Innovative Lead-Free Bilayer Perovskite Solar Cells Using SCAPS-1D and DFT Framework. ***Renewable Energy. (in peer-reviewed process).***

LIST OF COMUNICATIONS

1-M Alla, M Rouchdi, B Fares. DFT and SCAPS study of CsSnI3 Based perovskite solar cell, International Conference (New Frontiers of Natural Sciences) Selcuk university KONYA-TURKIYA. On Oct 17-19,2022.

2-M Alla, M Rouchdi, B Fares. Simulation and Analysis of MASnBr3 Based perovskite solar cell, The 2nd International Conference on Mechanics, Materials and Energy MME; ENSA El JADIDA -MOROCCO. On March 15-17,2022.

3- M Alla, M Rouchdi, B Fares. Defect Study and Modelling of Cs2AgSbF6 Based perovskite solar cell with efficiency exceeding ~28 %. The Second Edition of International Conference (On Circuit, Systems and Communication) university Sidi Mohamed Ben Abdellah Faculty of Sciences DHAR EL MAHRAZ, FEZ-MOROCCO. On July 07-08,2023.

4- M Alla, M Rouchdi, B Fares. Hight Stability in Cs2AgBiBr6 double perovskite solar cell with efficiency exceeding ~27 % International Multidisciplinary Doctorial Days, University of Ibn TOFAIL, KENITRA -MOROCCO. On February 24-26,2023.

5- M Alla, M Rouchdi, B Fares. Optimized CsSnBr3 based perovskite solar cell with efficiency approaching 30, national Doctorial Days, University Mohammed V Faculty of Sciences RABAT-MOROCCO. On November 24-26,2022.

6- M Alla. Applications of Semiconductors, Photovoltaic, Power electronics. national Doctorial Days, University Mohammed V Faculty of Sciences RABAT-MOROCCO. On May 15-20,2023.

7- M Alla. Numerical Analysis of Perovskite-based Prospective light Harvesters for photovoltaic applications. national Doctorial Days, University Mohammed V Faculty of Sciences RABAT-MOROCCO. On July 1-7,2024.

LIST OF FIGURES

Figure 1.1 Schematic depicting the crystal structure of organic-inorganic perovskite light harvesters.

Figure 1.2 Schematics depicting tunable bandgap of the perovskite light harvesters.

Figure 1.3 Schematics depicting the (a) mesoporous and (b) planar PSCs.

Figure 1.4 Schematics illustrating different synthesis techniques employed to fabricate perovskite light harvester.

Figure 2.1 Image depicting the front-end interface of the 1D-SCAPS program.

Figure 2.2 Image depicting the definition panel of the 1D-SCAPS program.

Figure 2.3 Image depicting the layer properties panel in the 1D-SCAPS program.

Figure 3.1 (a) Schematic representation and (b) Corresponding energy band diagram of the PSC device adopted in this study.

Figure 3.2 Thickness and the donor density of FTO layer dependent variation of solar cell parameters. (with other parameters as tabulated in Table 3.1)

Figure 3.3 Thickness and the donor density of the TiO_2 layer. . (with other parameters as tabulated in Table 3.1)

Figure 3.4 Thickness and the defect density of $CH_3NH_3PbI_{3-X}Cl_X$ perovskite light absorber layer dependent variation of solar cell parameters. (with other parameters as tabulated in Table 3.1)

Figure 3.5 Thickness and acceptor density of Spiro-OMeTAD layer-dependent variation of solar cell parameters. (with other parameters as tabulated in Table 3.1)

Figure 3.6 Thickness and acceptor density of CuSCN layer dependent variation of solar cell parameters. (with other parameters as tabulated in Table 3.1)

Figure 3.7 (a) Operating temperature-dependent variation of solar cell parameters. (with other parameters as tabulated in Table 3.1) (b) Variation in PCE depending on the counter electrode material.

Figure 3.8 (a) Shows the JV curve and (b) Quantum efficiency for the best performing FTO/TiO_2/$CH_3NH_3PbI_{3-X}Cl_X$/CuSCN/Au device structure.

Figure 4.1 Schematics depicting the PSC device architecture modeled in this study.

Figure 4.2 Absorption co-efficient of various ETLs (TiO_2, SnO_2, BSO, and La-BSO) and PLHs ($FAPbI_3$, $FASnI_3$, and $CsSnI_3$).

Figure 4.3 The effect of thickness of various ETLs on the performance of PSCs with (a) $FAPbI_3$, (b) $FASnI_3$, and (c) $CsSnI_3$ perovskite light absorbers.

Figure 4.4 The effect of donor doping density in various ETLs on the performance of PSCs with (a) $FAPbI_3$, (b) $FASnI_3$, and (c) $CsSnI_3$ perovskite light absorbers.

Figure 4.5 The effect of (a) $FAPbI_3$, (b) $FASnI_3$, and (c) $CsSnI_3$ perovskite harvester thickness on the performance of PSCs.

Figure 4.6 The effect of defect density in (a) $FAPbI_3$, (b) $FASnI_3$, and (c) $CsSnI_3$ PLHs on the performance of PSCs.

Figure 4.7 Variation in PCE depending on the counter electrode material with high-performance ETLs.

Figure 4.8 The effect of operating temperature on PSCs with (a) $FAPbI_3$, (b) $FASnI_3$, and (c) $CsSnI_3$ PLHs on the performance of PSCs.

Figure 4.9 (a) J-V curves and (b) IPCE curves of the PSCs with ITO/$SnO_2$$FAPbI_3$/CuSCN/Au (yellow color), ITO/SnO_2/$FASnI_3$/CuSCN/Au (wine color) and ITO/La-BSO/$CsSnI_3$/CuSCN/Au (red color).

Figure 5.1 Schematic depicting the device structure of Cs_2BiAgI_6 double perovskite solar cells considered in the present study.

Figure 5.2 (a) Thickness and (b) donor doping density of AZnO layer-related deviation of solar cell parameters (with other parameters as tabulated in Table 5.1)

Figure 5.3 (a) Thickness and (b) bulk defect density of Cs_2BiAgI_6 double perovskite absorber-related deviation of solar cell parameters (with other parameters as tabulated in Table 5.1).

Figure 5.4 (a) Thickness and (b) acceptor doping density of HTLs (MoO_3/CuSCN/Spiro-OMeTAD) related deviation of solar cell parameters (with other parameters as tabulated in Table 5.1).

Figure 5.5 The solar cell parameter variation associated with the interfacial defect density changes at (a) ETL/perovskite and (b) perovskite/HTL interface.

Figure 5.6 Counter electrode-related deviation in PCE. (with other parameters as tabulated in Table 5.1).

Figure 5.7 Operating temperature-related deviation solar cell parameters (with other parameters as tabulated in Table 5.1).

Figure 5.8 Quantum efficiency curves for the Cs_2BiAgI_6-based double perovskite solar cells comprising various HTLs (MoO_3/CuSCN/Spiro-OMeTAD).

Figure 5.9 J-V curves for the Cs_2BiAgI_6-based double perovskite solar cells comprising various HTLs (MoO_3/CuSCN/Spiro-OMeTAD).

Figure 6.1 Schematic illustrating the double perovskite solar cell mode simulated in the present work.

Figure 6.2 The simulated band alignment of Cs_2CuSbX_6 (where X = Cl, Br, I) based-double perovskite solar cells with (a) MoO_3 and (b) Cu_2O as HTL.

Figure 6.3 Absorption co-efficient of AZnO ETL, Cs_2CuSbX_6 (where X = Cl, Br, and I) double perovskite light harvester, MoO_3, and Cu_2O HTLs.

Figure 6.4 Thickness of light harvester-dependent performance of double perovskite solar cells with (a) MoO_3 and (b) Cu_2O as the HTLs. (with other parameters as tabulated in Table 6.1)

Figure 6.5 Effect of variation of bulk defect density on performance parameters of double perovskite solar cells with (a) MoO_3 and (b) Cu_2O as the HTLs. (with other parameters as tabulated in Table 6.1)

Figure 6.6 Effect of operating temperature variation on the performance of double perovskite solar cells with (a) MoO_3 and (b) Cu_2O as the HTLs. (with other parameters as tabulated in Table 6.1)

Figure 6.7 Comparison of the device performance with various back metal contact of double perovskite solar cells with (a) MoO_3 and (b) Cu_2O as the HTLs. (with other parameters as tabulated in Table 6.1)

Figure 6.8 The effect of parasitic (a) series and (b) shunt resistance on the performance of Cs_2CuSbX_6 double perovskite solar cells with MoO_3 as HTL.

Figure 6.9 The effect of parasitic (a) series and (b) shunt resistance on the performance of Cs_2CuSbX_6 double perovskite solar cells with Cu_2O as HTL.

Figure 6.10 (a) QE of the double perovskite solar cells and (b) Optimized efficiency of the device with Cu_2O as the HTL.

Figure 7.1 Schematics depicting the modeled double perovskite solar cell considered in this study.

Figure 7.2 Computed band structure of (a) $Cs_2AgSbCl_6$, (b) $Cs_2AgSbBr_6$, and (c) Cs_2AgSbI_6 double perovskite light harvesters along the noted symmetry direction of the Brillouin zone using the GGA-PBE functional.

Figure 7.3 Computed band structure of (a) $Cs_2AgSbCl_6$, (b) $Cs_2AgSbBr_6$, and (c) Cs_2AgSbI_6 double perovskite light harvesters along the noted symmetry direction of the Brillouin zone using the HSEO6 functional.

Figure 7.4 The variation in density of states of the Cs_2AgSbX_6 (where X = Cl, Br, and I) double perovskite light harvesters.

Figure 7.5 Energy-dependent variation in absorption coefficient (α) of the Cs_2AgSbX_6 (where X = Cl, Br, and I) double perovskite light harvesters. Yellow shaded region highlighting the solar spectrum.

Figure 7.6 Energy-dependent variation in (a) reflectivity, (b) refractive index, (c) dielectric function, and (d) conductivity of the Cs_2AgSbX_6 (where X = Cl, Br, and I) double perovskite light harvesters.

Figure 7.7 The variation in the performance of Cs_2AgSbX_6-based double perovskite solar cells corresponding to the changes in (a) thickness, and (b) bulk defect density in the light harvester films. (with other physical parameters as tabulated in Table 7.2).

Figure 7.8 The variation in the PCE of Cs_2AgSbX_6 double perovskite solar cells depending on the work function of the rear metal contact.

Figure 7.9 The (a) quantum efficiency (QE) indicating the spectral response and (b) J-V characteristics of the modeled Cs_2AgSbX_6 double perovskite solar cells.

Figure 8.1 Theoretical optimization of the device structure based on $CH_3NH_3PbI_{3-X}Cl_X$ light harvesters and the associated *J-V* curve demonstrating PCE of ~30%.

Figure 8.2 The schematics of the device considered for replacing the toxic lead ions with Sn ions and the corresponding absorption co-efficient subsequent layers.

Figure 8.3 The possible PCE of PSCs based on a double perovskite light harvester dependent on the long-term stability and toxicity.

Figure 8.4 Schematics of the optimized and environmentally benign double perovskite solar cells yielding PCE of ~29%.

Figure 8.5 DFT calculations aided numerical estimation of Cs_2AgSbX_6 based double perovskite light harvester and the corresponding optimized solar cells.

LIST OF TABLES

Table 3.1 List of parameters used in the simulation.

Table 5.1 The physical parameters used as input to examine and optimize solar cells (*Indicate the parameters varied in the present study).

Table 6.1 The physical input parameters used to simulate Cs_2CuSbX_6-based double perovskite solar cells (base values).

Table 7.1. The tolerance factor (*t*) and formational energy (ΔE_f) of various Cs_2AgSbX_6 double perovskites.

Table 7.2. The physical parameters loaded as input to simulate Cs_2AgSbX_6 double perovskite solar cells.

NOMENCLATURE

A	AZO	Aluminum Doped Zinc Oxide
	Au	Gold
B	BHJ	Bulk Hetero-junction
	BSO	Barium Stannate
	BE	Binding Energy
C	CASTEP	Cambridge Serial Total Energy Package
	CBm	Conduction Band Minimum
	Cs	Cesium
	C	Carbon
D	DFT	Density Functional Theory
	DFPT	Density Functional Perturbation Theory
	DSSC	Dye-Sensitized Solar Cell
E	ETL	Electron Transport Layer
	eV	Electron Volt
F	FA	Formamidinium
	FF	Fill Factor
	FTO	Fluorine doped Tin Oxide
H	HTL	Hole Transport Layer
I	ITO	Indium Doped Tin Oxide
J	J_{SC}	Short Circuit Current Density
L	l_d	diffusion length
M	MAPI	Methyl ammonium lead tri-iodide
	MoO_3	Molybdenum oxide
N	NiO	Nickel Oxide
P	PLH	Perovskite Light Harvester
	PCE	Power Conversion Efficiency
	PV	Photovoltaic
	PSC	Perovskite Solar Cell
S	SCAPS-1D	Solar Cell Capacitance Simulator-1D
	SnO_2	Tin oxide
T	t	Tolerance Factor
	TiO_2	Titanium dioxide
	TCO	Transparent Conducting Oxide
V	VBM	Valence Band Maximum
	V_{OC}	Open Circuit Voltage
Z	ZnO	Zinc Oxide

Table of contents

Dedicate i

REMERCIEMENTS ii

ACKNOWLEDGEMENTS iii

RÉSUMÉ iv

ABSTRACT v

LIST OF PUBLICATIONS xxi

LIST OF COMUNICATIONS xxiii

LIST OF FIGURES xxiv

LIST OF TABLES xxix

NOMENCLATURE xxx

Chapter 1 : Introduction 1

1.1 Overview of solar energy 2

1.2 Evolution of solar cells 3

1.2.1 First-generation solar cells 3

1.2.2 Second-generation solar cells 3

1.2.3 Third-generation solar cells 4

1.2.4 Fourth-generation solar cells 4

1.3 Perovskite solar cells 4

1.3.1 Perovskite solar cell architectures 8

1.3.2 Various supporting layers in perovskite solar cells and their functioning 9

1.3.3 The major challenges in perovskite solar cells 12

1.4 Motivation 13

1.5 Objectives of the thesis 15

1.6 References 16

Chapter 2 : Simulation thechnique 24

2.1 Introduction 25

2.2 1D Solar Cell Capacitance Simulator (SCAPS-1D) 25

2.2.1 Fundamental semiconductor equations 26

2.2.2 1D-SCAPS front interface (front end) 27
2.2.3 1D- SCAPS problem defining 28
2.2.4 Including layers to the solar cell structure 30
2.2.5 Simulating the baseline for numerical analysis of the solar cells 30
2.3 Cambridge Serial Total Energy Package (CASTEP) 31
2.4 References 32

Chapter 3 : Optimization of CH3NH3PbI3-XClX based perovskite..34

3.1 Introduction 35
3.2 Simulation procedure 37
3.3 Results and discussion 40
3.3.1 Influence of transparent conducting oxide 40
3.3.2 Influence of TiO_2 ETL 41
3.3.3 Influence of $CH_3NH_3PbI_{3-X}Cl_X$ perovskite light absorber 42
3.3.4 Influence of Spiro-OMeTAD HTL 44
3.3.5 Influence of CuSCN HTL 46
3.3.6 Influence of operating temperature and material 47
3.4 Conclusion 49
3.5 References 50

Chapter 4 : Towards lead-free all-inorganic perovskite solar cell..55

4.1 Introduction 56
4.2 Simulation procedure 58
4.3 Results and discussion 58
4.3.1 Absorption coefficient 58
4.3.2 The effect of thickness of various ETLs 59
4.3.3 The effect of donor doping density in various ETLs 60
4.3.4 The effect of the thickness of various light harvesters 61
4.3.5 The effect of defect density in various light harvesters 62
4.3.6 The effect of various counter electrodes and operating temperature ... 63
4.3.7 J-V and IPCE curves of the optimized device 65

4.4 Conclusion 66
4.5 References 67

Chapter 5 : Lead-free non-toxic Cs_2BiAgI_6 double perovskite……..70

5.1 Introduction 71
5.2 Device modeling and simulation procedure 74
5.3 Results and discussion 77
5.3.1 Effect of thickness and donor density of AZnO 77
5.3.2 Effect of thickness and bulk defect density of Cs_2BiAgI_6 78
5.3.3 Effect of thickness and acceptor density of HTLs 79
5.3.4 Effect of interfacial defect density 80
5.3.5 Effect of various counter electrodes and operating temperature 81
5.3.6 Quantum efficiency and J-V curves 83
5.4 Conclusion 85
5.5 References 86

Chapter 6 : Lead-free non-toxic Cs_2CuSbX_6 double perovskite…….89

6.1 Introduction 90
6.2 Device modeling and simulation procedure 92
6.3 Results and discussion 96
6.3.1 Absorption coefficient 96
6.3.2 Effect of thickness of light harvester 97
6.3.3 Effect of bulk defect density in light harvester 99
6.3.4 Effect of operating temperature and various counter electrodes 101
6.3.5 Effect of parasitic series and shunt resistances 103
6.3.6 J-V curves and external quantum efficiency 105
6.4 Conclusion 106
6.5 References 107

Chapter 7 : $Cs2AgSbX_6$ double perovskite : DFT/SCAPS studies..111

7.1 Introduction 112
7.2 Computational study and numerical simulations 114

7.2.1 DFT calculations of the Cs_2AgSbX_6 double perovskite light harvester .. 114
7.2.2 SCAPS-1D numerical simulation 115
7.3 Results and Discussion 116
7.3.1 DFT analysis 116
7.3.2 SCAPS-1D analysis 122
7.4 Conclusion 127
7.5 References 128
Chapter 8 : Summary and conclusion 131
8.1 Summary and conclusion 132
8.2 Future scope 139

Chapter 1

Introduction

1.1 Overview of solar energy

The way mankind uses and consumes high energy has altered over the decades. The potential demand for energy globally in the future may exceed 30 TW.[1] Energy consumption is a major factor in the economic development of civilization; however, it also negatively impacts the environment and causes other related pollution.[2] Thus, balancing energy production, consumption, and associated pollution is a hopeful step toward a green, developed, and civilized future, especially in light of the numerous agreements and disagreements on the subject.[3] Owing to the growing need for energy, it's critical to realize that conventional energy sources like oil, natural gas, and petroleum cannot provide a sustainable foundation. Consequently, it is crucial from a scientific perspective to explore renewable and sustainable sources. However sustainable and renewable sources impose a limit on the degree of efficiency that can be harnessed. [4, 5] In line with the above knowledge, the scientific and industrial society is enduring endless efforts in engineering innovative renewable technologies or improving the existing technology to achieve higher efficiencies. Ultimately, creating technology for utilizing renewable energy sources that can meet the future need for energy is critical.

While there are many different renewable energy sources such as wind,[6, 7] geothermal,[8, 9] biomass,[10] etc., using photovoltaic (PV) cells to capture solar radiation and convert it into electricity is a well-known process that produces the smallest carbon emissions.[11] Additionally, because of the low volumetric energy density, transitioning to other modern renewable energy systems, such as green hydrogen production by electro- or photo-catalysis, necessitates the highest level of preparedness owing to safety issues.[12, 13] Thus, one of the safest and best technologies that can ensure a sustainable future is solar cells that use a *p*-*n* junction to convert incoming electromagnetic radiation from the sun into electricity.[14] These PV cells can handle enormous amounts of energy, have a high power-to-weight ratio, and produce barely any pollution (derived from a range of post-operational waste).[15] Following the exposure to sunlight, photo-generated carriers from PV cells are disintegrated to generate current and voltage in the device which is coupled across a suitable load.[16] Evaluating how well incoming radiation is converted into electrical energy yields a realistic measure of the performance or efficiency of the solar cell. Nevertheless, the inherent resistance at the p-n junction interface, the density of defects in the *p* and *n* layers, the capacity of the relevant layer to generate carriers, etc., directly affect the

PCE of the solar cell. [17-20] Additionally, dusting, shielding from adverse conditions, monitoring, and other maintenance are all necessary to maintain the effectiveness of the solar cells. [21-23]

Overall, comparing PV systems to other renewable energy technologies, their inherent carbon footprint is generally the smallest.[24] Even if there may not be as much sunlight on a given day, the extra energy produced by the solar panels can be stored in batteries as chemical energy to meet energy needs without sunlight. By combining their efforts, batteries, and photovoltaic panels may effectively provide renewable energy while preventing the release of carbon into the environment, offering a sustainable and promising future.[25] As a result, solar cells can effectively meet the expected surge in the global energy demand.

1.2 Evolution of solar cells

Research and development in the field of solar technology has always focused on boosting power conversion efficiency because it is undoubtedly better to produce more electricity in a smaller area and is less expensive. In the course of boosting efficiency and reducing production costs, solar cells have evolved through time and can be categorized as follows.[11]

1.2.1 First-generation solar cells

One of the earliest categories of solar cells was made of silicon. First-generation solar cells typically use crystalline silicon with an energy bandgap of 1.1 eV, which is well-positioned for panchromatic absorption in the visible spectrum.[26] These cells exhibit broad-spectrum absorption and excellent carrier mobilities. At the moment, silicon is used to make the majority of commercial solar cells. The advantages of silicon cells include their huge abundance on the earth, their well-developed fabrication technique, and their non-toxicity a factor that is crucial when considering environmental impact. Dissipation of heat and high manufacturing costs are the downsides of these cells. [27, 28]

1.2.2 Second-generation solar cells

Semiconductor thin films are commonly employed as the absorber layer in second-generation solar cells. Amorphous Si, GaAs, CdTe, CIGS, and other materials are deposited as thin films of the necessary thickness and utilized as absorbers in second-generation solar cells. [29, 30] These solar cell types have several benefits, including affordability, flexibility, and

reduced weight making them the most viable option for building integrated photovoltaics. Nevertheless, the majority of these thin-film absorbers are made of hazardous materials, and the issue here is their lower efficiency when compared to silicon solar cells. Additionally, it also takes competence to synthesize these absorber thin films in the necessary phase.[31]

1.2.3 Third-generation solar cells

Third-generation solar cells use a variety of absorbers, including sensitive dyes, polymers, and nanocrystals. [32-34] These cells offer a low cost per watt, good efficiencies, high throughput, and low production costs. Presently the efficiencies of dye-sensitized solar cells (DSSCs) are outperformed by perovskite solar cells (PSCs). With a record power conversion efficiency of ~26%, the PSCs are on par with the first-generation silicon solar cells. PSCs typically have high absorption coefficients, cheap material costs, and are solution-processable.[35] However, these high-performing cells contain toxic lead atoms and usually suffer from degradation over time.

1.2.4 Fourth-generation solar cells

The combination of diverse absorbers, such as nanocrystals embedded in a polymer matrix, is flawless in the fourth generation of solar cells. Their enhanced charge carrier transport properties are typically the consequence of their lower recombination. Lithography, solvent engineering, self-assembly, etc. techniques are needed to regulate the morphology and evenly disperse the nanocrystals in the absorbers. These solar cells are more affordable than those from the first generation and have a high-power conversion efficiency because of their ability to harness various regions of the incoming electromagnetic spectrum.[36]

1.3 Perovskite solar cells

PSCs are the subject of high-caliber research because of their direct tunable bandgap, strong absorption in the visible region, solution processability, low material cost, etc. These perovskites form the AMX_3 structure, where A stands for an organic cation (such as $CH_3NH_3^+$, Cs, etc.), B for divalent metal ions (Pb, Sn), and X for halogen (Cl^-, I^-, Br^-) as shown in Fig. 1.1.[37]

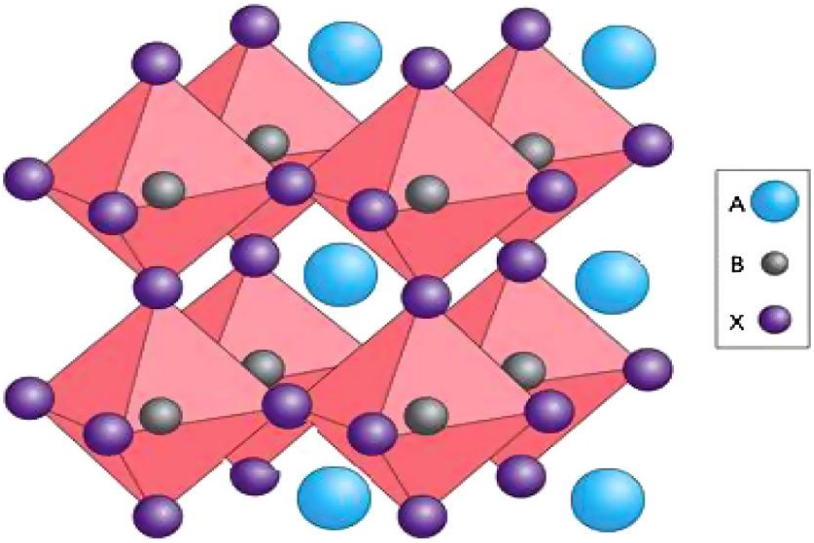

Figure 1.1 Schematic depicting the crystal structure of organic-inorganic perovskite light harvesters.

The tolerance factor (*t*) firmly limits the size of the three ions to maintain the stability of the perovskite structure (Eq. 1.1).[38]

$$t = \frac{Rb+Rx}{\sqrt{2}(Ra+Rx)} \quad (1.1)$$

where the ionic radii of the A, B, and X site elements are, respectively, Ra, Rb, and Rx. The empirical ionic radii can be calculated using the formula at ambient temperature. Ideal cubic perovskite can be produced when *t* equals 1, although in most situations, various perovskite structural distortions are seen (0.81 < t <1.11).[39] The *t* value and consequently the structural distortions play a critical role in determining the intrinsic electrical, magnetic, and dielectric properties of the perovskite light harvesters. The first known organometallic trihalide perovskite contained I-halide ions at site X, Pb metal ions at site B, and methylammonium $CH_3NH_3^+$ at site A. Miyasaka and co-workers initially reported the evolution of these organo-metallic-trihalide perovskites in early 2009; they sensitized TiO_2 photoanode with a $CH_3NH_3PbX_3$ ($MAPbI_3$) light harvester.[40] To reach a PCE of 9.7%, Kim et al. (2012) achieved a significant breakthrough by using $MAPbI_3$ as a light harvester in conjunction with the solid-state hole conductor 2,20,7,7,0-tetrakis-(N, N-dimethoxy phenyl-amine)-9, 90-spirobi-fluorene (spiro-MeOTAD) and n-type mesoporous TiO_2 (m-TiO_2) as electron transporter.[41] Presently, the power conversion efficiency of perovskite solar cells has reached ~26% with formamidinium lead triiodide ($FAPbI_3$) as a light harvester.[42]

To fabricate high-efficiency PSCs, a variety of supporting layers with ideal bandgap, thickness, optoelectronic characteristics, charge diffusion lengths, etc., are taken into consideration.[43] It is noteworthy that the bandgap of organometallic trihalide perovskites can be adjusted to an ideal range by either directly replacing the A, M, and X ions in AMX_3 structures or by directly modifying the M-X bond (Fig. 1.2).[44] The M-X bond alteration will directly impact the valence band maximum and conduction band minimum of the perovskite framework.[45] Based on UV-Vis spectroscopy, the band gap of $MAPbI_3$ was determined to be 1.50 to 1.55 eV.[46] Since the absorption is limited to 800 nm by the bandgap of $MAPbI_3$ (~1.55 eV), it is crucial to adjust the bandgap light harvesters for a broad absorption range while taking the S-Q limit into account. Antibonding states of Pb 6p and I 5s orbitals make up the conduction band minimum of $MAPbI_3$, whereas s-antibonding states of Pb 6s and I 5p orbitals account for the majority of the valence band maximum.[47] This demonstrates that the bandgap can shift to values below or over 1.55 eV with the substitution of metal ions and halides in the perovskite framework. A perovskite absorber with a larger bandgap would have lower efficiency because of reduced photo-current, but given the other modifications in its optoelectronic properties, it would still be a valuable absorber in tandem solar cell topologies.[48, 49] Koh et al observed a slightly favorable bandgap and broader absorption when they substituted the formamidinium cation ($HC(NH_2)_2^+$) for the standard $CH_3NH_3^+$ cation.[50] Due to the high toxicity and carcinogenicity of lead heavy metal, the traditional M site in the AMX_3 structure was partially or fully substituted with Sn or Ge ions, which increased the incident photon to electron conversion efficiency.[51] Likewise, when Cl^- was largely substituted for I-ion by Shi et al., the charge diffusion length increased.[52] Furthermore, the valence band maximum and conduction band minimum of each layer in the primary device structure of PSCs must align to facilitate the diffusion of holes and electrons toward the appropriate hole and electron-collecting contacts.[53] In addition, to enable incident light to reach the perovskite absorber, n-type or p-type materials with large bandgaps and high transparency must be utilized above the absorber. In theory, a functional PSC device might be realized if these requirements are satisfied.[54]

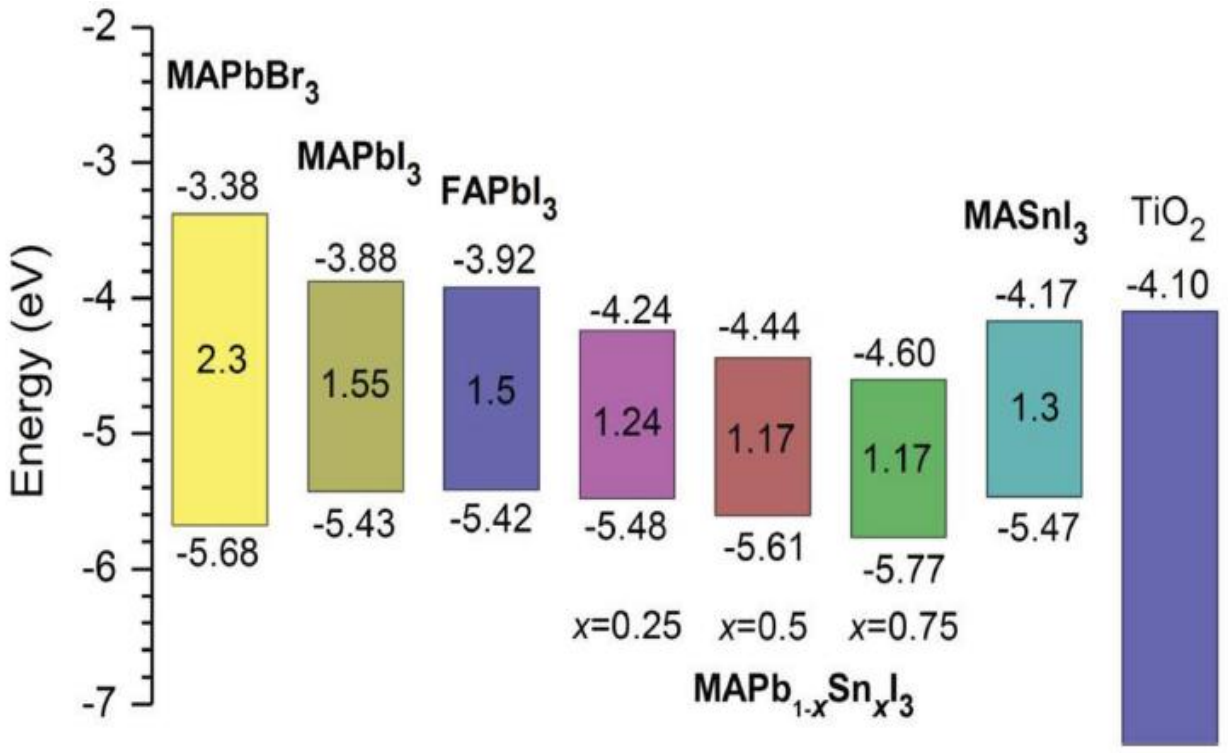

Figure 1.2 Schematics depicting tunable bandgap of the perovskite light harvesters.

Practical measurements of the absorption coefficient of $MAPbI_3$ is ~10^5 cm^{-1}.[55] Organometallic trihalide perovskites are semiconductors with a direct bandgap in which an electron can be photo-excited from the valence band to the conduction band without the need for crystal momentum (k=0).[56] Their wave function can be simply plotted by using Eq. 1.2.

$$E = \frac{\hbar (k)^2}{2m*} \qquad (1.2)$$

where ħ (= h/2p), k, and m* represent Planck's constant, effective momentum, and effective mass, respectively. High interactions of light with perovskite like direct bandgap materials are observed due to a reduction in germinate recombination and trap-assisted recombination.[57] Direct bandgap organometallic trihalide perovskite is therefore a very attractive option for usage as a light harvester in solar cells.

1.3.1 Perovskite solar cell architectures

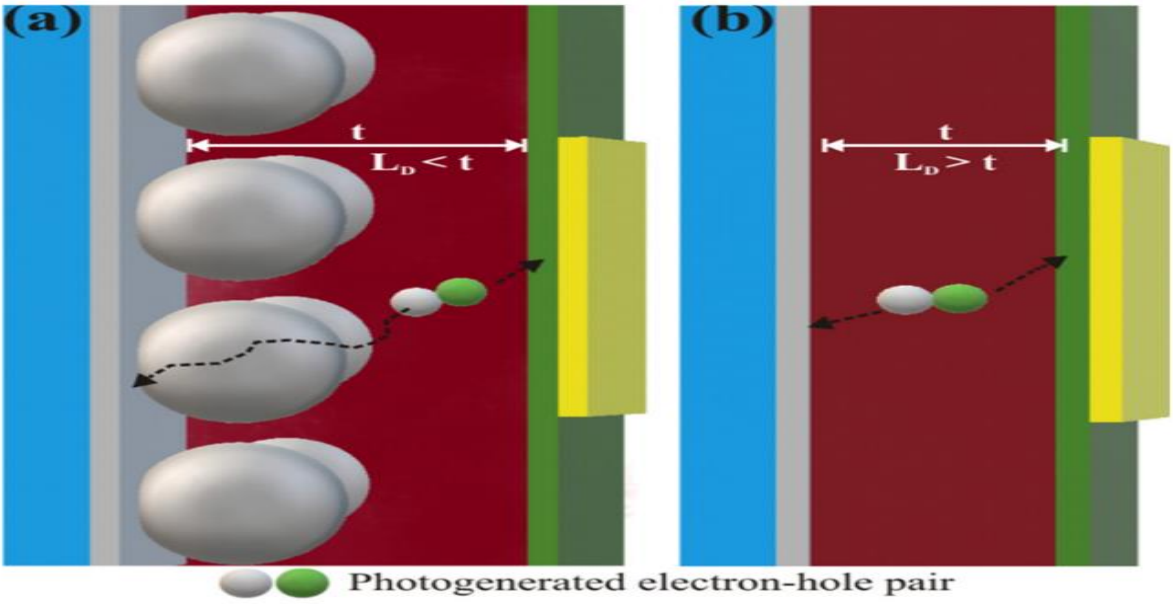

Figure 1.3 Schematics depicting the (a) mesoporous and (b) planar PSCs.

Mesoporous, mesostructured, and planar perovskite solar cells are the three categories given to PSCs based on the design of the transport layer they employ.[58] As seen in Fig. 1.3, the carrier diffusion length (l_d) and electron mobility in the transport layer are important factors in determining the device's construction.[11] Mesoporous device architecture is characterized by the use of a mesoporous transport layer above a compact layer. Usually, the mesoporous device architecture is adopted when the thickness of the film exceeds the l_d. Thus, the photogenerated charges in the mesoporous architecture will be injected into the mesoporous layer for further collection before they lose energy while drifting toward the transport layers.[59] Adopting the mesoporous architecture also increases the active p-n junction region between the transport layer and perovskite light harvester. One important aspect of mesoporous architecture is the mobility of charge carriers in the mesoporous transport layer. Charge accumulation at the perovskite and transport layer interface would result from reduced electron mobility in the mesoporous nanocrystalline layer relative to perovskite absorbers resulting in the charging of the device.[60] Thus, particle size, thickness, and film density optimization are crucial when using the mesoporous structure. Using a planar-structured PSC, Snaith et al attained high efficiency.[61] Planar architecture is employed when the l_d is greater than the

thickness of the perovskite absorber. Elimination of the mesoporous layer reduces the cost of the planar PSCs. Typically, planar architecture is vital in the vacuum processing of perovskite light harvester and supports in fabrication of large-area PSCs.[62]

Lee et al. demonstrated the first meso-structured PSC architecture, substituting Al_2O_3 meso-superstructures for mesoporous TiO_2, and achieved a PCE of 10%.[63] The observed significant increase in the open circuit voltage (V_{OC}) of the device could be attributed to the inherent insulating properties of Al_2O_3. Efficiency and device performance were directly impacted by an increase in open circuit voltage. Subsequently, Ball et al. claimed that ambipolar transport occurs in perovskite absorbers after depositing Al_2O_3 super-structured scaffolds using a low-temperature solution technique.[64]

1.3.2 Various supporting layers in perovskite solar cells and their functioning

Apart from the perovskite light harvester, various aiding layers are integrated during the fabrication of the PSCs. Each of these layers performs an individual function to support the overall functioning of the PSCs. The different layers in the PSC include transparent conductive contacts, electron transport layer (n-type), perovskite light harvester, hole transport layer (p-type), and metal contact.[65]

(a) Transparent conductive oxide (TCO)

Typically, one of the contacts must be extremely transparent to incoming visible electromagnetic radiation. The glass substrates coated with fluorine-doped tin oxide (FTO) and indium-doped tin oxide (ITO) are commonly utilized as transparent contacts because of their well-aligned work function, which charge collection easier. Transparent conductive oxide (TCO) constitutes a majority of the cost of the PSCs. Hence finding an alternate cheap TCO is essential. ITOs are chemically unstable at higher temperatures as compared to FTOs. Wide bandgap n-type materials like TiO_2 can be processed at temperatures above 450°C over FTO. In addition, while taking the TCO into account for applications in devices, the sheet resistance and roughness must be assessed. As the thickness of TCOs over the glass substrates increases the resistance decreases, meanwhile the absorption increases. Hence this leads to a trade-off between transmittance and sheet resistance.[66]

(b) Electron transport layer (ETL)

The performance of the PSCs heavily relies on the n-type electron transport layer (ETL). The primary purpose of the n-type ETLs is to aid in the diffusion of electrons from the absorber layer to the TCO and, ultimately, the external load.[67] Then, these ETLs must have a broad bandgap to permit the incident photon to reach the absorber. N-type material along with perovskite absorber forms hetero-junctions giving rise to p-n junction in HTM-free PSCs while devices with HTM layers form p-i-n or n-i-p hetero-junctions.[68] In contrast to silicon p-n homo-junctions, which are often created via inter-diffusion leading to smooth bandgap edge curves, PSCs and other thin film structures create abrupt junctions.[69] The formation of these junctions plays a vital role in evaluating the performance of the device. The other functionality of n-type materials is to block the hole carriers. A range of n-type materials including TiO_2, SnO_2, ZnO, WO_x, etc., with different dimensionality, have been studied by different research groups.[11]

(c) Perovskite light harvester

The perovskite light harvester is the heart of the device. Perovskite light harvesters are utilized as absorbers owing to their long carrier diffusion length, ideal tunable bandgap, good absorption across the solar spectrum range, longer carrier life, etc.[70] One-step coating, two-step coating, sequential deposition, electro-deposition, physical thermal evaporation, etc. methods are used to synthesize perovskite harvesters as shown in Fig. 1.4.[71, 72]

For a clear understanding of these techniques let us consider the solution process, vacuum approach, and hybrid approach being the combination of the first two. In one one-step solution approach, the precursor solution is made by dissolving equimolar precursor salts of metal halide and organic cations in polar solvents such as DMF, DMSO, etc. This precursor is either spin-coated or dip-coated over the transport material. Slightly excess organic/inorganic-halide cation can be considered to ensure complete ordered crystallization of perovskite films.[73] In a two-step solution approach, first, a layer of metal halide dissolved in its dissolving solvent is coated over the transport layer and dried. Following this, the organic/inorganic-halide cation dissolved in its dissolving solvent is deposited by either spin coating or dip-coating.[74]

However, complete conversion of the metal halide film into a perovskite light harvester should be ensured in two-step deposition. The sequential deposition process can be termed as a combination of a solution approach and a vacuum approach. In this method, metal halide solution is spin coated over the transport layer followed by thermal evaporation of organic/inorganic-halide cation.[75] A slight modification of sequential deposition is reported, in which following the formation of a metal halide thin film, the substrates are exposed to vapors of organic/inorganic-halide cation.[76]

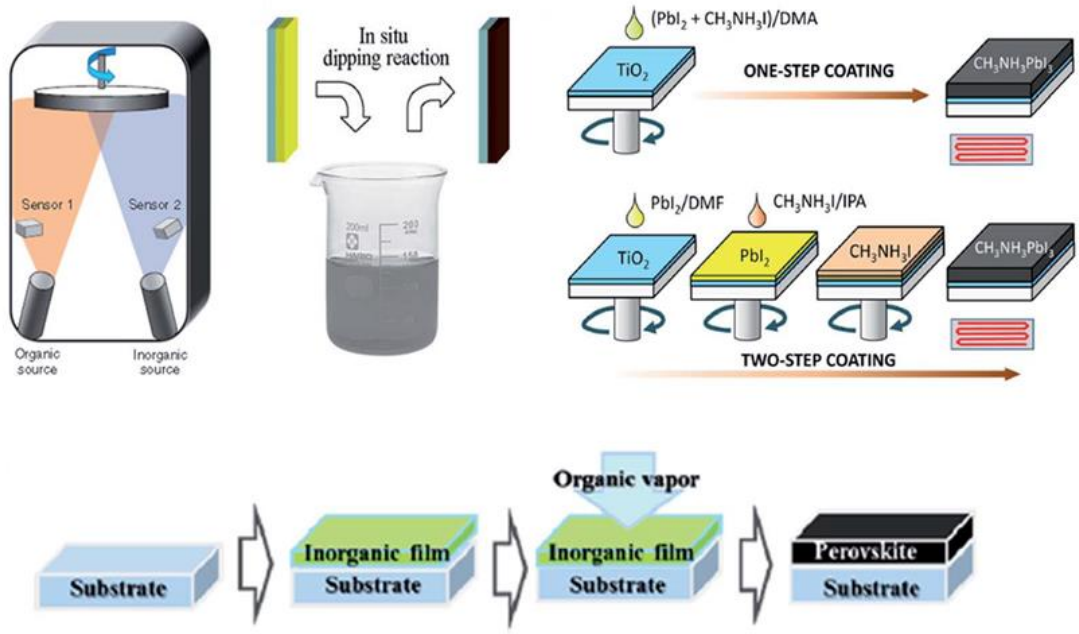

Figure 1.4 Schematics illustrating different synthesis techniques employed to fabricate perovskite light harvester.

(d) Hole transport layer (HTL)

The hole transporting layer (HTL) is a p-type layer that should have a well-aligned conduction band minimum or LUMO level and valence band maximum or HOMO level with the perovskite for efficient transport of hole carriers.[77] The function of the HTL (p-type) is to inject electrons from the cathode into the valence band of the perovskite absorber or transport free holes from the perovskite. Lately employing organic HTLs has shown promise in achieving high-efficiency PSCs. Few organic HTMs are doped with a small quantity of dopants to improve their carrier properties. Compared to various organic HTLs, spiro-OMeTAD has a long hole lifetime and

ensures better device performance.[78] One major drawback of these organic HTMs is low stability and high cost. The solution to this problem is to employ inorganic HTLs namely, NiO, CoO_x, CuSCN, CuI, etc. [79]

(e) Metal contact

Metals with good electron injection capability can be employed as the counter electrode. Just one point that needs to be considered is the alignment of work functions. Usually, gold metal is used as contact owing to its chemical inertness, high electrical conductivity, and well-aligned work function. Around 70 nm of gold is thermally evaporated to complete the device. Literature has also suggested the usage of silver, copper, aluminum, etc. However, using low-cost carbon electrodes can benefit in reducing the overall cost of the PSCs. [80, 81]

1.3.3 The major challenges in perovskite solar cells

Though these fascinating perovskite light harvesters have shown several tremendous capabilities toward high performance, yet, they suffer from two major drawbacks that hinder their commercialization. The lack of long-term stability and usage of carcinogenic lead in high throughput devices are the key downsides of these solar cells.

(a) Long-term stability

The organic-inorganic perovskites break down into their constituent precursors when exposed to moisture. Thus, the high-performance perovskite solar cells are majorly fabricated in a controlled environment. [82-84] The reactions which limit the fabrication of the perovskite solar cells are as follows:

$$CH_3NH_3PbI_3\ (s) \leftrightarrow PbI_2\ (s) + CH_3NH_3I\ (aq) \quad (1.3)$$

$$CH_3NH_3I\ (aq) \leftrightarrow CH_3NH_2\ (aq) + HI\ (aq) \quad (1.4)$$

$$4HI\ (aq) + O_2 \leftrightarrow 2I_2\ (s) + 2H_2O\ (aq) \quad (1.5)$$

$$2HI\ (aq) \leftrightarrow H_2\ (g) + I_2\ (s) \quad (1.6)$$

Therefore, it is of high scientific importance to develop perovskite light harvesters that can deliver both long-term stability and high efficiency.

(b) Toxicity of Pb metal ions

Despite the tremendous advances in perovskite solar cells, the high-efficiency cells comprise toxic lead atoms which are carcinogenic and banned in most countries.[85] However, the high light absorption in the perovskite light harvesters results from the filled *5s* orbitals at the valence band maximum and empty *6p* orbitals at the conduction band minimum of the lead cation.[47] Thus, replacing lead ions with a suitable cation is crucial in bolstering the commercialization of perovskite solar cells.

1.4 Motivation

(a) The most promising solar absorbers that can be designed to produce high-quality thin films are perovskite light harvesters. By engineering and managing the defects and interfaces at the nanoscale, their use in sustainable energy can be improved.

(b) The two major drawbacks of perovskite light harvesters, (i) the toxicity of Pb^{2+}, and (ii) the low stability needs to be addressed.

(c) Substitution of constituent elements can enhance the stability and alleviate toxicity in these light absorbers.

(d) Replacement of elements in perovskite crystal structure can provide a wide variety of possible thermodynamically stable crystal structures.

(e) At the device level, the most important factors that govern the efficiency of the perovskite solar cells are the thickness, defect density, and absorption coefficient of the constituent layers in the solar cell.

(f) Selecting suitable various low-cost counter electrodes and industrially matured compatible transport layers assist in fast-forwarding the real-time application of perovskite solar cells.

(g) A software tool that can solve the basic semiconductor device equations can be used to understand the transport of charge carriers in these heterojunction solar cells.

(h) The outcome of the theoretical investigations can provide experimental guidelines to fabricate novel non-toxic perovskite solar cells that have long-term stability.

Therefore, investigating the influence of probable and non-toxic perovskite light harvesters will be essential in the commercialization of perovskite solar cells. Recently, software tools have been adopted to theoretically scrutinize the best perovskite solar light harvester. Though various

perovskite light harvesters are checked for their potential, the systematic investigation towards optimizing each constituent layer in perovskite solar cells and their impact on performance is not well understood.

Moreover, considering the possible substitution of Pb^{2+} with Sn^{2+} has gained tremendous attention owing to their compatible ionic radii and electronic structures. However, following the replacement of Pb^{2+} in high-performing α-$FAPbI_3$ to yield $FASnI_3$, the PCE of the cells drops to ~14%. Also, the presence of the formamidinium (FA) cation compromises the long-term stability. Thus, the introduction of the cesium (Cs) cation in the above structure can produce stable and non-toxic perovskite light harvesters having long-term stability. Therefore, a study on the influence of the performance of the perovskite solar cells accounting for the replacement of Pb^{2+} and FA^{+} cations with Sn^{2+} and Cs^{+} ions, respectively is desirable.

Apart from the direct substitution of Pb^{2+} ions with Sn^{2+} ions, perovskite light harvesters obtained by transmutation of M^{2+} metal ions (in AMX_3 structure) with a combination of monovalent and trivalent cations result in 3D double perovskite with $A_2M'M''X_6$ double perovskite structures. Such replacements provide a wide range of probable thermodynamically stable perovskite structures which can deliver high efficiency and stability. Therefore, evaluating the potential of such lead-free non-toxic stable Cs_2BiAgI_6 double perovskite with various other charge transport layers is of scientific interest.

The low stability of the Cs_2BiAgI_6 can be addressed by assessing other Cs-based double perovskite light harvesters. Akin to Cs_2BiAgI_6, the Cs_2CuSbX_6 (where X = I, Cl, and Br) double perovskites have better theoretical thermodynamic stability. Thus, scrutinizing their ability to deliver the best PCE with cheap and inorganic transport layers namely, aluminium-doped zinc oxide (AZnO), molybdenum oxide (MoO_3), and cuprous oxide needs attention.

The bandgap of the double perovskite structures can be tuned for panchromatic light absorption. By replacing the Cu ions in the Cs_2CuSbX_6 with Ag ions can produce another novel class of thermodynamically stable Cs_2AgSbX_6 double perovskites which can deliver both efficiency and stability. The DFT study of the Cs_2AgSbX_6 double perovskites can produce insights into their intrinsic optoelectronic properties. With these optoelectronic properties, the theoretical estimation of Cs_2AgSbX_6 of double perovskites with AZnO and MoO_3 as electron transport layer

(ETL) and hole transport layer (HTL), respectively, can deliver guidelines for experimental fabrication.

1.5 Objectives of the thesis

This thesis presents research on the following aims to address questions originating from the literature review. The effect of thickness, defect, and doping density of the constituent layers in the perovskite layers are investigated. The possible replacement of the toxic Pb^{2+} ions in the perovskite light harvesters is scrutinized to mitigate toxicity. The potential of various thermodynamically stable double perovskites is studied with various industrially feasible assisting layers.

The objectives of the thesis are:

- To theoretically investigate the effect of the thickness, defect, and doping density of the constituent layers in a perovskite solar cell considering $CH_3NH_3PbI_{3-X}Cl_X$ light harvester.
- To check the performance of the perovskite light harvesters obtained by the replacement of toxic Pb^{2+} with Sn^{2+} metal ions to yield both high efficiency and long-term stability.
- To study the double perovskite light harvesters obtained by the transmutation of Pb^{2+} ions with monovalent and trivalent cations.
- To assess the potential of lead-free non-toxic stable Cs_2BiAgI_6 double perovskite with various other charge transport layers.
- To study the thermodynamically stable Cs_2CuSbX_6 (where X = I, Cl, and Br) double perovskites with various charge transport layers.
- To replace the Cu ions in the Cs_2CuSbX_6 double perovskites with Ag ions and investigate the optoelectronic properties with DFT studies. To use the results obtained from DFT calculations as the input to theoretically evaluate the capability of the Cs_2CuSbX_6 double perovskite light harvester.

1.6 References

[1] T. Ahmad, R. Madonski, D. Zhang, C. Huang, A. Mujeeb, Data-driven probabilistic machine learning in sustainable smart energy/smart energy systems: Key developments, challenges, and future research opportunities in the context of smart grid paradigm, Renewable and Sustainable Energy Reviews, 160 (2022) 112128.

[2] M. Alharthi, I. Hanif, H. Alamoudi, Impact of environmental pollution on human health and financial status of households in MENA countries: Future of using renewable energy to eliminate the environmental pollution, Renewable Energy, 190 (2022) 338-346.

[3] S. Nathaniel, O. Anyanwu, M. Shah, Renewable energy, urbanization, and ecological footprint in the Middle East and North Africa region, Environmental Science and Pollution Research, 27 (2020) 14601-14613.

[4] S. Gawusu, X. Zhang, S.A. Jamatutu, A. Ahmed, A.A. Amadu, E. Djam Miensah, The dynamics of green supply chain management within the framework of renewable energy, International Journal of Energy Research, 46 (2022) 684-711.

[5] A. Rabiee, A. Keane, A. Soroudi, Technical barriers for harnessing the green hydrogen: A power system perspective, Renewable Energy, 163 (2021) 1580-1587.

[6] J. Li, G. Wang, Z. Li, S. Yang, W.T. Chong, X. Xiang, A review on development of offshore wind energy conversion system, International Journal of Energy Research, 44 (2020) 9283-9297.

[7] P. Sadorsky, Wind energy for sustainable development: Driving factors and future outlook, Journal of Cleaner Production, 289 (2021) 125779.

[8] J.W. Lund, A.N. Toth, Direct utilization of geothermal energy 2020 worldwide review, Geothermics, 90 (2021) 101915.

[9] M. Soltani, F. Moradi Kashkooli, M. Souri, B. Rafiei, M. Jabarifar, K. Gharali, J.S. Nathwani, Environmental, economic, and social impacts of geothermal energy systems, Renewable and Sustainable Energy Reviews, 140 (2021) 110750.

[10] A. Favero, A. Daigneault, B. Sohngen, Forests: Carbon sequestration, biomass energy, or both?, Science Advances, 6 eaay6792.

[11] V. Manjunath, S. Bimli, P.A. Shaikh, S.B. Ogale, R.S. Devan, Understanding the role of inorganic carrier transport layer materials and interfaces in emerging perovskite solar cells, Journal of Materials Chemistry C, 10 (2022) 15725-15780.

[12] A.M. Abdalla, S. Hossain, O.B. Nisfindy, A.T. Azad, M. Dawood, A.K. Azad, Hydrogen production, storage, transportation and key challenges with applications: A review, Energy Conversion and Management, 165 (2018) 602-627.

[13] J. Xiao, J. Zhang, L. Pan, C. Shi, X. Zhang, J.-J. Zou, Photocatalytic Synthesis of High-Energy-Density Fuel: Catalysts, Mechanisms, and Challenges, Transactions of Tianjin University, 27 (2021) 280-294.

[14] M.K.H. Rabaia, M.A. Abdelkareem, E.T. Sayed, K. Elsaid, K.-J. Chae, T. Wilberforce, A.G. Olabi, Environmental impacts of solar energy systems: A review, Science of The Total Environment, 754 (2021) 141989.

[15] W. Yang, W. Wang, Y. Wang, R. Sun, J. Guo, H. Li, M. Shi, J. Guo, Y. Wu, T. Wang, G. Lu, C.J. Brabec, Y. Li, J. Min, Balancing the efficiency, stability, and cost potential for organic solar cells via a new figure of merit, Joule, 5 (2021) 1209-1230.

[16] J. He, S. Wang, X. Li, F. Zhang, Seeding Agents in Metal Halide Perovskite Solar Cells: From Material to Mechanism, ChemSusChem, 16 (2023) e202202109.

[17] Y. Qi, D. Ndaleh, W.E. Meador, J.H. Delcamp, G. Hill, N.R. Pradhan, Q. Dai, Interface Passivation of Inverted Perovskite Solar Cells by Dye Molecules, ACS Applied Energy Materials, 4 (2021) 9525-9533.

[18] D. Xin, S. Tie, R. Yuan, X. Zheng, J. Zhu, W.-H. Zhang, Defect Passivation in Hybrid Perovskite Solar Cells by Tailoring the Electron Density Distribution in Passivation Molecules, ACS Applied Materials & Interfaces, 11 (2019) 44233-44240.

[19] Y. Guo, D. Zhao, M. Yu, M. Liu, Y. Zhang, Z. Zheng, A simple strategy to obtain graphitic carbon nitride modified TiO2 layer for efficient perovskite solar cells, Nanotechnology, 35 (2024) 075201.

[20] K. Dey, B. Roose, S.D. Stranks, Optoelectronic Properties of Low-Bandgap Halide Perovskites for Solar Cell Applications, Advanced Materials, 33 (2021) 2102300.

[21] J. Wang, G. Jin, Q. Zhen, C. He, Y. Duan, Bulk Passivation and Interfacial Passivation for Perovskite Solar Cells: Which One is More Effective?, Advanced Materials Interfaces, 8 (2021) 2002078.

[22] S. Zhang, Z. Liu, W. Zhang, Z. Jiang, W. Chen, R. Chen, Y. Huang, Z. Yang, Y. Zhang, L. Han, W. Chen, Barrier Designs in Perovskite Solar Cells for Long-Term Stability, Advanced Energy Materials, 10 (2020) 2001610.

[23] S.A.M. Said, G. Hassan, H.M. Walwil, N. Al-Aqeeli, The effect of environmental factors and dust accumulation on photovoltaic modules and dust-accumulation mitigation strategies, Renewable and Sustainable Energy Reviews, 82 (2018) 743-760.

[24] N. Stylos, C. Koroneos, Carbon footprint of polycrystalline photovoltaic systems, Journal of Cleaner Production, 64 (2014) 639-645.

[25] V. Vega-Garita, A. Hanif, N. Narayan, L. Ramirez-Elizondo, P. Bauer, Selecting a suitable battery technology for the photovoltaic battery integrated module, Journal of Power Sources, 438 (2019) 227011.

[26] Z. Sun, X. Chen, Y. He, J. Li, J. Wang, H. Yan, Y. Zhang, Toward Efficiency Limits of Crystalline Silicon Solar Cells: Recent Progress in High-Efficiency Silicon Heterojunction Solar Cells, Advanced Energy Materials, 12 (2022) 2200015.

[27] T. Dannenberg, J. Vollmer, M. Passig, C. Scheiwe, D. Brunner, A. Pediaditakis, U. Jäger, I. Wang, W. Xie, S. Xu, J. Wu, K. Krieg, C. Teßmann, M. Zimmer, H. Kühnlein, Past, Present, and Future Outlook for Edge Isolation Processes in Highly Efficient Silicon Solar Cell Manufacturing, Solar RRL, 7 (2023) 2200594.

[28] F. Fu, J. Li, T.C.-J. Yang, H. Liang, A. Faes, Q. Jeangros, C. Ballif, Y. Hou, Monolithic Perovskite-Silicon Tandem Solar Cells: From the Lab to Fab?, Advanced Materials, 34 (2022) 2106540.

[29] P. Kumar, S. You, A. Vomiero, Recent Progress in Materials and Device Design for Semitransparent Photovoltaic Technologies, Advanced Energy Materials, 13 (2023) 2301555.

[30] M. Kangsabanik, R.N. Gayen, A Comprehensive Review on the Recent Strategy of Cation Substitution in CZTS(Se) Thin Films to Achieve Highly Efficient Kesterite Solar Cells, Solar RRL, 7 (2023) 2300670.

[31] S. Bae, J.-H. Kim, H.-S. Lee, B.K. Min, Toward Understanding Chalcopyrite Solar Cells via Advanced Characterization Techniques, Advanced Materials Interfaces, 9 (2022) 2200128.

[32] F. Grifoni, M. Bonomo, W. Naim, N. Barbero, T. Alnasser, I. Dzeba, M. Giordano, A. Tsaturyan, M. Urbani, T. Torres, C. Barolo, F. Sauvage, Toward Sustainable, Colorless, and

Transparent Photovoltaics: State of the Art and Perspectives for the Development of Selective Near-Infrared Dye-Sensitized Solar Cells, Advanced Energy Materials, 11 (2021) 2101598.

[33] H. Li, K. Lu, Z. Wei, Polymer/Small Molecule/Fullerene Based Ternary Solar Cells, Advanced Energy Materials, 7 (2017) 1602540.

[34] R. Zhou, J. Xu, P. Luo, L. Hu, X. Pan, J. Xu, Y. Jiang, L. Wang, Near-Infrared Photoactive Semiconductor Quantum Dots for Solar Cells, Advanced Energy Materials, 11 (2021) 2101923.

[35] J. Park, J. Kim, H.-S. Yun, M.J. Paik, E. Noh, H.J. Mun, M.G. Kim, T.J. Shin, S.I. Seok, Controlled growth of perovskite layers with volatile alkylammonium chlorides, Nature, 616 (2023) 724-730.

[36] T. Ameri, G. Dennler, C. Lungenschmied, C.J. Brabec, Organic tandem solar cells: A review, Energy & Environmental Science, 2 (2009) 347-363.

[37] H.S. Jung, N.-G. Park, Perovskite Solar Cells: From Materials to Devices, Small, 11 (2015) 10-25.

[38] H.W. Qiao, S. Yang, Y. Wang, X. Chen, T.Y. Wen, L.J. Tang, Q. Cheng, Y. Hou, H. Zhao, H.G. Yang, A Gradient Heterostructure Based on Tolerance Factor in High-Performance Perovskite Solar Cells with 0.84 Fill Factor, Advanced Materials, 31 (2019) 1804217.

[39] K.Y. Tsui, N. Onishi, R.F. Berger, Tolerance Factors Revisited: Geometrically Designing the Ideal Environment for Perovskite Dopants, The Journal of Physical Chemistry C, 120 (2016) 23293-23298.

[40] A. Kojima, K. Teshima, Y. Shirai, T. Miyasaka, Organometal Halide Perovskites as Visible-Light Sensitizers for Photovoltaic Cells, Journal of the American Chemical Society, 131 (2009) 6050-6051.

[41] H.-S. Kim, C.-R. Lee, J.-H. Im, K.-B. Lee, T. Moehl, A. Marchioro, S.-J. Moon, R. Humphry-Baker, J.-H. Yum, J.E. Moser, M. Grätzel, N.-G. Park, Lead Iodide Perovskite Sensitized All-Solid-State Submicron Thin Film Mesoscopic Solar Cell with Efficiency Exceeding 9%, Scientific Reports, 2 (2012) 591.

[42] J. Jeong, M. Kim, J. Seo, H. Lu, P. Ahlawat, A. Mishra, Y. Yang, M.A. Hope, F.T. Eickemeyer, M. Kim, Y.J. Yoon, I.W. Choi, B.P. Darwich, S.J. Choi, Y. Jo, J.H. Lee, B. Walker, S.M. Zakeeruddin, L. Emsley, U. Rothlisberger, A. Hagfeldt, D.S. Kim, M. Grätzel,

J.Y. Kim, Pseudo-halide anion engineering for α-FAPbI3 perovskite solar cells, Nature, 592 (2021) 381-385.

[43] N.E. Courtier, J.M. Cave, J.M. Foster, A.B. Walker, G. Richardson, How transport layer properties affect perovskite solar cell performance: insights from a coupled charge transport/ion migration model, Energy & Environmental Science, 12 (2019) 396-409.

[44] J. Sala, M. Heydarian, S. Lammar, Y. Abdulraheem, T. Aernouts, A. Hadipour, J. Poortmans, Compositional Investigation for Bandgap Engineering of Wide Bandgap Triple Cation Perovskite, ACS Applied Energy Materials, 4 (2021) 6377-6384.

[45] L. Bai, M. Guli, Y. Yang, Q. Chen, Y. Zhang, Optimization of Sn defects through multiple coordination effect to realize stable Sn–Pb mixed perovskite solar cells, Solar Energy Materials and Solar Cells, 254 (2023) 112283.

[46] M.I. Khan, S.A. Aldulmani, M.A. Nadeem, S. Hussain, W.S. Subhani, M. Saleem, M. Fatima, B. Mehmood, A. BaQais, S.A. Alissa, 700 keV Au ions beam effect on the structural, optical and photovoltaic properties of MAPbI3 solar cells, Ceramics International, 49 (2023) 8546-8553.

[47] A.H. Slavney, T. Hu, A.M. Lindenberg, H.I. Karunadasa, A Bismuth-Halide Double Perovskite with Long Carrier Recombination Lifetime for Photovoltaic Applications, Journal of the American Chemical Society, 138 (2016) 2138-2141.

[48] M. Jošt, L. Kegelmann, L. Korte, S. Albrecht, Monolithic Perovskite Tandem Solar Cells: A Review of the Present Status and Advanced Characterization Methods Toward 30% Efficiency, Advanced Energy Materials, 10 (2020) 1904102.

[49] H.A. Dewi, H. Wang, J. Li, M. Thway, R. Sridharan, R. Stangl, F. Lin, A.G. Aberle, N. Mathews, A. Bruno, S. Mhaisalkar, Highly Efficient Semitransparent Perovskite Solar Cells for Four Terminal Perovskite-Silicon Tandems, ACS Applied Materials & Interfaces, 11 (2019) 34178-34187.

[50] T.M. Koh, K. Fu, Y. Fang, S. Chen, T.C. Sum, N. Mathews, S.G. Mhaisalkar, P.P. Boix, T. Baikie, Formamidinium-Containing Metal-Halide: An Alternative Material for Near-IR Absorption Perovskite Solar Cells, The Journal of Physical Chemistry C, 118 (2014) 16458-16462.

[51] A. Aftab, M.I. Ahmad, A review of stability and progress in tin halide perovskite solar cell, Solar Energy, 216 (2021) 26-47.

[52] Y. Shi, Y. Xing, Y. Li, Q. Dong, K. Wang, Y. Du, X. Bai, S. Wang, Z. Chen, T. Ma, CH3NH3PbI3 and CH3NH3PbI3–xClx in Planar or Mesoporous Perovskite Solar Cells: Comprehensive Insight into the Dependence of Performance on Architecture, The Journal of Physical Chemistry C, 119 (2015) 15868-15873.

[53] C.A. Ubani, M.A. Ibrahim, M.A.M. Teridi, Moving into the domain of perovskite sensitized solar cell, Renewable and Sustainable Energy Reviews, 72 (2017) 907-915.

[54] V. Gonzalez-Pedro, E.J. Juarez-Perez, W.-S. Arsyad, E.M. Barea, F. Fabregat-Santiago, I. Mora-Sero, J. Bisquert, General Working Principles of CH3NH3PbX3 Perovskite Solar Cells, Nano Letters, 14 (2014) 888-893.

[55] P. Zhao, J. Su, Z. Lin, J. Wang, J. Zhang, Y. Hao, X. Ouyang, J. Chang, The crystal anisotropy effect of MAPbI3 perovskite on optoelectronic devices, Materials Today Energy, 17 (2020) 100481.

[56] M. Chen, G. Kapil, L. Wang, S. Razey Sahamir, A.K. Baranwal, K. Nishimura, Y. Sanehira, Z. Zhang, M. Akmal Kamarudin, Q. Shen, S. Hayase, High performance wide bandgap Lead-free perovskite solar cells by monolayer engineering, Chemical Engineering Journal, 436 (2022) 135196.

[57] C.M. Wolff, P. Caprioglio, M. Stolterfoht, D. Neher, Nonradiative Recombination in Perovskite Solar Cells: The Role of Interfaces, Advanced Materials, 31 (2019) 1902762.

[58] I. Hussain, H.P. Tran, J. Jaksik, J. Moore, N. Islam, M.J. Uddin, Functional materials, device architecture, and flexibility of perovskite solar cell, Emergent Materials, 1 (2018) 133-154.

[59] T. Webb, S.J. Sweeney, W. Zhang, Device Architecture Engineering: Progress toward Next Generation Perovskite Solar Cells, Advanced Functional Materials, 31 (2021) 2103121.

[60] H. Pan, X. Zhao, X. Gong, H. Li, N.H. Ladi, X.L. Zhang, W. Huang, S. Ahmad, L. Ding, Y. Shen, M. Wang, Y. Fu, Advances in design engineering and merits of electron transporting layers in perovskite solar cells, Materials Horizons, 7 (2020) 2276-2291.

[61] S. Bai, P. Da, C. Li, Z. Wang, Z. Yuan, F. Fu, M. Kawecki, X. Liu, N. Sakai, J.T.-W. Wang, S. Huettner, S. Buecheler, M. Fahlman, F. Gao, H.J. Snaith, Planar perovskite solar cells with long-term stability using ionic liquid additives, Nature, 571 (2019) 245-250.

[62] J. Lee, K. Lee, K. Kim, N.-G. Park, Vacuum-Processed Perovskite Solar Cells: Materials and Methods, Solar RRL, 6 (2022) 2200623.

[63] M.M. Lee, J. Teuscher, T. Miyasaka, T.N. Murakami, H.J. Snaith, Efficient Hybrid Solar Cells Based on Meso-Superstructured Organometal Halide Perovskites, Science, 338 (2012) 643-647.

[64] J.M. Ball, M.M. Lee, A. Hey, H.J. Snaith, Low-temperature processed meso-superstructured to thin-film perovskite solar cells, Energy & Environmental Science, 6 (2013) 1739-1743.

[65] M. Saliba, J.-P. Correa-Baena, C.M. Wolff, M. Stolterfoht, N. Phung, S. Albrecht, D. Neher, A. Abate, How to Make over 20% Efficient Perovskite Solar Cells in Regular (n–i–p) and Inverted (p–i–n) Architectures, Chemistry of Materials, 30 (2018) 4193-4201.

[66] M.A. Riza, M.A. Ibrahim, U.C. Ahamefula, M.A. Mat Teridi, N. Ahmad Ludin, S. Sepeai, K. Sopian, Prospects and challenges of perovskite type transparent conductive oxides in photovoltaic applications. Part I – Material developments, Solar Energy, 137 (2016) 371-378.

[67] K. Valadi, S. Gharibi, R. Taheri-Ledari, S. Akin, A. Maleki, A.E. Shalan, Metal oxide electron transport materials for perovskite solar cells: a review, Environmental Chemistry Letters, 19 (2021) 2185-2207.

[68] J.-T. Lin, T.-C. Chu, D.-G. Chen, Z.-X. Huang, H.-C. Chen, C.-S. Li, C.-I. Wu, P.-T. Chou, C.-W. Chiu, H.M. Chen, Vertical 2D/3D Heterojunction of Tin Perovskites for Highly Efficient HTM-Free Perovskite Solar Cell, ACS Applied Energy Materials, 4 (2021) 2041-2048.

[69] Y. Wang, Z. Hu, C. Gao, C. Yang, H. Zhang, J. Zhang, X. Zhou, Y. Zhu, Charge Carrier Dynamics in Electron-Transport-Layer-Free Perovskite Solar Cells, ACS Applied Electronic Materials, 1 (2019) 2334-2341.

[70] S. Rahmany, L. Etgar, Semitransparent Perovskite Solar Cells, ACS Energy Letters, 5 (2020) 1519-1531.

[71] Z. Li, T.R. Klein, D.H. Kim, M. Yang, J.J. Berry, M.F.A.M. van Hest, K. Zhu, Scalable fabrication of perovskite solar cells, Nature Reviews Materials, 3 (2018) 18017.

[72] J.-W. Lee, D.-K. Lee, D.-N. Jeong, N.-G. Park, Control of Crystal Growth toward Scalable Fabrication of Perovskite Solar Cells, Advanced Functional Materials, 29 (2019) 1807047.

[73] J.R. Bautista-Quijano, O. Telschow, F. Paulus, Y. Vaynzof, Solvent–antisolvent interactions in metal halide perovskites, Chemical Communications, 59 (2023) 10588-10603.

[74] Z. Wu, E. Bi, C. Li, L. Chen, Z. Song, Y. Yan, Scalable Two-Step Production of High-Efficiency Perovskite Solar Cells and Modules, Solar RRL, 7 (2023) 2200571.

[75] P. Chen, Y. Xiao, L. Li, L. Zhao, M. Yu, S. Li, J. Hu, B. Liu, Y. Yang, D. Luo, C.-H. Hou, X. Guo, J.-J. Shyue, Z.-H. Lu, Q. Gong, H.J. Snaith, R. Zhu, Efficient Inverted Perovskite Solar Cells via Improved Sequential Deposition, Advanced Materials, 35 (2023) 2206345.

[76] I. Susic, A. Kama, L. Gil-Escrig, C. Dreessen, F. Palazon, D. Cahen, M. Sessolo, H.J. Bolink, Combinatorial Vacuum-Deposition of Wide Bandgap Perovskite Films and Solar Cells, Advanced Materials Interfaces, 10 (2023) 2202271.

[77] D. Ouyang, Z. Huang, W.C.H. Choy, Solution-Processed Metal Oxide Nanocrystals as Carrier Transport Layers in Organic and Perovskite Solar Cells, Advanced Functional Materials, 29 (2019) 1804660.

[78] Y. Shen, K. Deng, L. Li, Spiro-OMeTAD-Based Hole Transport Layer Engineering toward Stable Perovskite Solar Cells, Small Methods, 6 (2022) 2200757.

[79] X. Jing, Z. Zhang, T. Chen, J. Luo, Review of Inorganic Hole Transport Materials for Perovskite Solar Cells, Energy Technology, 11 (2023) 2201005.

[80] C.-F. Lin, T.-F. Lin, M.-H. Li, P.-Y. Lin, I. Raifuku, P.-T. Hsieh, P. Chen, Back-contact perovskite solar cells, Semiconductor Science and Technology, 36 (2021) 083001.

[81] A. Abate, J.-P. Correa-Baena, M. Saliba, M.S. Su'ait, F. Bella, Perovskite Solar Cells: From the Laboratory to the Assembly Line, Chemistry – A European Journal, 24 (2018) 3083-3100.

[82] N. Ahn, M. Choi, Towards Long-Term Stable Perovskite Solar Cells: Degradation Mechanisms and Stabilization Techniques, Advanced Science, 11 (2024) 2306110.

[83] H. Shahivandi, M. Vaezzadeh, M. Saeidi, Theory of light-induced degradation in perovskite solar cells, Solar Energy Materials and Solar Cells, 208 (2020) 110383.

[84] A.A. Mamun, T.T. Ava, H.R. Byun, H.J. Jeong, M.S. Jeong, L. Nguyen, C. Gausin, G. Namkoong, Unveiling the irreversible performance degradation of organo-inorganic halide perovskite films and solar cells during heating and cooling processes, Physical Chemistry Chemical Physics, 19 (2017) 19487-19495.

[85] M. Ikram, R. Malik, R. Raees, M. Imran, F. Wang, S. Ali, M. Khan, Q. Khan, M. Maqbool, Recent advancements and future insight of lead-free non-toxic perovskite solar cells for sustainable and clean energy production: A review, Sustainable Energy Technologies and Assessments, 53 (2022) 102433.

Chapter 2

Simulation Techniques

2.1 Introduction

Using real-world problems to integrate numerical calculations into a computer-like virtual machine environment is seen as an essential task. Owing to the use of computers in numerical problem-solving, the researcher has found the most efficient way to complete challenging problem-solving tasks. Computers are used to save time, and it is easy to optimize any real-time design challenges without physically subjecting them to real test conditions. This supports the justification for giving priority to computer-based learning across global universities. The adoption of computerized learning systems has benefited semiconductor device researchers. Presently, most of the world market is dominated by semiconductor devices like mobile phones, laptops, computers, street lights, solar products, etc. Among them, owing to the global electrical energy demand, solar cells that convert incoming solar radiation into electrical energy have gained popular interest. With the use of cutting-edge technologies, high-performance solar cell configurations are being produced very rapidly. However, for commercial development, there are still challenges concerning the cost, availability of raw materials, and long-term stability of the devices. As a result, computer-based numerical analysis of solar cells can be crucial to resolving these issues. Therefore, the computer facilitates the formulation of versatile, plausible issues, which streamlines the method of analyzing various concepts. Furthermore, it is frequently possible to obtain an exhaustive list of device details with minimal cost, time, and effort required than a limited collection of manually calculated single-point values. In line with the above discussion, it is clear that numerical analysis of photovoltaic cells is a necessary route to evaluate the viability of the proposed physical structure and its performance, hence enabling rapid design and efficiency improvements.

2.2 1D Solar Cell Capacitance Simulator (SCAPS-1D)

The specialized SCAPS-1D simulation program can be used for device modeling.[1] A variety of physical factors, including absorber thickness and doping concentration, buffer and window layer thickness, temperature effect, and solar cell illumination power, can be analyzed to assess the performance of a photovoltaic device.[2] SCAPS-1D was designed at the University of Gent, Belgium.[3] The initial SCAPS-1D program was created for the CdTe and $CuInSe_2$-based solar cells. However, due to recent advancements, the software is now used in various homojunction and heterojunction solar cells. [4, 5]

2.2.1 Fundamental semiconductor equations

Fundamental semiconductor equations are generally solved to examine solar cells using computational tools. [6, 7] The aforementioned equations are vital when evaluating the performance and prospective output of solar cells. The Poison equation, which dictates electrostatic potential, is one of these equations. Poison's electrostatic potential equation is represented by Eq. 2.1.

$$\frac{d^2V}{dx^2} = \frac{\rho}{\varepsilon} \tag{2.1}$$

where charge density (C/cm^3) is represented by ρ and the ε denoted the product of permittivity of the semiconductor and vacuum. With the premise that the dopant is completely ionized, Eq. 2.2 can be used to describe the charge neutrality equation (ρ).

$$\rho = q(p - n + N_D + N_A) \tag{2.2}$$

where q represents the electronic charge, p and n are the concentrations of holes and electrons, respectively. N_D and N_A denote the ionized donor and acceptor dopant carrier concentration, respectively. Substituting Eq. 2.2 in Eq. 2.1 yields Eq. 2.3.

$$\frac{d^2V}{dx^2} = \frac{q(p - n + N_D + N_A)}{\varepsilon} \tag{2.3}$$

Additionally, the expression for the concentration of carriers (p, n) must be rearranged to solve equation 4.3 for V as a function position value of x. The drift, diffusion, recombination, and generation are regulated by hole and electron continuity equations Eq. 2.4 and Eq. 2.5, respectively.

$$\frac{\partial p}{\partial t} = \frac{1}{q}\frac{\partial J_p}{\partial x} + (G_p - R_p) \tag{2.4}$$

$$\frac{\partial n}{\partial t} = \frac{1}{q}\frac{\partial J_n}{\partial x} + (G_n - R_n) \tag{2.5}$$

There are non-linear relationships between the output of Eq. 2.1, Eq. 2.4, and Eq. 2.5 and the charge carrier concentration (n, p). Therefore, these equations can be solved numerically using common methods such as discretization of the device, discretization of the equation, and boundary conditions. Solving the drift and diffusion equations assists in understanding the carrier characteristics of the solar cell. The Eq. 2.5 and Eq. 2.6 represents the drift-diffusion equations for holes and electrons.

$$J_p = q\mu_p p\varepsilon - qD_p \partial p) \quad (2.6)$$

$$J_n = q\mu_{np} n\varepsilon + qD_n \partial n) \quad (2.7)$$

where Jp and Jn denote the current density of electrons and holes, respectively. The mobility of the charge carriers is represented by μn and μp for electrons and holes, respectively. Dp and Dn are diffusion coefficients for holes and electrons, respectively (diffusion coefficient depends on carrier mobility multiplied by carrier lifetime). The dependence of the mobility of carriers on the Dn is given by Eq. 2.8.

$$D_{(n,p)} = \mu_{(n,p)} \frac{KT}{q} \quad (2.8)$$

The values of generation and recombination (G, R), which can also be written as net recombination in the device (U), are additional quantities that must be solved to solve Eq. 2.3, Eq. 2.4, and Eq. 2.5. Thus, the net recombination is given by Eq. 2.9.

$$U = \frac{p - p_0}{\tau_p} \quad (2.9)$$

Therefore, several software is developed to solve such fundamental semiconductor equations to analyze the performance of the solar cells.[8-12] The following is a list of programs that may be downloaded for free and used by researchers.

i. AMPS-1D (Analysis of Microelectronics and Photonics Structures)
ii. ASA (Amorphous Semiconductor Analysis)
iii. AFORS-HET (Automat FOR Simulation of Heterostructures)
iv. PC1D
v. 1D-SCAPS (1D- Solar Cell Capacitance Simulator)

SCAPS is one of the software packages that provides heterojunction simulations. We employed the SCAPS program because of its large volume of published literature, user-friendly interface, and potential for solar cell evaluation in our work.

2.2.2 1D-SCAPS front interface (front end)

The front-end interface of the SCAPS-1D software is displayed in Fig. 2.1. It is generally divided into 4 panels, an outline of which is given below.

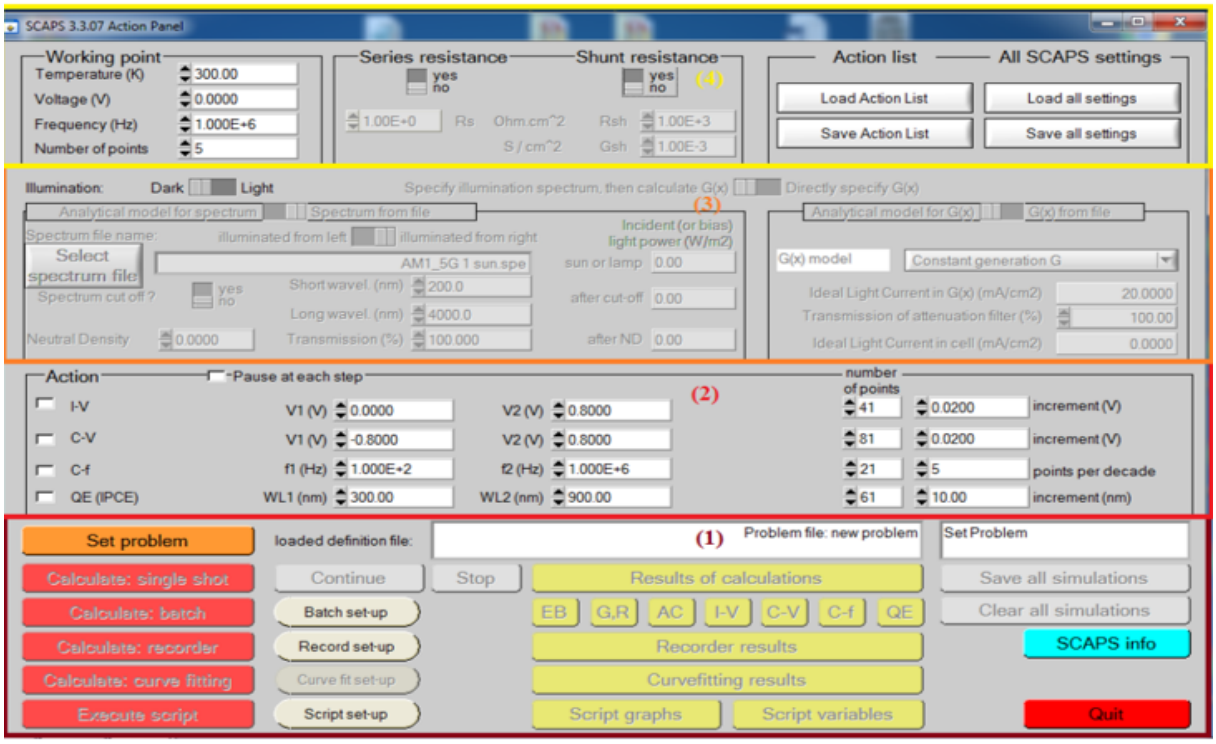

Figure 2.1 Image depicting the front-end interface of the 1D-SCAPS program.

i. The problem description panel is used to create a desired solar cell framework in the SCAPS application, assess the simulated result, store simulated output data, and remove SCAPS's simulated history. To define the structure of a solar cell, we must click on the establish problem button.

ii. The I-V characteristics scale calibration and setting, the C-V capacitance-voltage setting, the C-F capacitance frequency setting, and the QE quantum efficiency setting are all located on the action panel, which is used to read scale settings.

iii. The illumination panel controls the spectrum and the path of light coming into the solar cell assembly.

iv. The operational temperature can be defined with the working point panel.

2.2.3 1D- SCAPS problem defining

Hitting the "Set problem" button in SCAPS will cause an additional interface to appear that will enable to specify or define a solar cell framework. The structure of a solar cell device

can be defined in this interface, which we term the "Solar cell definition panel. Due to its definition and representation of the structure, this panel is essential to understanding solar cells. This panel is separated into three groups as shown in Fig. 2.2.

i. Comprises five keys that can be utilized to store an existing modeled structure to the SCAPS definition library or load a structure file from the library. Clicking "OK" brings us back to the main front-end interface where we may continue our analysis after loading the file or constructing the new structure.

ii. This includes the layers that we will define for the construction of our solar cell as well as the contacts. It is evident from Fig. 2.2 that SCAPS is limited to supporting structures with seven layers for numerical analysis of solar cells.

iii. The stated solar cell framework with irradiation from the front or back contact is visualized in this portion. Certain controls that define illumination from the front or rear contact, provided potential, and current reference is located in this section.

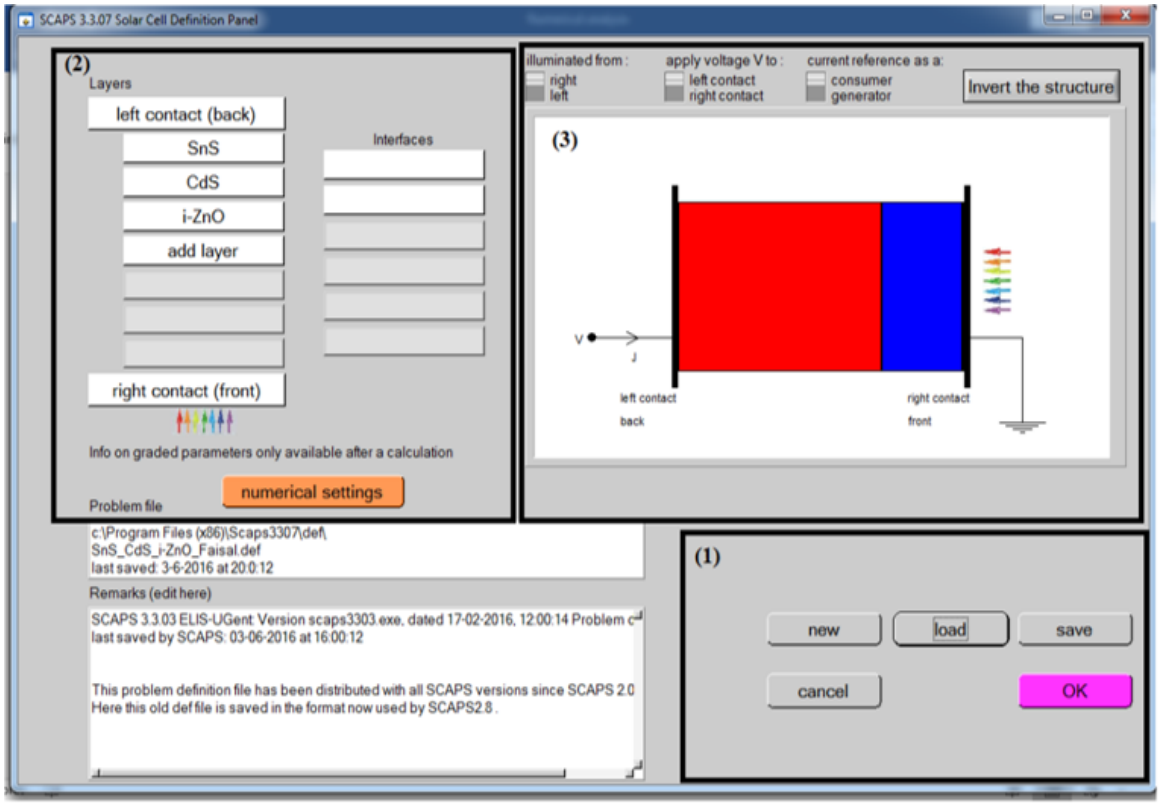

Figure 2.2 Image depicting the definition panel of the 1D-SCAPS program.

2.2.4 Including layers to the solar cell structure

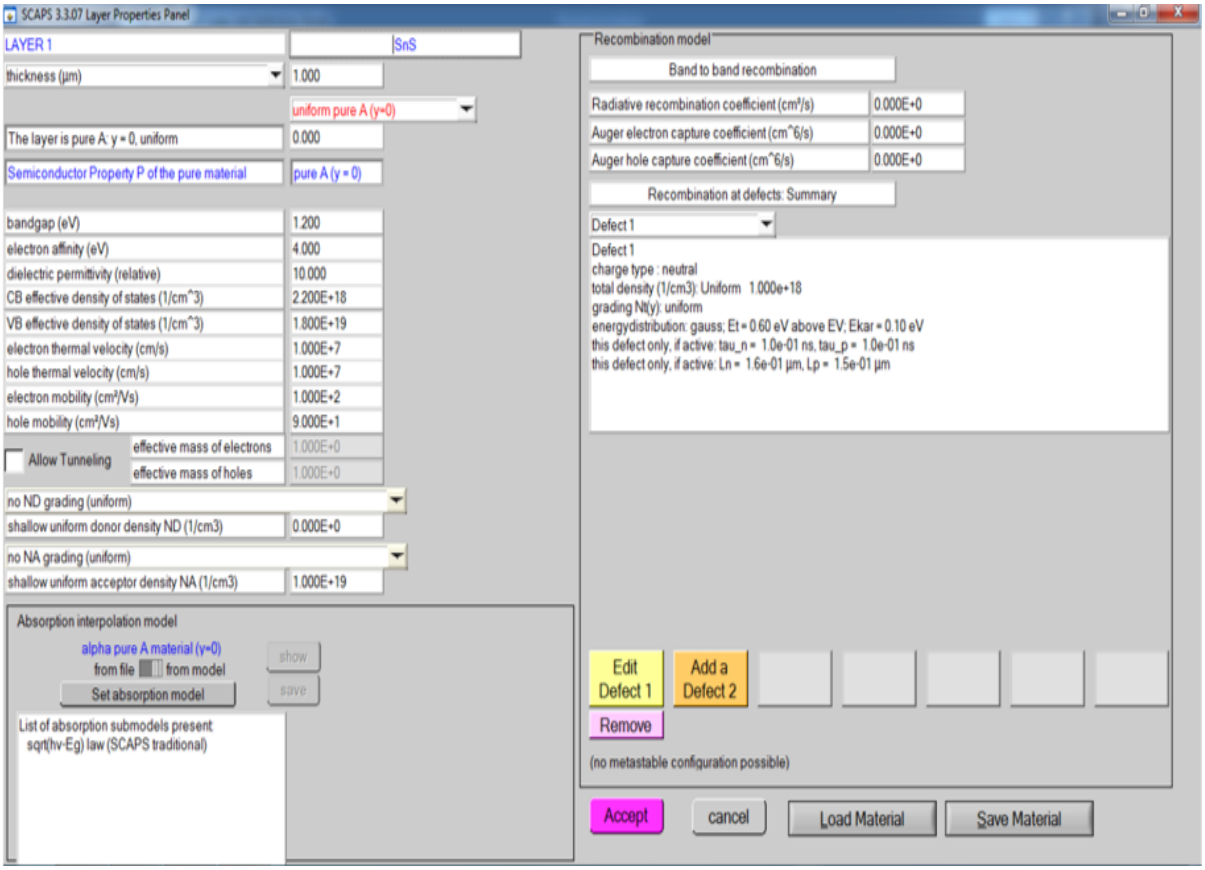

Figure 2.3 Image depicting the layer properties panel in the 1D-SCAPS program.

As indicated in Fig. 2.2 (section 2), by selecting an add layer in SCAPS to designate layers for the development of the solar cell structure. Upon selecting "Add Layer," a new panel known as the "Layer properties panel" will emerge. The fundamental physical properties of the subsequent layer in this panel can be configured, as illustrated in Fig. 2.3. The following task after establishing the problem in the SCAPS framework is to carry out a numerical analysis for the defined layout and examine how various physical parameters, such as operating temperature, buffer layer thickness, absorber layer doping concentration, and buffer layer, affect the performance of solar cells.

2.2.5 Simulating the baseline for numerical analysis of the solar cells

The electrical properties (AC and DC) of solar cells (heterojunction) were determined utilizing the simulation model that was configured in the SCAPS application. In this context, the solution that was produced for the scenario of the simulations includes the results

of illumination and darkness current in addition to a few other features. In particular, SCAPS was able to accurately analyze the steady-state band diagram, recombination profile, and transport carrier in 1D based on the Poison equation, electron equation, and hole current equation. The concentration of charge carriers, the thickness of the solar cell, as well as its optical and electrical characteristics, all have a significant impact on the output of a photovoltaic device.

2.3 Cambridge Serial Total Energy Package (CASTEP)

The CASTEP algorithm is utilized for electronic structure simulations that use DFT and plane wave basis sets. The electron-ion potentials are defined by ab initio pseudopotentials inside norm-conserving or ultrasoft constructions. Energy minimization serves to determine the electronic wavefunctions and associated charge density in an independent approach. The CASTEP code is suitable for examining the band structures and electronic charge densities as well as the effects of stress, forces, and total energy on crystal structures. The algorithm is capable of determining phonon frequencies and eigenvectors through Density Functional Perturbation Theory (DFPT), which may be applied to determine phase equilibrium, entropy, enthalpy, Gibbs free energy, and Debye temperature.

Similar to previous computational research, the precision of these computations is contingent upon the degree of theory employed and other user-specified variables, such as the number of *K*-points, the magnitude of the pseudopotentials, the basis set cutoff point, the function employed, etc. There are several instances of computational results that are inaccurate both qualitatively and statistically as a result of poor parameter selection, and the impact of the theory level utilized is less predictable. On the one hand, in this thesis, we have always selected parameters that converge relative energies to at least 1 meV/atom, and the influence of numerical accuracy can be validated.

2.4 References

[1] F. Baig, Y.H. Khattak, A. Shuja, K. Riaz, B.M. Soucase, Performance investigation of Sb2Se3 based solar cell by device optimization, band offset engineering and Hole Transport Layer in SCAPS-1D, Current Applied Physics, 20 (2020) 973-981.

[2] F. Baig, Y.H. Khattak, S. Ullah, B.M. Soucase, S. Beg, H. Ullah, Numerical analysis a guide to improve the efficiency of experimentally designed solar cell, Applied Physics A, 124 (2018) 471.

[3] J. Serhan, Z. Djebbour, W. Favre, A. Migan-Dubois, A. Darga, D. Mencaraglia, N. Naghavi, G. Renou, J.F. Guillemoles, D. Lincot, Investigation of the metastability behavior of CIGS based solar cells with ZnMgO–Zn(S,O,OH) window-buffer layers, Thin Solid Films, 519 (2011) 7606-7610.

[4] J. Liang, Y. Wang, Y. Zhang, X. Liu, J. Lin, Construction of perovskite homojunction for highly efficient perovskite solar cells by SCAPS-1D, Materials Science and Engineering: B, 301 (2024) 117196.

[5] A.S. Mathur, P.P. Singh, S. Upadhyay, N. Yadav, K.S. Singh, D. Singh, B.P. Singh, Role of absorber and buffer layer thickness on Cu2O/TiO2 heterojunction solar cells, Solar Energy, 233 (2022) 287-291.

[6] N.T. Jacob, J. Lauwaert, B. Vermang, J. Lauwaert, Numerical device modeling for direct Z-scheme junctions using a solar cell simulator, Solar Energy, 259 (2023) 320-327.

[7] E. Danladi, P.R. Jubu, A.M. Tighezza, I. Hossain, N.N. Tasie, M.O. Abdulmalik, A.C. Egbugha, M.O. Awoji, M. Kashif, E.D. Onoja, M.I. Amanyi, Highly efficient, hole transport layer (HTL)-free perovskite solar cell based on lithium-doped electron transport layer by device simulation, Emergent Materials, 6 (2023) 1779-1795.

[8] A.D. Adewoyin, M.A. Olopade, M. Chendo, Prediction and optimization of the performance characteristics of CZTS thin film solar cell using band gap grading, Optical and Quantum Electronics, 49 (2017) 336.

[9] D. Zhang, I.A. Digdaya, R. Santbergen, R.A.C.M.M. van Swaaij, P. Bronsveld, M. Zeman, J.A.M. van Roosmalen, A.W. Weeber, Design and fabrication of a SiOx/ITO double-layer anti-reflective coating for heterojunction silicon solar cells, Solar Energy Materials and Solar Cells, 117 (2013) 132-138.

[10] D.P. Pham, S. Lee, J. Yi, Optimisation of four-terminal GaAs//Si tandem solar cells using numerical simulation, Materials Science in Semiconductor Processing, 139 (2022) 106365.

[11] X. Cai, X. Zhou, Z. Liu, F. Jiang, Q. Yu, An in-depth analysis of the silicon solar cell key parameters' optimal magnitudes using PC1D simulations, Optik, 164 (2018) 105-113.

[12] K. Miyano, N. Tripathi, M. Yanagida, Y. Shirai, Lead Halide Perovskite Photovoltaic as a Model p–i–n Diode, Accounts of Chemical Research, 49 (2016) 303-310.

Chapter 3

Optimization of $CH_3NH_3PbI_{3-x}Cl_x$ based perovskite solar cells

3.1 Introduction

Perovskite light absorbers have gained a lot of attention in research over the past ten years due to their excellent photovoltaic properties, which include low exciton binding energy (~40 meV), ambipolar long charge diffusion lengths, low bulk defect densities, cheap solution processability, and high panchromatic absorption co-efficient (1.5 × 104 cm−1 at 550 nm).[3] However, additional charge transport layers and electrodes are needed to build high-efficiency perovskite solar cells (PSCs).[4, 5] As a result, numerous research teams have attempted to determine whether charge transport layer and perovskite light absorber combinations work best..[6] The optical, electrical, and interfacial property of perovskite light absorbers and charge transport layers plays a significant role in developing high-efficiency PSCs.[7] Techniques such as bilateral interface modification of room temperature synthesized $CsPbBr_3$ to reduce the defect at ETL/perovskite interface and induce graded fermi levels to increase built-in potential are reported in the literature.[8] Apart from the optoelectronic properties, the choice of precursor, thickness of films, synthesis procedure, and environment have been known to influence the overall performance of PSCs.[9] Nevertheless, they can be exploited to engineer high-efficiency PSCs at a low cost. In brief, mixed halide perovskite has shown higher stability in ambient synthesis.[10] As the PSCs result from dye-sensitized solar cells, the researchers prefer inorganic titanium dioxide (TiO_2) as an electron transport layer (ETL) over other counterparts.[11, 12] Similarly, spiro-OMeTAD, the solid-state electrolyte with lithium (Li) doping, is the widely preferred hole transport material (HTL).[13] Depending on the cost, stability, application, and processing temperature, the choice of transparent conducting substrates and counter electrodes is usually made.[14] Compared to other properties, the thickness, defect, and doping density of each layer directly influence the light management and charge carrier dynamics in the PSCs.

Given the above discussion, it becomes necessary to understand the variation in performance parameters of PSCs (i.e., open-circuit voltage (V_{OC}), short circuit current density (J_{SC}), fill factor (FF), and power conversion efficiency (PCE)) concerning variation in thickness, defect and doping density of the thin films. Also, experimentally studying these changes in performance is a myriad task. Therefore, researchers usually employ various simulation packages to study the parameters that have the slightest and highest control over the overall performance of PSCs. In general, any software that could solve basic semiconductor equations can simulate solar

cells. Finite difference time domain method (FDTD),[15] SILVACO ATLAS, [16, 17] wxAMPS,[18] AFORS-HET[19] are used to simulate the PSCs. Among these software packages, 1D Solar Cell Capacitance Simulator (SCAPS-1D), developed at Gent University, Belgium, offers a heterojunction and multi-junction solar cell devices simulation. [20, 21]

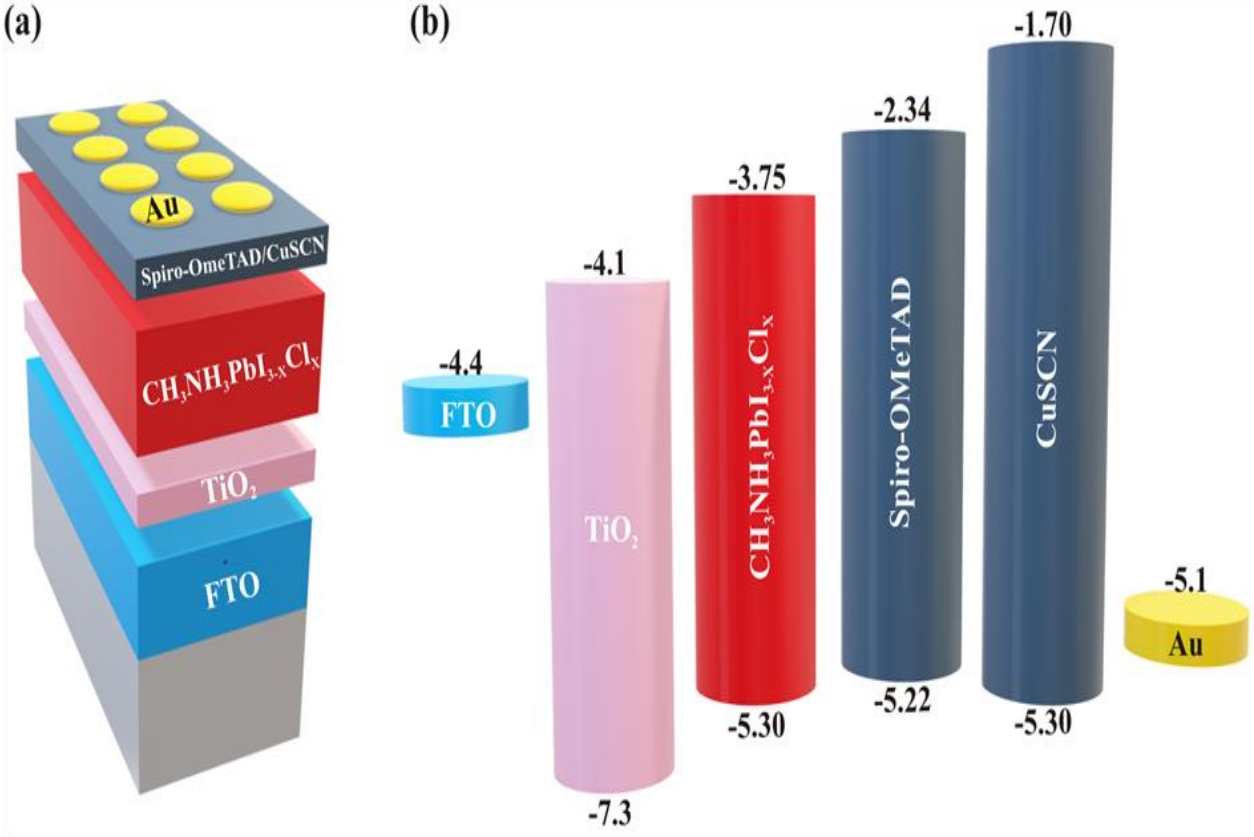

Figure 3.1 (a) Schematic representation and (b) Corresponding energy band diagram of the PSC device adopted in this study.

Therefore, in this chapter, SCAPS-1D is used to perform a preliminary study on $CH_3NH_3PbI_{3-X}Cl_X$ perovskite light absorber with fluorine-doped tin oxide (FTO) as transparent conducting oxide, TiO_2 as ETL, both expensive organic Spiro-OMeTAD, and cheap inorganic copper thiocyanate (CuSCN) as HTLs, and various counter electrodes to experimentally build high-performance PSC structure. A high PCE of ~30% is simulated with low-cost materials known for their simple and efficient processing. The device structure adopted in this study is as shown in Fig. 3.1(a). The exact reasons behind selecting each layer are elaborated in the subsequent sections.

Moreover, this simulation methodology can be extended in studying other perovskite light absorbers and transport layers.

3.2 Simulation procedure

Planar PSCs (n-i-p) with FTO/TiO_2/$CH_3NH_3PbI_{3-X}Cl_X$/spiro-OMeTAD/counter electrode and FTO/TiO_2/$CH_3NH_3PbI_{3-X}Cl_X$/CuSCN/counter electrode configurations are used. The corresponding band diagram is as shown in Fig. 3.1(b), where FTO coated glass substrates is used as the transparent conducting substrate, TiO_2 is the electron transport or hole blocking layer, $CH_3NH_3PbI_{3-X}Cl_X$ is perovskite light absorber, spiro-OMeTAD, and CuSCN are the hole transport or electron blocking layers and Au is considered as the counter electrode. The simulation is carried out under a global AM 1.5 spectrum with an incident power of 100mW/cm^2. Solar cells parameters can be obtained on solving fundamental semiconductor equations (Eq. 1, 2, and 3), which dictate the charge transport in the semiconductor are listed below,

Poisson Equation (Eq. 3.1):

$$\frac{dy}{dx} = -\frac{d^2\Psi}{dx^2} = \frac{q}{\varepsilon}[p(x) - n(x) + N_D^+(x) - N_A^- + p_t(x) - n_t(x)] \quad (3.1)$$

where Ψ is the electrostatic potential, q is the electron charge, ε is the dielectric constant of the semiconductor material, p (n) is the hole (electron) concentration, N_A^- (N_D^+) is the density of the ionized acceptors (donors), n_t (p_t) is the trapped electron (hole), and x is the position coordinate.

Electron (Eq. 3.2) and hole (Eq. 3.3) continuity equations:

$$\frac{dn_p}{dt} = G_n - \frac{n_p - n_{p0}}{\tau_n} + n_p\mu_n\frac{dE}{dx} + \mu_n E\frac{dn_p}{dx} + D_n\frac{d^2n_p}{dx^2} \quad (3.2)$$

$$\frac{dp_n}{dt} = G_p - \frac{p_n - p_{n0}}{\tau_p} + p_n\mu_p\frac{dE}{dx} + \mu_p E\frac{dp_n}{dx} + D_p\frac{d^2p_n}{dx^2} \quad (3.3)$$

where G_n and G_p are the electron and hole generation rates, n_p and p_n are the electron and hole concentrations in p-region and n-region, respectively, n_{p0} and p_{n0} are the equilibrium electron and hole concentrations in p-region and n-region, τ_n and τ_p denotes electron and hole lifetime, μ_p and μ_n are the hole and electron mobilities, E is the electric field, D_n and D_p are the electron and hole diffusion coefficients. The carrier transport occurring by drift and diffusion for electrons (Eq. 3.4) and holes (Eq. 3.5) is expressed as:

$$J_n(x) = qn\mu_n E + qD_n \frac{dn}{dx} = n\mu_n \frac{dE_{Fn}}{dx} \quad (3.4)$$

$$J_p(x) = qp\mu_p E - qD_p \frac{dp}{dx} = p\mu_p \frac{dE_{Fp}}{dx} \quad (3.5)$$

where E_{Fn} and E_{Fp} are the quasi-Fermi levels for electrons and holes. The physical parameters used in the simulation of PSCs are tabulated in Table 3.1.

Table 3.1. List of parameters used in the simulation.

Term	**FTO**	**TiO_2**	**$CH_3NH_3PbI_{3-X}Cl_X$**	**Spiro-OMeTAD**	**CuSCN**
Thickness (μm)	0.1	0.03	0.90	0.05	0.05
Bandgap (eV)	3.5	3.2	1.55	2.88	3.60
Electron affinity (eV)	4.0	4.0	3.90	2.05	1.70
Relative dielectric permittivity	9.0	100	6.50	3.00	10.0
Conduction band effective density of states (cm^{-3})	2.2×10^{18}	10^{19}	2.2×10^{17}	2.2×10^{18}	2.2×10^{19}
Valence band effective density of states (cm^{-3})	1.8×10^{19}	10^{19}	1.8×10^{19}	1.8×10^{19}	1.8×10^{19}
Electron thermal velocity (cm/s)	10^7	10^7	10^7	10^7	10^7

Hole velocity (cm/s)	10^7	10^7	10^7	10^7	10^7
Electron mobility (cm^2/Vs)	20	6×10^{-3}	2	2×10^{-4}	100
Hole mobility (cm^2/Vs)	10	6×10^{-3}	2	2×10^{-4}	0.25
Shallow uniform donor density, N_D (cm^{-3})	2×10^{19}	10^{19}	10^{17}	1	-
Shallow uniform acceptor density, N_A (cm^{-3})	-	-	-	2×10^{19}	2×10^{19}
Defect density, N_t (cm^{-3})	10^{15}	10^{15}	10^{13}	10^{15}	10^{15}
Ref.	[22]	[22]	[23]	[22]	[24]

3.3 Results and discussion

3.3.1 Influence of transparent conducting oxide

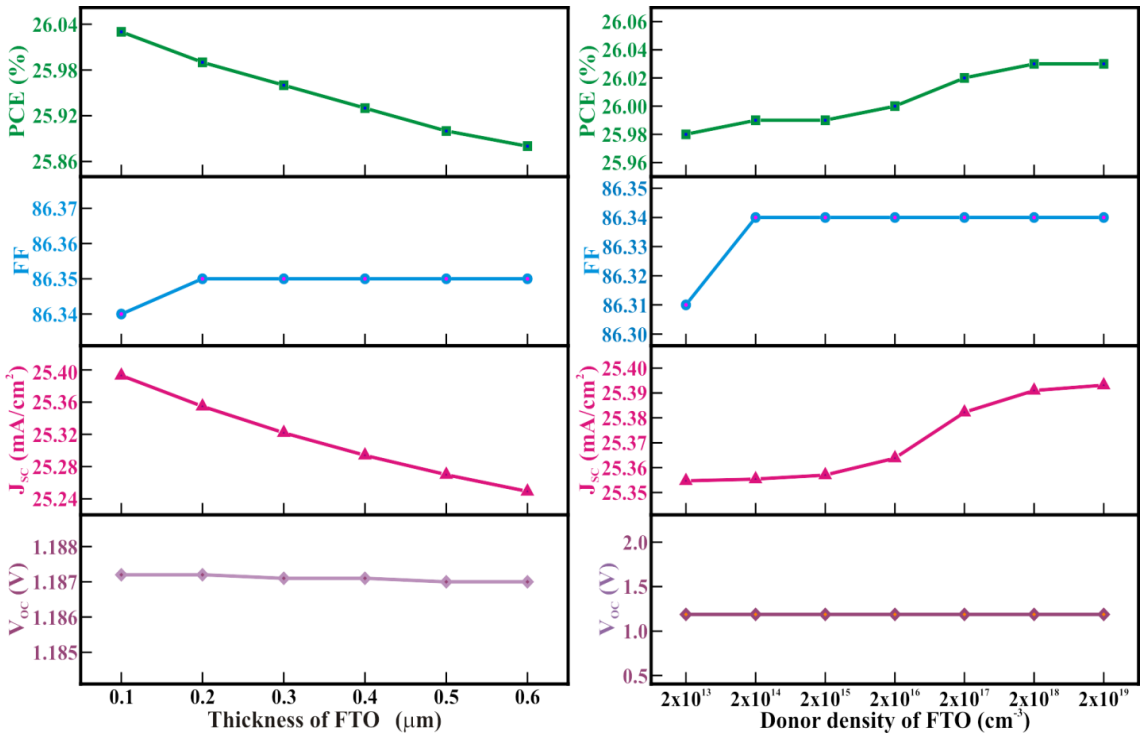

Figure 3.2 Thickness and the donor density of FTO layer dependent variation of solar cell parameters. (with other parameters as tabulated in Table 3.1)

The fabrication of PSCs starts with careful optimization of transparent conducting electrodes. In this study, FTO was considered due to its high thermal (500℃) and chemical stability relative to other counterparts. Further, the thickness of the FTO coating over the glass slides determines both the sheet resistance and transparency of the films. The sheet resistance is indirectly proportional to thickness. Thus, an increase in the thickness of the FTO film decreases its sheet resistance leading to lower series resistance in PSC devices resulting in high J_{SC} and PCE. On the contrary, an increase in the thickness of the FTO film absorbs incident radiation lowering the radiation reaching the perovskite absorber. Thus, donor doping density in FTO films is varied to counter this trade-off. Fig. 3.2 shows the variation of solar cell parameters with respect to the variation in thickness and donor doping density of the FTO film. In line with the commercially available FTO, the thickness of the FTO film was varied from 100 to 600

nm. It is to be noted that, as the thickness of the FTO films increased, a ~0.2% drop in PCE was observed. This drop can be attributed to a gradual decrease in J_{SC} arising from lower irradiation reaching the perovskite absorber. Further, as the FF remains reasonably constant, it can be concluded that the sheet resistance of the FTO films has no significant variation with respect to the increase in thickness of FTO film from 100 to 600 nm. Since the variation in thickness of the FTO films does not affect the energy levels of the FTO, V_{OC} has remained constant.

3.3.2 Influence of TiO_2 ETL

It is well known that the PSCs are the resultant evolution of dye-sensitized solar cells.[25] Many research groups prefer TiO_2 as ETL in PSCs. TiO_2 performs the following functionalities (i) serves as the template for perovskite over layer, (ii) blocks ultra-violet radiation from reaching perovskite absorber, (iii) blocks hole transport, and (iv) helps in dissociation of exciton at the TiO_2/perovskite interface.[26] Thus it is vital to optimize the thickness and donor density of TiO_2 for the fabrication of high-efficiency PSCs. Fig. 3.3 shows the variation of solar cell parameters with respect to the variation in thickness and donor doping density of the TiO_2 film. In line with the literature, the thickness of TiO_2 film was varied from 30 to 210 nm. As the thickness of the TiO_2 films increased, ~0.4% reduction in PCE was observed. This decrease in PCE can be attributed to the corresponding decline in J_{SC}. Since the V_{OC} and FF have fairly remained constant, it can be concluded that as the thickness of TiO_2 film increases, the charge diffusion length and mobility of electrons in TiO_2 ETL decreases due to increased charge trap defects in thicker TiO_2 films, resulting in lower J_{SC}. However, experimentally synthesizing pinhole-free TiO_2 thin films (<45 nm), which have low charge trap states, requires high-cost thin-film techniques. Furthermore, as the thickness of the TiO_2 ETL increases, the irradiation reaching the $CH_3NH_3PbI_{3-X}Cl_X$ perovskite light absorber in the n-i-p device structure decreases. Lower irradiation on the $CH_3NH_3PbI_{3-X}Cl_X$ perovskite light absorber lowers the photogeneration in the light absorber leading to lower J_{SC} in PSCs. Thus, various research groups have used doping as a strategy to increase the charge mobility and diffusion length of electrons in TiO_2 films. As the donor density of TiO_2 films increases to sufficiently higher levels (i.e.,

10^{17} cm^{-3}), a ~0.15% increase in PCE is observed. This increase in PCE results from higher J_{SC} obtained at the same donor density (i.e., 10^{17} cm^{-3}). Moreover, negligible variation in V_{OC} and FF is observed with varying donor densities.

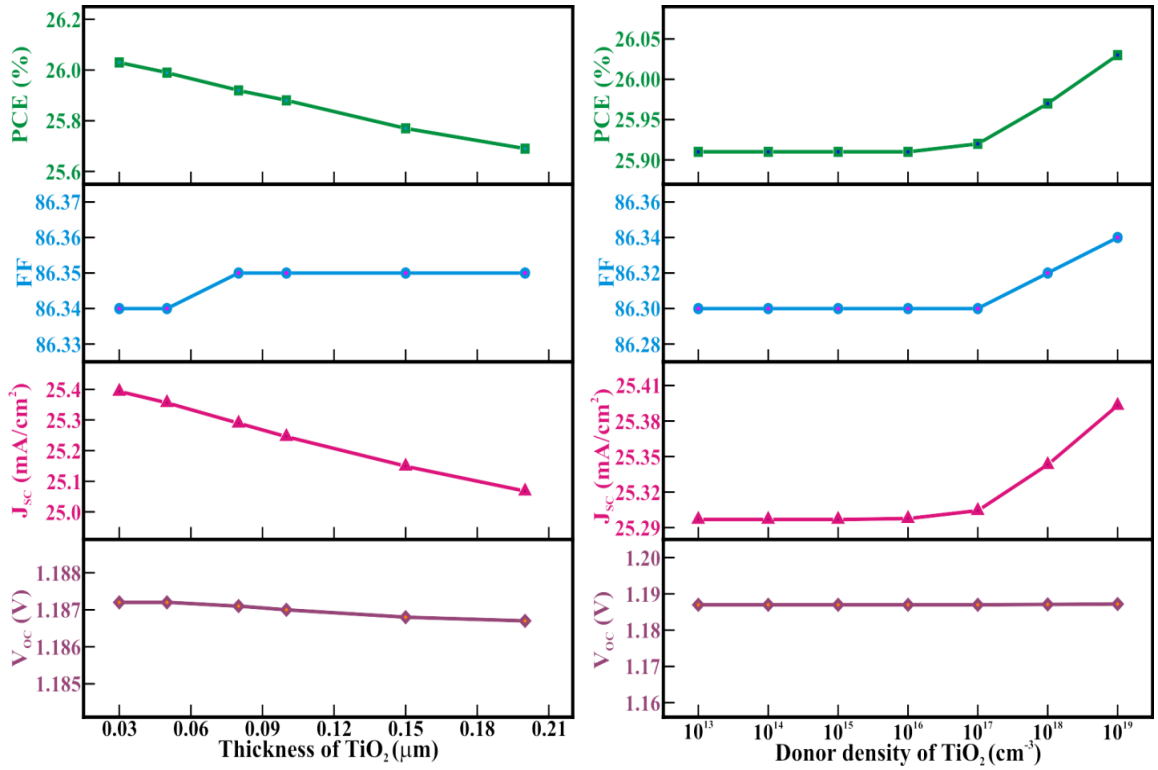

Figure 3.3 Thickness and the donor density of the TiO_2 layer. (with other parameters as tabulated in Table 3.1)

3.3.3 Influence of $CH_3NH_3PbI_{3-X}Cl_X$ perovskite light absorber

The use of $CH_3NH_3PbI_{3-X}Cl_X$ perovskite light absorbers can improve the performance of PSCs as they can provide uniform coverage with negligible hysteresis.[27] The presence of chlorine ions in the perovskite absorber layer, precisely at the TiO_2/perovskite interface, reduces the hysteresis effect.[28] Furthermore, $CH_3NH_3PbI_{3-X}Cl_X$ has the advantage of high-quality film deposition in ambient conditions with excellent photovoltaic properties.[29] Additionally, the charge diffusion length in $CH_3NH_3PbI_{3-X}Cl_X$ can exceed 1 μm.[30]

Furthermore, the thickness of $CH_3NH_3PbI_{3-X}Cl_X$ perovskite light absorber films has been known to influence the overall performance of the PSCs. Though perovskite

absorbers have a high absorption coefficient, yet the minimum thickness of the film is necessary for complete panchromatic absorption. However, increasing the thickness beyond charge diffusion lengths can lead to charge recombination and decline performance.[3] Thus in this study, the thickness of perovskite was varied from 100 to 900 nm.

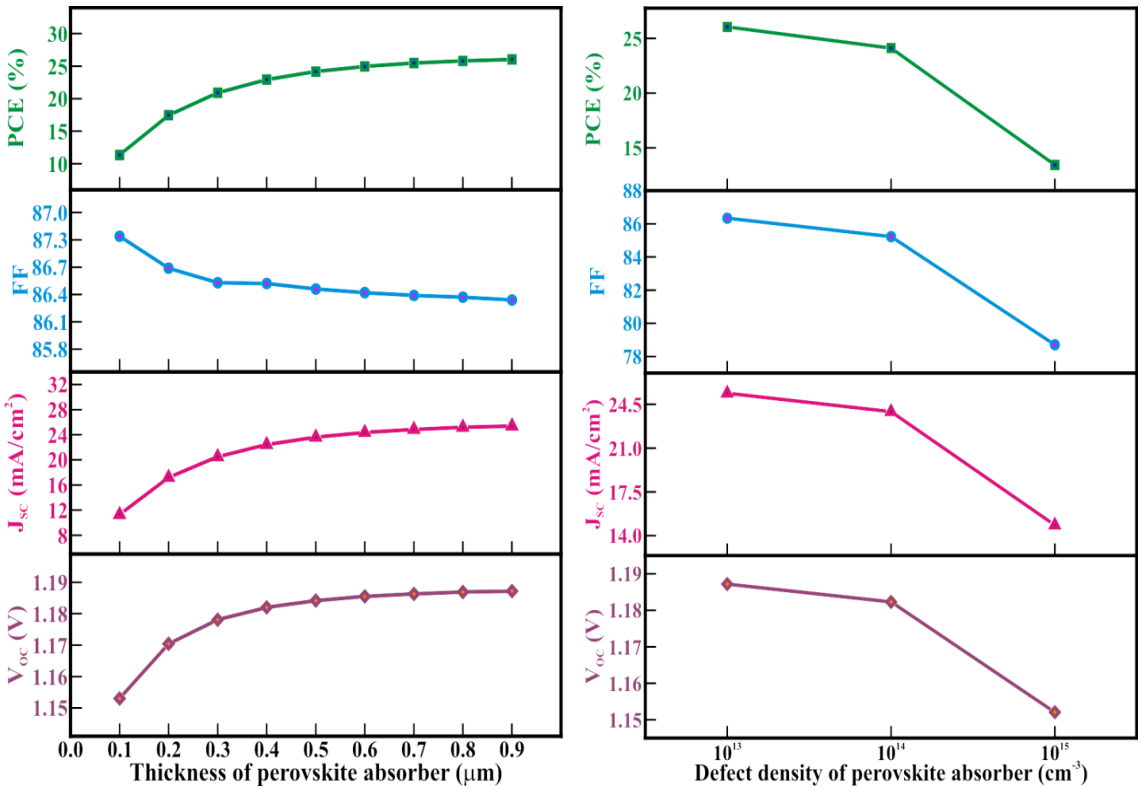

Figure 3.4 Thickness and the defect density of $CH_3NH_3PbI_{3-X}Cl_X$ perovskite light absorber layer dependent variation of solar cell parameters. (with other parameters as tabulated in Table 3.1)

Fig. 3.4 shows the variation of solar cell parameters with respect to the variation in thickness and defect density of the $CH_3NH_3PbI_{3-X}Cl_X$ perovskite light absorber. An astonishing 150% increase in PCE is observed as the perovskite absorber layer thickness increases from 100 to 900 nm. The main contributor to such a high increase in PCE can be correlated to the corresponding rise in J_{SC}. Moreover, as the thickness of the perovskite absorber increases, minimal changes in the V_{OC} and FF are observed. Apart from the thickness of the perovskite absorber, the defect density in the perovskite

absorber layer plays a significant role in deciding the performance of PSCs. However, perovskite light absorbers are known to have low defect densities [25] in an attempt to further decrease the defect densities, numerous thin film synthesis techniques,[31] solvent engineering,[32] ionic salt additives,[33] controlled synthesis,[34], etc., are used. Therefore, depending on the synthesis technique adopted, defect densities in the perovskite vary and play a prominent role in PCEs. In this study, the defect density directly impacts all the solar cell parameters, i.e., V_{OC}, J_{SC}, FF, and PCE. As the defect density of the $CH_3NH_3PbI_{3-X}Cl_X$ perovskite light absorber increases from 10^{13} to 10^{15} cm^{-3}, PCE dropped from ~26% to less than 14%. This drop is contributed by drop FF, $J_{SC,}$ and V_{OC}. Lowering of J_{SC} can be caused by defect-assisted charge recombination, which reduces the FF due to increased series resistance of the cells.

3.3.4 Influence of Spiro-OMeTAD HTL

Spiro-OMeTAD became a prominent HTL or the perovskite regeneration solid-state electrolyte as the PSCs evolved [35] to date, most of the high-efficiency PSCs report using Spiro-OMeTAD with Li salts doping to enhance the conductivity. The majority of the reports use the spin coating technique to coat Spiro-OMeTAD during the fabrication of the PSCs.[36] Therefore given the thickness obtained from the spin coating of Spiro-OMeTAD, the thickness of Spiro-OMeTAD was varied from 50 to 200 nm. Fig. 3.5 shows the variation of solar cell parameters with respect to the variation in thickness and acceptor density of the Spiro-OMeTAD. Negligible variation in PCE is observed with varying the thickness of the Spiro-OMeTAD layer. It is evident in n-i-p planar structures that Spiro-OMeTAD never interferes in the optics of the PSCs. However, the effect of the thickness of Spiro-OMeTAD may influence the PCE when the p-i-n inverted PSC device structure is adopted. The acceptor density of Spiro-OMeTAD is extensively tailored experimentally by doping [37]

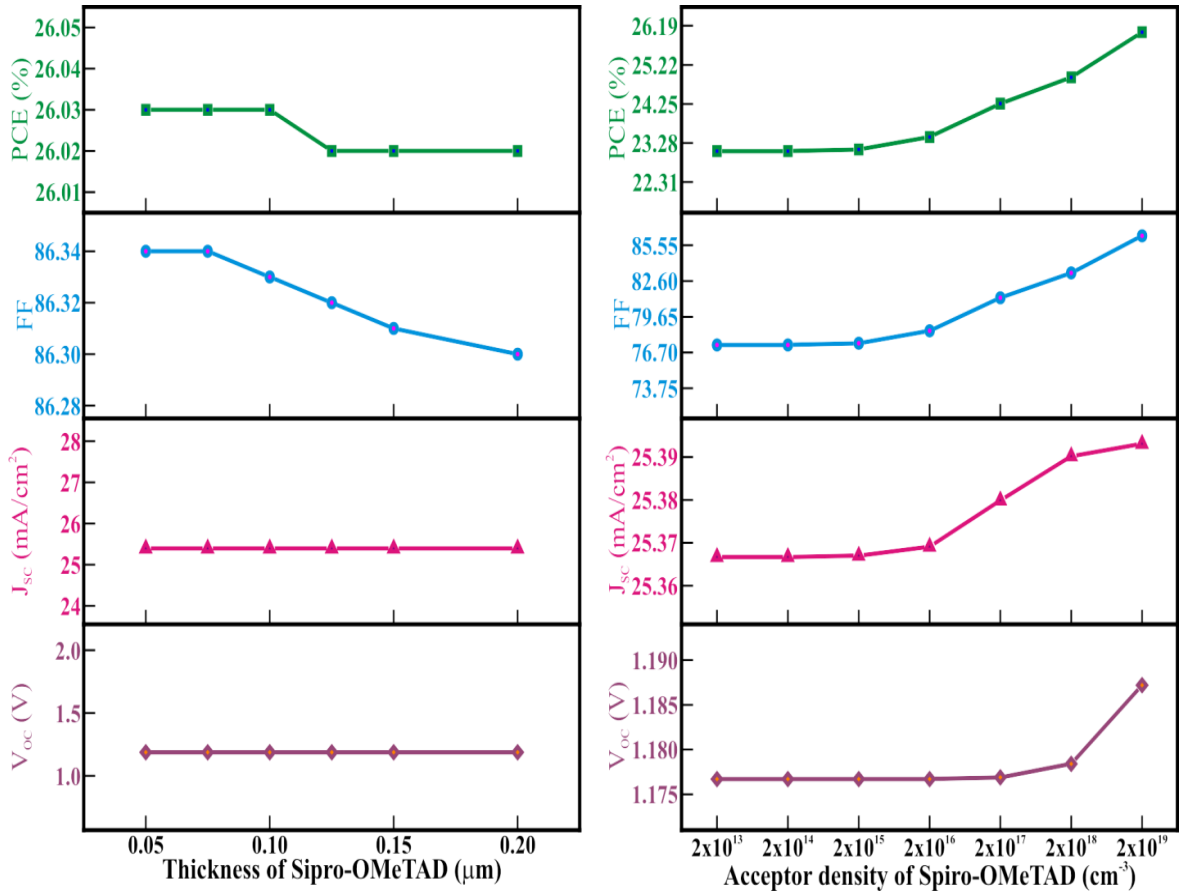

Figure 3.5 Thickness and acceptor density of Spiro-OMeTAD layer dependent variation of solar cell parameters. (with other parameters as tabulated in Table 3.1)

Thus, in this study, acceptor density is varied from 2×10^{13} to 2×10^{19} cm^{-3}. As acceptor density increases, the corresponding increase in PCE is observed. At acceptor density levels of 2×10^{19} cm^{-3}, the PCE exceeds 26%. The principal contributor to this increase is the FF and V_{OC}. So, it is apparent that the acceptor density in Spiro-OMeTAD altered the series resistance of the PSC. The variation in V_{OC} is expected as the doping in Spiro-OMeTAD varies the HOMO and LUMO levels altering the band offset.

3.3.5 Influence of CuSCN HTL

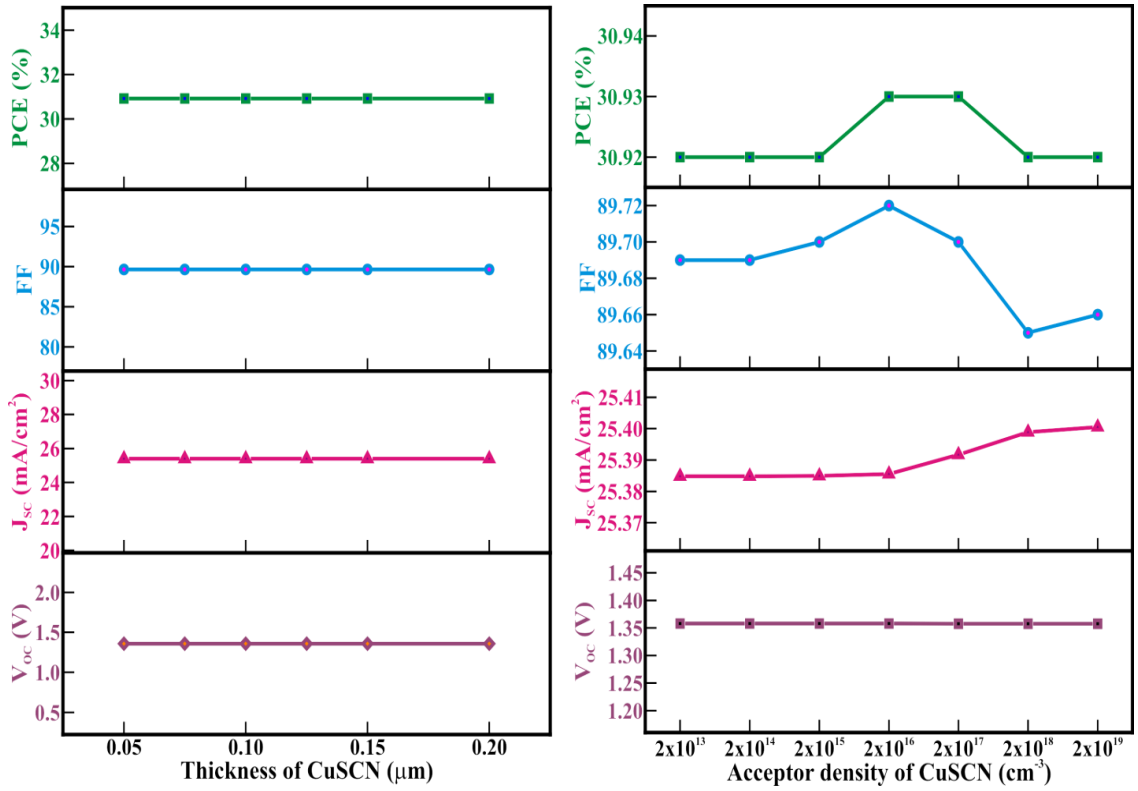

Figure 3.6 Thickness and acceptor density of CuSCN layer dependent variation of solar cell parameters. (with other parameters as tabulated in Table 3.1)

Spiro-OMeTAD thin film synthesis requires inert atmosphere processing and deteriorates with time, leading to short-time stability of PSCs. Therefore, in an attempt to find other cheap ambient-friendly alternatives, CuSCN is also considered in this study.[38] Unlike Spiro-OMeTAD, CuSCN processing is not limited to spin coating.[39] Fig. 3.6 shows the variation of solar cell parameters with respect to the variation in thickness and acceptor density of the CuSCN film. Excellent PCE of over 30% can be achieved with CuSCN as HTL from the PSC configuration adopted in this study. Furthermore, PCE and other solar cell parameters remained constant with varying thickness of the CuSCN layer. Similar to Spiro-OMeTAD, the acceptor density of CuSCN is varied; however, variation of acceptor density of CuSCN had a negligible effect on the solar cell parameters, and efficiency close to 31% is observed. A sharp increase in J_{SC} observed at the acceptor density of 2×10^{16} cm^{-3} results from the increase

in electrical conductivity of the CuSCN film. Therefore, a corresponding rise in FF up to an acceptor density of 2×10^{16} cm^{-3} is observed. Further, when the acceptor density increases beyond 2×10^{16} cm^{-3}, the FF declines to lower values may be due to increased leakage current at the perovskite/CuSCN interface caused by increased acceptor doping density in CuSCN films. Thus, the PCE of the PSC encountered a similar rise at an acceptor density of 2×10^{16} cm^{-3}.

3.3.6 Influence of operating temperature and material of the counter electrode

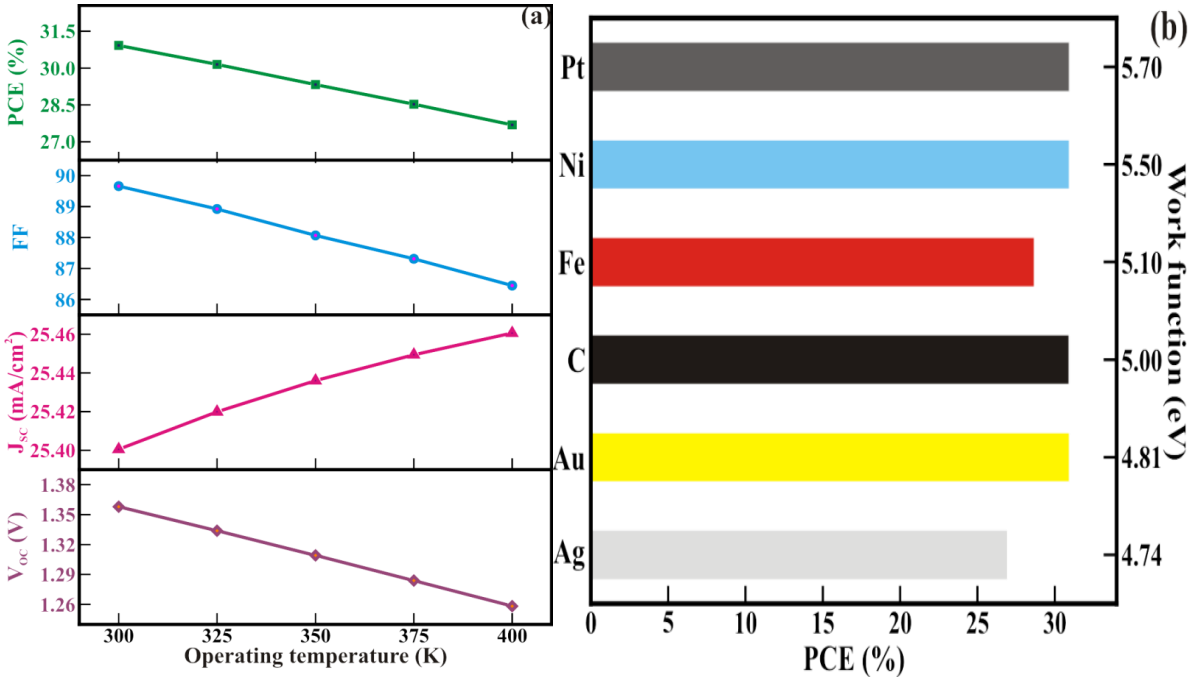

Figure 3.7 (a) Operating temperature-dependent variation of solar cell parameters. (with other parameters as tabulated in Table 3.1) (b) Variation in PCE depending on the counter electrode material.

For the real-time application of PSCs, operating temperature plays a prominent role in influencing the overall performance. Moreover, the perovskite light absorbers are known to degrade with temperature and moisture. [40, 41] Therefore, in this study, the operating temperature was varied from 300 to 400 K. Fig. 3.7(a) shows the operating temperature-dependent variation of solar cell parameters. When the temperature is raised from 300 to 400 K, ~3.5% drop in PCE is observed. This loss in PCE with temperature is associated with a corresponding decline in FF and V_{OC}. The negligible

variation in J_{SC} shows the thermal stability of the $CH_3NH_3PbI_{3-X}Cl_X$ perovskite light absorber.[42] The decrease in V_{OC} with increasing temperature results from higher recombination probabilities. Furthermore, at elevated temperatures, interfacial charge recombination is the dominant factor that reduces the FF of the PSCs.[43]

The counter electrode material used alters the PCE of PSCs, as shown in Fig. 3.7(b). Though high efficiencies are obtained with most metals, certain metals diffuse into the perovskite absorber layer and form a metal halide complex, decreasing the efficiency and durability of the PSCs.[44] Further, around 20% of the manufacturing cost is consumed by Au when used as the counter electrode. Conversely, carbon electrodes are cheap alternatives to replace Au and Ag in PSCs.[14] Apart from the suitable work function needed for the proper functioning of the device, the conductivity of the counter electrodes also needs to be considered. Fig. 3.8 shows the JV characteristics and quantum efficiency curve for the best-performing $FTO/TiO_2/CH_3NH_3PbI_{3-X}Cl_X/CuSCN/Au$ device structure with PCE exceeding 30%.

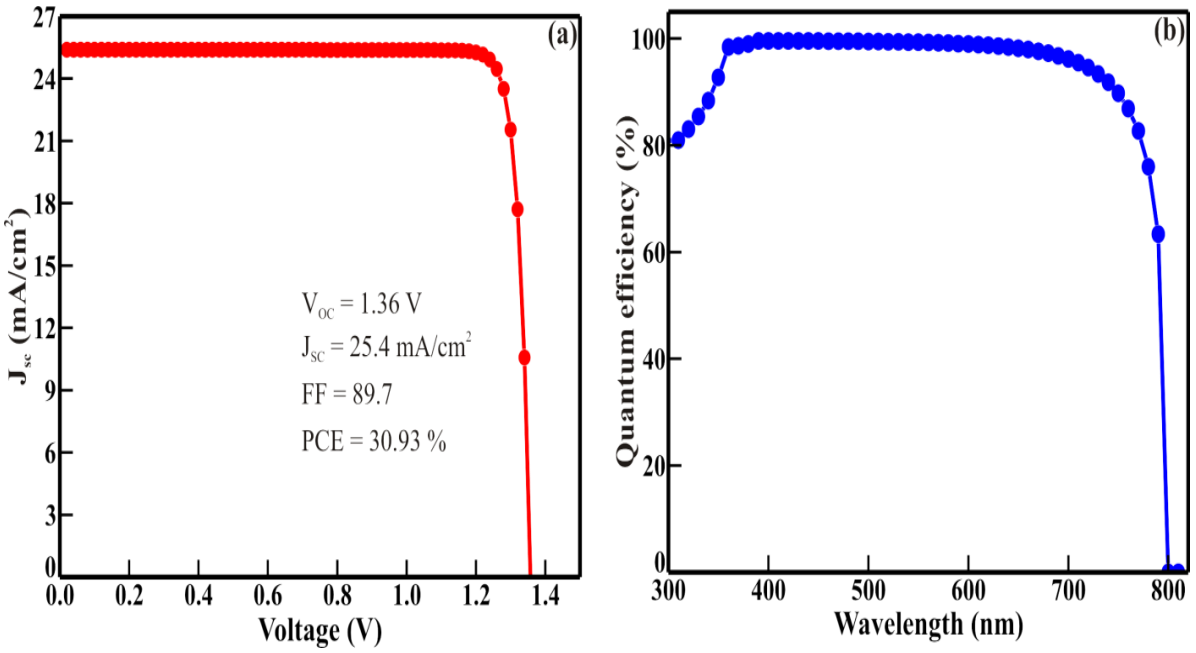

Figure 3.8 (a) Shows the JV curve and (b) Quantum efficiency for the best performing $FTO/TiO_2/CH_3NH_3PbI_{3-X}Cl_X/CuSCN/Au$ device structure.

3.4 Conclusion

In conclusion, we used SCAPS 1D software to simulate the $CH_3NH_3PbI_{3-X}Cl_X$ perovskite light absorber. Planar PSCs (n-i-p) with FTO/TiO_2/$CH_3NH_3PbI_{3-X}Cl_X$/spiro-OMeTAD/counter electrode and FTO/TiO_2/$CH_3NH_3PbI_{3-X}Cl_X$/CuSCN/counter electrode configurations are used. A systematic study on the influence of each layer on the performance of PSCs is evaluated. The thickness and defect density of the $CH_3NH_3PbI_{3-X}Cl_X$ perovskite absorber layer has the highest impact on the PCE and other solar cell parameters. Both expensive organic Spiro-OMeTAD's and cheap inorganic CuSCN thickness and acceptor density had negligible impact on the performance of PSCs. Further, the thickness and the donor density of FTO and TiO_2 had minimal impact on the PCE of the PSCs. Nonetheless, PSCs with CuSCN showed high efficiency (~31%) compared to devices with Spiro-OMeTAD (~26%) due to high intrinsic hole mobility of CuSCN (i.e., 2.5×10^{-1} cm^2/Vs) as compared to Spiro-OmeTAD (i.e., 2.0×10^{-4} cm^2/Vs). However, experimentally CuSCN films are synthesized with the assistance of polar solvents, which are corrosive to perovskite light absorbers and may dissolve the perovskite films during deposition. Thus, practically the PCE of PSCs with CuSCN is around 20% as compared to the PSCs with Spiro-OmeTAD (~25%). On the contrary, experimentally using intermediate processing conditions to negate the effect of polar solvents on perovskite absorbers or by using suitable solvents to synthesize pristine CuSCN films or tailoring the device architecture to minimize the grazing of polar solvents over perovskite films may lead to better performing PSCs. The present preliminary studies on $CH_3NH_3PbI_{3-X}Cl_X$ perovskite absorber-based solar cells can be used to develop PSCs exceeding 30% PCE experimentally. Also, the technique and conclusion presented can be extended to other perovskite light absorbers and other optoelectronic devices.

3.5 References

[1] Park, N.-G., Perovskite solar cells: an emerging photovoltaic technology. Mater. Today, 2015. 18: p. 65-72. DOI: 10.1016/j.mattod.2014.07.007.

[2] Soufiani, A.M., et al., Polaronic exciton binding energy in iodide and bromide organic-inorganic lead halide perovskites. Appl. Phys. Lett., 2015. 107: p. 231902. DOI: 10.1063/1.4936418.

[3] Jung, H.S., and N.-G. Park, Perovskite Solar Cells: From Materials to Devices. Small, 2015. 11: p. 10-25. DOI: 10.1002/smll.201402767.

[4] Valadi, K., et al., Metal oxide electron transport materials for perovskite solar cells: a review. Environ. Chem. Lett., 2021. 19: p. 2185-2207. DOI: 10.1007/s10311-020-01171-x.

[5] Arumugam, G.M., et al., Inorganic hole transport layers in inverted perovskite solar cells: A review. Nano Select, 2021. 2: p. 1081-1116. DOI: 10.1002/nano.202000200

[6] Lakhdar, N. and Hima, A. Electron transport material effect on performance of perovskite solar cells based on $CH_3NH_3GeI_3$. Opt. Mater., 2020. 99: p. 109517. DOI: 10.1016/j.optmat.2019.109517.

[7] Liu, Z., et al., Morphology-Tailored Halide Perovskite Platelets, and Wires: From Synthesis, Properties to Optoelectronic Devices. Adv. Opt. Mater., 2018. 6: p. 1800413. DOI: 10.1002/adom.201800413.

[8] Zhang, J., et al., $CsPbBr_3$ nanocrystal induced bilateral interface modification for efficient planar perovskite solar cells. Adv. Sci. 2021. 8: p. 2102648. DOI: 10.1002/advs.202102648.

[9] Manjunath, V., et al., Oxidized Nickel films as highly transparent HTLs for inverted planar perovskite solar cells. Sol. Energy, 2019. 193: p. 387-394. DOI: 10.1016/j.solener.2019.09.070.

[10] Du, Y., et al., Flexible Perovskite Solar Cells onto Plastic Substrate Exceeding 13% Efficiency Owing to the Optimization of $CH_3NH_3PbI_{3-x}Cl_x$ Film via H_2O Additive. ACS Sustain. Chem. Eng., 2018. 6: p. 1083-1090. DOI: 10.1021/acssuschemeng.7b03382.

[11] Dileep, R., et al., Room-temperature curable carbon cathode for hole-conductor free perovskite solar cells. Sol. Energy, 2019. 187: p. 261-268. DOI: 10.1016/j.solener.2019.05.045.

[12] Karthikeyan, V., et al., Hydrothermally tailored anatase TiO_2 nanoplates with exposed {111} facets for highly efficient dye-sensitized solar cells. Sol. Energy, 2017. 147: p. 202-208. DOI: 10.1016/j.solener.2017.03.049.

[13] Jeong, J., et al., Pseudo-halide anion engineering for α-$FAPbI_3$ perovskite solar cells. Nature, 2021. 592: p. 381-385. DOI: 10.1038/s41586-021-03406-5.

[14] Maniarasu, S., et al., Recent advancement in metal cathode and hole-conductor-free perovskite solar cells for low-cost and high stability: A route towards commercialization. Renew. Sust. Energy Rev., 2018. 82: p. 845-857. DOI: 10.1016/j.rser.2017.09.095.

[15] Saffari, M., et al., DFT analysis and FDTD simulation of $CH_3NH_3PbI_{3-x}Cl_x$ mixed halide perovskite solar cells: role of halide mixing and light trapping technique. J. Phys. D: Appl. Phys., 2017. 50: p. 415501. DOI: 10.1088/1361-6463/aa83c8.

[16] Mehrabian, M. and S. Dalir, 11.73% efficient perovskite heterojunction solar cell simulated by SILVACO ATLAS software. Optik, 2017. 139: p. 44-47. DOI: 10.1016/j.ijleo.2017.03.077.

[17] Bacha, M., A. Saadoune, and I. Youcef, Numerical simulation and optimization of $CH_3NH_3PbI_{3-x}Br_x$ perovskite solar cell for high conversion efficiency. Opt. Mater., 2021. 122: p. 111734. DOI: 10.1016/j.optmat.2021.111734.

[18] Smucker, J. and J. Gong, A comparative study on the band diagrams and efficiencies of silicon and perovskite solar cells using wxAMPS and AMPS-1D. Sol. Energy, 2021. 228: p. 187-199. DOI: 10.1016/j.solener.2021.09.066.

[19] Yadav, C. and S. Kumar, Numerical simulation of novel designed perovskite/silicon heterojunction solar cell. Opt. Mater., 2022. 123: p. 111847. DOI: 10.1016/j.optmat.2021.111847.

[20] Karthick, S., S. Velumani, and J. Bouclé, Experimental and SCAPS simulated formamidinium perovskite solar cells: A comparison of device performance. Sol. Energy, 2020. 205: p. 349-357. DOI: 10.1016/j.solener.2020.05.041.

[21] Lakhdar, N. and A. Hima, Electron transport material effect on performance of perovskite solar cells based on $CH_3NH_3GeI_3$. Opt. Mater., 2020. 99: p. 109517. DOI: 10.1016/j.optmat.2019.109517.

[22] Abdelaziz, S., et al., Investigating the performance of formamidinium tin-based perovskite solar cell by SCAPS device simulation. Opt. Mater., 2020. 101: p. 109738. DOI: 10.1016/j.optmat.2020.109738.

[23] Rai, S., B.K. Pandey, and D.K. Dwivedi, Device simulation of low cost HTM free perovskite solar cell based on TiO_2 electron transport layer. AIP Conference Proceedings, 2020. 2220: p. 140022. DOI: 10.1063/5.0001230.

[24] Raoui, Y., et al., Performance analysis of $MAPbI_3$ based perovskite solar cells employing diverse charge selective contacts: Simulation study. Sol. Energy, 2019. 193: p. 948-955. DOI: 10.1016/j.solener.2019.10.009.

[25] Snaith, H.J., Perovskites: The emergence of a new era for low-cost, high-efficiency solar cells. J. Phys. Chem. Lett., 2013. 4: p. 3623-3630. DOI: 10.1021/jz4020162.

[26] Sun, S., T. Buonassisi, and J.-P. Correa-Baena, State-of-the-art electron-selective contacts in perovskite solar cells. Adv. Mater. Interfaces, 2018. 5: p. 1800408. DOI: 10.1002/admi.201800408.

[27] Song, D.-h., et al., Reproducible formation of uniform $CH_3NH_3PbI_{3-x}Cl_x$ mixed halide perovskite film by separation of the powder formation and spin-coating process. J. Power Sources, 2016. 310: p. 130-136. DOI: 10.1016/j.jpowsour.2016.02.010.

[28] Yang, Y., et al., Enhanced crystalline phase purity of $CH_3NH_3Pbi_{3-x}Cl_x$ film for high-efficiency hysteresis-free perovskite solar cells. ACS Appl. Mater. Interfaces, 2017. 9: p. 23141-23151. DOI: 10.1021/acsami.7b03941.

[29] Wang, Y., et al., Ambient-air-solution-processed efficient and highly stable perovskite solar cells based on $CH_3NH_3PbI_{3-x}Cl_x$-NiO composite with Al_2O_3/NiO interfacial engineering. Nano Energy, 2017. 40: p. 408-417. DOI: 10.1016/j.nanoen.2017.08.047.

[30] Lee, M.M., et al., Efficient hybrid solar cells based on meso-superstructured organometal halide perovskites. Science, 2012. 338: p. 643-647. DOI: 10.1126/science.1228604.

[31] Song, T.-B., et al., Perovskite solar cells: film formation and properties. J. Mater. Chem. A, 2015. 3: p. 9032-9050. DOI: 10.1039/C4TA05246C.

[32] Chao, L., et al., Solvent engineering of the precursor solution toward large-area production of perovskite solar cells. Adv. Mater., 2021. 33: p. 2005410. DOI: 10.1002/adma.202005410.

[33] Shahiduzzaman, M., et al., The benefits of ionic liquids for the fabrication of efficient and stable perovskite photovoltaics. Chem. Eng. J., 2021. 411: p. 128461. DOI: 10.1016/j.cej.2021.128461.

[34] Sánchez, S., et al., Rapid hybrid perovskite film crystallization from solution. Chem. Soc. Rev., 2021. 50: p. 7108-7131. DOI: 10.1039/D0CS01272F.

[35] Kim, H.-S., et al., Lead iodide perovskite sensitized all-solid-state submicron thin film mesoscopic solar cell with efficiency exceeding 9%. Sci. Rep., 2012. 2: p. 591. DOI: 10.1038/srep00591.

[36] Kim, G.-W., et al., Hole transport materials in conventional structural (n–i–p) perovskite solar cells: from past to the future. Adv. Energy Mater., 2020. 10: p. 1903403. DOI: 10.1002/aenm.201903403.

[37] Wang, Z.-K., and L.-S. Liao, Doped charge-transporting layers in planar perovskite solar cells. Adv. Opt. Mater., 2018. 6: p. 1800276. DOI: 10.1002/adom.201800276.

[38] Matebese, F., R. Taziwa, and D. Mutukwa, Progress on the synthesis and application of CuSCN inorganic hole transport material in perovskite solar cells. Materials, 2018. 11: p. 2592. DOI: 10.3390/ma11122592.

[39] Ye, T., et al., Recent advances of Cu-based hole transport materials and their interface engineering concerning different processing methods in perovskite solar cells. J. Energy Chem., 2021. 62: p. 459-476. DOI: 10.1016/j.jechem.2021.04.002.

[40] Yan, X., et al., Origin of thermal instability of $CH_3NH_3PbI_{3-x}Cl_x$ films for photovoltaic devices. Mater. Lett., 2016. 176: p. 114-117. DOI: 10.1016/j.matlet.2016.04.095.

[41] Manjunath, V., et al., Perovskite-based facile $NiO/CH_3NH_3PbI_3$ heterojunction self-powered broadband photodetector. ACS Appl. Electron. Mater., 2021. 3: p. 4548-4557. DOI: 10.1021/acsaelm.1c00679.

[42] Mbumba, M.T., et al., Degradation mechanism and addressing techniques of thermal instability in halide perovskite solar cells. Sol. Energy, 2021. 230: p. 954-978. DOI: 10.1016/j.solener.2021.10.070.

[43] Sheikh, A.D., et al., Effects of high temperature and thermal cycling on the performance of perovskite solar cells: Acceleration of charge recombination and deterioration of charge extraction. ACS Appl. Mater. Interfaces, 2017. 9: p. 35018-35029. DOI: 10.1021/acsami.7b11250.

[44] Boyd, C.C., et al., Barrier design to prevent metal-induced degradation and improve thermal stability in perovskite solar cells. ACS Energy Lett., 2018. 3: p. 1772-1778. DOI: 10.1021/acsenergylett.8b00926.

Chapter 4

Towards lead-free all-inorganic perovskite solar cell

4.1 Introduction

Organic-inorganic halide perovskite light harvesters (PLHs) have shown exceptional progress in the recent decade. These halide perovskites with the chemical formula AMX_3, where A is the organic monovalent cation, B is the divalent metal cation, and X represents halogen, showcase remarkable intrinsic properties, namely, long charge diffusion length, low exciton binding energy (~40 meV),[1] high visible light panchromatic absorption co-efficient (1.5×10^4 cm^{-1} at 550 nm),[2] etc. Additionally, these inherent properties can be tuned by substituting the ions in the AMX_3 structure,[3] rendering them in various optoelectronic applications, namely, solar cells,[4, 5] LEDs,[4] neuromorphic computing,[6] photodetectors,[7] and nuclear radiation measurements.[8] Accounting from all the above-mentioned superiority, recently, a power conversion efficiency (PCE) of ~25% is achieved with halide PLHs.[9] Though such high PCEs are achieved with PLHs, yet they suffer from toxicity and long-term stability.[10] Most high-performing PLHs comprise carcinogenic lead (Pb), which facilitates the intense direct visible light absorption originating from the filled 6s at the valence band maximum and empty 6p orbital at the conduction band minimum of the divalent Pb cation.[11] Therefore, Pb has been replaced with divalent tin (Sn^{2+}) or germanium (Ge^{2+}) cations to mitigate the toxicity. Apart from replacing Pb^{2+} with Sn^{2+} or Ge^{2+} cations, various other techniques are reported to alleviate toxicity, such as lowering the dimensionality of the PLH to 2D or 0D and forming double perovskite structures. [12, 13] However, lower dimension perovskites and double perovskites have compromised PCEs compared to 3D halide perovskites with Pb. Furthermore, the 3D PLHs comprising organic cations degrade when exposed to moisture, ultraviolet (UV) light, and elevated temperature, thereby hindering them from real-time application.[14] Conversely, using hydrophobic transport layers will enhance the long-term stability of the PSCs, thus, Hossain, M. I., et al. developed hydrophobic thin-films of SnO_X (n-type), TiO_2 (n-type), MoO_X (p-type), and NiO_X (p-type) transport layers with reactive sputtering in an oxygen environment.[5]

With the preceding discussion, experimentally, α-formamidinium lead iodide (α-$FAPbI_3$) light harvester has shown the highest certified PCE of 25.2%,[9] but the inclusion of Pb can impede its utility. Thus, when Pb^{2+} is replaced with Sn^{2+} to form formamidinium tin iodide ($FASnI_3$), the PCE drops to ~14%.[15] However, the inclusion of FA crunches the long-term stability of the perovskite solar cells (PSCs). Therefore, after several studies, all inorganic light absorbers, namely

cesium tin iodide ($CsSnI_3$), have been demonstrated as the most suitable lead-free inorganic PLH due to the superior intrinsic properties of $CsSnI_3$ such as narrow bandgap (1.3 eV) and higher carrier mobility. Experimentally, the PCE of PSCs with $CsSnI_3$ PLHs further drops down to ~10%.[16] On the other hand, apart from the PLH, the transport layers (both electron and hole) play a significant role in delivering high PCEs in PSCs. However, the well-matched band alignment and carrier mobility are essential at the transport layer perovskite interface for the smooth transfer of photogenerated charges.[17]

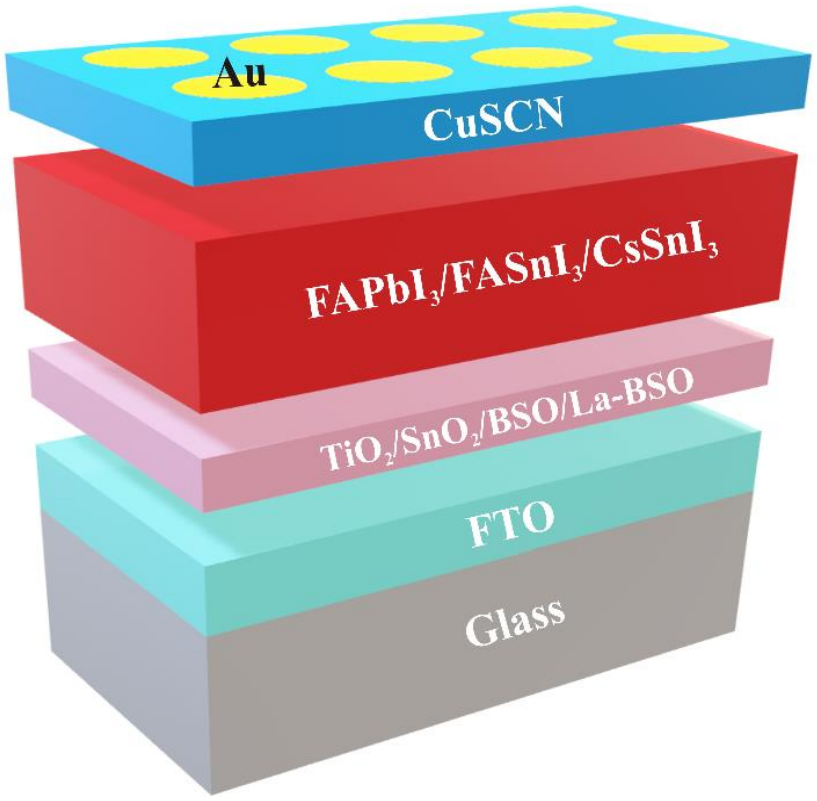

Figure 4.1 Schematics depicting the PSC device architecture modeled in this study.

Therefore, it is necessary to assess the potential of $CsSnI_3$-based PSCs compared to $FAPbI_3$ and $FASnI_3$-based PSCs. Experimentally evaluating and comparing the potential of $FAPbI_3$, $FASnI_3$, and $CsSnI_3$ is a myriad task. Nevertheless, researchers employ various software packages, namely finite difference time domain method, AFORS-HET, SILVACO ATLAS, wxAMPS, and SCAPS-1D. [18] However, SCAPS-1D simulates multi-junction and heterojunction solar cells by solving fundamental semiconductor equations.[19] Using SCAPS-1D, Abdelfatah, M., et al. optimized the thickness, bandgap and carrier concentration of subsequent layers in the Cu_2O

homojunction solar cells. With optimized physical parameters a numerical efficiency of ~8% was achieved for all oxide solar cells.[20] Similarly, Moustafa, M., et al. provided guidelines to improve the efficiency of CZTS solar cells from 12.14% to 16.71% by inserting a p-type MoS_2 layer between CZTS light harvester and Mo rear contact using SCAPS-1D software package.[21]

Thus, in this chapter, the SCAPS-1D software package is used to ascertain the potential of $FAPbI_3$, $FASnI_3$, and $CsSnI_3$ light absorbers. Each of the PLHs is preliminarily scrutinized with various ETLs, namely titanium dioxide (TiO_2), tin oxide (SnO_2), barium stannate ($BaSnO_3$/BSO), and lanthanum doped BSO (La-BSO) with copper thiocyanate (CuSCN) as the standard hole transport layer to fabricate high-performance PCE experimentally. Further, physical parameters, namely thickness, doping, and defect densities, are varied for the constituent layers in PSCs to yield high performance. The type of counter electrode and operating temperature-related changes in the performance of PSCs are analyzed for their real-time application. The PSC device structure modeled in this study is shown in Fig. 4.1.

4.2 Simulation procedure

Planar PSCs (n-i-p) device structure comprising ITO/various ETLs (TiO_2, SnO_2, BSO, and La-BSO)/ PLH ($FAPbI_3$, $FASnI_3$, and $CsSnI_3$)/hole transport layer (CuSCN)/counter electrode is analyzed. For all simulations, apart from variation in the work function of the counter electrode, gold (Au) is chosen as the counter electrode. The simulation with illumination is carried out under a global AM 1.5 spectrum with an irradiation intensity of 1000 W cm^{-2}. Using the fundamental equations that govern semiconductor transport the SCAPS-1D extracts the device performance.

4.3 Results and discussion

4.3.1 Absorption coefficient

Optical management of the incoming irradiation ensures maximum photogeneration in PLHs. It is essential for all incoming visible radiation to strike the PLH. Fig. 4.2 shows the simulated absorption coefficient of the constituent layers. The PLHs show an absorption onset at ~821nm, ~879nm, and ~960 nm for $FAPbI_3$, $FASnI_3$, and $CsSnI_3$, respectively. Further, all the perovskite harvesters absorb in the entire visible range with an absorption coefficient of ~10^5 at 550 nm. However, all the ETLs except SnO_2 absorb high-energy photons in the UV range, whereas the absorption onset

of SnO_2 is at ~480nm. Conversely, the PLHs degrade under UV illumination. Thus, these results indicate, apart from providing energy levels for smooth electron transport, the ETLs also shield the PLHs from the incoming UV irradiation.

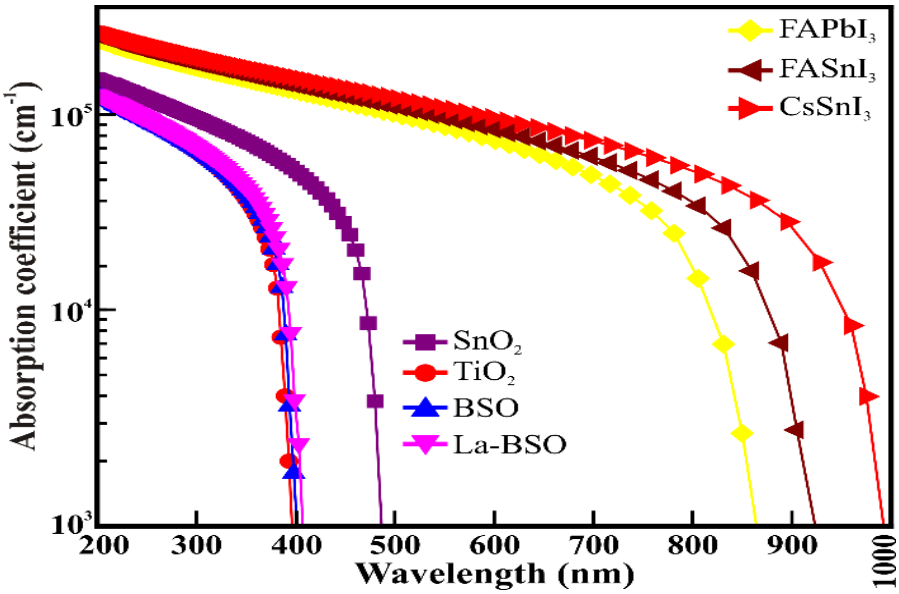

Figure 4.2 Absorption co-efficient of various ETLs (TiO_2, SnO_2, BSO, and La-BSO) and PLHs ($FAPbI_3$, $FASnI_3$, and $CsSnI_3$).

4.3.2 The effect of thickness of various ETLs

Optimizing the thickness of subsequent layers in the PSCs is a prerequisite to achieve maximum performance. For all the PLHs, the thickness of the ETLs is varied from 30 to 200 nm, given the experimentally reported thin-film techniques, as shown in Fig. 4.3. For all the PLH ($FAPbI_3$ (Fig. 4.3(a)), $FASnI_3$ (Fig. 4.3(b)), and $CsSnI_3$ (Fig. 4.3(c)) with various ETLs, the PCE almost remained constant with an increase in thickness of the ETL. Since the open-circuit voltage (V_{OC}), short circuit current density (J_{SC}), and fill factor (FF) show minimal variation, it can be concluded that there are no changes in the band offset, intrinsic resistance, and defect density in ETLs with an increase in thickness. However, the PCE varied independently depending on the intrinsic properties of the specific PLH with ETLs. The highest PCE of ~25% in PSCs with $FAPbI_3$ light harvester is obtained with SnO_2, TiO_2, and BSO ETLs, whereas the PCE drops to ~23% with La-BSO. For the $FASnI_3$ light harvester, the highest PCE of ~27% are found with all ETLs. However, the highest PCE of ~22% (±5%) is attained

with all ETLs for the $CsSnI_3$ light absorber. Thus, it can be concluded that all the ETLs considered in this modeling can be physically employed with a stable lead-free $CsSnI_3$ light harvester. However, other experimental factors such as processing temperature, cost, and toxicity of the precursors used to fabricate ETLs require equal attention before fabrication.

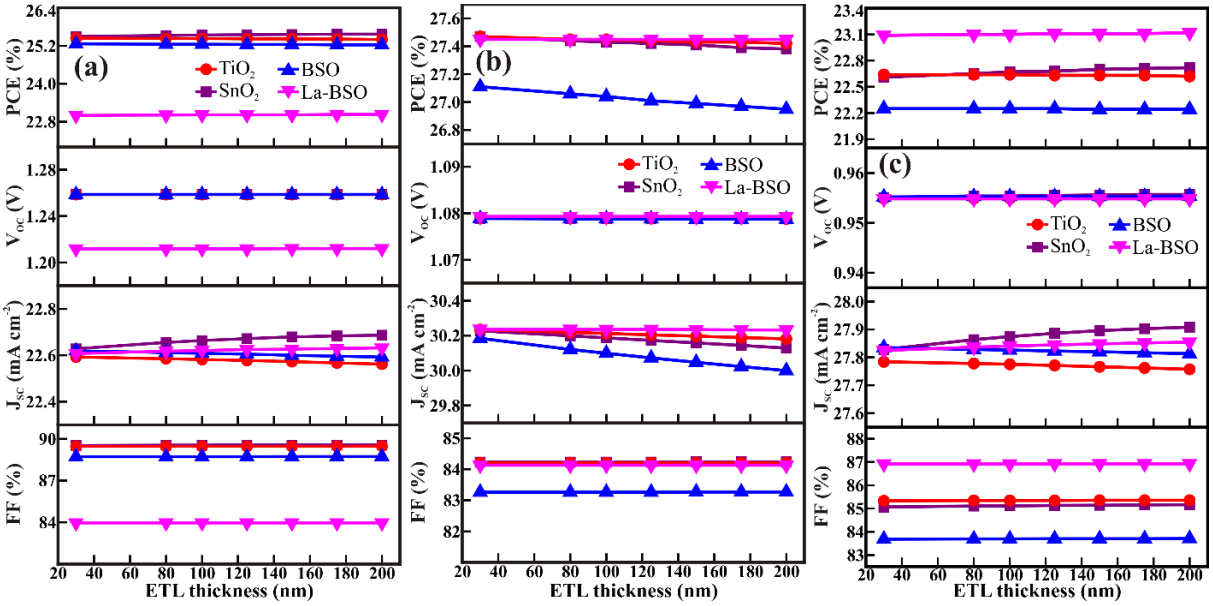

Figure 4.3 The effect of thickness of various ETLs on the performance of PSCs with (a) $FAPbI_3$, (b) $FASnI_3$, and (c) $CsSnI_3$ perovskite light absorbers.

4.3.3 The effect of donor doping density in various ETLs

Following the optimization of ETLs thickness (30 nm), the performance of the PSCs can further be tailored by varying the donor doping density. Experimentally, researchers use various dopants to increase the donor charge density of the ETLs. In this study, the donor doping density in the ETLs is varied from 10^{18} to 10^{20} cm^{-3}, as shown in Fig. 4.4. For PSCs with $FAPbI_3$ light harvester (Fig. 4.4(a)), the PCE remained constant for TiO_2 and SnO_2 ETLs with increasing their donor doping density. However, for the ternary metal oxide ETLs, the PCE increased with increasing the donor doping density. This increase in PCE is ascribed to the change in band offsets at the ETL/$FAPbI_3$ interface. Nevertheless, for the $FASnI_3$ light harvester (Fig. 4.4 (b)), the PCE remained constant for all ETLs except for BSO, which shows a slight rise at a

donor doping density of 10^{19} cm^{-3} arising from decreased series resistance. However, for the $CsSnI_3$ light harvester, all the ETLs showed a minimal increase (+5 %) in PCE with an increase in donor doping concentration; such small surge is due to the slight reduction in series resistance of the PSCs, as shown in Fig. 4.4(c). Therefore, for the stable and lead-free $CsSnI_3$, doping the ETLs has minimal effect on the performance of PSCs. Furthermore, excessive doping will increase non-radiative recombination and provide donor defects which will increase the series resistance in the PSCs leading to lower PCEs.

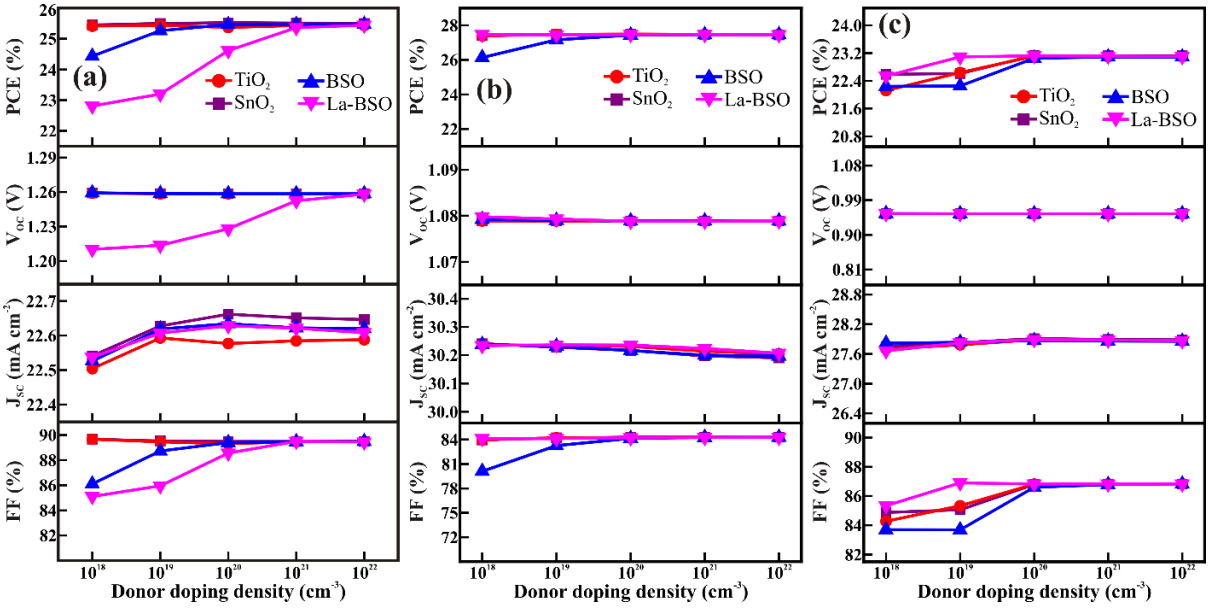

Figure 4.4 The effect of donor doping density in various ETLs on the performance of PSCs with (a) $FAPbI_3$, (b) $FASnI_3$, and (c) $CsSnI_3$ perovskite light absorbers.

4.3.4 The effect of the thickness of various light harvesters

After scrutinizing the ETLs, the high-performing ETLs are considered for optimizing the thickness of perovskite harvester, i.e., SnO_2 as ETL with $FAPbI_3$ and $FASnI_3$ light harvesters, and La-BSO with $CsSnI_3$ PLH. The thickness of the PLHs is varied from 400 to 800 nm (Fig. 4.5). Decreasing thickness below this range can produce films with pinholes, and increasing thickness beyond can cause charge recombination, which deteriorates the performance of the PSCs. For all PLHs with corresponding high-performance ETLs (i.e., $FAPbI_3$ with SnO_2 (Fig. 4.5(a)), $FASnI_3$

with SnO_2 (Fig. 4.5(b)), and $CsSnI_3$ with La-BSO (Fig. 4.5(c))), the PCE of the PSCs enhanced with increase in thickness of the PLH due to corresponding increase in J_{SC} originating from higher photogeneration in the thick absorber films. The V_{OC} and FF have fairly remained constant owing to no changes in band offsets at the ETL/perovskite interface and intrinsic resistance, respectively. At a thickness of 800 nm, a PCE of 25.5 %, 27.47 %, and 23.09 % is obtained for $FAPbI_3$, $FASnI_3$, and $CsSnI_3$ PLHs, respectively. The specified thickness range of the PLHs can be obtained with various thin-film techniques ranging from solution processing to vacuum deposition.

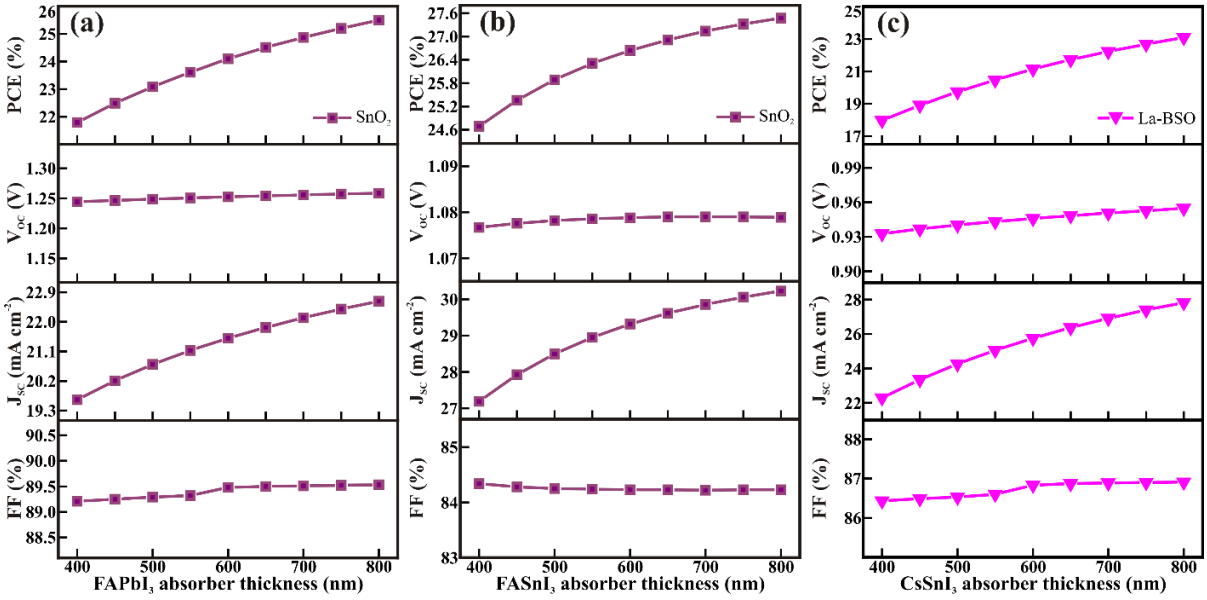

Figure 4.5 The effect of (a) $FAPbI_3$, (b) $FASnI_3$, and (c) $CsSnI_3$ perovskite harvester thickness on the performance of PSCs.

4.3.5 The effect of defect density in various light harvesters

Depending on the synthesis technique, the defect density in the PLH can be tuned for high performance. Thus, the defect density in the PLH is varied from 10^{11} to 10^{16} cm^{-3}, as shown in Fig. 4.6. For all the PLHs, the PCE declines as the bulk defect density increases beyond 10^{14} cm^{-3}. The decline in PCE is due to the corresponding decrease in V_{OC}, J_{SC}, and FF originating from increased trap states favoring the recombination of the photogenerated carriers. Thus, the suitable thin-film synthesis technique which offers low bulk defect density in the perovskite light absorber film is of utmost necessity

to fabricate high-performance PSCs. Further, the stable and lead-free $CsSnI_3$ light harvester can yield PCE > 23%.

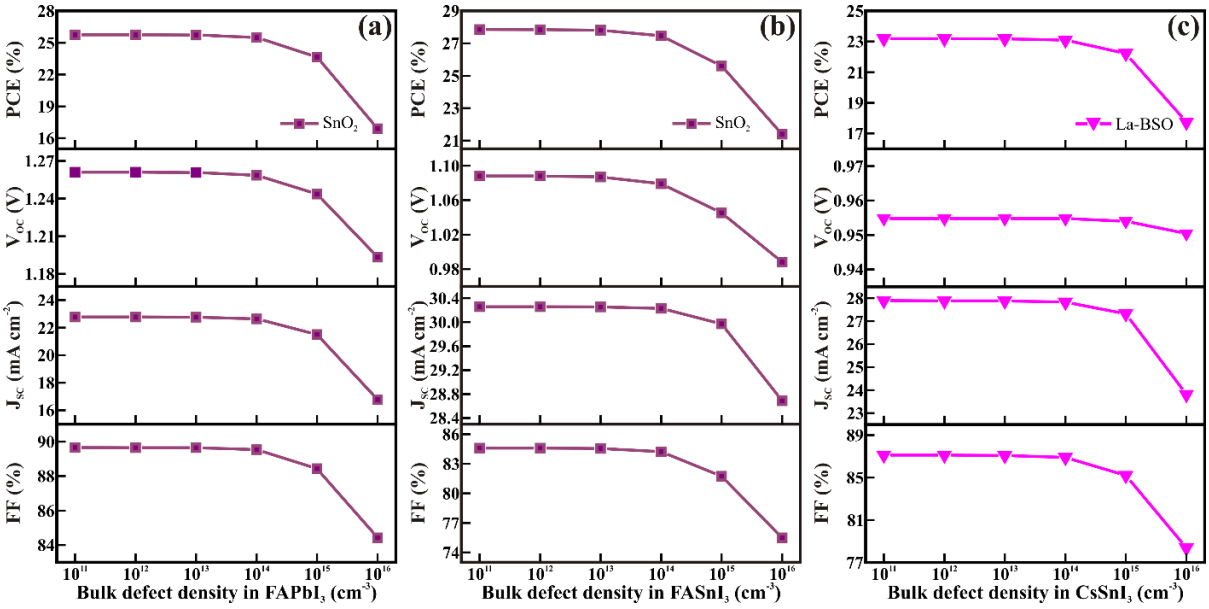

Figure 4.6 The effect of defect density in (a) $FAPbI_3$, (b) $FASnI_3$, and (c) $CsSnI_3$ PLHs on the performance of PSCs.

4.3.6 The effect of various counter electrodes and operating temperature

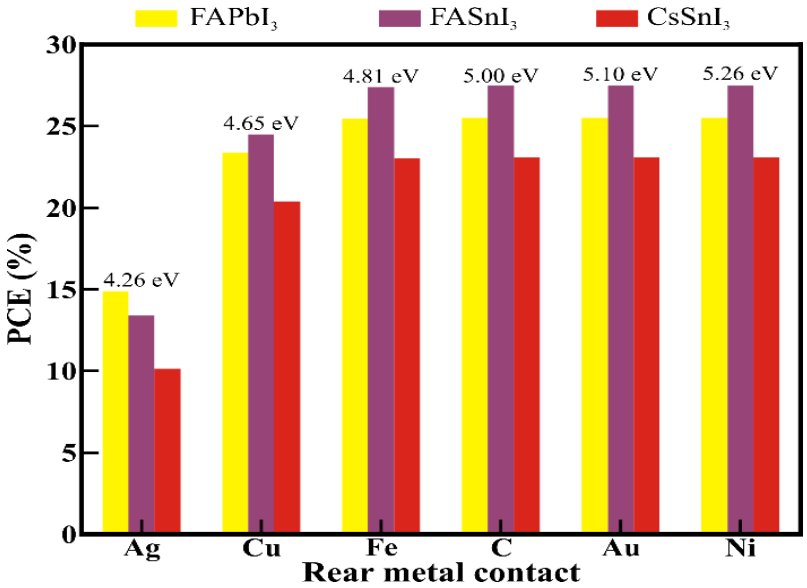

Figure 4.7 Variation in PCE depending on the counter electrode material with high-performance ETLs.

The counter electrode work function alters the performance of PSCs. Around 19 % of the cost to fabricate PSCs arises from gold as the counter electrode.[22] Thus, it is necessary to find alternate counter electrodes and assess the performance of PSCs. Almost similar PCEs are obtained for Fe, C, Au, and Ni counter electrodes, as shown in Fig. 4.7. However, the PCE varies depending on the perovskite light absorber for a counter electrode. Apart from the cost, the conductivity, chemical, and physical inertness need to be considered for developing stable PSCs with low cost.

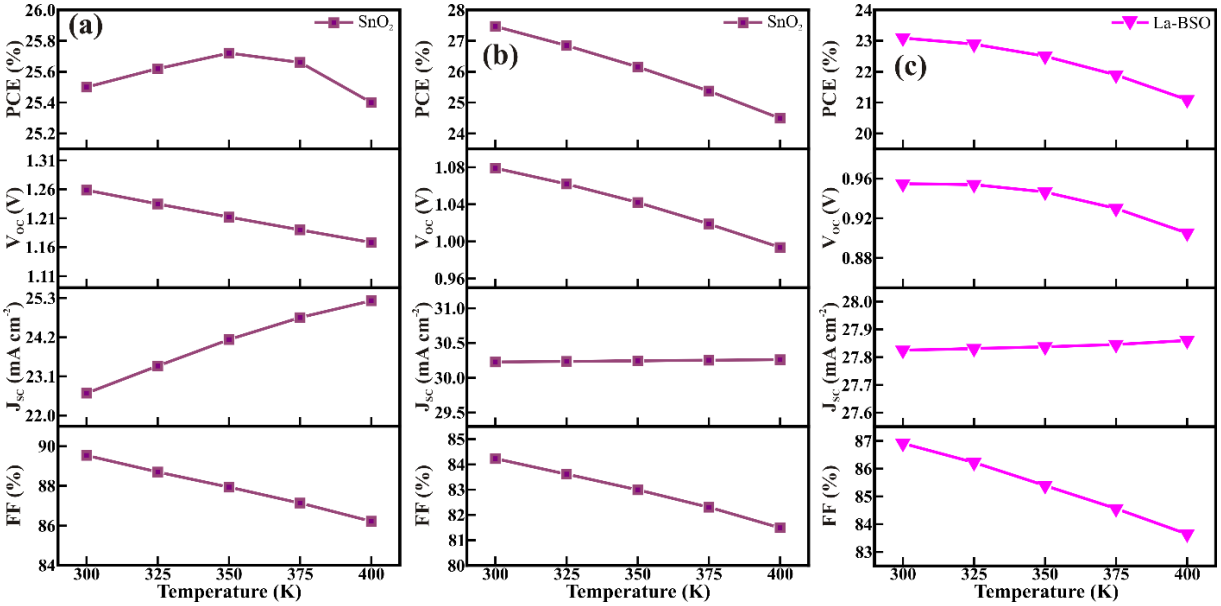

Figure 4.8 The effect of operating temperature on PSCs with (a) $FAPbI_3$, (b) $FASnI_3$, and (c) $CsSnI_3$ PLHs on the performance of PSCs.

Since the PLHs are prone to degrade with moisture and at elevated temperatures, the operating temperature influences the overall performance of the PSCs, which is a critical factor during real-time application. Therefore, the performance of the PSCs is analyzed by varying the operating temperature from 300 to 400 K, as shown in Fig. 4.8. For the $FASnI_3$ perovskite absorber, the PCE slightly increases with an increase in temperature up to 350 K due to associated thermal generation in the perovskite film (Fig. 4.8(a)). Though a decline in V_{OC} and FF is observed due to increased saturation current, the J_{SC} has increased with increased temperature. On the other hand, for both $FASnI_3$ (Fig. 4.8(b)) and $CsSnI_3$ (Fig. 4.8(c)) light harvesters, the PCE reduces with an

increase in the operating temperature resulting from a corresponding decline in V_{OC} and *FF* arising due to increased reverse saturation current which lowers the *FF* of PSCs. However, it is to be noted that even at an elevated operating temperature of 350 K, the PCE of PSCs with $FAPbI_3$, $FASnI_3$, and $CsSnI_3$ remains above 25%, 26%, and 22%, respectively.

4.3.7 *J-V* and IPCE curves of the optimized device

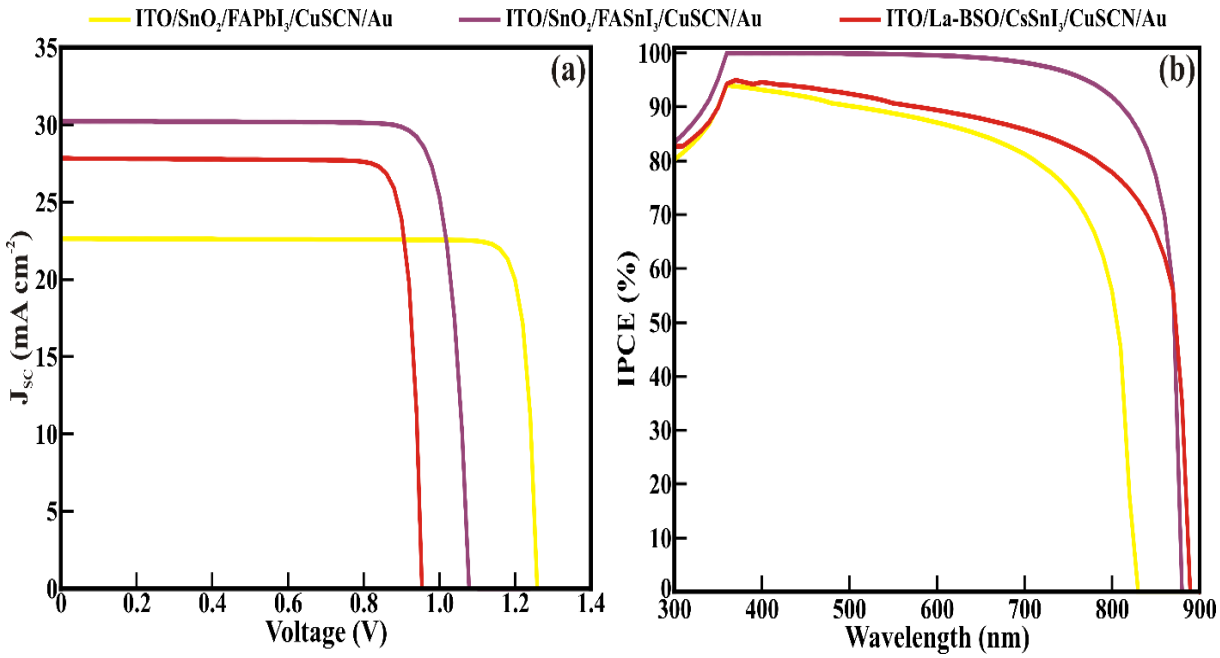

Figure 4.9 (a) J-V curves and (b) IPCE curves of the PSCs with ITO/$SnO_2$$FAPbI_3$/CuSCN/Au (yellow color), ITO/SnO_2/$FASnI_3$/CuSCN/Au (wine color) and ITO/La-BSO/$CsSnI_3$/CuSCN/Au (red color).

The J-V curves of the PSCs with standard physical parameters are shown in Fig. 4.9(a). The PSCs with $FAPbI_3$ show the highest efficiency of 25.5%, comparable to the experimental report. The values of V_{OC}, $J_{SC,}$ and *FF* are 1.255 V, 22.62 mA cm^{-2}, and 89.53 %, respectively. Conversely, the PSCs with $FASnI_3$ light harvester yield a PCE of 27.47 % with V_{OC} = 1.07 V, J_{SC} = 30.22 mA $cm^{-2,}$ and *FF* = 84.22 %. However, the stable lead-free all-inorganic $CsSnI_3$ absorber exhibits PCE of 23.09 % with V_{OC} = 0.95 V, J_{SC} = 27.82 mA cm^{-2} and *FF* = 86.91%. Nevertheless, such high values of PCE with $FASnI_3$ and $CsSnI_3$ light harvesters are yet to be achieved practically due to low

solubility to the constituent precursors. The IPCE curves of the PSCs with standard physical parameters are shown in Fig. 4.9(b). The IPCE onset corresponds to the bandgap of the PLH. Comparatively, PSCs with $FASnI_3$ showed higher IPCE, followed by PSCs with $CsSnI_3$ and $FAPbI_3$.

4.4 Conclusion

In conclusion, the study represents the optimization of a stable lead-free all-inorganic 3D bulk $CsSnI_3$ perovskite absorber. We used SCAPS- 1D software to simulate four different perovskites ETLs, namely TiO_2, SnO_2, BSO, and La-BSO, with three distinct PLHs $FAPbI_3$, $FASnI_3$, and $CsSnI_3$. A systematic study on the influence of each layer on the performance of PSCs is evaluated. The thickness, defect, and doping densities of the subsequent layers are varied to show variation in the performance of PSCs. The $FAPbI_3$ and $FASnI_3$ PLHs are highly compatible with SnO_2 ETL and deliver optimized PCE greater than 25% and 27 %, respectively, whereas the $CsSnI_3$ light harvester shows the highest PCE (~23%) with La-BSO ETL. Though experimentally, the PCE of PSCs with $FAPbI_3$ has crossed 25%, it is imperative to develop techniques to enhance the performance of the $CsSnI_3$ light harvester, which is hindered by its low solubility in standard precursor solvents. Thus, strategies such as vapor-assisted synthesis and mixed solvents can be used to uniform $CsSnI_3$ films with low bulk defect density.

4.5 References

[1] A.M. Soufiani, F. Huang, P. Reece, R. Sheng, A. Ho-Baillie, M.A. Green, Polaronic exciton binding energy in iodide and bromide organic-inorganic lead halide perovskites, Applied Physics Letters, 107 (2015) 231902. DOI: 10.1063/1.4936418

[2] N.-G. Park, Perovskite solar cells: an emerging photovoltaic technology, Materials Today, 18 (2015) 65-72. DOI: 10.1016/j.mattod.2014.07.007

[3] H.S. Jung, N.-G. Park, Perovskite solar cells: From Materials to Devices, Small, 11 (2015) 10-25. DOI: 10.1002/smll.201402767

[4] V. Manjunath, S. Bimli, K.H. Parmar, P.M. Shirage, R.S. Devan, Oxidized Nickel films as highly transparent HTLs for inverted planar perovskite solar cells, Solar Energy, 193 (2019) 387-394. DOI: 10.1016/j.solener.2019.09.070

[5] M.I. Hossain, Y. Zakaria, A. Zikri, A. Samara, B. Aissa, F. El-Mellouhi, N.S. Hasan, A. Belaidi, A. Mahmood, S. Mansour, E-beam evaporated hydrophobic metal oxide thin films as carrier transport materials for large scale perovskite solar cells, Materials Technology, 37 (2022) 248-259. DOI: 10.1080/10667857.2020.1830551

[6] R.A. John, N. Yantara, Y.F. Ng, G. Narasimman, E. Mosconi, D. Meggiolaro, M.R. Kulkarni, P.K. Gopalakrishnan, C.A. Nguyen, F. De Angelis, S.G. Mhaisalkar, A. Basu, N. Mathews, Ionotronic halide perovskite drift-diffusive synapses for low-power neuromorphic computation, Advanced Materials, 30 (2018) 1805454. DOI: 10.1002/adma.201805454

[7] V. Manjunath, P.K. Mishra, R. Dobhal, S. Bimli, P.M. Shirage, S. Sen, P.A. Shaikh, R.S. Devan, Perovskite-based facile NiO/$CH_3NH_3PbI_3$ heterojunction self-powered broadband photodetector, ACS Applied Electronic Materials, 3 (2021) 4548-4557. DOI: 10.1021/acsaelm.1c00679

[8] Q. Sun, Y. Xu, H. Zhang, B. Xiao, X. Liu, J. Dong, Y. Cheng, B. Zhang, W. Jie, M.G. Kanatzidis, Optical and electronic anisotropies in perovskitoid crystals of $Cs_3Bi_2I_9$ studies of nuclear radiation detection, Journal of Materials Chemistry A, 6 (2018) 23388-23395. DOI: 10.1039/C8TA09525F

[9] J. Jeong, M. Kim, J. Seo, H. Lu, P. Ahlawat, A. Mishra, Y. Yang, M.A. Hope, F.T. Eickemeyer, M. Kim, Y.J. Yoon, I.W. Choi, B.P. Darwich, S.J. Choi, Y. Jo, J.H. Lee, B. Walker, S.M. Zakeeruddin, L. Emsley, U. Rothlisberger, A. Hagfeldt, D.S. Kim, M. Grätzel,

J.Y. Kim, Pseudo-halide anion engineering for α-$FAPbI_3$ perovskite solar cells, Nature, 592 (2021) 381-385. DOI: 10.1038/s41586-021-03406-5

[10] S. Ndlovu, M.A. Ollengo, E. Muchuweni, V.O. Nyamori, Current advances in perovskite oxides supported on graphene-based materials as interfacial layers of perovskite solar cells, Critical Reviews in Solid State and Materials Sciences, (2022) 1-20. DOI: 10.1080/10408436.2022.2041395

[11] A.H. Slavney, T. Hu, A.M. Lindenberg, H.I. Karunadasa, A bismuth-halide double perovskite with long carrier recombination lifetime for photovoltaic applications, Journal of the American Chemical Society, 138 (2016) 2138-2141. DOI: 10.1021/jacs.5b13294

[12] C. Zhou, H. Lin, S. Lee, M. Chaaban, B. Ma, Organic–inorganic metal halide hybrids beyond perovskites, Materials Research Letters, 6 (2018) 552-569. DOI: 10.1080/21663831.2018.1500951

[13] S. Sun, M. Lu, X. Gao, Z. Shi, X. Bai, W.W. Yu, Y. Zhang, 0D Perovskites: Unique properties, synthesis, and their applications, Advanced Science, 8 (2021) 2102689. DOI: 10.1002/advs.202102689

[14] W. Chi, S.K. Banerjee, Stability improvement of perovskite solar cells by compositional and interfacial engineering, Chemistry of Materials, 33 (2021) 1540-1570. DOI: 10.1021/acs.chemmater.0c04931

[15] G. Wang, J. Chang, J. Bi, M. Lei, C. Wang, Q. Qiao, Inorganic $CsSnI_3$ perovskite solar cells: the progress and future prospects, Solar RRL, (2021) 2100841. DOI: 10.1002/solr.202100841

[16] L. Xu, C. Zhang, X. Feng, W. Lv, Z. Huang, W. Lv, C. Zheng, G. Xing, W. Huang, R. Chen, Vapor incubation of $FASnI_3$ films for efficient and stable lead-free inverted perovskite solar cells, Journal of Materials Chemistry A, 9 (2021) 16943-16951. DOI: 10.1039/D1TA04722A

[17] K. Valadi, S. Gharibi, R. Taheri-Ledari, S. Akin, A. Maleki, A.E. Shalan, Metal oxide electron transport materials for perovskite solar cells: A review, Environmental Chemistry Letters, 19 (2021) 2185-2207. DOI: 10.1007/s10311-020-01171-x

[18] S. Ghosh, S. Porwal, T. Singh, Investigation of the role of back contact work function for hole transporting layer free perovskite solar cells applications, Optik, 256 (2022) 168749. DOI: 10.1016/j.ijleo.2022.168749

[19] M. Alla, V. Manjunath, N. Chawki, D. Singh, S.C. Yadav, M. Rouchdi, F. Boubker, Optimized $CH_3NH_3PbI_{3-X}Cl_X$ based perovskite solar cell with theoretical efficiency exceeding 30%, Optical Materials, 124 (2022) 112044. DOI: 10.1016/j.optmat.2022.112044

[20] A. Mahmoud, W. Ismail, N. M. El-Shafai, A. El-Shaer. Effect of thickness, bandgap, and carrier concentration on the basic parameters of Cu_2O nanostructures photovoltaics: numerical simulation study. Materials Technology, 36 (2021) 712-720. DOI: 10.1080/10667857.2020.1830551

[21] M. Mohamed, T. AlZoubi, S. Yasin. Towards high-efficiency CZTS solar cells via p-MoS_2 interfacial layer optimisation. Materials Technology (2021) 1-10. DOI: 10.1080/10667857.2021.1964214

[22] S. Maniarasu, T.B. Korukonda, V. Manjunath, E. Ramasamy, M. Ramesh, G. Veerappan, Recent advancement in metal cathode and hole-conductor-free perovskite solar cells for low-cost and high stability: A route towards commercialization, Renewable and Sustainable Energy Reviews, 82 (2018) 845-857. DOI: 10.1016/j.rser.2017.09.095

Chapter 5

Lead-free non-toxic Cs_2BiAgI_6 double perovskite solar cell

5.1 Introduction

Accounting from high absorption co-efficient (~10^5 cm^{-1}),[1] long charge diffusion length (~1 μm),[2] ease of processing, low recombination rates, etc.,[3,4] the power conversion efficiency (PCE) of single junction thin film solar cells comprising perovskite light absorbers has witnessed a quantum jump from 3.8 % to 25.6 %, approaching the matured crystalline silicon solar cell at 26.7 %.[5] Owing to the tunability of their crystal structure and optoelectronic properties, the perovskite light harvesters can be tailored into 2D perovskites, layered double perovskites, double perovskites, etc.[6,7] Despite these advances, the high-efficiency perovskite solar cells contain carcinogenic Pb^{2+}, and the crystal structure disintegrates when exposed to moisture, hindering their real-time implementation.[8,9] Various encapsulation techniques are experimented to address the poor stability of the perovskite absorbers.[10] However, the intense direct visible light absorption in perovskites originates from filled 6s orbitals at the valence-band maximum and empty 6p orbitals at the conduction-band minimum of the Pb cation.[11,12] Therefore, replacing the Pb atom in the crystal structure is crucial for achieving high efficiency. Thus, initially, Pb^{2+} was substituted with Ge^{2+} or Sn^{2+} cations, but the higher energy of 4s and 5s orbitals of Ge^{2+} and Sn^{2+} cations, respectively, produce oxidation centers in the crystal structure resulting in poor stability.[13] However, lately, several non-toxic lead-free lower dimension perovskites (0D and 2D) attained by hetero-valent substitution of Pb^{2+} with Bi^{3+} or Sb^{3+}, and 3D double perovskites are studied for their suitability as a light harvester.[14,15] Nevertheless, a stable and non-toxic perovskite light harvester with optoelectronic properties akin to lead-containing 3D perovskites is yet to be unraveled. Among all the Pb-free alternatives, perovskites obtained by transmutation of M^{2+} cation with a combination of monovalent and trivalent cations result in 3D double perovskite with chemical formula $A_2M'M''X_6$ where A, M′, M″, and X are monovalent cation, monovalent metal ion, trivalent metal ion, and halogen, respectively. Thus, the unit cell is doubled, and a pair of M^{2+} cations are replaced with M^+ and M^{3+} cations and forms the 3D double perovskite structure, which crystallizes in the cubic crystal system with $Fm\bar{3}m$ space group.[16] Though the 3D double perovskites possess relatively high indirect bandgap, yet several approaches, namely, doping at M″ site doping,[17] dilute alloying,[18] and pressure-assisted bandgap tuning[19] can be applied to reduce the bandgap towards panchromatic absorption. Further, depending on the M′ and M″ combinations, the lead-free halide double perovskite can be classified as (i) nitrogen/alkali

metals (M′ = Sb^{3+}, Bi^{3+} and M″ = N^{+}, K^{+}), (ii) nitrogen family/transitional metals (M′ = Sb^{3+} and Bi^{3+} and M″ = Tl^{+}, In^{+}), (iii) post-transitional/noble metals (M′ = In^{3+}, Ga^{3+} and M″ = Cu^{+}, Ag^{+}), and (iv) nitrogen family/noble metals (M′ = Sb^{3+}, Bi^{3+} and M″ = Cu^{+}, Ag^{+}). Unlike the AMX_3 structure, in double perovskites, there is a need to consider a specific octahedral factor for each type of octahedron. However, for the tolerance factor, the average ionic radii of the M′ and M″ sites can be used. The theoretical conditions for a stable structure are $\mu > 0.41$ and $0.75 < t < 1$. The theoretical conditions for a stable structure are $\mu > 0.41$ and $0.75 < t < 1$.[20]

Consequently, the Pb atom can be replaced with Bi and Ag hetero-valent substitution to form Cs_2BiAgI_6 double perovskite crystal structures. Moreover, $Cs_2BiAgCl_6$ and $Cs_2BiAgBr_6$ double perovskites are experimentally synthesized via solid-state reactions and solution processing. Such double perovskites crystallize into elpasolite structure (symmetric face-centered cubic double perovskite) with corner-sharing octahedra, with Cs in the middle of the cubic-octahedral cavity. The centers of the octahedra are either occupied by Bi or Ag, alternating in a rock-salt configuration rendering isotropic carrier transport properties.[21] Additionally, the Cs_2BiAgI_6 double perovskite having a relatively low bandgap, is inorganic, environmentally benign, and can provide long-term stability. On the other hand, apart from the perovskite light absorber, two carrier-selective transport layers are required to achieve effective carrier extraction at both external terminals. The optoelectronic properties of electron and hole transport layers play a crucial role in attaining high performance. Among the compatible electron transport layers (ETLs), aluminum-doped zinc oxide (AZnO) is a promising n-type wide bandgap semiconductor (3.33 eV) with high transparency and excellent optoelectronic properties.[22,23] Several industrial processes, namely, spray coating, dip coating, screen printing, bar coating, etc.,[24,25] are developed to coat large-area conformal thin films. Further, owing to better band alignment and processibility, molybdenum oxide (MoO_3),[26] copper thiocyanate (CuSCN), and spiro-OMeTAD have been extensively investigated for extracting holes towards the external terminal.[26] Additionally, producing high PCE solar cells requires precise tuning of thickness, doping, and bulk defect densities of the subsequent layers.[27,28] However, experimentally tailoring these properties and achieving high performance is a myriad task. Therefore, researchers use various software packages, namely, SILVACO ATLAS, wxAMPS, finite difference time domain method, etc. All these software programs generally solve basic semiconductor second-order differential equations by applying boundary conditions at the interfaces.[29] Among all the

software packages, the 1D Solar Cell Capacitance Simulator (SCAPS-1D) offers multijunction and heterojunction simulations.[30,31]

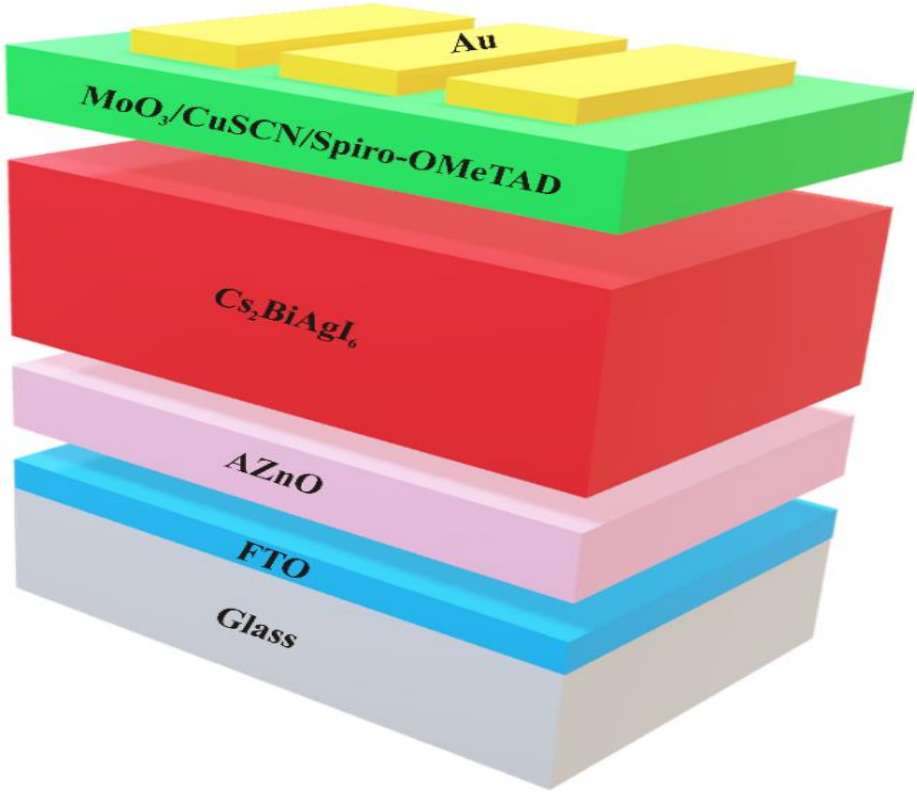

Figure 5.1 Schematic depicting the device structure of Cs_2BiAgI_6 double perovskite solar cells considered in the present study.

This chapter employs the SCAPS-1D software package to model and scrutinize perovskite solar cells with a double perovskite light harvester and three distinct hole-transporting layers (HTLs). The modeled device structure, FTO/AZnO (ETL)/Cs_2BiAgI_6/HTLs (MoO_3 or CuSCN or spiro-OMeTAD)/rear metal contact, is as shown in Fig. 5.1. The Cs_2BiAgI_6-based double perovskite solar cells are optimized in terms of thickness, bulk, and doping densities, with three distinct HTLs (i.e., MoO_3, CuSCN, and spiro-OMeTAD) and AZnO as ETL. Various possible rear electrodes are selected, and the effect on the performance of the Cs_2BiAgI_6-based double perovskite solar cells is analyzed. Further, to assess the real-time application of Cs_2BiAgI_6-based double perovskite solar cells, the performance is also evaluated concerning the change in operating

temperature. The present technique used for optimization can provide guidelines for experimental implementation and can be extended to other optoelectronic devices.

5.2 Device modeling and simulation procedure

The planar double perovskite solar cell in n-i-p configuration is modeled as FTO/AZnO (ETL)/Cs_2BiAgI_6/HTLs (MoO_3 or CuSCN or spiro-OMeTAD)/rear metal contact (Fig. 5.1). Owing to thermal stability and chemical inertness, fluorine-doped tin oxide (FTO) layered glass substrates are employed as transparent conducting substrates. Gold (Au) is chosen as the counter electrode for all simulations except for the simulations in which the work function of the counter electrode is varied. Global AM 1.5 spectrum with an irradiation intensity of 1000 Wm^{-2} is used for all simulations.

In principle, the SCAPS-1D software solves the basic semiconductor equations that dictate the charge transport in the semiconductor.[32] However, additional requirements are needed to simulate polycrystalline thin solar cells. Therefore, along with these semiconductor equations, SCPAS offers grading of all input parameters, namely, the type of recombination, defect levels (bulk and interfacial), charge type (idealization, charge type (donor or acceptor), and valency (monovalent, divalent, or multivalent)), defect level distribution (gaussian, single level, uniform or combinations), optical properties (direct excitation of light), and contact properties (flat band or work function). Voltage, frequency, and operating temperature can also be controlled to perform reasonable computations. Therefore, the three underlying equations that regulate the carrier transport in semiconductors are listed below:

Poisson Equation (Eq. 5.1):

$$\frac{dy}{dx} = -\frac{d^2\Psi}{dx^2} = \frac{q}{\varepsilon}[p(x) - n(x) + N_D^+(x) - N_A^- + p_t(x) - n_t(x)] \qquad (5.1)$$

where Ψ represents the electrostatic potential, q is the charge of an electron, ε denotes the dielectric constant of the material, p is the concentration of holes, n is the concentration of electrons, N_A^- indicates ionized acceptor density, N_D^+ signifies ionized donor density, n_t and p_t represents electron and hole traps, respectively, and x is the position coordinate.

Electron (Eq. 5.2) and hole (Eq. 5.3) continuity equations:

$$\frac{dn_p}{dt} = G_n - \frac{n_p - n_{p0}}{\tau_n} + n_p\mu_n\frac{dE}{dx} + \mu_n E\frac{dn_p}{dx} + D_n\frac{d^2n_p}{dx^2} \quad (5.2)$$

$$\frac{dp_n}{dt} = G_p - \frac{p_n - p_{n0}}{\tau_p} + p_n\mu_p\frac{dE}{dx} + \mu_p E\frac{dp_n}{dx} + D_p\frac{d^2p_n}{dx^2} \quad (5.3)$$

where G_p and G_n represent generation rates of hole and electron, p_n and n_p denote concentrations of hole and electron in the n and p region, respectively, pn_0 and np_0 indicate equilibrium concentrations of hole and electron in the n and p region, respectively, τ_p and τ_n represents a lifetime of hole and electron, μ_p and μ_n denotes the mobilities of hole and electron, E signifies the electric field, and D_p and D_n indicate the diffusion coefficient of holes and electrons. The carrier transport happening due to drift and diffusion for electrons (Eq. 5.4) and holes (Eq. 5.5) is expressed as:

$$J_n(x) = qn\mu_n E + qD_n\frac{dn}{dx} = n\mu_n\frac{dE_{Fn}}{dx} \quad (5.4)$$

$$J_p(x) = qp\mu_p E - qD_p\frac{dp}{dx} = p\mu_p\frac{dE_{Fp}}{dx} \quad (5.5)$$

where E_{Fp} and E_{Fn} denote the hole's and electron's quasi-Fermi levels. The physical and defect parameters used in the simulation of PSCs are tabulated in Table 5.1. Further, the series and shunt resistances are 5 Ω/cm^2 and 1 MΩ/cm^2, respectively.

Table 5.1 The physical parameters used as input to examine and optimize solar cells (*Indicate the parameters varied in the present study).

Parameters	FTO	AZnO	Cs_2BiAgI_6	Spiro-OMeTAD	CuSCN	MoO_3
Thickness (μm)	0.1	0.03*	0.90*	0.03*	0.03*	0.03*
Bandgap Eg (eV)	3.5	3.33	1.6	2.88	3.6	3.0
Electron affinity χ (eV)	4	4.55	3.90	2.05	1.7	2.5
Dielectric permittivity (Relative)	9	8.12	6.5	3.0	10.0	12.5

Effective density of states in CB Nc (cm-3)	2.2×10^{18}	4.1×10^{18}	1×10^{19}	2.2×10^{18}	2.2×10^{19}	2.2×10^{19}
Effective density of states in VB N_v (cm^{-3})	1.8×10^{19}	8.2×10^{19}	1×10^{19}	1.8×10^{19}	1.8×10^{18}	1.8×10^{19}
Velocity of electrons (Thermal) $V_{th,e}$ ($cm\ s^{-1}$)	1×10^{7}	1×10^{7}	1×10^{7}	1×10^{7}	1×10^{7}	1×10^{7}
Velocity of holes (Thermal) $V_{th,p}$ ($cm\ s^{-1}$)	1×10^{7}	1×10^{7}	1×10^{7}	1×10^{7}	1×10^{7}	1×10^{7}
Mobility of electrons μ_n ($cm^2\ V^{-1}\ s^{-1}$)	20	100	200	2×10^{-4}	100	25
Mobility of holes μ_p ($cm^2\ V^{-1}\ s^{-1}$)	10	20	2	2×10^{-4}	2.5×10^{-1}	100
Shallow uniform donor density N_D (cm^{-3})	21×10^{19}	$11\times10^{13*}$	0	1	0	0
Shallow uniform acceptor density N_A (cm^{-3})	0	0	1×10^{19}	$1\times10^{19*}$	$1\times10^{19*}$	$1\times10^{19*}$
Density of defect N_t (cm^{-3})	1×10^{15}	1×10^{17}	$1\times10^{14*}$	1×10^{15}	1×10^{15}	1×10^{15}
Ref.	[30]	[33]	[34]	[30]	[30]	[35]

5.3 Results and discussion

5.3.1 Effect of thickness and donor density of AZnO

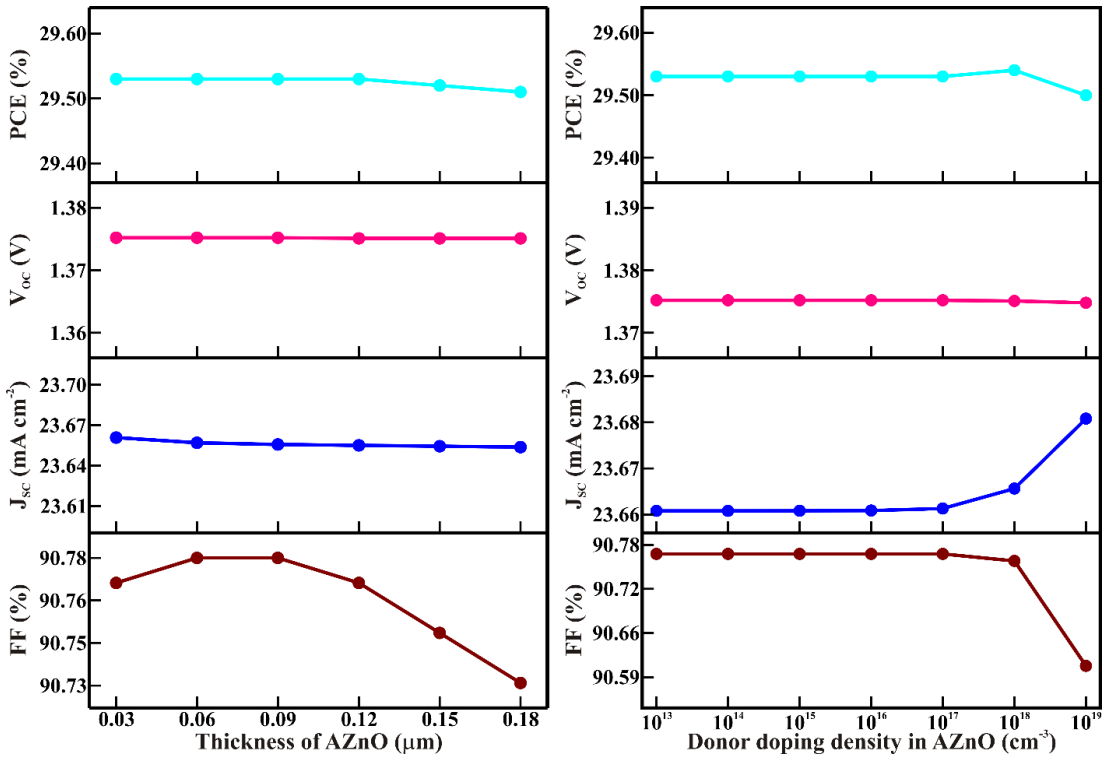

Figure 5.2 (a) Thickness and (b) donor doping density of AZnO layer-related deviation of solar cell parameters (with other parameters as tabulated in Table 5.1)

The AZnO film is considered ETL in the present modeling. The AZnO accomplishes the following functionalities, (i) serves as the template for perovskite overlayer, (ii) blinds ultra-violet radiation from striking the double perovskite over layer, (iii) blocks hole transport, and (iv) aids in dissociation of electron-hole pairs at the AZnO/double perovskite interface. Therefore, it is essential to optimize the thickness and donor doping density of the AZnO ETL. Experimentally, there are several scalable techniques to synthesize large-area conformal AZnO thin films. Thus, the thickness of AZnO is varied from 30 to 180 nm, as shown in Fig. 5.2(a).

Increasing thickness beyond 180 nm may lead to parasitic optical losses. Though the thickness of AZnO film is varied from 30 to 180 nm, the PCE remained constant (~29.55 %), originating from unaltered open circuit voltage (V_{OC}) and short circuit current density (J_{SC}). However, a minute variation in fill factor (FF) with increasing

thickness of the AZnO can be ascribed to a minor increase in series resistance in the thicker AZnO films. Further, the donor doping density in the AZnO ETL is varied from 10^{13} to 10^{19} cm^{-3}, as shown in Fig. 5.2(b). With increasing donor doping concentration in AZnO ETL, the PCE and V_{OC} of the double perovskite solar cell remained constant. Marginal increase in the J_{SC} and decrease in FF at higher doping can be ascribed to an increase in carrier conductivity in the AZnO films. These results indicate that the Cs_2BiAgI_6 double perovskite-based solar cells are independent of the thickness and donor doping density in the AZnO ETL.

5.3.2 Effect of thickness and bulk defect density of Cs_2BiAgI_6

Furthermore, the thickness of the Cs_2BiAgI_6 double perovskite light harvester is varied from 100 to 900 nm, as shown in Fig. 5.3(a). As the thickness of the Cs_2BiAgI_6 double perovskite increases, the corresponding rise in the PCE of the Cs_2BiAgI_6 double perovskite-based solar cells increases, owing to the rise in J_{SC} resulting from higher photogeneration in the thicker Cs_2BiAgI_6 films. At the thickness of 900 nm, the Cs_2BiAgI_6 double perovskite-based solar cell delivers a PCE of ~30%. The marginal decrease in V_{OC} and FF in thicker Cs_2BiAgI_6 films can be ascribed to higher recombination and a minor rise in series resistance, respectively. Besides the thickness, experimentally, the bulk defect density of the Cs_2BiAgI_6 double perovskite harvester varies depending on the synthesis protocol. The bulk defect density in the Cs_2BiAgI_6 double perovskite is varied from 10^{14} to 10^{16} cm^{-3}, as shown in Fig. 5.3(b). As the bulk defect density rises, a steady decrease in the PCE is observed (PCE declines from ~29 % to ~16 % when bulk defect density increases from 10^{14} to 10^{16} cm^{-3}), owing to the corresponding decline in the V_{OC}, J_{SC}, and FF. The decline in V_{OC}, J_{SC}, and FF can be associated to change in Fermi level, trap-assisted recombination, and an increase in resistance, respectively, in Cs_2BiAgI_6 films with high bulk defect density. These results illustrate the thickness and bulk defect density in the Cs_2BiAgI_6 double perovskite absorber play a crucial role in achieving high performance.

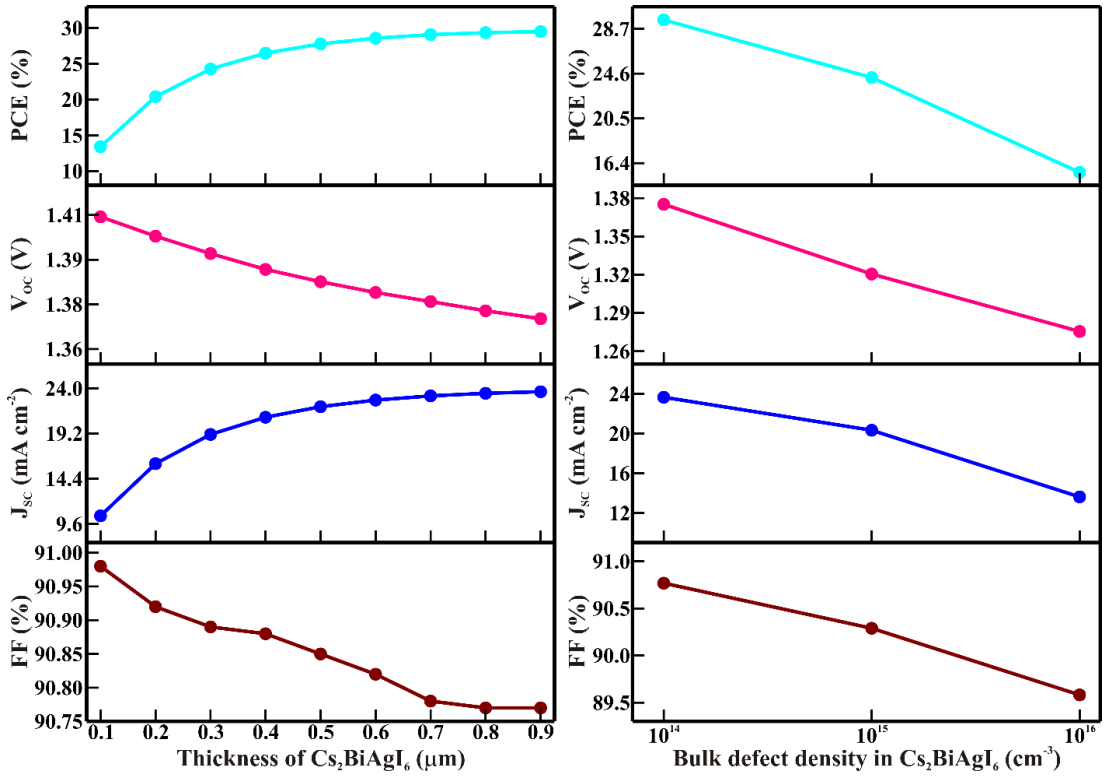

Figure 5.3 (a) Thickness and (b) bulk defect density of Cs_2BiAgI_6 double perovskite absorber-related deviation of solar cell parameters (with other parameters as tabulated in Table 5.1).

5.3.3 Effect of thickness and acceptor density of HTLs

To understand the effect of HTL thickness on the performance of Cs_2BiAgI_6 double perovskite solar cells, the thickness of HTL is varied from 30 to 180 nm (Fig. 5.4(a)). Similar to the thickness of the ETL, the increase in thickness of the HTLs did not affect all the solar cell parameters. However, depending on the type of HTL, the PCE varied independently. Cs_2BiAgI_6 double perovskite solar cells with MoO_3 as HTL showed the highest efficiency of ~29.53 %, followed by CuSCN (~29.34 %) and spiro-OmeTAD (~29.22 %). Further, upon increasing the acceptor doping density from 10^{13} to 10^{19} cm^{-3}, the PCE and all other solar cell parameters remained constant for MoO_3 and CuSCN HTLs (Fig. 5.4(b)). However, at higher doping concentrations, an increase in PCE of the Cs_2BiAgI_6 double perovskite solar cell with spiro-OMeTAD HTL is observed, ascribed to the rise in the FF of the solar cells. The increase in FF is associated with lower resistance in highly doped spiro-OMeTAD films.

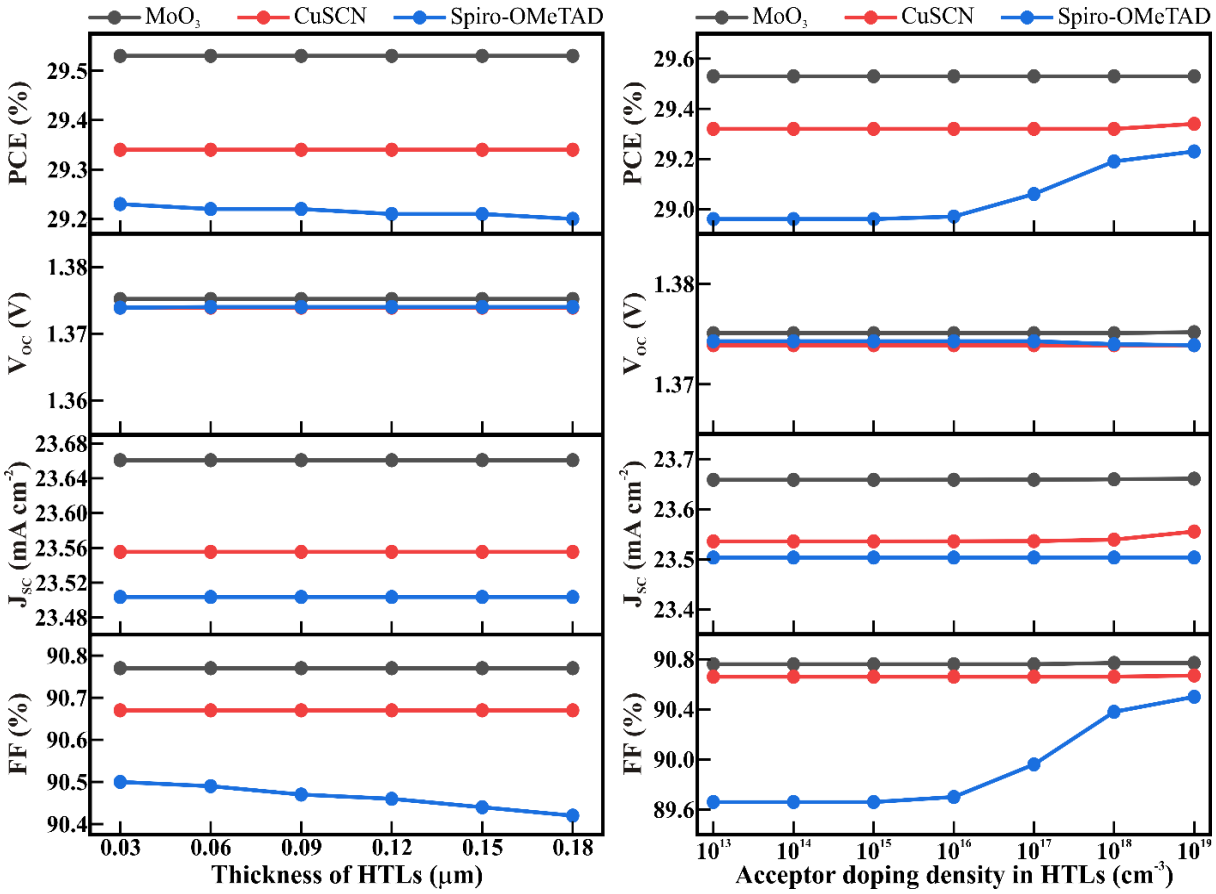

Figure 5.4 (a) Thickness and (b) acceptor doping density of HTLs (MoO_3/CuSCN/Spiro-OMeTAD) related deviation of solar cell parameters (with other parameters as tabulated in Table 5.1).

5.3.4 Effect of interfacial defect density

The interfacial properties between the subsequent layers in the perovskite solar cells are crucial in achieving better performance. [36, 37] Thus, the interfacial defect density at AZnO/perovskite and perovskite/MoO_3 is varied from 10^{10} to 10^{16} cm^{-3}, as shown in Fig. 5.5(a) and Fig. 5.5(b), respectively. As the interfacial defect density at AZnO/perovskite interface is increased from 10^{10} to 10^{16} cm^{-3}, the PCE steadily declines from ~ 21 to 12 %. This decline in PCE can be ascribed to a decrease in the V_{OC} and FF of the solar cells. However, the J_{SC} remains constant, but the V_{OC} and FF decrease due to interfacial losses originating change in band offset developed at the AZnO/perovskite interface. Conversely, when the defect density at the perovskite/MoO_3 is increased up

to 10^{13} cm^{-3}, the PCE remains constant, indicating high defect tolerance of the perovskite/MoO_3 interface. Further, when the defect increases beyond $10^{13}cm^{-3}$, the PCE decreases owing to the decrease in J_{SC}. The decline in J_{SC} is attributed to the defect-assisted recombination losses at the perovskite/HTL interface.

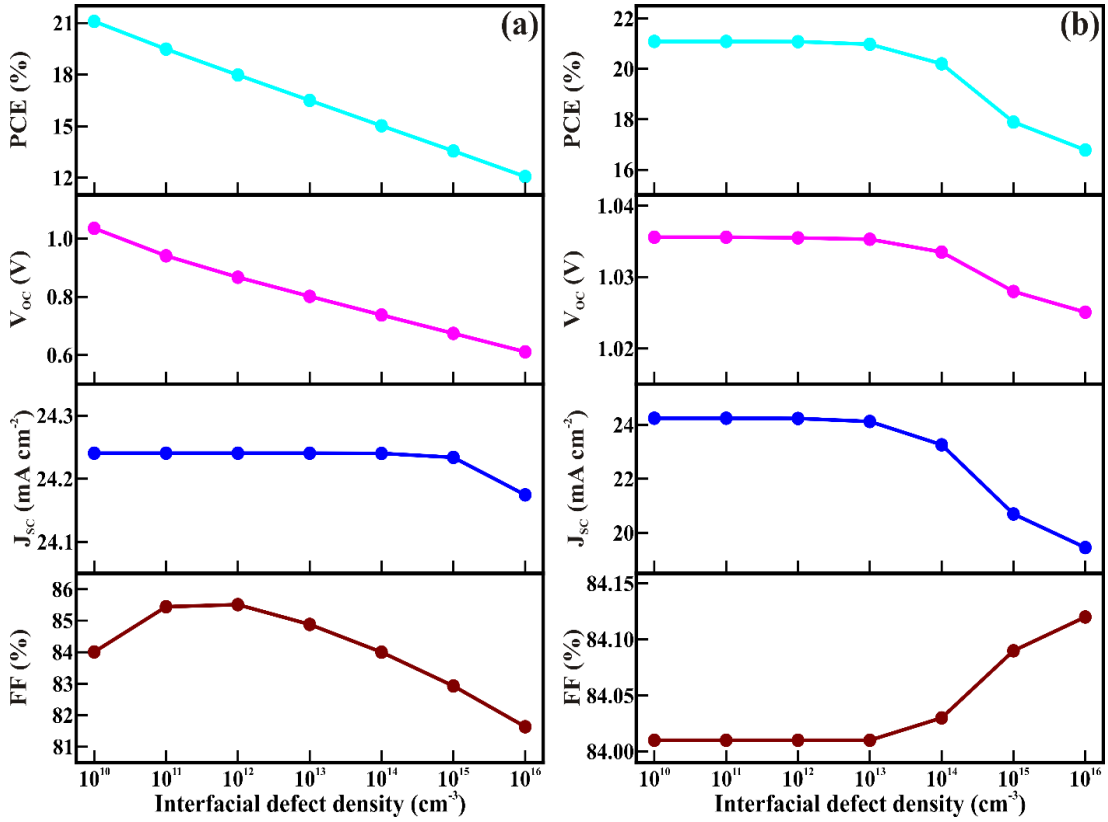

Figure 5.5 The solar cell parameter variation associated with the interfacial defect density changes at (a) ETL/perovskite and (b) perovskite/HTL interface.

5.3.5 Effect of various counter electrodes and operating temperature

Various rear contacts possessing distinct work functions are assessed for their applicability in Cs_2BiAgI_6-based double perovskite solar cells, as shown in Fig. 5.6. However, the chemical reactivity, conductivity, and processing directly influence the cost and performance of solar cells.[38] The work function of the rear contact directly impacts the performance of the solar cells. The PCE of the Cs_2BiAgI_6-based double perovskite solar cells increased with increasing the work function of the rear metal contact up to 5 eV. However, employing rear contacts having a work function beyond

5 eV had a minor change in the PCE. These results indicate even cost-effective carbon as counter electrodes can deliver ~29 % PCE.

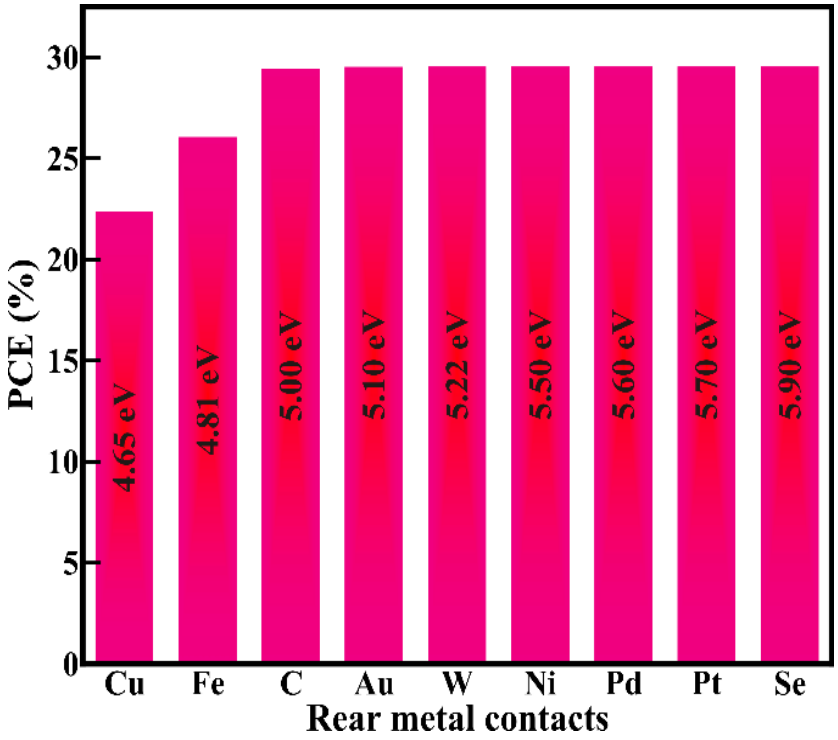

Figure 5.6 Counter electrode-related deviation in PCE. (with other parameters as tabulated in Table 5.1).

Understanding the effect of operating temperature on the performance of solar cells is essential for real-time implementation. [39, 40] Thus, the influence of operating temperature is analyzed for temperatures ranging from 300 to 400 K, as shown in Fig. 5.7. As the operating temperature rises from 300 to 400 K, a steady decline in the PCE is observed due to the reduction in V_{OC} and FF. The V_{OC} reduces due to an increment in the reverse saturation current in the Cs_2BiAgI_6-based double perovskite solar cell. However, the increase in J_{SC}, with an increase in the operating temperature, can be attributed to the thermal generation of electrons. Conversely, it is to be noted that, even when the operating temperature shoots to 400 K, the Cs_2BiAgI_6-based double perovskite solar cell delivered a PCE of ~26 %.

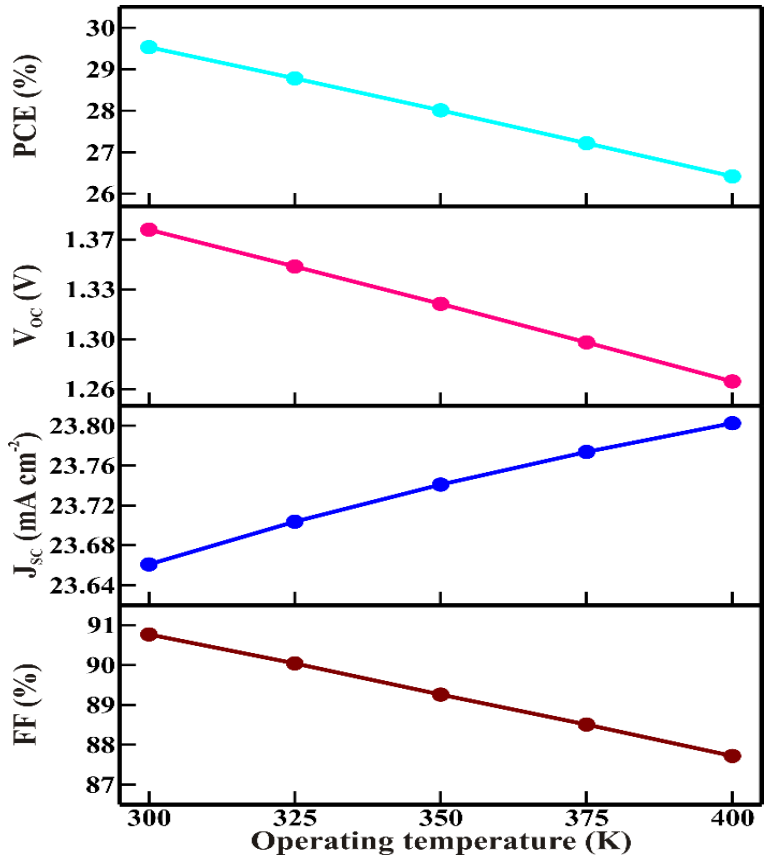

Figure 5.7 Operating temperature-related deviation solar cell parameters (with other parameters as tabulated in Table 5.1).

5.3.6 Quantum efficiency and *J-V* curves

Evaluating the spectral response of the solar cells is essential in understanding the incident photon to electron conversion efficiency or quantum efficiency. The quantum efficiency of the Cs_2BiAgI_6-based double perovskite solar cells is shown in Fig. 5.8. Cs_2BiAgI_6-based double perovskite solar cells with different HTLs showed a broad absorption in the complete visible range (400 to 800 nm). Further, the J-V curves of Cs_2BiAgI_6-based double perovskite solar cells with different HTLs are shown in Fig. 5.9. The optimum solar cell parameters evaluated for all Cs_2BiAgI_6-based solar cells show high efficiency of ~29 %. The solar cells show V_{OC}, J_{SC}, and FF in the range of ~1.37 V, ~23 mA cm^{-2}, and ~90 %, respectively.

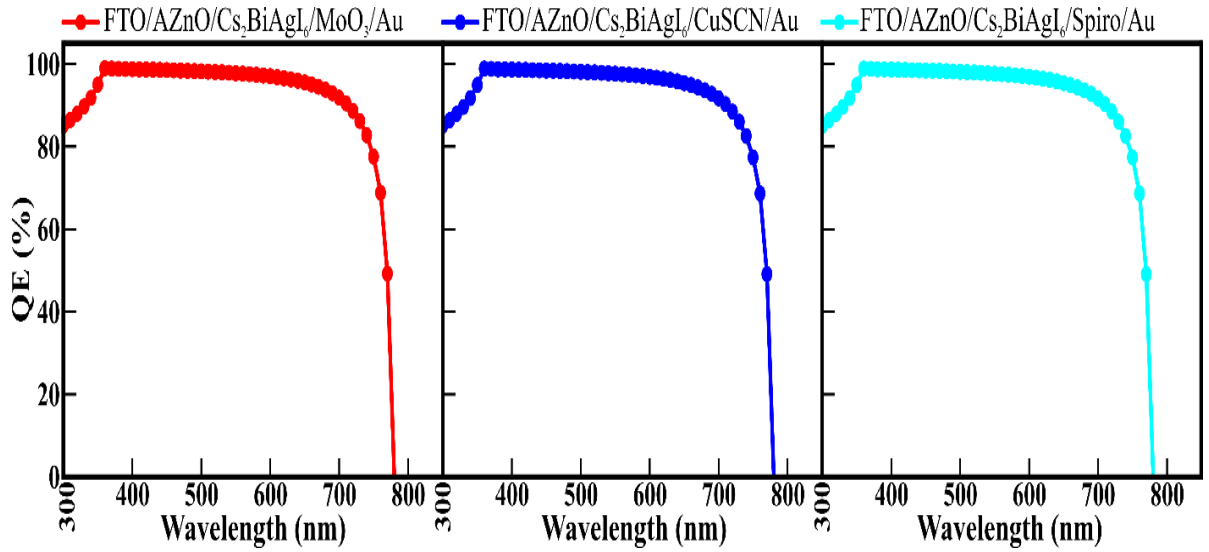

Figure 5.8 Quantum efficiency curves for the Cs_2BiAgI_6-based double perovskite solar cells comprising various HTLs (MoO_3/CuSCN/Spiro-OMeTAD).

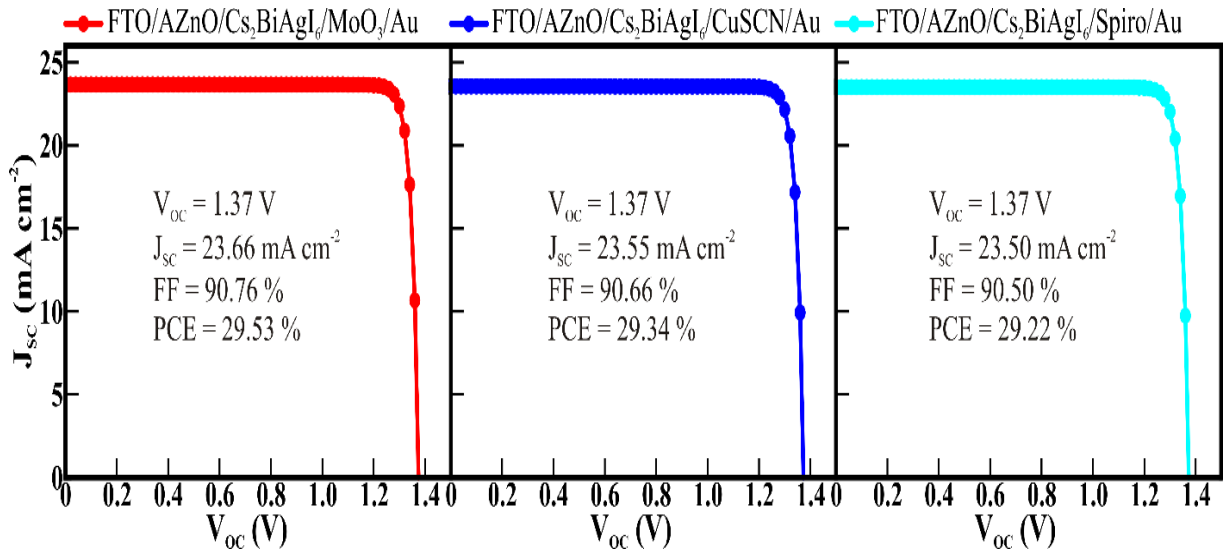

Figure 5.9 J-V curves for the Cs_2BiAgI_6-based double perovskite solar cells comprising various HTLs (MoO_3/CuSCN/Spiro-OMeTAD).

5.4 Conclusion

In conclusion, the theoretical potential of the Cs_2BiAgI_6 double perovskite light harvester is evaluated using the SCAPS-1D software package. Cs_2BiAgI_6 light harvesters are environmentally benign and render long-term stability. The high-efficiency solar cells are optimized based on the AZnO ETL and three different HTLs. Solar cells based on all three HTLs at optimized conditions delivered PCEs ~29 %. Compared to all the physical parameters varied in the optimization, the thickness and bulk defect density of the Cs_2BiAgI_6 double perovskite light harvester had the highest control over performance. The cheap and economical carbon electrodes could deliver a PCE of ~29 % in the modeled Cs_2BiAgI_6-based double perovskite solar cells. Further, even when the operating temperature shoots up to 400 K, the Cs_2BiAgI_6-based double perovskite solar cells delivered a PCE of ~26 %. Therefore, while experimentally fabricating Cs_2BiAgI_6 double perovskite solar cells, it should be noted that Cs_2BiAgI_6 perovskite is unstable. Hence, it is imperative to produce films with very low bulk defect density and prefer a practical rear contact. The present preliminary analysis accurately illustrates the factors which govern the PCE of Cs_2BiAgI_6 solar cells. The procedure employed in this assessment can provide guidelines for experimental implementation and be further expanded to examine additional light harvesters for optoelectronic applications.

5.5 References

[1] T. Baikie, Y. Fang, J. M. Kadro, M. Schreyer, F. Wei, S. G. Mhaisalkar, M. Graetzel, T. J. White, *J. Mater. Chem. A* **2013**, 1, 5628.

[2] M. M. Lee, J. Teuscher, T. Miyasaka, T. N. Murakami, H. J. Snaith, *Science* **2012**, 338, 643.

[3] H. S. Jung, N.-G. Park, *Small* **2015**, 11, 10.

[4] V. Manjunath, S. Bimli, P. Shaikh, S. Ogale, R. S. Devan, *J. Mater. Chem. C* **2022**, https://doi.org/10.1039/D2TC02911A.

[5] J. Jeong, M. Kim, J. Seo, H. Z. Lu, P. Ahlawat, A. Mishra, Y. G. Yang, M. A. Hope, F. T. Eickemeyer, M. Kim, Y. J. Yoon, I. W. Choi, B. P. Darwich, S. J. Choi, Y. Jo, J. H. Lee, B. Walker, S. M. Zakeeruddin, L. Emsley, U. Rothlisberger, A. Hagfeldt, D. S. Kim, M. Gratzel, J. Y. Kim, *Nature* **2021**, 592, 381.

[6] S. Chand Yadav, A. Srivastava, V. Manjunath, A. Kanwade, R. S. Devan, P. M. Shirage, *Mater. Today Phys.* **2022**, 26, 100731.

[7] H. Kim, K. A. Huynh, S. Y. Kim, Q. V. Le, H. W. Jang, *Phys. Status Solidi Rapid Res. Lett.* **2020**, 14, 1900435.

[8] M. M. Tavakoli, Z. Fazel, R. Tavakoli, S. Akin, S. Satapathi, D. Prochowicz, P. Yadav, *Solar RRL*. **2022**, 6, 2200106.

[9] V. Manjunath, P. K. Mishra, R. Dobhal, S. Bimli, P. M. Shirage, S. Sen, P. A. Shaikh, R. S. Devan, *ACS Appl. Electron. Mater.* **2021**, 3, 4548.

[10] S. Ma, Y. Bai, H. Wang, H. C. Zai, J. F. Wu, L. Li, S. S. Xiang, N. Liu, L. Liu, C. Zhu, G. L. Liu, X. X. Niu, H. N. Chen, H. P. Zhou, Y. J. Li, Q. Chen, *Adv. Energy Mater.* **2020**, 10, 1902472.

[11] A. H. Slavney, T. Hu, A. M. Lindenberg, H. I. Karunadasa, *J. Am. Chem. Soc.* **2016**, 138, 2138.

[12] S. C. Yadav, V. Manjunath, A. Srivastava, R. S. Devan, P. M. Shirage, *Opt. Mater.* **2022**, 132, 112676.

[13] Z. W. Xiao, W. W. Meng, J. B. Wang, Y. F. Yan, *Chemsuschem* **2016**, 9, 2628.

[14] X. B. Kong, Y. Q. Wu, F. Xu, S. K. Yang, B. Q. Cao, *Phys. Status Solidi Rapid Res. Lett.* **2021**, 15, 2100134.

[15] Q. H. Chen, K. M. Deng, Y. Shen, L. Li, *Infomat* **2022**, 4, e12303.

[16] J. N. Li, X. H. Meng, Z. H. Wu, Y. Y. Duan, R. X. Guo, W. D. Xiao, Y. S. Zhang, Y. K. Li, Y. L. Shen, W. Zhang, G. S. Shao, *Adv. Funct. Mater.* **2022**, 32, 2112991.

[17] K. Z. Du, W. W. Meng, X. M. Wang, Y. F. Yan, D. B. Mitzi, *Angew. Chem.* Int. *Ed.* **2017**, 56, 8158.

[18] A. H. Slavney, L. Leppert, D. Bartesaghi, A. Gold-Parker, M. F. Toney, T. J. Savenije, J. B. Neaton, H. I. Karunadasa, *J. Am. Chem. Soc.* **2017**, 139, 5015.

[19] Q. Li, Y. G. Wang, W. C. Pan, W. G. Yang, B. Zou, J. Tang, Z. W. Quan, *Angew. Chem. Int. Ed.* **2017**, 56, 15969.

[20] X. G. Zhao, D. Yang, J. C. Ren, Y. Sun, Z. Xiao, L. Zhang, *Joule* **2018**, 2, 1662.

[21] M. R. Filip, S. Hillman, A. A. Haghighirad, H. J. Snaith, F. Giustino, *J. Phys. Chem. Lett.* **2016**, 7, 2579.

[22] X. Y. Zhao, H. P. Shen, Y. Zhang, X. Li, X. C. Zhao, M. Q. Tai, J. F. Li, J. B. Li, X. Li, H. Lin, *ACS Appl. Mater. Interfaces* **2016**, 8, 7826;

[23] J. Kruszynska, J. Ostapko, V. Ozkaya, B. Surucu, O. Szawcow, K. Nikiforow, M. Holdynski, M. M. Tavakoli, P. Yadav, M. Kot, G. P. Kolodziej, M. Wlazlo, S. Satapathi, S. Akin, D. Prochowicz, *Adv. Mater. Interfaces* **2022**, 9, 2200575.

[24] S. Mandati, K. R. Dileep, G. Veerappan, E. Ramasamy, *Solar Energy* **2022**, 240, 258.

[25] S. Maniarasu, M. K. Rajbhar, R. K. Dileep, E. Ramasamy, G. Veerappan, *Mater. Lett.* **2019**, 245, 226.

[26] S. Seo, K. Akino, J. S. Nam, A. Shawky, H. S. Lin, H. Nagaya, E. I. Kauppinen, R. Xiang, Y. Matsuo, I. Jeon, S. Maruyama, *Adv. Mater. Interfaces* **2022**, 9, 2101515.

[27] V. Manjunath, S. Bimli, K. H. Parmar, P. M. Shirage, R. S. Devan, *Sol. Energy* **2019**, 193, 387.

[28] V. Karthikeyan, S. Maniarasu, V. Manjunath, E. Ramasamy, G. Veerappan, *Sol. Energy* **2017**, 147, 202.

[29] V. Manjunath, Y. K. Reddy, S. Bimli, R. J. Choudhary, R. S. Devan, *Mater. Today Commun.* **2022**, 32, 104061.

[30] M. Alla, V. Manjunath, N. Chawki, D. Singh, S. C. Yadav, M. Rouchdi, F. Boubker, *Opt. Mater.* **2022**, 124, 112044.

[31] M. Mottakin, K. Sobayel, R. C. Ismail, M. Shahiduzzaman, G. Muhammad, M. A. Ibrahim, M. Akhtaruzzaman, E. S. Hossain, *Phys. Status Solidi Rapid Res. Lett.* **2022**, 2200216.

[32] M. Alla, S. Bimli, V. Manjunath, M. Samtham, A. Kasaudhan, E. Choudhary, M. Rouchdi, F. Boubker, *Mater. Technol.* **2022**, 1-7, DOI: 10.1080/10667857.2022.20911951.

[33] A. Ait Abdelkadir, E. Oublal, M. Sahal, A. Gibaud, *Results Opt.* **2022**, 8, 100257.

[34] S. Srivastava, A. K. Singh, P. Kumar, B. Pradhan, *J. Appl. Phys.* **2022**, 131, 175001.

[35] S. Ahmed, F. Jannat, M. A. K. Khan, M. A. Alim, *Optik* **2021**, 225, 165765.

[36] D. K. Sarkar, A. K. M. Hasan, M. Mottakin, V. Selvanathan, K. Sobayel, M. A. Islam, G. Muhammad, M. Aminuzzaman, M. Shahiduzzaman, K. Sopian, M. Akhtaruzzaman, *Sol. Energy* **2022**, 243, 215.

[37] K. Sobayel, M. Shahinuzzaman, N. Amin, M.R. Karim, M.A. Dar, R. Gul, M.A. Alghoul, K. Sopian, A.K.M. Hasan, M. Akhtaruzzaman, *Sol. Energy* **2020**, 207, 479.

[38] Y. K. Reddy, V. Manjunath, S. Bimli, R. S. Devan, *Sol. Energy* **2022**, 244, 75.

[39] I. Mesquita, L. Andrade, A. Mendes, *Chemsuschem* **2019**, 12, 2186;

[40] F. *Haque*, M. Mativenga, *Phys. Status Solidi Rapid Res. Lett.* **2021**, 15.

Chapter 6

Lead-free non-toxic Cs_2CuSbX_6 double perovskite solar cell

6.1 Introduction

Lately, single-junction thin film solar cells based on perovskite light harvesters have experienced a significant increase in research momentum owing to their record power conversion efficiency (PCE), which is comparable to single-junction crystalline silicon solar cells [1]. The high efficiency of the perovskite solar cells (PSCs) is attained owing to their excellent optoelectronic characteristics, namely, extended charge diffusion length (~1 mm), reduced exciton binding energy, flexible bandgap, significant panchromatic visible light absorption coefficient, etc. [2]. Furthermore, it should be mentioned that the full *6s* and vacant *6p* orbitals at the valence band maximum and conduction band minimum of the lead metal cations, respectively, are the origin of the high visible light absorption in organic-inorganic perovskites [3, 4]. Despite the fact that lead cation aids in the intrinsic features of perovskites, these perovskites are carcinogenic and are therefore prohibited in many nations. Hence, the first alternative was to substitute Ge^{2+} or Sn^{2+} ions for Pb^{2+} ions; however, the *4s* and *5s* orbitals of the Ge^{2+} and Sn^{2+}, respectively, provide centers for oxidation, compromising the long-term durability [5]. In contrast, the next method involved creating double perovskites by hetero-valent swapping Pb^{2+} ions with a blend of monovalent and trivalent cations. The double perovskites with $A_2M'M''X_6$ (where *A*, *M′*, *M″*, and *X* are monovalent cation, monovalent metal ion, trivalent metal ion, and halogen, respectively) chemical formula crystallizes in the cubic crystal structure with $Fm\bar{3}m$ space group [6]. Ionic radii of the M′ and M″ sites can be averaged to determine the tolerance factor for double perovskite structures. When $\mu > 0.41$ and $0.75 < t < 1$, the double perovskite structures become stable [7]. Further, in the double perovskites with *M″* ions mostly being the 15th group elements, the *M′* ions can be either alkali metal or transitional or post-transitional metal ions, leading to a wide range of available lead-free double perovskite light harvesters. Among the possible permutations, the majority of the double perovskite light harvesters are thermodynamically unstable or have a broad bandgap [4]. However, for the thermodynamically stable double perovskites with wide bandgap, multiple methods, including dilute alloying [8], doping at the *M″* site [9], and pressure-assisted tuning [10], are exploited to tailor the bandgap for panchromatic visible light absorption.

Furthermore, among the various possible double perovskite light harvesters, $Cs_2BiAgCl_6$ and $Cs_2BiAgBr_6$ double perovskites synthesized by heterovalent replacement of hazardous Pb ions with Bi and Ag ions are extensively experimentally and theoretically explored to attain high-

performance and long-term durability [11-14]. Nevertheless, the double perovskite crystal with elpasolite structures (symmetric face-centered cubic double perovskite) with corner-sharing octahedra renders other probable environmentally benign and thermodynamically stable double perovskite light harvesters, which can offer high PCE [7], [15-17]. Among such double perovskites, Cs_2CuSbX_6 (where X = Cl, Br, and I) double perovskite light harvesters potentially have low bandgap and offer excellent optoelectronic characteristics [18]. In light of the above discussion, Zhou et al. have experimentally developed $Cs_2CuSbCl_6$ double perovskite nanocrystals with a bandgap of ~1.66 eV, which showed superior stability when exposed to ambient [19]. However, the experimental evaluation of Cs_2CuSbX_6 double perovskite light harvesters with prospective transport layers and rear contacts is a challenging issue. In these circumstances, investigators employ an array of software tools that essentially solve the boundary-constrained second-order fundamental semiconductor equations. Among the various software packages, the 1D Solar Cell Capacitance Simulator (SCAPS-1D) software package offers a simulation of heterojunctions [20-24]. On similar grounds, Karthick et al. have employed SCAPS-1D to validate and compare the experimentally synthesized solar cells based on formamidinium lead iodide ($CH(NH_2)_2PbI_3$) and cesium (Cs) doped formamidinium lead iodide light harvesters [25]. Parallelly, to corroborate the experimental performance of mesoscopic solar cells based on $CH_3NH_3PbI_3$ light harvester and graphene oxide hole transport layer (HTL), the SCAPS-1D software was used [26].

As a result, in this chapter, for the first time, we present the computational evaluation of Cs_2CuSbX_6 (where X = Cl, Br, and I) double perovskite solar cells using the SCAPS-1D software package. The potential of three different double perovskite light harvesters, i.e., $Cs_2CuSbCl_6$, $Cs_2CuSbBr_6$, and Cs_2CuSbI_6, is evaluated with aluminum doped zinc oxide (AZnO) as electron transport layer (ETL), MoO_3/Cu_2O as HTL, and various rear contacts [27]. Further, owing to better band alignment and established industrially feasible synthesis protocol, MoO_3, and Cu_2O have been extensively investigated for extracting holes toward the external terminal. Moreover, the inorganic nature of MoO_3 and Cu_2O HTL can improve the long-term stability of perovskite solar cells compared to the traditionally used organic spiro-OMeTAD HTL. Experimentally, MoO_3 and Cu_2O are known to enhance charge extraction in perovskite solar cells [28]. The Cs_2CuSbX_6 double perovskite solar cells are assessed by adjusting the thickness and defect densities of the subsequent layers to extract higher PCE. For the real-time assessment of Cs_2CuSbX_6-based double

perovskite solar cells, the operating temperature is varied, and the concerned fluctuations in performance are also presented. The variables and methodology applied in this investigation will offer recommendations for experimentally implementing high PCE Cs_2CuSbX_6-based double perovskite solar cells.

6.2 Device modeling and simulation procedure

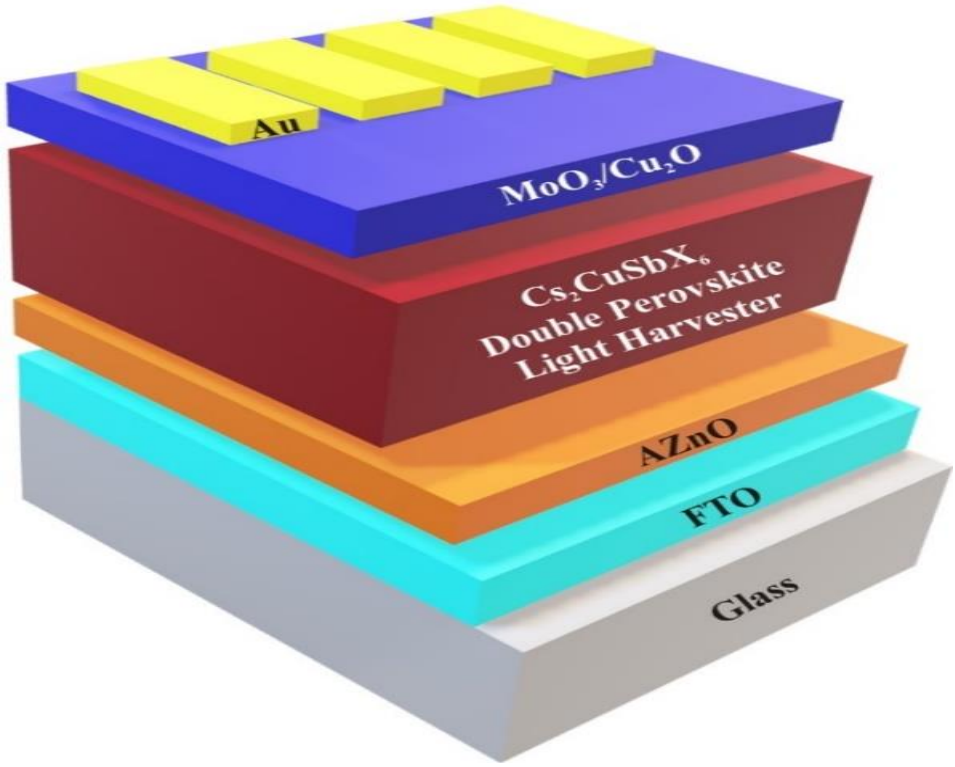

Figure 6.1. Schematic illustrating the double perovskite solar cell mode simulated in the present work.

Apart from solving second-order fundamental semiconductor equations, SCPAS-1D offers scaling of all input variables, such as recombination type, defect levels (bulk and interfacial), charge type, valency, defect distribution, type of light excitation, contact properties (work function or flat band), etc., to reasonably replicate the operation of the polycrystalline solar cells [29]. The Cs_2CuSbX_6-based double perovskite solar cells are modeled in the planar n-i-p configuration, i.e., FTO/AZnO/$Cs_2CuSbCl_6$ or $Cs_2CuSbBr_6$ or Cs_2CuSbI_6/MoO_3 or Cu_2O/Au, as shown in Fig. 6.1. The high thermal stability and chemical inertness of FTO, make it a standard alternative for

transparent conducting substrates. All simulations use Au as the back contact, with the exception of those that vary the counter electrode's work function.

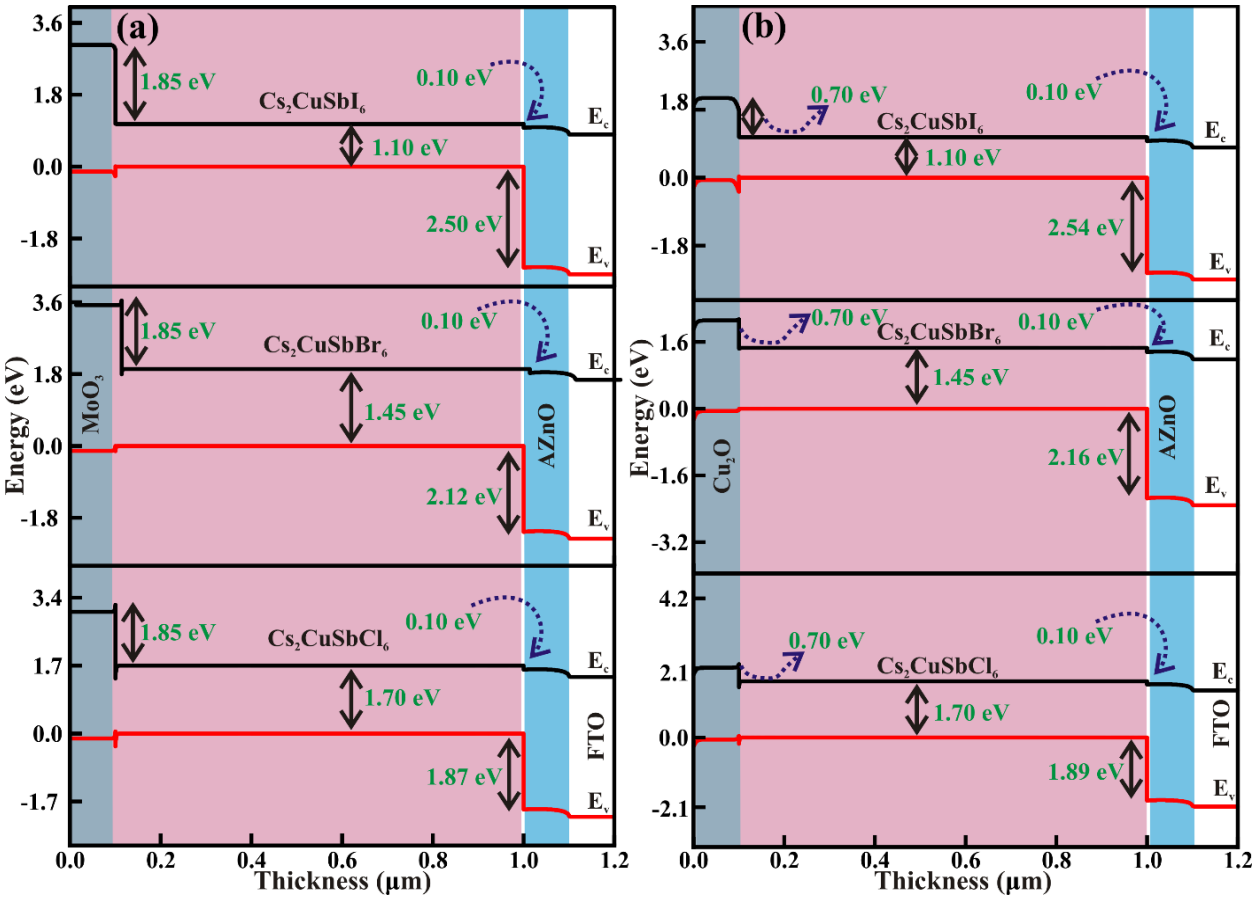

Figure 6.2 The simulated band alignment of Cs_2CuSbX_6 (where X = Cl, Br, I) based-double perovskite solar cells with (a) MoO_3 and (b) Cu_2O as HTL.

Fig. 6.2 shows the energy band diagram alignment of the device stack considered in this study. The conduction band minimum (CBm) for Cs_2CuSbI_6, $Cs_2CuSbBr_6$, and $Cs_2CuSbCl_6$ are found to be 1.07 eV, 1.45 eV, and 1.74 eV, respectively. Thus, the conduction band offset for different double perovskites at the Cs_2CuSbX_6/AZnO interface is 0.10 eV. Conversely, the valence band offset of 2.50 eV, 2.12 eV, and 1.87 eV was estimated for Cs_2CuSbI_6, $Cs_2CuSbBr_6$, and $Cs_2CuSbCl_6$ double perovskite light harvesters, respectively at the Cs_2CuSbX_6/AZnO interface. For, MoO_3 as HTL, the obtained band offsets and bandgap of the different double perovskite light harvesters are shown in Fig. 6.2(a). The conduction band offset of ~1.85 eV was calculated for all Cs_2CuSbX_6 light harvesters at the perovskite/MoO_3 (HTL) interface. Similarly, the conduction

band offset of ~0.7 eV was calculated for Cs_2CuSbX_6 light harvesters at the perovskite/Cu_2O (HTL) interface as shown in Fig. 6.2(b). These results show the good band level alignment of various double perovskite light harvesters with different HTLs (MoO_3 and Cu_2O) and AZnO ETL facilitating the extraction of photogenerated carriers in one direction by restricting their flow in opposite direction. Global AM1.5 spectrum intensity (1000 W/m^2) is considered for all simulations under illumination. The three underlying equations that regulate the carrier transport in semiconductors are the Poisson equation (Eq. 1), electron (Eq. 2) and hole (Eq. 3) continuity equations, and electron (Eq. 4) and hole (Eq. 5) drift-diffusion equations listed below:

$$\frac{dy}{dx} = -\frac{d^2\Psi}{dx^2} = \frac{q}{\varepsilon}[p(x) - n(x) + N_D^+(x) - N_A^- + p_t(x) - n_t(x)] \quad (6.1)$$

$$\frac{dn_p}{dt} = G_n - \frac{n_p - n_{p0}}{\tau_n} + n_p\mu_n\frac{dE}{dx} + \mu_n E\frac{dn_p}{dx} + D_n\frac{d^2n_p}{dx^2} \quad (6.2)$$

$$\frac{dp_n}{dt} = G_p - \frac{p_n - p_{n0}}{\tau_p} + p_n\mu_p\frac{dE}{dx} + \mu_p E\frac{dp_n}{dx} + D_p\frac{d^2p_n}{dx^2} \quad (6.3)$$

$$J_n(x) = qn\mu_n E + qD_n\frac{dn}{dx} = n\mu_n\frac{dE_{Fn}}{dx} \quad (6.4)$$

$$J_p(x) = qp\mu_p E - qD_p\frac{dp}{dx} = p\mu_p\frac{dE_{Fp}}{dx} \quad (6.5)$$

where Ψ is the electrostatic potential, q is the electron charge, ε is the dielectric constant of the semiconductor material, p is the hole concentration, n is the electron concentration, N_A^- is the density of the ionized acceptors, N_D^+ is the density of the ionized donors, n_t is the trapped electrons, and p_t is the trapped holes, x is the position coordinate, G_n and G_p are the electron and hole generation rates, n_p and p_n are the electron and hole concentrations in the p and n region, respectively, n_{po} and p_{no} are the equilibrium electron and hole concentrations in the p and n region, τ_n and τ_p denotes electron and hole lifetime, μ_p and μ_n are the hole and electron mobilities, E is the electric field, D_n and D_p are the electron and hole diffusion coefficients, E_{Fn} and E_{Fp} are the quasi-Fermi levels for electrons and holes. The series and shunt resistance values are 5 Ω/cm^2 and 1 MΩ/cm^2, respectively. Table 6.1 shows the physical parameters used to simulate Cs_2CuSbX_6-based double perovskite solar cells.

Table 6.1 The physical input parameters used to simulate Cs_2CuSbX_6-based double perovskite solar cells (base values).

Parameters	**FTO**	**AZnO**	**$Cs_2CuSbCl_6$**	**$Cs_2CuSbBr_6$**	**Cs_2CuSbI_6**	**MoO_3**	**Cu_2O**
Thickness (μm)	0 .1	0.10	0.90	0.90	0.90	0.10	0.10
Bandgap (E_g) (eV)	3.50	3.50	1.70	1.45	1.10	3.17	2.17
Electron affinity (χ) (eV)	4.00	4.00	3.90	3.90	3.90	2.05	3.20
Relative dielectric permittivity	9.00	8.12	6.50	6.00	6.20	12.50	7.11
CB effective density of states (N_C) ($1/cm^3$)	2.2×10^{18}	4.1×10^{18}	1×10^{19}	1×10^{19}	1×10^{19}	2.21×10^{18}	1×10^{17}
VB effective density of states (N_V) ($1/cm^3$)	1.8×10^{19}	8.2×10^{18}	1×10^{19}	1×10^{19}	1×10^{19}	1.8×10^{19}	1×10^{19}
Thermal velocity of electrons ($V_{th,e}$) (cm/s)	1×10^{7}	1×10^{7}	1×10^{7}	1×10^{7}	1×10^{7}	1×10^{7}	1×10^{7}
Thermal velocity of holes ($V_{th,h}$) (cm/s)	1×10^{7}	1×10^{7}	1×10^{7}	1×10^{7}	1×10^{7}	1×10^{7}	1×10^{7}
Electron mobility (μ_n) (cm^2/s)	20	100	2.0	2.0	2.0	25	50
Hole mobility (μ_p) (cm^2/s)	10	20	2	2	2	100	50
donor density (N_D) ($1/cm^3$)	2×10^{19}	1×10^{13}	0	0	0	0	0
acceptor density (N_A) ($1/cm^3$)	0	0	1×10^{19}	1×10^{19}	1×10^{19}	1×10^{18}	1×10^{18}
Defect density (N_t) ($1/cm^3$)	1×10^{15}	1×10^{17}	1×10^{14}	1×10^{14}	1×10^{14}	1×10^{15}	1×10^{14}
References	[23]	[30], [31]	[17]	[17]	[17]	[4]	[32]

6.3 Results and discussion

6.3.1 Absorption coefficient

Maximal photogeneration in solar cells is ensured through optical management of the incoming irradiation. It is essential for all incoming radiation to strike the double perovskite light harvester. The simulated absorption coefficient of the individual layers is shown in Fig. 6.3. The absorption onset at ~737 nm, ~1141 nm, and ~1162 nm is absorbed for $Cs_2CuSbCl_6$, $Cs_2CuSbBr_6$, and Cs_2CuSbI_6, respectively. All the double perovskite light harvesters showed excellent absorption in the visible range with an absorption coefficient of ~10^5 cm^{-1} at 550 nm. Owing to the high transparency of the AZnO and MoO_3 showed good transmittance to the visible spectrum. Though Cu_2O absorbs the low energy visible spectrum, they do not influence the performance in n-i-p device architecture. Thus, the light harvester is the most fundamental component of a solar cell; hence it is crucial to comprehend how the performance of solar cells is impacted by the thickness and defect density of light harvester films.

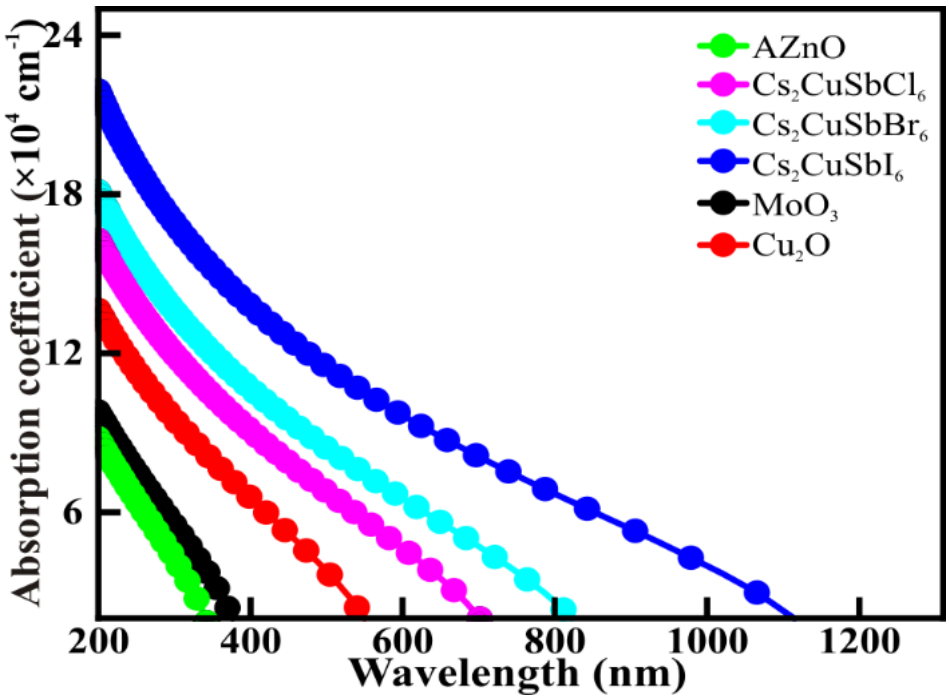

Figure 6.3 Absorption co-efficient of AZnO ETL, Cs_2CuSbX_6 (where X = Cl, Br, and I) double perovskite light harvester, MoO_3, and Cu_2O HTLs.

6.3.2 Effect of thickness of light harvester

Thus, the light harvester is the most fundamental component of a solar cell; hence it is crucial to comprehend how the performance of solar cells is impacted by the thickness and defect density of light harvester films. Thus, initially, the thickness of the three different light harvesters ($Cs_2CuSbCl_6$, $Cs_2CuSbBr_6$, and Cs_2CuSbI_6) is varied as shown in Fig. 6.4. For the double perovskite solar cells with MoO_3 as the HTL (Fig. 6.4(a)), the PCE of double perovskite solar cells increases with an increase in the thickness up to ~600 nm for all the light harvesters i.e., at a thickness of 600 nm, a PCE of 27.65 %, 28.56 %, and 29.54 % is observed for $Cs_2CuSbCl_6$, $Cs_2CuSbBr_6$, and Cs_2CuSbI_6 light harvesters (with MoO_3 HTL) respectively. Beyond the thickness of ~600 nm, the PCE for all the light harvesters mostly saturates. This increase in the PCE can be ascribed to the relative rise in the short circuit current density (J_{SC}), owing to the increase in photogeneration in the thicker light harvester films. Moreover, a marginal increment in the FF is also observed with an increase in the thickness of the absorber layer. This increment corresponds to the decrease in intrinsic resistivity of the device with the rise in photogenerated charge carriers.

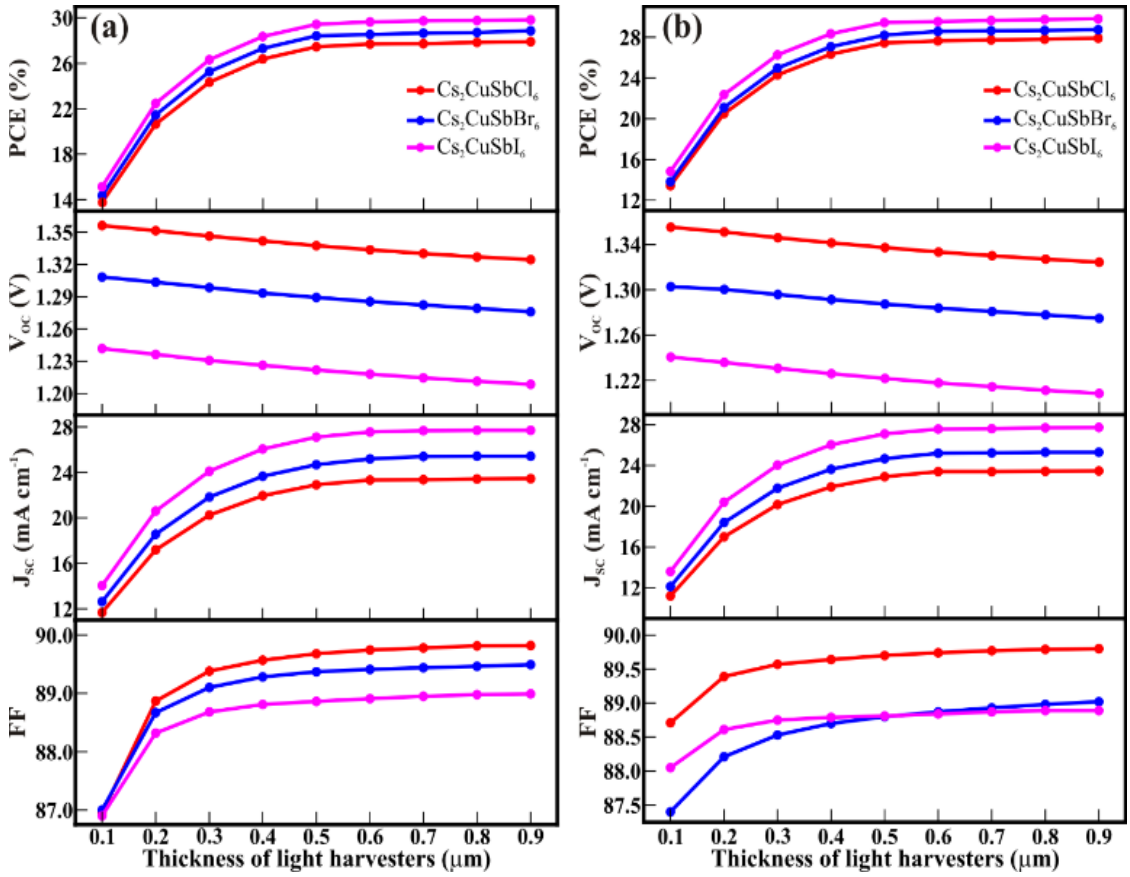

Figure 6.4 Thickness of light harvester-dependent performance of double perovskite solar cells with (a) MoO_3 and (b) Cu_2O as the HTLs. (with other parameters as tabulated in Table 6.1)

Further, a similar rise in the PCE was observed for the double perovskite solar cells with Cu_2O as the HTL (Fig. 6.4(b)), with the increase in the thickness of different absorber materials. The device with $Cs_2CuSbCl_6$, $Cs_2CuSbBr_6$, and Cs_2CuSbI_6 absorber layer with a thickness of 600 nm delivers an optimum efficiency of 27.69 %, 28.55 %, and 29.66 %, respectively, and the further increment in absorber thickness leads to the saturation of PCE. The higher thickness of the absorber layer will lead to increased charge recombination and therefore saturates the J_{SC} and PCE of the device. Moreover, out of all the halide perovskite absorbers, the iodide-based perovskite exhibits the highest PCE. The J_{SC} and PCE of the device rise as a result of the reduced bandgap of the Cs_2CuSbI_6 absorber layer, which leads to greater photo-generated charge carriers.

Additionally, the diffusion length in the perovskite light harvester needs to be considered while experimenting with thicker absorber films.

6.3.3 Effect of bulk defect density in light harvester

The quality of the absorber layer is equally important for better device performance. With different experimental techniques offer altering defect densities, hence, it is important to study the effect of bulk defect density of the absorber layer on the performance of the device. Films with inferior quality will have higher bulk defect density and result in poor device performance. Higher defect density will create localized recombination centers within the absorber material which will induce the defect-assisted recombination, and consequently reduce the charge collection efficiency. Therefore, in this study, we have utilized the Shockley-Read-Hall (SRH) model to analyze the recombination mechanism (Eq. 6.6):

$$R_{SRH} = \frac{(np - n_i^2)}{\tau\left(p + n + 2n_i \cosh\left(\frac{E_i - E_t}{k_B T}\right)\right)} \tag{6.6}$$

where p(n) is the concentration of holes (electron), τ is the lifetime of the charge carrier, n_i is the intrinsic carrier concentration, E_i is the intrinsic energy level, E_t is the energy level of trap states, k_B is the Boltzmann constant, and T is the operating temperature of the device.

The effect of varying defect densities on device performance is shown in Fig. 6.5. Here, we have varied the bulk defect density from 10^{14} to 10^{16} cm^{-3}. A steady reduction in all the solar cell parameters is observed with an increase in the bulk defect density of the device. The PCE of the devices with MoO_3 HTL shows a reduction of ~4.1 %, ~4.5 %, and ~2.2 % for $Cs_2CuSbCl_6$, $Cs_2CuSbBr_6$, and Cs_2CuSbI_6 absorber layer, respectively is shown in Fig. 6.5(a). The reduction in J_{SC} corresponds to the defect-induced recombination within the absorber layer. These localized energy levels will alter the energy band offset of the absorber and charge transport layers, thus resulting in a reduction in the V_{OC} of the device [32,33].

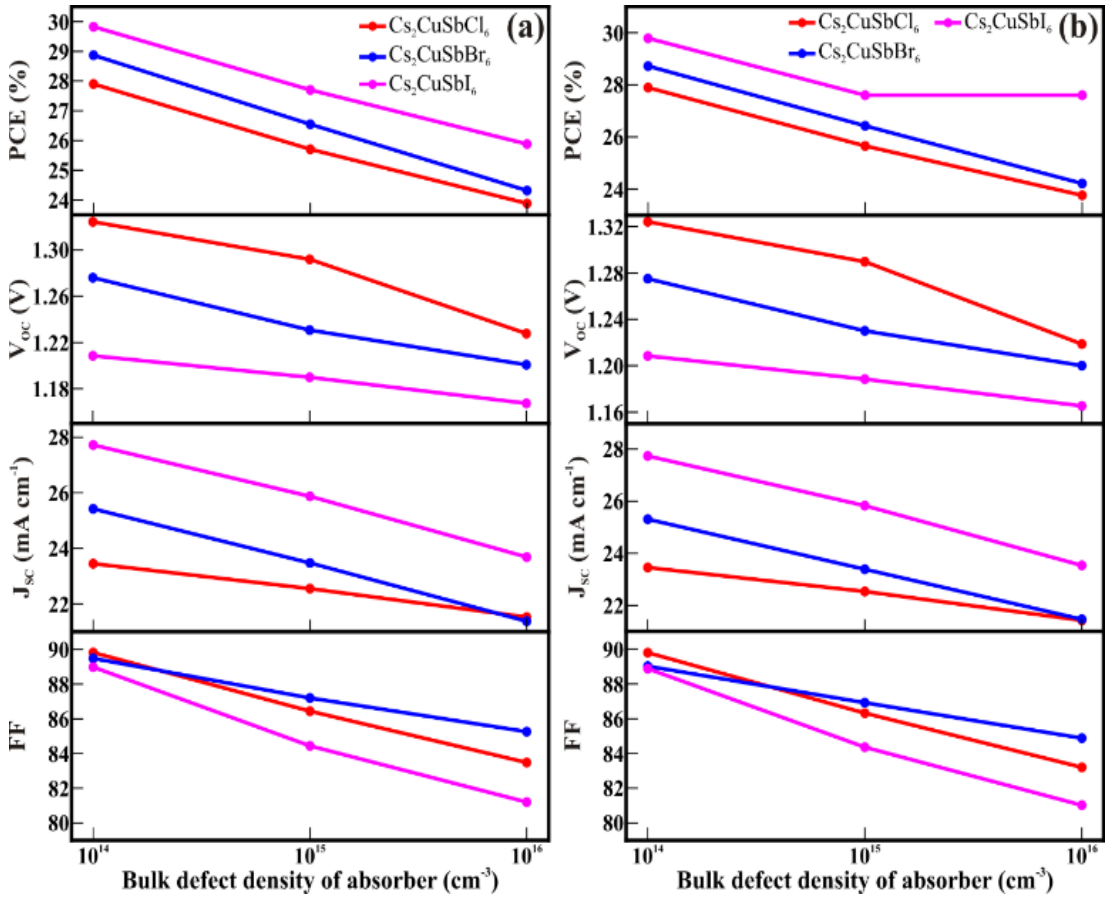

Figure 6.5 Effect of variation of bulk defect density on performance parameters of double perovskite solar cells with (a) MoO_3 and (b) Cu_2O as the HTLs. (with other parameters as tabulated in Table 6.1)

Similarly, these defects will increase the parasitic resistance of the device which results in the reduction of FF with the increase in defect density. The maximum efficiency of 27.89 %, 28.72 %, and 29.79 % is observed at a lower defect density of 10^{14} cm^{-3} for $Cs_2CuSbCl_6$, $Cs_2CuSbBr_6$, and Cs_2CuSbI_6 absorber layer, respectively. A similar trend of PCE has been observed for devices with Cu_2O HTL with the variation of defect density and is shown in Fig. 6.5(b). However, the devices with Cu_2O show marginally better performance than MoO_3 as HTL. The reduction in PCE of ~4.0 %, ~4.5 %, and ~3.9% is observed for $Cs_2CuSbCl_6$, $Cs_2CuSbBr_6$, and Cs_2CuSbI_6 absorber layer, respectively. The device with $Cs_2CuSbCl_6$, $Cs_2CuSbBr_6$, and Cs_2CuSbI_6 absorber layer delivers a maximum efficiency of 27.90 %, 28.87 %, and 29.82 %, respectively at

lower defect density of 10^{14} cm^{-3}. However, when the bulk defect density exceeds 10^{16} cm^{-3}, the performance is expected to decline further in Cs_2CuSbX_6 double perovskite solar cells for both MoO_3 and Cu_2O as HTLs.

6.3.4 Effect of operating temperature and various counter electrodes

Solar cells are designed to operate in different temperature conditions during real-time application. The increase in operating temperature may lead to poor device performance, due to induced thermal stresses in the absorber layer at a higher temperature.[34] Therefore, analysis of device performance at different operating temperatures is equally important. The effect of temperature variation on the performance parameter of the cell is shown in Fig. 6.6. The PCE of the device with MoO_3 and Cu_2O HTL shows a similar trend as we increase the operating temperature of the device as shown in Fig. 6.6(a) and Fig. 6.6(b). A linear reduction is observed in the V_{OC} and FF of the device, which reduces the performance of the device. The reduction in the V_{OC} is attributed to the increase in reverse saturation current with an increase in operating temperature. At higher temperature, the collision between the charge carriers increases, which increase the internal resistance of the device. However, a marginal increment in the photocurrent is observed with an increase in temperature due to more excitation of the charge carrier. The maximum efficiency of 27.89, 28.72, and 29.79 % is observed for $Cs_2CuSbCl_6$, $Cs_2CuSbBr_6$, and Cs_2CuSbI_6 absorber layer, respectively at 300 K for MoO_3 HTL. Similarly, a maximum efficiency of 27.90, 28.87, and 29.82 % is observed for $Cs_2CuSbCl_6$, $Cs_2CuSbBr_6$, and Cs_2CuSbI_6 absorber layer, respectively at 300 K for Cu_2O HTL.

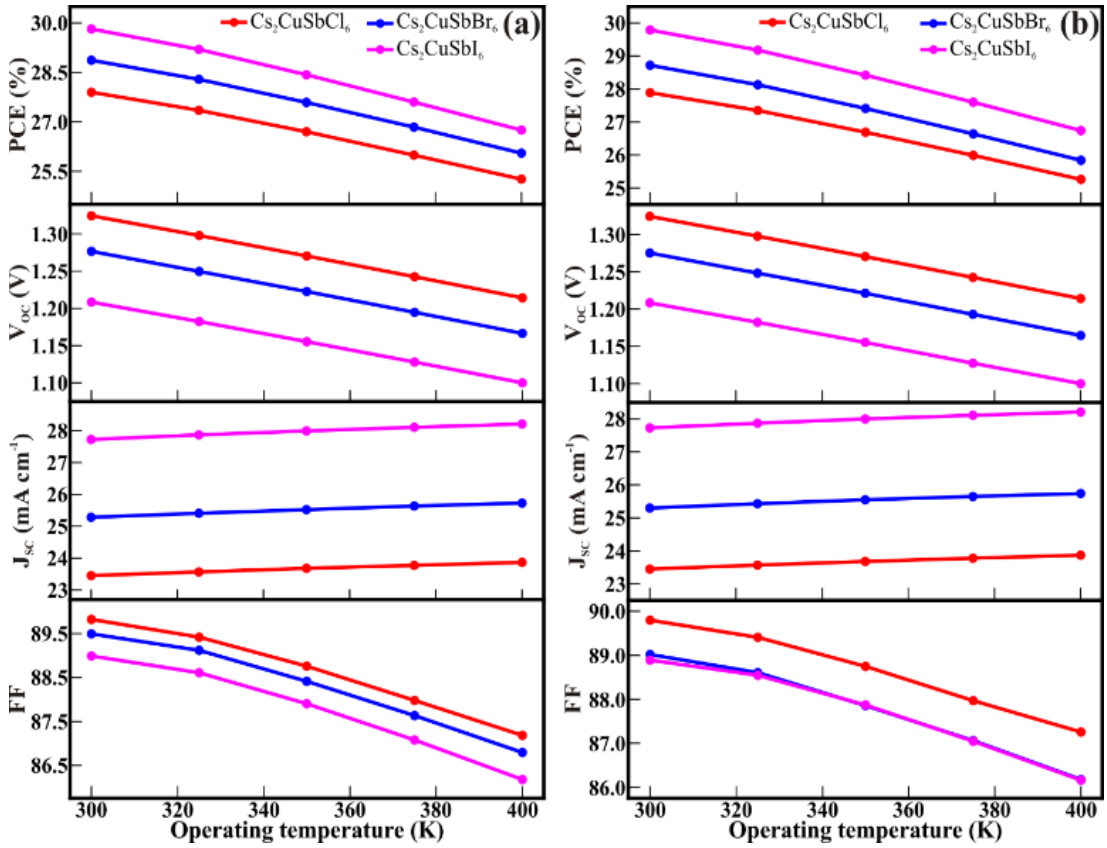

Figure6.6 Effect of operating temperature variation on the performance of double perovskite solar cells with (a) MoO_3 and (b) Cu_2O as the HTLs. (with other parameters as tabulated in Table 6.1)

The work function of the counter electrode will decide the built-in potential of the device. Therefore, it is important to check the compatibility of various metal and carbon (C) electrodes with our device. In this study, several metals namely Cu, Fe, C, Au, W, Ni, Pd, Pt, and Se are studied and their effect on the device performance is shown in Fig. 6.7 [35]. It is evident, that the PCE of the device increases with an increase in work function (W_F) of < 5 eV and it saturates afterward for both MoO_3 and Cu_2O HTL with iodide-based double perovskite showing maximum efficiency among the $Cs_2CuSbCl_6$, $Cs_2CuSbBr_6$, and Cs_2CuSbI_6 absorber as shown in Fig. 6.7(a) and Fig. 6.7(b). However, for Cu (4.65 eV) electrode, Cl-based double perovskite shows the maximum efficiency and the reason is yet not known to us. The Au, W, and Pt metal contact delivered a maximum PCE of ~30 % for the Cs_2CuSbI_6 absorber layer for both MoO_3 and Cu_2O HTL but the higher cost limits the usage in device fabrication Cu

having good electrical conductivity and lower cost gives an advantage over other metals, but it leads lower device performance. Metals like Pd and Se also show excellent device performance, but the rarity of these metals will increase the cost of the cell. Moreover, Ni shows excellent PCE as compared to Au, but surface oxidation of Ni to NiO_X may happen at ambient conditions, resulting in reduced PCE. However, C delivered equivalent PCE to Au and Pt, and can be an economical alternative for counter electrodes and will reduce the overall cost of the device by altering its performance.

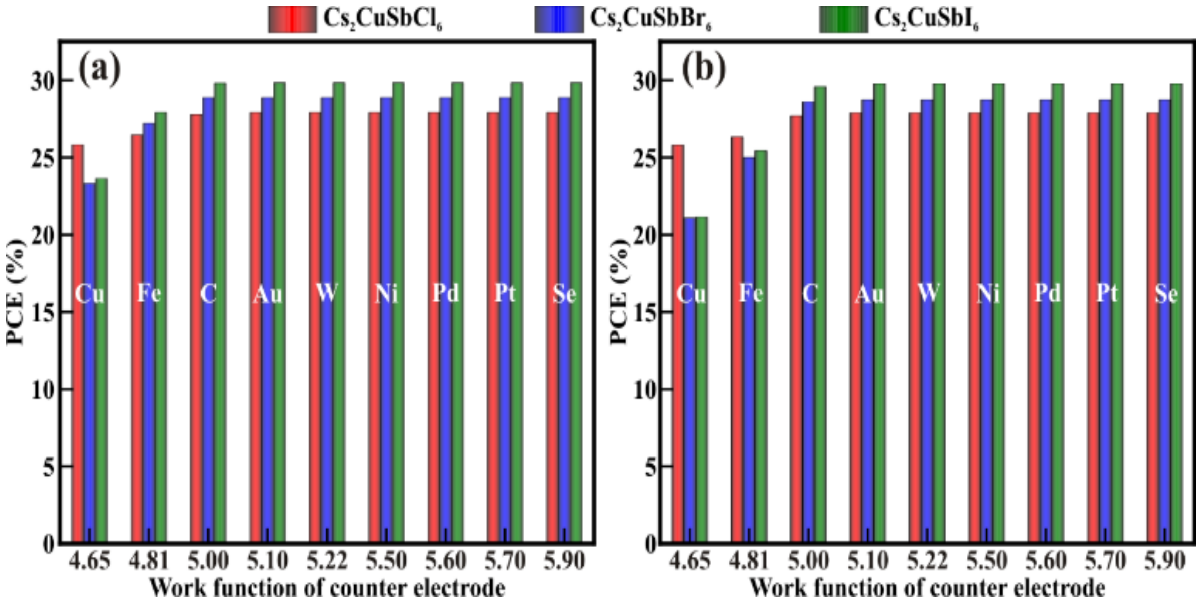

Figure 6.7 Comparison of the device performance with various back metal contact of double perovskite solar cells with (a) MoO_3 and (b) Cu_2O as the HTLs. (with other parameters as tabulated in Table 6.1)

6.3.5 Effect of parasitic series and shunt resistances

Theoretically understanding the effect of parasitic series and shunt resistances of modeled Cs_2CuSbX_6 based-double perovskite solar cells is essential to achieve high efficiency. For, MoO_3 as HTL, the effect of series and shunt resistance on the Cs_2CuSbX_6 double perovskite solar cell is shown in Fig. 6.8(a) and Fig. 6.8(b), respectively. As the series resistance increases from 1 to 10 W cm^{-2}, a steady decline in the PCE is observed for all the light harvesters originating from decreasing the FF. Such

decrease in the FF can be attributed to the ohmic losses in the solar cell. Conversely, as the shunt resistance is varied from 100 to 900 W cm^{-2}, the increase in the PCE of the Cs_2CuSbX_6 double perovskite solar cell is observed. The rise in PCE is ascribed to the corresponding increase in the FF of the solar cells. Further, the effect of series and shunt resistance on the performance of Cs_2CuSbX_6 double perovskite solar cells with Cu_2O has HTL is shown in Fig. 6.9(a) and Fig. 6.9(b), respectively. Akin to the devices with MoO_3 as HTL, the performance of Cs_2CuSbX_6 double perovskite solar cells with Cu_2O decreases and increases with rise and decline in series and resistance, respectively. Moreover, experimentally, the series and shunt resistance can be tuned by synthesizing high-quality films without pinholes.

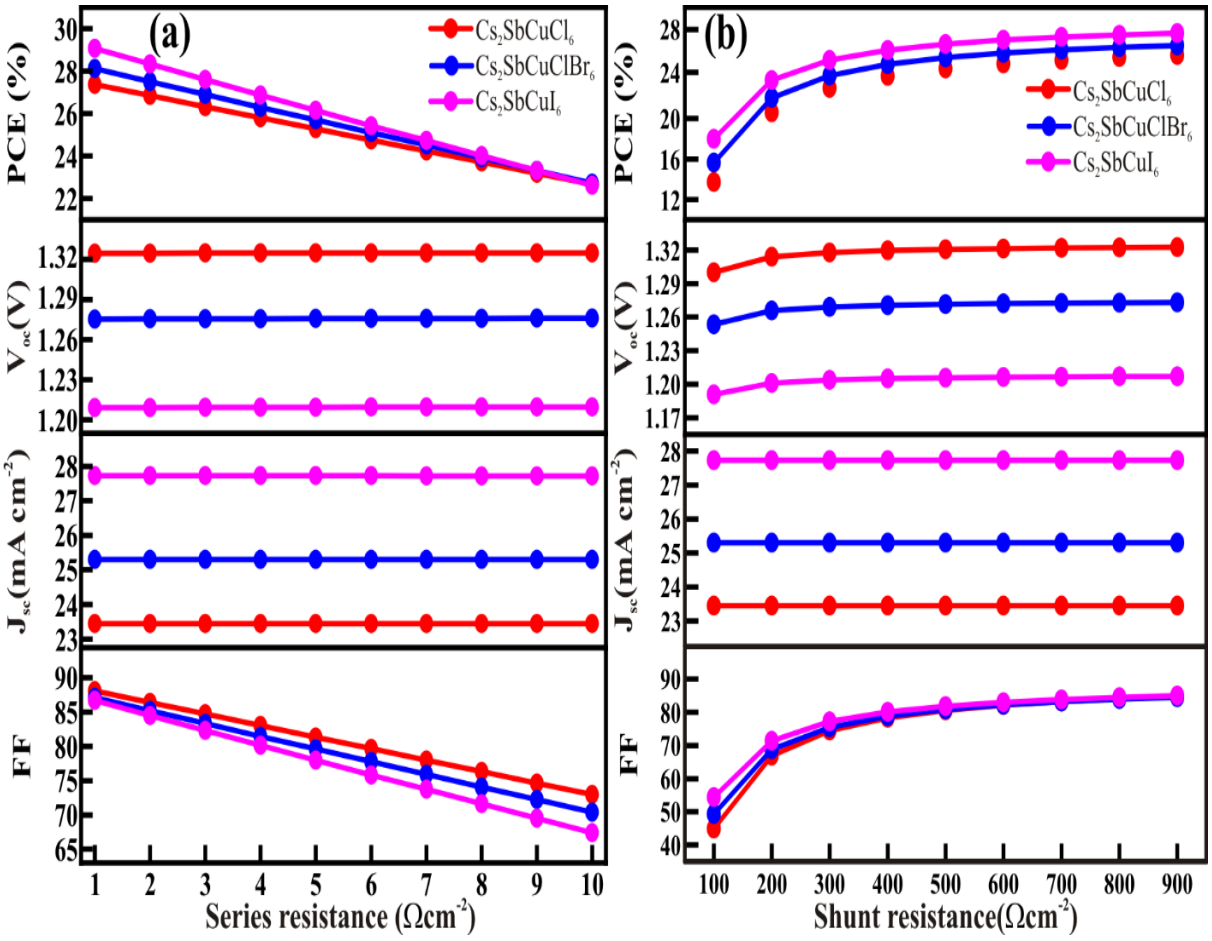

Figure 6.8 The effect of parasitic (a) series and (b) shunt resistance on the performance of Cs_2CuSbX_6 double perovskite solar cells with MoO_3 as HTL.

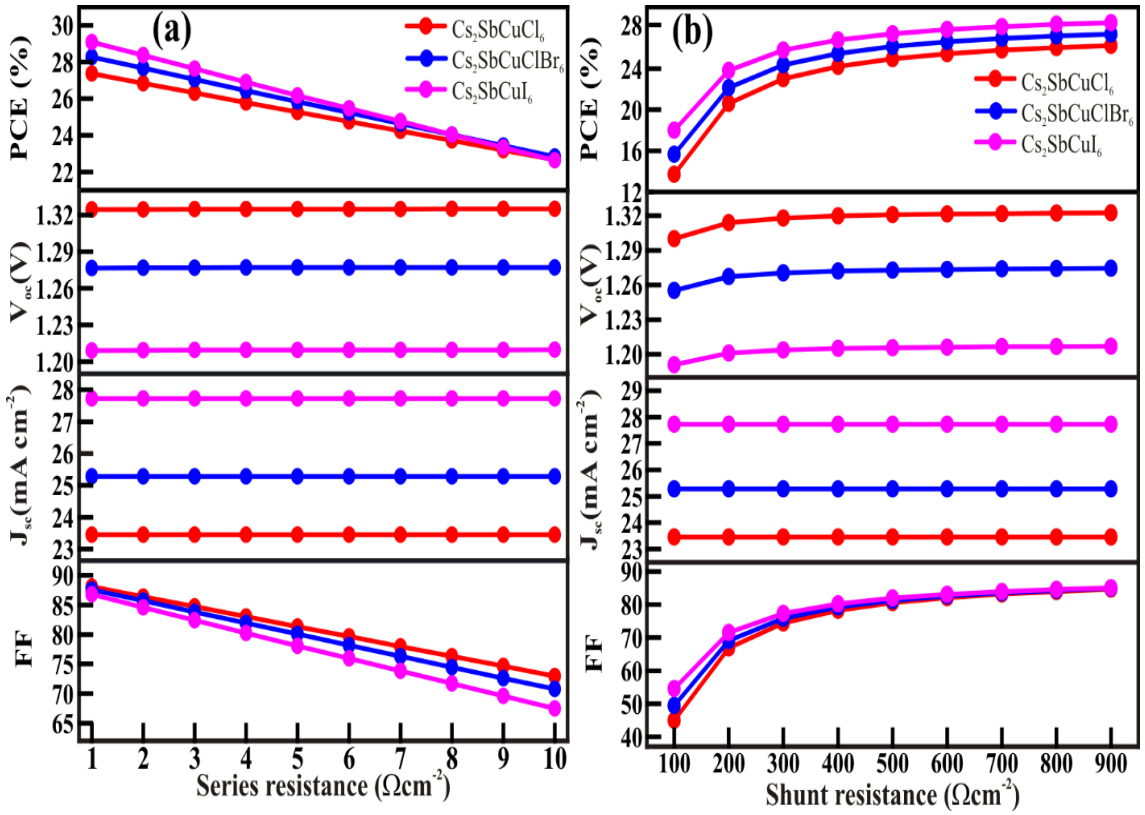

Figure 6.9 The effect of parasitic (a) series and (b) shunt resistance on the performance of Cs_2CuSbX_6 double perovskite solar cells with Cu_2O as HTL.

6.3.6 J-V curves and external quantum efficiency

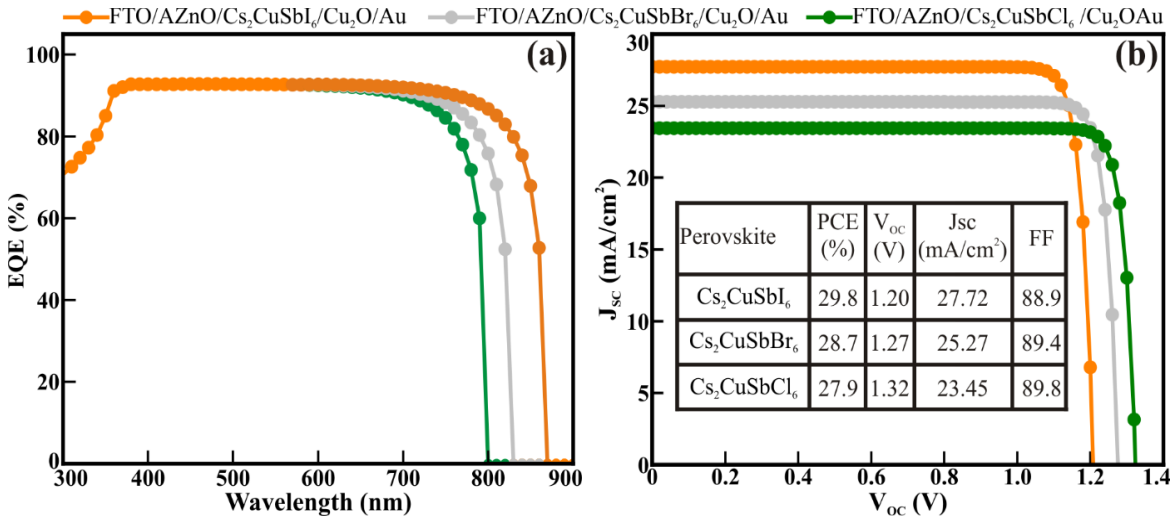

Figure 6.10 (a) QE of the double perovskite solar cells and (b) Optimized efficiency of the device with Cu_2O as the HTL.

The external quantum efficiency (EQE) of the device gives a deeper insight into the photogeneration phenomenon relative to the wavelength of the incident light. Fig. 6.10(a) shows the QE of the devices with Cl, Br, and I-based double perovskite solar cells. It is depicted above that all the perovskite absorber has reasonably good QE of ~93 % in the visible spectra and therefore leads to better conversion of the incident photon to current. Moreover, the device with I based double perovskite cell has a slightly higher absorption onset at ~900 nm than other halide-based perovskites, which allows it to absorb a photon of slightly lower energy. Fig. 6.10(b) shows the J-V characteristics of the device with various perovskite absorbers and Cu_2O HTL under constant illumination of AM 1.5G and 300 K temperature. Here, the device with Cl based perovskite absorber shows the highest V_{OC}, but its lower QE will lead to lower photogeneration capability and therefore has the lowest J_{SC} among all the halide perovskite absorbers. However, the device with I-based perovskite will give the highest J_{SC} and results in maximum PCE. The devices with optimized physical parameters of the absorber layer delivered a maximum PCE of 27.9, 28.7, and 29.8 % for $Cs_2CuSbCl_6$, $Cs_2CuSbBr_6$, and Cs_2CuSbI_6, respectively. All the devices with Cs_2CuSbX_6 absorber material show excellent performance. Therefore, it is evident that the Cs_2CuSbX_6 double perovskite absorber can be an alternative to toxic Pb-based perovskite light absorber.

6.4 Conclusion

There are several challenges like toxicity and stability which are quite difficult to overcome for present-day Pb-based organometallic perovskite solar cells. Therefore, in this study, we have suggested a more stable and environmentally benign Cs_2CuSbX_6 absorber, to efficiently harvest the solar spectra. The proposed device architecture comprises FTO/AZnO/Cs_2CuSbX_6/HTL/Au, with $Cs_2CuSbCl_6$, $Cs_2CuSbBr_6$, and Cs_2CuSbI_6 as light harvesters and HTLs (MoO_3 and Cu_2O). Here, we have systematically investigated the effect of various physical parameters such as thickness and bulk defect of the Cs_2CuSbX_6 absorber layer. Thereafter, the effect of operating temperature and work function of the counter electrode is also analyzed. The simulated device exhibits outstanding PCE, and this study can function as a manual for the researcher as they fabricate the experimental device.

6.5 References

[1] V. Manjunath, S. Bimli, P. A. Shaikh, S. B. Ogale, R. S. Devan, "Understanding the role of inorganic carrier transport layer materials and interfaces in emerging perovskite solar cells," *J. Mater. Chem. C*, vol. 10, pp. 15725-15780, Sep. 2022, doi: 10.1039/D2TC02911A.

[2] H. S. Jung, N.-G. Park, "Perovskite solar cells: From materials to devices," *Small*, vol. 11, pp. 10-25, Oct. 2015, doi: 10.1002/smll.201402767.

[3] S. C. Yadav, V. Manjunath, A. Srivastava, R. S. Devan, P. M. Shirage, "Stable lead-free $Cs_4CuSb_2Cl_{12}$ layered double perovskite solar cells yielding theoretical efficiency close to 30%," *Opt. Mater.*, vol. 132, pp. 112676, Oct. 2022, doi: 10.1016/j.optmat.2022.112676.

[4] M. Alla, V. Manjunath, E. Choudhary, M. Samtham, S. Sharma, P. A. Shaikh, M. Rouchdi, B. Fares, "Evaluating the potential of lead-free nontoxic Cs_2BiAgI_6-based double perovskite solar cell," *Phys. Status Solidi (A)*, vol. 220, pp. 2200642, Nov. 2022, doi: 10.1002/pssa.202200642.

[5] Z. Xiao, W. Meng, J. Wang, Y. Yan, "Thermodynamic stability and defect chemistry of bismuth-based lead-free double perovskites," *ChemSusChem*, vol. 9, pp. 2628-2633, Aug. 2016, doi: 10.1002/cssc.201600771.

[6] J. Li, X. Meng, Z. Wu, Y. Duan, R. Guo, W. Xiao, Y. Zhang, Y. Li, Y. Shen, W. Zhang, G. Shao, "Pinning bromide ion with ionic liquid in lead-free $Cs_2AgBiBr_6$ double perovskite solar cells," *Adv. Funct. Mater.*, vol. 32, pp. 2112991, Mar. 2022, doi: 10.1002/adfm.202112991.

[7] X.-G. Zhao, D. Yang, J.-C. Ren, Y. Sun, Z. Xiao, L. Zhang, "Rational design of halide double perovskites for optoelectronic applications," *Joule*, vol. 2, pp. 1662-1673, Sep. 2018, doi: 10.1016/j.joule.2018.06.017.

[8] A. H. Slavney, L. Leppert, D. Bartesaghi, A. Gold-Parker, M. F. Toney, T. J. Savenije, J. B. Neaton, H. I. Karunadasa, "Defect-induced band-edge reconstruction of a bismuth-halide double perovskite for visible-light absorption," *J. Am. Chem. Soc.*, vol. 139, pp. 5015-5018, Mar. 2017, doi: 10.1021/jacs.7b01629.

[9] K.-z. Du, W. Meng, X. Wang, Y. Yan, D. B. Mitzi, "Bandgap engineering of lead-free double perovskite $Cs_2AgBiBr_6$ through trivalent metal alloying," *Angew. Chem. Int. Ed.*, vol. 56, pp. 8158-8162, May 2017, doi: 10.1002/anie.201703970.

[10] Q. Li, Y. Wang, W. Pan, W. Yang, B. Zou, J. Tang, Z. Quan, "High-pressure band-gap engineering in lead-free $Cs_2AgBiBr_6$ double perovskite, *Angew. Chem. Int. Ed.*, vol. 56, pp. 15969-15973, Oct. 2017, doi: 10.1002/anie.201708684.

[11] D. Huang, H. Xiao, D. Liu, Q. Ouyang, Y. Kong, B. Wang, H. Lian, J. Lin, "All-inorganic tin-doped $Cs_2BiAgCl_6$ double perovskites with stable blue photoluminescence for WLEDs," *J. Mater. Chem. C*, vol. 9, pp. 8862-8873, Jun. 2021, doi: 10.1039/D1TC02168K.

[12] Z. Weng, J. Qin, A.A. Umar, J. Wang, X. Zhang, H. Wang, X. Cui, X. Li, L. Zheng, Y. Zhan, "Lead-free $Cs_2BiAgBr_6$ double perovskite-based humidity sensor with superfast recovery time," *Adv. Funct. Mater.*, vol. 29, pp. 1902234, Apr. 2019, doi: 10.1002/adfm.201902234.

[13] E. Haque, M. A. Hossain, "Origin of ultra-low lattice thermal conductivity in Cs_2BiAgX_6 (X=Cl, Br) and its impact on thermoelectric performance," *J. Alloys Compd.*, vol. 748, pp. 63-72, Jun. 2018, doi: 10.1016/j.jallcom.2018.03.137.

[14] J. Su, Z. Zhang, J. Hou, M. Liu, Z. Lin, Z. Hu, J. Chang, Y. Hao, "Pressure-dependent mechanical and thermal properties of lead-free halide double perovskite $Cs_2AgB''X_6$ (B″=In, Bi; X=Cl, Br, I)," *Adv. Theory Simul.*, vol. 2, pp. 1900164, Oct. 2019, doi: 10.1002/adts.201900164.

[15] N. R. Wolf, B. A. Connor, A. H. Slavney, H. I. Karunadasa, "Doubling the stakes: The promise of halide double perovskites," *Angew. Chem. Int. Ed.*, vol. 60, pp. 16264-16278, Feb. 2021, doi: 10.1002/ange.202016185.

[16] S. Chand Yadav, A. Srivastava, V. Manjunath, A. Kanwade, R. S. Devan, P. M. Shirage, "Properties, performance and multidimensional applications of stable lead-free $Cs_2AgBiBr_6$ double perovskite," *Mater. Today Phys.*, vol. 26, pp. 100731, Sep. 2022, doi: 10.1016/j.mtphys.2022.100731.

[17] A.J. Kale, R. Chaurasiya, A. Dixit, Lead-free $Cs_2BB'X_6$ (B: Ag/Au/Cu, B′: Bi/Sb/Tl, and X: Br/Cl/I) double perovskites and their potential in energy conversion applications, *ACS Appl. Energy Mater.*, vol. 5, pp. 10427-10445, Aug. 2022, doi: 10.1021/acsaem.2c00672.

[18] A. Mera, G. Nazir, Q. Mahmood, N. A. Kattan, T. Alshahrani, A. Rehman, H. Sultana, M. A. Amin, H. Elhosiny Ali, "The bandgap engineering of double perovskites Cs_2CuSbX_6 (X = Cl, Br, I) for solar cell and thermoelectric applications," *Inorg. Chem. Commun.*, vol. 148, pp. 110303, Feb. 2023, doi: 10.1016/j.inoche.2022.110303.

[19] W. Zhou, P. Han, X. Zhang, D. Zheng, S. Yang, Y. Yang, C. Luo, B. Yang, F. Hong, D. Wei, R. Lu, K. Han, "Lead-free small-bandgap $Cs_2CuSbCl_6$ double perovskite nanocrystals," *J. Phys. Chem. Lett.*, vol. 11, pp. 6463-6467, Jul. 2020, doi: 10.1021/acs.jpclett.0c01968.

[20] M. Alla, S. Bimli, V. Manjunath, M. Samtham, A. Kasaudhan, E. Choudhary, M. Rouchdi, F. Boubker, "Towards lead-free all-inorganic perovskite solar cell with theoretical efficiency approaching 23%," *Mater. Technol.*, vol. 37, pp. 2963-2969, Jun. 2022, doi: 10.1080/10667857.2022.2091195.

[21] V. Manjunath, Y. K. Reddy, S. Bimli, R. J. Choudhary, R. S. Devan, "22% efficient kusachiite solar cells of $CuBi_2O_4$ light harvester and ABO_3 buffer layers: A theoretical analysis," *Mater. Today Commun.*, vol. 32, pp. 104061, Aug. 2022, doi: 10.1016/j.mtcomm.2022.104061.

[22] Y. K. Reddy, V. Manjunath, S. Bimli, R. S. Devan, "Futuristic kusachiite solar cells of $CuBi_2O_4$ absorber and metal sulfide buffer Layers: Theoretical efficiency approaching 28 %," *Sol. Energy*, vol. 244, pp. 75-83, Aug. 2022, doi: 10.1016/j.solener.2022.08.034.

[23] M. Alla, V. Manjunath, N. Chawki, D. Singh, S. C. Yadav, M. Rouchdi, F. Boubker, "Optimized $CH_3NH_3PbI_{3-X}Cl_X$ based perovskite solar cell with theoretical efficiency exceeding 30%," *Opt. Mater.*, vol. 124, pp. 112044, Feb. 2022, doi: 10.1016/j.optmat.2022.112044.

[24] Sadanand, D. K. Dwivedi, "Modeling of photovoltaic solar cell based on $CuSbS_2$ absorber for the enhancement of performance," *IEEE Trans. Electron Devices*, vol. 68, pp. 1121-1128, Mar. 2021, doi: 10.1109/TED.2020.3048326.

[25] S. Karthick, S. Velumani, J. Bouclé, "Experimental and SCAPS simulated formamidinium perovskite solar cells: A comparison of device performance." *Sol. Energy*, vol. 205, pp. 349-357, Jul 2020, doi: 10.1016/j.solener.2020.05.041.

[26] E. Widianto, E. S. Rosa, K. Triyana, N. M. Nursam, I. Santoso, "Performance analysis of carbon-based perovskite solar cells by graphene oxide as hole transport layer: Experimental and numerical simulation." *Opt. Mater.*, vol. 121, pp.111584. Nov. 2021, doi: 10.1016/j.optmat.2021.111584.

[27] S. Rai, B. K. Pandey, A. Garg, D. K. Dwivedi, "Hole transporting layer optimization for an efficient lead-free double perovskite solar cell by numerical simulation." Opt. Mater., vol. 121, pp. 111645, Nov 2021, doi: 10.1016/j.optmat.2021.111645.

[28] D. Perez-del-Rey, L. Gil-Escrig, K. P. Zanoni, C. Dreessen, M. Sessolo, P. P. Boix, H. J. Bolink, "Molecular passivation of MoO_3: Band alignment and protection of charge transport layers in vacuum-deposited perovskite solar cells." Chem. Mater., vol. 31, pp. 6945-6949, Jun. 2019, doi: 10.1021/acs.chemmater.9b01396.

[29] D. Pal, "A comprehensive analysis of eco-friendly Cs_2SnI_6 based tin halide perovskite solar cell through device modeling," *Adv. Theory Simul.*, vol. 6, pp. 2200856, Jan. 2023, doi: 10.1002/adts.202200856.

[30] A. A. Abdelkadir, E. Oublal, M. Sahal, A. Gibaud, "Numerical simulation and optimization of n-Al-ZnO/n-CdS/p-CZTSe/p-NiO (HTL)/Mo solar cell system using SCAPS-1D," *Results in Opt.*, vol. 8, pp. 100257, Aug. 2022, doi: 10.1016/j.rio.2022.100257.

[31] I. M. D. L Santos, A. A. Perez-Orozco, D. A. Lina-Martinez, M. Courel, C. A. Meza-Avendano, J. A. Borrego-Perez, L. M. Perez, D. Laroze, "Towards a CdTe solar cell efficiency promotion: The role of ZnO:Al and CuSCN nanolayers," *Nanomaterials*, vol. 13, pp. 1335, Apr. 2023, doi: 10.3390/nano13081335.

[32] S. Porwal, M. Paul, H. Dixit, S. Mishra, T. Singh, "Investigation of defects in Cs_2SnI_6-based double perovskite solar cells via SCAPS-1D," *Adv. Theory Simul.*, vol. 5, pp. 2200207, Jul. 2022, doi: 10.1002/adts.202200207.

[33] S. Bimli, Y. K. Reddy, V. Manjunath, R. S. Devan, "Performance evaluation of metal oxide transport and absorber layers for all oxide heterostructure solar cells with ~26% efficiency," *Chinese J. Phys.*, vol. 82, pp. 120-133, Apr. 2023, doi: 10.1016/j.cjph.2023.01.007.

[34] N. Rolston, K. A. Bush, A. D. Printz, A. Gold-Parker, Y. Ding, M. F. Toney, M. D. McGehee, R. H. Dauskardt, "Engineering stress in perovskite solar cells to improve stability," *Adv. Energy Mater.*, vol. 8, pp. 1802139, Sep. 2018, doi: 10.1002/aenm.201802139.

[35] S. Maniarasu, T. B. Korukonda, V. Manjunath, E. Ramasamy, M. Ramesh, G. Veerappan, "Recent advancement in metal cathode and hole-conductor-free perovskite solar cells for low-cost and high stability: A route towards commercialization," *Renew. Sust. Energy Rev.*, vol. 82, part – 1, pp. 845-857, Feb. 2018, doi: 10.1016/j.rser.2017.09.095.

Chapter 7

$Cs2AgSbX_6$ double perovskite: DFT and SCAPS studies

7.1 Introduction

Due to their high-power conversion efficiency (PCE) and low production costs, perovskite-based thin film solar cells have recently acquired research traction.[1] The carcinogenic lead (Pb) ions found in the perovskite light harvesters facilitate, panchromatic visible light absorption emanating from the filled *6s* and empty *6p* orbital at conduction band maximum and valence band minimum, respectively. [2, 3] Thus, to mitigate toxicity, the Pb cation was replaced by divalent Sn or Ge cations. Nevertheless, the Sn^{2+} and Ge^{2+} cations comprise higher energy *4s* and *5s* orbitals, respectively, rendering oxidation centers, which limit their long-term stability.[4] To combat both toxicity and stability issues, the tunability of the perovskite crystal structure was exploited to engineer layered double perovskite, double perovskite, and low dimensional (0 and 2D) perovskite light harvesters.[5-8] Despite such breakthroughs, a perovskite light harvester with optoelectronics characteristics analogous to Pb-containing counterparts is yet to be untangled. One of these potential perovskite light harvesters that has shown promise is the double perovskite with the chemical formula $A_2M'M''X_6$ (where A, M′, M″, and X are monovalent cations, monovalent metal ions, trivalent metal ions, and halogen, respectively).[9,10] The double perovskites crystallize into a cubic crystal system with $Fm\bar{3}m$ space group is obtained by hetero-valent switching Pb^{2+} ions with a combination of monovalent and trivalent cations.[11] Despite the fact that such 3D double perovskites have a substantially large indirect bandgap, the bandgap can be regulated for visible light absorption using a variety of strategies, ranging from M″ doping, diluted alloying, and pressure-assisted tuning.[3, 12, 13] Besides, a variety of lead-free 3D double perovskites are chemically feasible relying on the M′ and M″ configurations. By averaging the ionic radii of the M″ and M′ sites, the tolerance factor (t) of the double perovskites is estimated. Theoretically, double perovskite structures require $0.75 < t < 1$ to be stable.[14] Among the double perovskite light harvesters, Cs_2BiAgX_6 is scrutinized significantly to achieve high performance. [15-17] However, there are other prospective thermodynamically stable and environmentally friendly double perovskites light harvesters that can provide high performance at a reasonable cost.

Accordingly, the Cs_2AgSbX_6 double perovskite obtained by hetero-valent replacement of Pb ions with Ag and Sb ions is ecologically safe, capable of retaining long-term stability, and reported to be thermodynamically stable. [18, 19] Such double perovskites crystallize into the symmetric face-centered cubic double perovskite referred to as the elpasolite crystal structure,

which has corner-sharing octahedra with Cs occupying the cavity in the center. In a rock-salt arrangement, the centers of the octahedra are alternately occupied by Ag or Sb ions, resulting in isotropic carrier transport capabilities.[20] Moreover, the tunability of the 'X' site in the Cs_2AgSbX_6 double perovskite structure renders tailoring of the bandgap for panchromatic visible light absorption. Thus, it is important to scrutinize the Cs_2AgSbX_6 double perovskite for its light-harvesting efficacy. However, the operation of the double perovskite requires the assistance of other probable charge transport layers akin to perovskite solar cells. Owing to the industrial feasibility, matured synthesis protocol, optoelectronic properties, and suitable band alignment with Cs_2AgSbX_6 double perovskite, aluminum doped zinc oxide (AZnO) and molybdenum oxide (MoO_3) are determined as the aiding electron and hole transport layers (ETL and HTL), respectively. [21,22] Therefore, experimentally investigating the performance of the Cs_2AgSbX_6 double perovskite solar cell is a challenging task. Nevertheless, researchers employ various numerical techniques based on density functional theory (DFT) and software packages such as the 1D Solar Cell Capacitance Simulator (SCAPS-1D) to understand the electronic structure of light harvesters and solar cell performance, respectively. [23-27]

This chapter initially scrutinizes the Cs_2AgSbX_6 double perovskite light harvester based on the DFT calculations, through the Cambridge Serial Total Energy Package (CASTEP). The obtained fundamental understanding of the electronic structure and the physical characteristics of Cs_2AgSbX_6 double perovskite was thoroughly examined and loaded as input to the SCAPS-1D with other aiding layers. Device performance of the double perovskite solar cell based on a Cs_2AgSbX_6 light harvester was estimated with a device structure comprising fluorine doped tin oxide (FTO)/AZnO/Cs_2AgSbX_6/MoO_3/rear contact as shown in Fig. 7.1 (using SCAPS-1D). The DFT analysis showed the tunability of the bandgap with other beneficial optoelectronic properties of Cs_2AgSbX_6 double perovskite light harvesters.

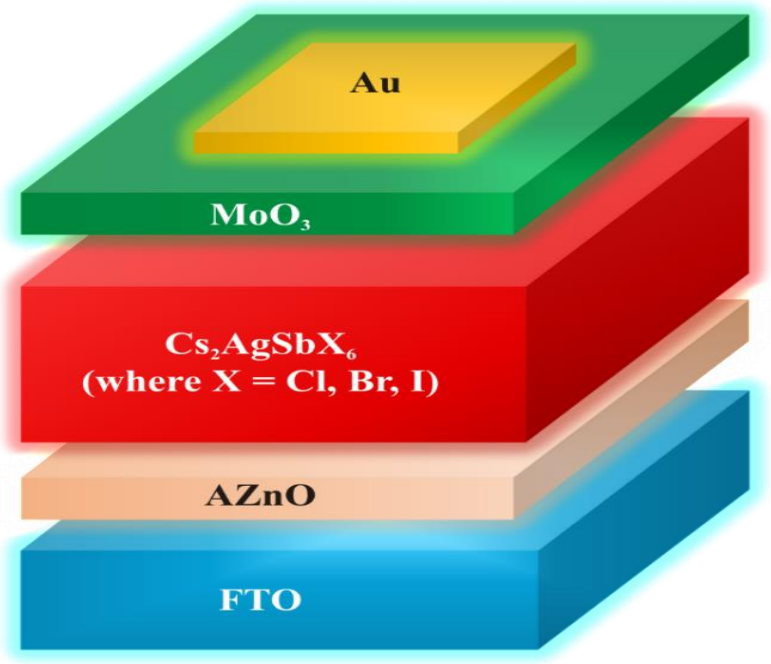

Figure 7.1 Schematics depicting the modeled double perovskite solar cell considered in this study.

7.2 Computational study and numerical simulations

7.2.1 DFT calculations of the Cs_2AgSbX_6 double perovskite light harvester

This study performed first-principle calculations through the CASTEP which is committed to DFT, and incorporating the principle of calculating the total energy of pseudo-potential plane waves (PP-PW).[28] The ultrasoft Vanderbilt-type pseudopotential was utilized to create electron-ion interactions. In the Perdew Burke Ernzerhof, generalized gradient approximation (PBE-GGA) approach a cut-off energy of 600 eV is applied. The Monkhorst–Pack scheme was used by taking a 7×7×7 *k*-point mesh, which was set to an ultrafine mode for the first Brillouin zone. However, to analyze the electron charge density pattern undoubtedly, a larger (12×12×12) *k*-point grid was used. The Broyden-Fletcher-Goldfarb-Shanno (BFGS) algorithm was also applied during structural optimization. The lattice parameters and atomic positions were relaxed following the structural optimization. The optimal convergent functions to obtain the ground state structure were selected as a maximum force within 0.01eV, maximum ion displacement within 5×10^{-4} Å, a total energy difference within 5×10^{-6} eV per atom, and maximum stress within 0.02 GPa.

7.2.2 SCAPS-1D numerical simulation

SCAPS-1D basically solves the second-order semiconductor differential equation by applying boundary conditions (in one direction), which govern the charge transport in a semiconductor. The three fundamental equations are Poison's equation (Eq. 7.1), electron (Eq. 7.2) and hole (Eq. 7.3) continuity equations, and drift and diffusion equations for electrons (Eq. 7.4) and holes (Eq. 7.5). For all the illuminated simulations global, the AM1.5 spectrum with an irradiation intensity of 1000 W m^{-2} was considered. The double perovskite solar cell based on Cs_2AgSbX_6 was modelled with an n-i-p planar configuration.

$$\frac{dy}{dx} = -\frac{d^2\Psi}{dx^2} = \frac{q}{\varepsilon}[p(x) - n(x) + N_D^+(x) - N_A^- + p_t(x) - n_t(x)] \quad (7.1)$$

$$\frac{dn_p}{dt} = G_n - \frac{n_p - n_{p0}}{\tau_n} + n_p\mu_n\frac{dE}{dx} + \mu_n E\frac{dn_p}{dx} + D_n\frac{d^2n_p}{dx^2} \quad (7.2)$$

$$\frac{dp_n}{dt} = G_p - \frac{p_n - p_{n0}}{\tau_p} + p_n\mu_p\frac{dE}{dx} + \mu_p E\frac{dp_n}{dx} + D_p\frac{d^2p_n}{dx^2} \quad (7.3)$$

$$J_n(x) = qn\mu_n E + qD_n\frac{dn}{dx} = n\mu_n\frac{dE_{Fn}}{dx} \quad (7.4)$$

$$J_p(x) = qp\mu_p E - qD_p\frac{dp}{dx} = p\mu_p\frac{dE_{Fp}}{dx} \quad (7.5)$$

where Ψ is the electrostatic potential, q is the electron charge, ε is the dielectric constant of the semiconductor material, p is the hole concentration, n is the electron concentration, N_A^- is the density of the ionized acceptors, N_D^+ is the density of the ionized donors, n_t is the trapped electrons, and p_t is the trapped holes, x is the position coordinate, G_n and G_p are the electron and hole generation rates, n_p and p_n are the electron and hole concentrations in the p and n region, respectively, n_{po} and p_{no} are the equilibrium electron and hole concentrations in the p and n region, τ_n and τ_p denote the electron and hole lifetime, μ_p and μ_n are the hole and electron mobilities, E is the electric field, D_n and D_p are the electron and hole diffusion coefficients, and E_{Fn} and E_{Fp} are the quasi-Fermi levels (E_F) for electrons and holes.

7.3 Results and Discussion

7.3.1 DFT analysis

The stability of the Cs_2AgSbX_6 (where X = Cl, Br, I) double perovskites was assessed from formational energy. The crystal structure of Cs_2AgSbX_6 is a cubic double-perovskite-type system with $Fm\bar{3}m$ space group.[28] The $Cs_2AgSbCl_6$, $Cs_2AgSbBr_6$, and Cs_2AgSbI_6 double perovskites possessed a calculated lattice parameter (a) of 10.793 Å, 11.430 Å, and 12.313 Å, respectively. The variation in the atomic radii of Cl, Br, and I ions induces associated changes in the lattice parameters. Further, the formation energy (ΔE_f) for $Cs_2AgSbCl_6$, $Cs_2AgSbBr_6$, and Cs_2AgSbI_6 double perovskites were calculated using Eq. 7.6, Eq. 7.7, and Eq. 7.8, respectively. The negative value of ΔE_f for all the Cs_2AgSbX_6 double perovskites is listed in Table 7.1, which confirms the thermodynamic stability of such double perovskites.

$$\Delta E_{f\,(Cs_2AgSbCl_6)} = \frac{[E_{Total}(Cs_2AgSbCl_6) - 2E_S(Cs) - E_S(Ag) - E_S(Sb) - 6E_S(Cl)]}{N} \quad (7.6)$$

$$\Delta E_{f\,(Cs_2AgSbBr_6)} = \frac{[E_{Total}(Cs_2AgSbBr_6) - 2E_S(Cs) - E_S(Ag) - E_S(Sb) - 6E_S(Br)]}{N} \quad (7.7)$$

$$\Delta E_{f\,(Cs_2AgSbI_6)} = \frac{[E_{Total}(Cs_2AgSbI_6) - 2E_S(Cs) - E_S(Ag) - E_S(Sb) - 6E_S(I)]}{N} \quad (7.8)$$

where E_S(Cs), E_S(Ag), E_S(Sb), E_S(Cl), E_S(Br), and E_S(I) are the energy of Cs, Ag, Sb, Cl, Br, and I atoms, respectively. N represents the number of atoms in the unit cell.

Further, the empirical Goldschmidt's tolerance factor (t) was calculated using Eq. 9 to confirm the structural stability of Cs_2AgSbX_6 double perovskites. Typically, the value of t between 0.75 and 1.023 corresponds to a stable double perovskite structure.[29] The value of t obtained for all Cs_2AgSbX_6 double perovskites (Table 7.1) illustrates the stability of the crystal structures.

$$t = \frac{(R_A + R_X)}{\sqrt{2}\,(R_B + R_X)} \quad (7.9)$$

where R_A, R_B, and R_X are the ionic radii of the ions at the A, B, and X positions, respectively.

Table 7.1 The tolerance factor (*t*) and formational energy (ΔE_f) of various Cs_2AgSbX_6 double perovskites.

Perovskite	*a* (Å)	Volume (Å^3)	*t*	ΔE_f (eV atom^{-1})
$Cs_2AgSbCl_6$	10.79	1257.26	0.984	-2.73
$Cs_2AgSbBr_6$	11.43	1493.27	0.978	-2.67
Cs_2AgSbI_6	12.31	1866.77	0.971	-2.60

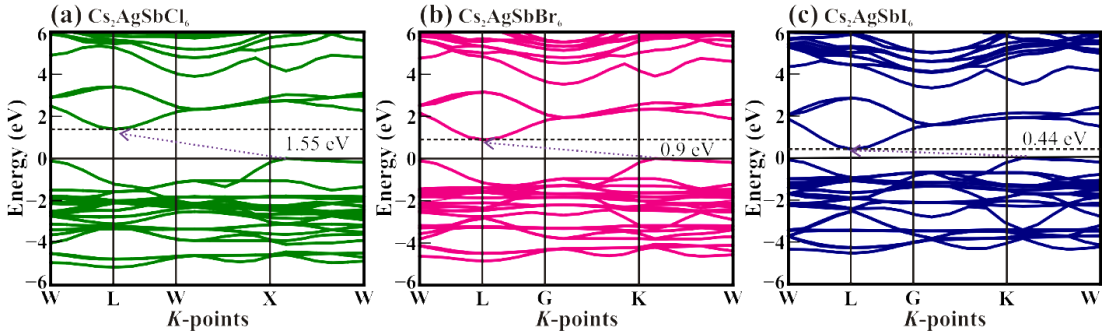

Figure 7.2 Computed band structure of (a) $Cs_2AgSbCl_6$, (b) $Cs_2AgSbBr_6$, and (c) Cs_2AgSbI_6 double perovskite light harvesters along the noted symmetry direction of the Brillouin zone using the GGA-PBE functional.

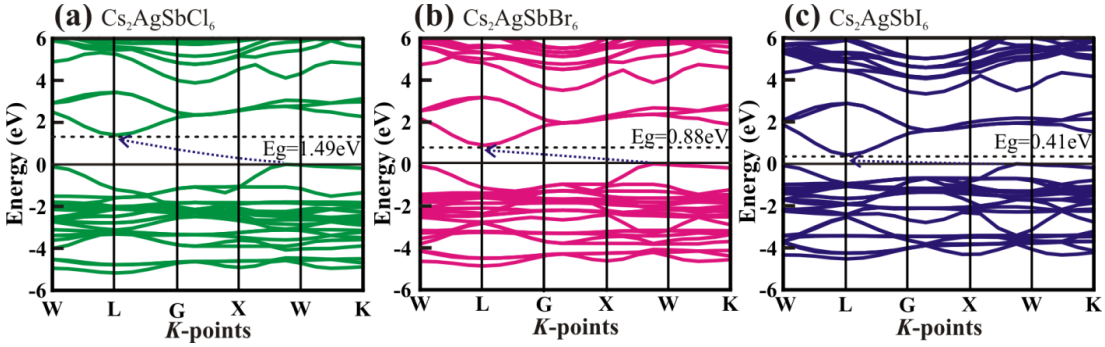

Figure 7.3 Computed band structure of (a) $Cs_2AgSbCl_6$, (b) $Cs_2AgSbBr_6$, and (c) Cs_2AgSbI_6 double perovskite light harvesters along the noted symmetry direction of the Brillouin zone using the HSEO6 functional.

The electronic band diagram of Cs_2AgSbX_6 (where X = Cl, Br, I) double perovskite toward the symmetry Brillouin zone direction as shown in Figure 2. All three double perovskite light harvesters illustrated an indirect transition with bandgap (E_g) ranging from 1.55 to 0.44 eV. The highest bandgap of 1.55 eV was observed for

$Cs_2AgSbCl_6$ light harvester (Fig. 7.2(a)), followed by $Cs_2AgSbBr_6$ (0.9 eV) (Fig. 7.2(b)) and Cs_2AgSbI_6 (0.44 eV) (Fig. 7.2(c)) light harvesters. Moreover, it should be noted that the E_g values were lower in comparison to the reported values. Such discrepancy can arise due to the usage of PBE-GGA potentials (average potential) which debate the E_g of the light harvesters. [30, 31] Thus, apart from PBE-GGA potentials, the HSEO6 functional was also used to estimate the E_g of the Cs_2AgSbX_6 (where X = Cl, Br, I) double perovskite. Compared to the E_g obtained from the PBE-GGA model, the E_g marginally reduced (~10 m eV) with HSEO6 functional. The E_g of 1.49 eV, 0.88 eV, and 0.41 eV were estimated for $Cs_2AgSbCl_6$, $Cs_2AgSbBr_6$, and Cs_2AgSbI_6 double perovskites, respectively as shown in Fig. 7.3. Additionally, such variation in the bandgap can be further engineered for panchromatic visible light absorption by tuning the combination of the halide ions in the Cs_2AgSbX_6 double perovskite light harvester.[32]

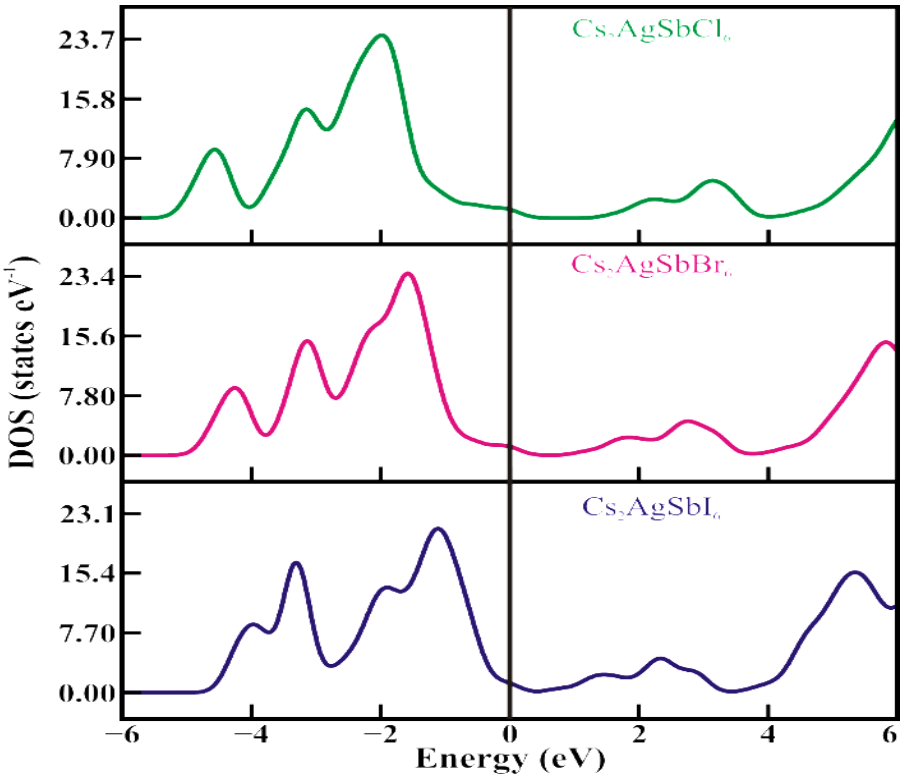

Figure 7.4 The variation in density of states of the Cs_2AgSbX_6 (where X = Cl, Br, and I) double perovskite light harvesters.

The obtained DOS of the light harvester is shown in Fig. 7.4. The DOS state curves estimated small values of ~1.32, ~1.19, and ~1.17 states eV^{-1} when X = Cl, Br, and I, respectively at E_F showcasing the semiconducting nature of the Cs_2AgSbX_6 double perovskites light harvesters. Additionally, DOS curves also indicated p-type carriers in the Cs_2AgSbX_6 double perovskites. Understanding the absorption coefficient (α) of the light harvester is important to comprehend the possible PCE of the solar cell.

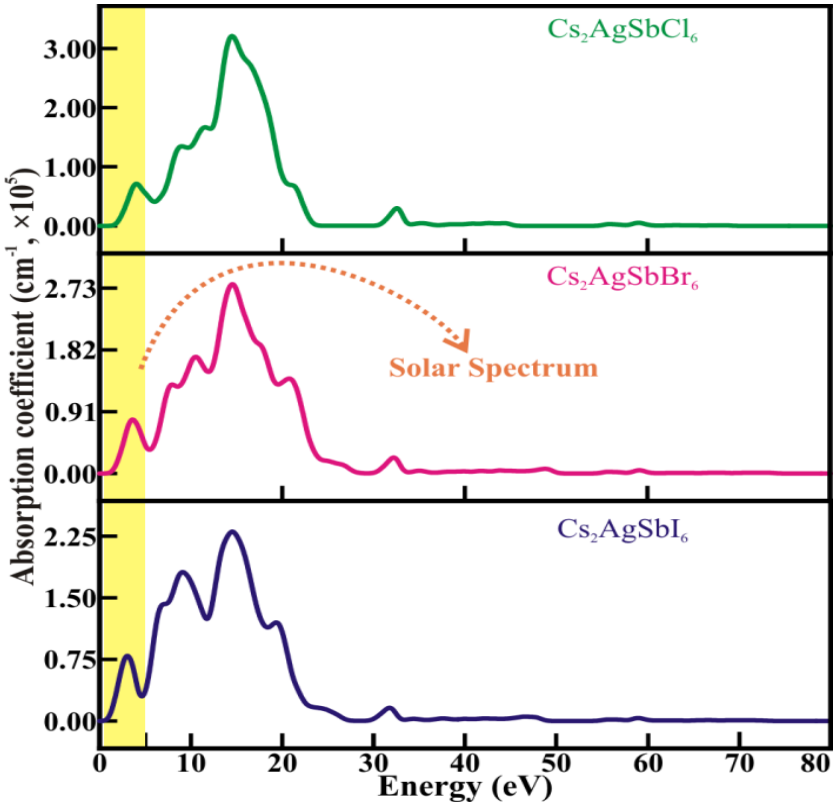

Figure 7.5 Energy-dependent variation in absorption coefficient (α) of the Cs_2AgSbX_6 (where X = Cl, Br, and I) double perovskite light harvesters. Yellow shaded region highlighting the solar spectrum.

The energy-dependent variation in absorption coefficient (α) of the Cs_2AgSbX_6 (where X = Cl, Br, and I) double perovskite light harvesters is shown in Figure 5. The absorption onset at ~1.5, ~0.9, and ~0.5 eV when X = Cl, Br, and I, respectively, reflected the semiconducting nature and the bandgap obtained from the E-*K* diagram (Fig. 7.2 and Fig. 7.3) for Cs_2AgSbX_6 double perovskites light harvesters. All the Cs_2AgSbX_6 double perovskites light harvesters, showed absorption in the solar

spectrum i.e. ~0.5 to ~5 eV (highlighted with the yellow shaded region in Fig. 7.5). Moreover, for all the Cs_2AgSbX_6 double perovskites light harvesters, α showed three main peaks, demonstrating the panchromatic absorption of the electromagnetic spectrum with the dominant ultraviolet (UV) region. It is often noted that the peaks in the low energy infrared region originate due to the intraband transition, whereas the interband transition produces the peaks in the high-frequency level of absorption.[33] Thus, for all the Cs_2AgSbX_6 double perovskites light harvesters, the highest absorption is observed above 14 eV indicating interband transitions. Nevertheless, the minor peaks at high energy region (i.e., > 30 eV) can be ascribed to the interband electronic transitions.

In the context of optoelectronics and nano-electronic devices, optical functions are crucial in comprehending electronic structure with and prospective optical applications. The energy-dependent reflectivity of the Cs_2AgSbX_6 (where X = Cl, Br, and I) light harvester is shown in Fig. 7.6(a). The static part of the reflectivity (0.13) was obtained at 0 eV, whereas the highest reflectivity (0.49) was observed in the UV region for the $Cs_2AgSbCl_6$ light harvester. However, when the Cl was replaced by Br ions in the Cs_2AgSbX_6 light harvester, the static reflectivity increased to 0.17 with the highest reflectivity of 0.31 in the UV region. Notably, the static and highest reflectivity of 0.24 and 0.34, respectively, were estimated for the Cs_2AgSbI_6 double perovskite light harvester. Additionally, using the obtained reflectivity, the other required optical constants can be calculated by employing the Kramers–Kroning equation.

Further, when the electromagnetic radiation passes through the Cs_2AgSbX_6 light harvester, the refractive index and extinction coefficient account for the changes in the phase velocity and the absorption losses. The energy-dependent variation in refractive index and extinction coefficient are shown in Fig. 7.6(b). The n (0) of 2.20, 2.48, and 2.98 were estimated for $Cs_2AgSbCl_6$, $Cs_2AgSbBr_6$, and Cs_2AgSbI_6 double perovskite light harvesters. Additionally, the refractive index increases with increasing energy, and a minimum refractive index was recorded for $Cs2AgSbCl_6$ (i.e., 2.58 at 2.32 eV) followed by $Cs_2AgSbBr_6$ (i.e., 2.91 at 1.81 eV) and Cs_2AgSbI_6 (i.e., 3.32 at 1.32 eV). Moreover, the refractive index varied with changing energy indicating the

photorefractive nature of the Cs_2AgSbX_6 double perovskite light harvester. Overall, the n (0) for all Cs_2AgSbX_6 double perovskite light harvesters were found comparable to GaAs and $K_2Cu_2GeS_4$ semiconductors.[34]

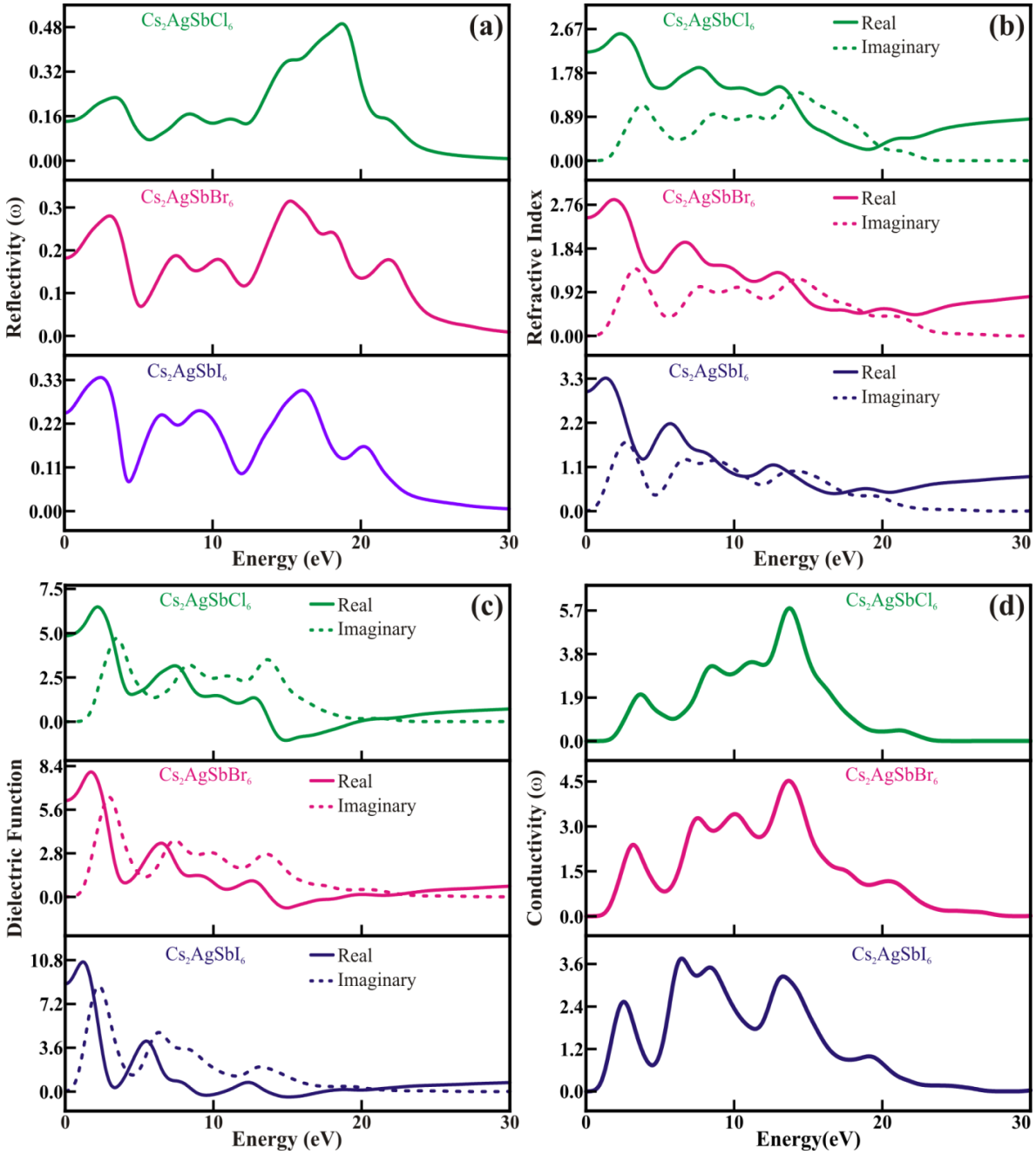

Figure 7.6 Energy-dependent variation in (a) reflectivity, (b) refractive index, (c) dielectric function, and (d) conductivity of the Cs_2AgSbX_6 (where X = Cl, Br, and I) double perovskite light harvesters.

Fig. 7.6(c) illustrates the variation of the real (ε1) and imaginary (ε2) parts of the dielectric function depending on the energy. The ε1 at zero energy indicating the electronic part of the static dielectric function was estimated to be 4.96, 6.22, and 8.94 for $Cs_2AgSbCl_6$, $Cs_2AgSbBr_6$, and Cs_2AgSbI_6, respectively. Additionally, the ε1 for all Cs_2AgSbX_6 double perovskite light harvesters steadily increased and attained a maximum value. Moreover, the intraband and interband transitions can be correlated to the dielectric function where the intraband represents the absorption of free or conduction electrons. The maximum ε1 of 10.66 (at 1.20 eV) was recorded for Cs_2AgSbI_6 followed by $Cs_2AgSbBr_6$ (i.e., 8.01 at 1.74 eV) and $Cs_2AgSbCl_6$ (i.e., 6.49 at 2.18 eV) light harvesters in the visible region. For energies > 20 eV, the dielectric constant of Cs_2AgSbX_6 double perovskite light harvesters remained almost constant indicating an energy loss of the electrons originating from electronic transitions. The ε2 for all Cs_2AgSbX_6 double perovskite light harvesters attained zero beyond an energy of 20 eV proving their transparent and anisotropic (optical) nature. Fig. 7.6(d) illustrates the photoconductivity of the Cs_2AgSbX_6 light harvesters. The initiation of the photoconductivity curve from 0 eV shows the degenerative nature of the Cs_2AgSbX_6 light harvesters showcasing their applicability in high-efficiency solar cells. Nevertheless, the highest conductivity was observed for $Cs_2AgSbCl_6$ (at 13.73 eV) followed by $Cs_2AgSbBr_6$ (at 13.67 eV) and Cs_2AgSbI_6 (at 6.44 eV) light harvesters. Overall, the optical properties of Cs_2AgSbX_6 double perovskite light harvesters demonstrated their suitability for fabricating high-efficiency solar cells.

7.3.2 SCAPS-1D analysis

With the prerequisites pertaining to the electronic and optical properties of Cs_2AgSbX_6 double perovskite light harvesters, the physical parameters employed in the SCAPS-1D device simulation are tabulated in Table 7.2. The series and shunt resistance values are 5 Ω cm^{-2} and 1 M Ω cm^{-2}, respectively.

Table 7.2 The physical parameters loaded as input to simulate Cs_2AgSbX_6 double perovskite solar cells.

Parameters	FTO	AZnO	$Cs_2AgSbCl_6$	$Cs_2AgSbBr_6$	Cs_2AgSbI_6	MoO_3
Thickness (μm)	0.1	0.03	0.9	0.9	0.9	0.3
Bandgap (eV)	3.5	3.33	1.55	0.9	0.44	3.0
Electron affinity (eV)	4.0	4.55	3.9	3.9	3.9	2.5
Relative dielectric permittivity	9.0	8.120	6.5	6.0	6.2	12.5
CB effective density of states (cm^{-3})	2.2×10^{18}	4.1×10^{18}	1×10^{19}	1×10^{19}	1×10^{19}	2.2×10^{18}
VB effective density of states (cm^{-3})	1.8×10^{19}	8.2×10^{18}	1×10^{19}	1×10^{19}	1×10^{19}	1.8×10^{19}
Thermal velocity of electrons ($cm\ s^{-1}$)	1×10^{7}	1×10^{7}	1×10^{7}	1×10^{7}	1×10^{7}	1×10^{7}
Thermal velocity of holes ($cm\ s^{-1}$)	1×10^{7}	1×10^{7}	1×10^{7}	1×10^{7}	1×10^{7}	1×10^{7}
Mobility of electrons ($cm^2\ V^{-1}\ s^{-1}$)	20	100	2	2	2	2.5
Mobility of holes ($cm^2\ V^{-1}\ s^{-1}$)	1	20	2	2	2	100
donor density, N_D (cm^{-3})	2×10^{19}	1×10^{13}	0	0	0	0

acceptor density, N_A (cm^{-3})	0	0	1×10^{19}	1×10^{19}	1×10^{19}	1×10^{18}
Defect density, N_t (cm^{-3})	1×10^{15}	1×10^{17}	1×10^{14}	1×10^{14}	1×10^{14}	1×10^{15}
References	[35]	[25]	[36]	[37]	[28]	[2]

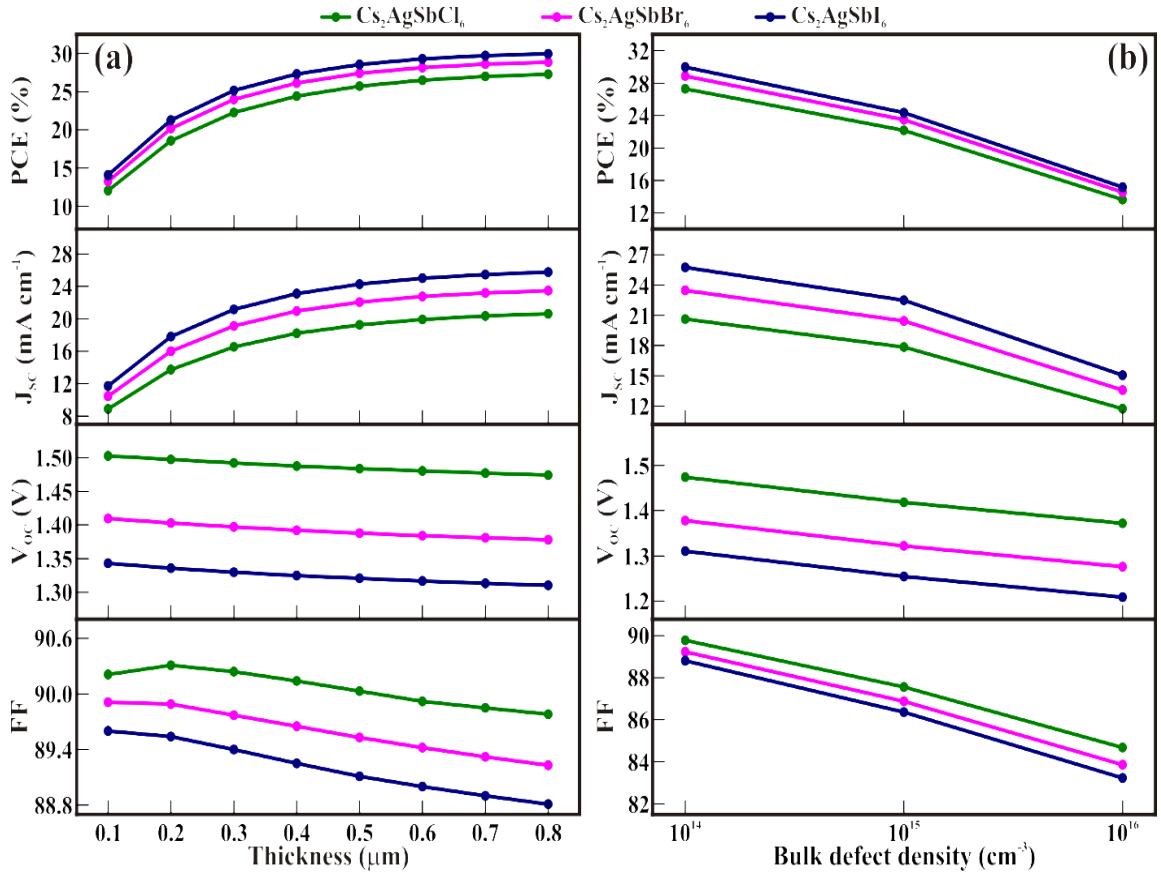

Figure 7.7 The variation in the performance of Cs_2AgSbX_6-based double perovskite solar cells corresponding to the changes in (a) thickness, and (b) bulk defect density in the light harvester films. (with other physical parameters as tabulated in Table 7.2)

The thickness of the light harvester films directly influences the performance of Cs_2AgSbX_6-based double perovskite solar cells. The optimum thickness of the light harvester film is necessary, as increasing the thickness beyond charge diffusion lengths can lead to charge recombination and decline performance. The variation in the

performance of Cs_2AgSbX_6-based double perovskite solar cells corresponding to the changes in thickness is shown in Fig. 7.7(a). As the thickness of the light harvester was increased from 100 to 800 nm, the associated steady rise in PCE of the Cs_2AgSbX_6 double perovskite solar cell was observed. The main contributor to such a high increase in PCE can be correlated to the corresponding rise in J_{SC}. The increase in J_{SC} can be ascribed to the higher photogeneration in relatively thicker light harvester films.[38] Additionally, beyond a thickness of 600 nm, the PCE of Cs_2AgSbX_6 double perovskite solar cells saturated. At a thickness of 600 nm, a PCE of ~26.5 %, ~28.16 %, and ~29.30% was estimated for $Cs_2AgSbCl_6$, $Cs_2AgSbBr_6$, and Cs_2AgSbI_6 light harvester. Moreover, the open circuit voltage (V_{OC}) and fill factor (FF) of Cs_2AgSbX_6 double perovskite solar cells remain constant for all the light harvesters with varying thicknesses.

Experimentally, depending on the synthesis protocol, the bulk defect density in the Cs_2AgSbX_6 films varies. Thus, the bulk defect density of the Cs_2AgSbX_6 double perovskite light harvester was varied from 10^{13} to 10^{16} cm^{-3} as shown in Fig. 7.7(b). With the rise in bulk defect density, an associated decline in the PCE was observed for all the Cs_2AgSbX_6 light harvesters. Even at a higher bulk defect density of 10^{16} cm^{-3}, the PCEs of 13.62 %, 14.54 %, and 15.15 % were estimated for $Cs_2AgSbCl_6$, $Cs_2AgSbBr_6$, and Cs_2AgSbI_6, respectively. The deduction in the PCE at high bulk defect density can be ascribed to the corresponding reduction in J_{SC} originating from defect-assisted recombination which reduces the effective charge diffusion length in the defective light harvesters. Moreover, the marginal decline in the V_{OC} can be associated with the formation of defect energy levels, which modifies the effective bandgap in the Cs_2AgSbX_6 double perovskite light harvesters. The change in J_{SC} and V_{OC} results in declining the FF of high bulk defect density films.

While evaluating the performance and economic viability of Cs_2AgSbX_6 double perovskite solar cells, it is essential to consider the application of several potential rear contacts based on their conductivity, work function, reactivity, and cost.[39] The variation in the PCE of Cs_2AgSbX_6 double perovskite solar cells depending on the work function of the rear metal contact is shown in Fig. 7.8. The PCE of Cs_2AgSbX_6 double perovskite solar cells increased with the increase in the work function of the rear

contacts. The PCE of the Cs_2AgSbX_6 double perovskite solar cells saturated beyond a work function of 5 eV (carbon). These findings pointed to the possibility of using inexpensive and chemically inert carbon electrodes as rear contacts for the Cs_2AgSbX_6 double perovskite solar cells without sacrificing PCE.

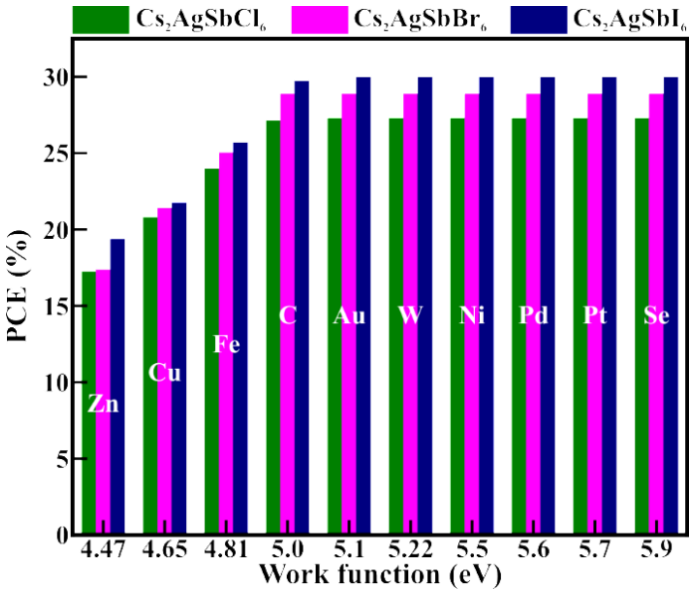

Figure 7.8 The variation in the PCE of Cs_2AgSbX_6 double perovskite solar cells depending on the work function of the rear metal contact.

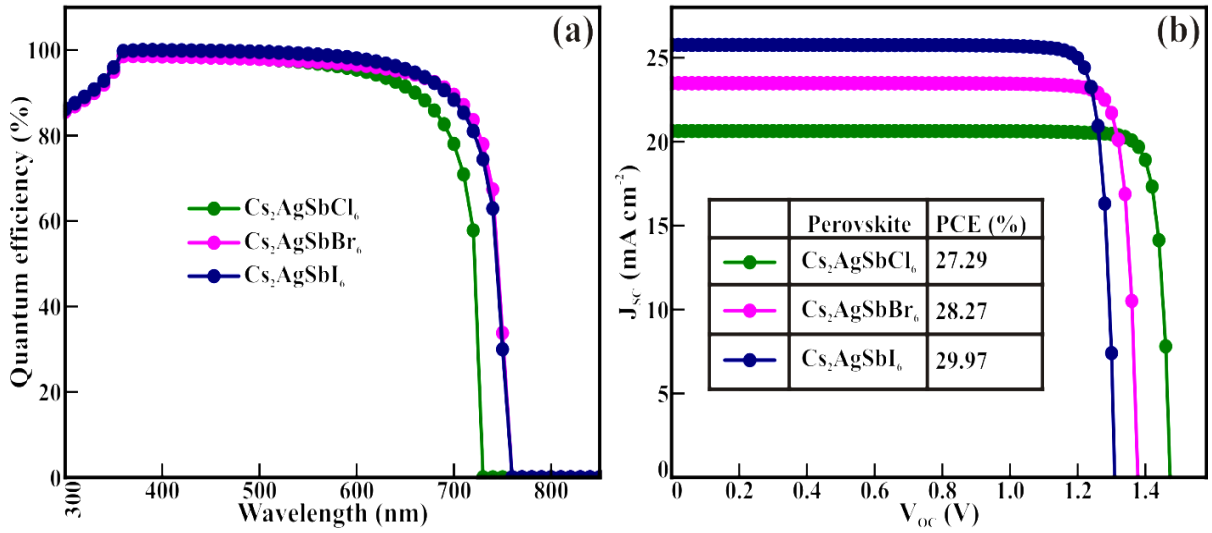

Figure 7.9 The (a) quantum efficiency (QE) indicating the spectral response and (b) J-V characteristics of the modeled Cs_2AgSbX_6 double perovskite solar cells.

Comprehending the spectral response is essential in interpreting the incident photon to electron conversion or quantum efficiency (QE) of Cs_2AgSbX_6 double perovskite solar cells. The QE of Cs_2AgSbX_6 double perovskite solar cells is shown in Fig. 7.9(a). All the Cs_2AgSbX_6 (where X = Cl. Br, I) light harvesters showed broad absorption in the visible range. The associated J-V curves depending on the type of light harvester are shown in Fig. 7.9(b). The highest PCE of ~29.9 % was estimated for Cs_2AgSbI_6 light harvester followed by $Cs_2AgSbBr_6$ (~28.2 %) and $Cs_2AgSbCl_6$ (~27.29 %). Overall, these findings show the possible potential PCE of the Cs_2AgSbX_6 double perovskite solar cells and the physical parameters that control them. The methodical approach used to comprehend the optoelectronic characteristics and interpret the potential device applications can be adopted for various other heterojunction photovoltaics and optoelectronic devices.

7.4 Conclusion

In conclusion, the CASTEP software program, which is dedicated to DFT, was first used to probe the Cs_2AgSbX_6 (where X = Cl, Br, and I) double perovskite light harvesters. The tunable bandgap (indirect) and related semiconducting nature of Cs_2AgSbX_6 double perovskite light harvesters were revealed by the DFT analysis. The optoelectronic characteristics of Cs_2AgSbX_6 light harvesters, such as their absorption coefficient, reflectivity, refractive index, and dielectric characteristics, highlight their theoretical potential for excellent solar energy conversion. Additionally, the device simulation using SCAPS-1D programming demonstrated the impact of several physical factors on the performance of the modeled double perovskite solar cells based on Cs_2AgSbX= (FTO/AZnO/Cs_2AgSbX_6/MoO_3/rear contact). The thickness and bulk defect density of the light harvesters showed higher control over the PCE of the cells. The change in PCE with possible rear contacts demonstrates the applicability of cost-effective carbon electrodes. The highest PCE of ~29.9 %, ~28.2 %, and ~27.2 % was estimated for Cs_2AgSbI_6, $Cs_2AgSbBr_6$, and $Cs_2AgSbCl_6$ double perovskite light harvesters, respectively. The present theoretical estimation illustrated in this study can be stretched to other optoelectronic devices.

7.5 References

[1] V. Manjunath, S. Bimli, P.A. Shaikh, S.B. Ogale, R.S. Devan, J. Mater. Chem. C, **2022**, 10, 15725-15780.

[2] M. Alla, V. Manjunath, E. Choudhary, M. Samtham, S. Sharma, P.A. Shaikh, M. Rouchdi, B. Fares, Phys. Status Solidi (a), **2023**, 220, 2200642.

[3] A.H. Slavney, L. Leppert, D. Bartesaghi, A. Gold-Parker, M.F. Toney, T.J. Savenije, J.B. Neaton, H.I. Karunadasa, J. Am. Chem. Soc., **2017**, 139, 5015-5018.

[4] Z. Xiao, W. Meng, J. Wang, Y. Yan, ChemSusChem, **2016**, 9, 2628-2633.

[5] S. Chand Yadav, A. Srivastava, V. Manjunath, A. Kanwade, R.S. Devan, P.M. Shirage, Mater. Today Phys, **2022**, 26, 100731.

[6] B. Fett, Ö.Ş. Kabaklı, C.A.R. Sierra, P.S.C. Schulze, S. Yoon, B. Herbig, S.W. Glunz, J.C. Goldschmidt, G. Sextl, K. Mandel, ACS Appl. Energy Mater., **2023**, 6, 4372-4379.

[7] M. Faizan, X. Wang, S.A.M. Abdelmohsen, K.C. Bhamu, S. Sappati, A. Laref, N. Muhammad, M. Mushtaq, A.M.M. Abdelbacki, R. Khenata, Energy Fuels, **2022**, 36, 7065-7074.

[8] M.N. Tran, I.J. Cleveland, E.S. Aydil, ACS Appl. Electron. Mater., **2022**, 4, 4588-4594.

[9] W.B. Dai, S. Xu, J. Zhou, J. Hu, K. Huang, M. Xu, Sol. Energy Mater. Sol. Cells, **2019**, 192, 140-146.

[10] M. Zhai, C. Chen, M. Cheng, Sol. Energy, **2023**, 253, 563-583.

[11] J. Li, X. Meng, Z. Wu, Y. Duan, R. Guo, W. Xiao, Y. Zhang, Y. Li, Y. Shen, W. Zhang, G. Shao, Adv. Funct. Mater., **2022**, 32, 2112991.

[12] Q. Li, Y. Wang, W. Pan, W. Yang, B. Zou, J. Tang, Z. Quan, Angew. Chem. Int. Ed., **2017**, 56, 15969-15973.

[13] K.-z. Du, W. Meng, X. Wang, Y. Yan, D.B. Mitzi, Angew. Chem. Int. Ed., **2017**, 56, 8158-8162.

[14] X.-G. Zhao, D. Yang, J.-C. Ren, Y. Sun, Z. Xiao, L. Zhang, Joule, **2018**, 2, 1662-1673.

[15] M.K. Hossain, D.P. Samajdar, R.C. Das, A.A. Arnab, M.F. Rahman, M.H.K. Rubel, M.R. Islam, H. Bencherif, R. Pandey, J. Madan, M.K.A. Mohammed, Energy Fuels, **2023**, 37, 3957-3979.

[16] M. Palummo, E. Berrios, D. Varsano, G. Giorgi, ACS Energy Lett., **2020**, 5, 457-463.

[17] M.R. Filip, X. Liu, A. Miglio, G. Hautier, F. Giustino, J. Phys. Chem. C, **2018**, 122, 158-170.

[18] D.-Y. Hu, X.-H. Zhao, T.-Y. Tang, L.-M. Lu, L. Li, L.-K. Gao, Y.-L. Tang, Mater. Sci. Semicond. Process., **2022**, 152, 107077.

[19] N. Rajeev Kumar, S.G. Ramaraj, P.C. Karthika, N.P. Mathew, R. Radhakrishnan, Comput. Mater. Sci., **2023**, 218, 111975.

[20] M.R. Filip, S. Hillman, A.A. Haghighirad, H.J. Snaith, F. Giustino, J. Phys. Chem. Lett., **2016**, 7, 2579-2585.

[21] J. Kruszyńska, J. Ostapko, V. Ozkaya, B. Surucu, O. Szawcow, K. Nikiforow, M. Hołdyński, M.M. Tavakoli, P. Yadav, M. Kot, G.P. Kołodziej, M. Wlazło, S. Satapathi, S. Akin, D. Prochowicz, Adv. Mater, Interfaces, **2022**, 9, 2200575.

[22] M. Adnan, J.K. Lee, RSC Adv., **2020**, 10, 5454-5461.

[23] S. Bimli, V. Manjunath, S.R. Mulani, A. Miglani, O.S. Game, R.S. Devan, Sol. Energy, **2023**, 256, 76-87.

[24] S. Bimli, Y.K. Reddy, V. Manjunath, R.S. Devan, Chinese J. Phys., **2023**, 82, 120-133.

[25] M. Alla, S. Bimli, V. Manjunath, M. Samtham, A. Kasaudhan, E. Choudhary, M. Rouchdi, F. Boubker, Mater. Technol., **2022**, 37, 2963-2969.

[26] Y.K. Reddy, V. Manjunath, S. Bimli, R.S. Devan, Sol. Energy, **2022**, 244, 75-83.

[27] M.K. Hossain, M.H.K. Rubel, G.F.I. Toki, I. Alam, M.F. Rahman, H. Bencherif, ACS Omega, **2022**, 7, 43210-43230.

[28] M.K. Hossain, A.A. Arnab, R.C. Das, K.M. Hossain, M.H.K. Rubel, M.F. Rahman, H. Bencherif, M.E. Emetere, M.K.A. Mohammed, R. Pandey, RSC Adv., **2022**, 12, 35002-35025.

[29] F. Elfatouaki, R. Takassa, O. Farkad, S, Hassine, O. Choukri, A. El Mouncharih, E. A. Ibnouelghazi, A. Outzourhit, D. Abouelaoualim, Mater. Today. Sustain., **2023**, In-presss. https://doi.org/10.1016/j.mtsust.2023.100572.

[30] N. Guechi, A. Bouhemadou, S. Bin-Omran, A. Bourzami, L. Louail, Elastic, J. Electron. Mater., **2018**, 47, 1533-1545.

[31] M. Irfan, S. Azam, S. Hussain, S.A. Khan, M. Sohail, M. Ahmad, S. Goumri-Said, J. Phys. Chem. Solids, **2018**, 119, 85-93.

[32] H.S. Jung, N.-G. Park, Small, **2015**, 11, 10-25.

[33] Z. Lin, J. Lei, P. Wang, X. Zhang, L. Xu, M. Chen, Y. Kang, G. Wei, J. Alloys Compd., **2022**, 892, 162165.

[34] M.A. Ali, M. Anwar Hossain, M.A. Rayhan, M.M. Hossain, M.M. Uddin, M. Roknuzzaman, K. Ostrikov, A.K.M.A. Islam, S.H. Naqib, J. Alloys Compd., **2019**, 781, 37-46.

[35] M. Alla, V. Manjunath, N. Chawki, D. Singh, S.C. Yadav, M. Rouchdi, F. Boubker, Opt. Mater., **2022**, 124, 112044.

[36] Y. Guo, Y. Lou, J. Chen, Y. Zhao, ChemSusChem, **2022**, 15, e202102334.

[37] D. Kumar, J. Kaur, P.P. Mohanty, R. Ahuja, S. Chakraborty, ACS Omega, **2021**, 6, 33240-33252.

[38] V. Manjunath, Y.K. Reddy, S. Bimli, R.J. Choudhary, R.S. Devan, Mater. Today Commun., **2022**, 32 (2022) 104061.

[39] S. Maniarasu, T.B. Korukonda, V. Manjunath, E. Ramasamy, M. Ramesh, G. Veerappan, Renew. Sust. Energy Rev., **2018**, 82, 845-857.

Chapter 8

Summary and conclusion

8.1 Summary and conclusion

The amount of energy globally is anticipated to rise about 30 TW by 2050 to 46 TW by 2100. Conventional energy sources like coal, oil, natural gas, etc., cannot keep up with the projections owing to the ever-increasing demand. Consequently, an extensive evaluation of sustainable and renewable energy sources must be conducted to address the staggering energy demand of the future. Of the various kinds of green energy solutions readily accessible, photovoltaic (PV) cells for solar energy conversion are of special interest to the scientific and industrial sectors. Owing to the high power-to-weight ratio, the PV cells can handle large demands and the output of the PV cell can be integrated into existing power grids making them the best-suited choice. Consequently, there are several PV technologies based on the type of light harvester used and the associated manufacturing cost. However, the cost is further linked to the abundance and ease of processing of the light harvester. Overall, solar cell technology has progressed and is classified depending on decreasing cost. Nevertheless, finding environmentally benign light harvesters with ideal optoelectronic properties is of utmost importance to combat the modern-day challenges which include global warming. In general, photovoltaic panels will be effective ways to meet future energy needs in a sustainable manner.

Among the developed solar cell technologies, the third-generation perovskite solar cells have recently captured the limelight. Presently, the efficiency of the single junction perovskite solar cells is comparable to the established first-generation crystalline silicon technology. Moreover, the robustness of the perovskite crystal structure renders cost-effective manufacturing which comprises simple thin film techniques at relatively low temperatures. Thus, the modern perovskite light harvesters are currently demonstrating considerable assurance. But, the shortcomings of their toxicity and long-term stability remain the biggest concern. However, the crystal structure of the perovskite light harvesters offers tunability which can be modulated towards non-toxic, stable, and highly efficient perovskite solar cells. Depending on the ionic radii and oxidation states several replacements in the perovskite crystal structures are researched to substitute the toxic and unstable ions at the operating conditions. Apart from the perovskite light harvesters, the associated assisting layers which aid in the formation of n-i-p or p-i-n junctions can also help boost both the long-term stability and PCE of the perovskite solar cells.

Therefore, investigating the possible perovskite light harvesters obtained by tailoring their crystal structure towards non-toxicity and high efficiency is essential in assessing the potential of perovskite solar cells. It is a laborious process to experimentally investigate various perovskite light harvesters in conjunction with additional supporting films. However, the influence of the thickness, doping, and defect densities of the subsequent layer on the performance of the perovskite solar cells is not well understood. Thus, the optimizations required to enhance the PCE of PSCs based on the SCAPS-1D software program are evaluated. The effect of the replacement of toxic Pb ions with Sn ions in the perovskite crystal structure and concomitant changes in the performance needs evaluation. The possible theoretical performance considering the physical parameters is discussed and optimized with the SCAPS-1D program. Other possible perovskite light harvesters obtained by transmutation of the toxic Pb ions resulting in double perovskite crystal structures need scrutinization for solar energy harvesting. The performance of all inorganic and non-toxic double perovskites is optimized. By understanding the thermodynamic stability, the potential of other inorganic non-toxic double perovskite light harvesters is also evaluated. Further, the DFT calculations based on the CASTEP software program are performed on the double perovskite light harvesters to understand their intrinsic optoelectronic properties. The obtained optoelectronics properties were used as input to numerically comprehend the light harvesters.

Therefore, we have addressed the following objective in this thesis work.

- Optimization of the subsequent layers in perovskite solar cells based on $CH_3NH_3PbI_{3-X}Cl_X$ light harvesters to yield high efficiency.
- The effect of replacement of toxic and unstable ions in the perovskite structurers on the performance of solar cells.
- The influence of heterogenous substitution of the toxic lead ions in the perovskite light harvester to form double perovskite and their solar cell performance.
- The influence of thickness, defect, and doping densities of the subsequent layers in the double perovskite solar cells on the perovskite solar cells.
- The study on optoelectronic properties of possible perovskite light harvesters and their associated changes in the performance.

Organic-inorganic perovskite light absorbers have shown tremendous progress over the last decade. Single junction solar cells with perovskite light absorbers have achieved power

conversion efficiencies exceeding 25%. Further optimization of the subsequent thin-films in the perovskite solar cells is essential to attain higher power conversion efficiencies reaching the Shockley-Queisser limit. Herein, we report the preliminary studies on how the subsequent thin-films thickness and properties can be tuned to achieve efficiencies exceeding 30%. We used SCAPS-1D software to optimize the thickness, donor, defect, and acceptor densities of each thin film of the perovskite solar cells. The thickness and defect densities of the $CH_3NH_3PbI_{3-X}Cl_X$ light absorber had the highest control over power conversion efficiencies. The thickness and acceptor densities of the hole transporting films had the slightest control over power conversion efficiencies. We have also studied the operating temperature-dependent variation in power conversion efficiency and other solar cell parameters. In an attempt to replace the high-cost gold counter electrode, we compared the variation of power conversion efficiency with other possible counter electrodes. Overall, the current approach of utilizing SCAPS-1D software to optimize high-efficiency perovskite solar cells theoretically can be extended to other solar cells and optoelectronic devices.

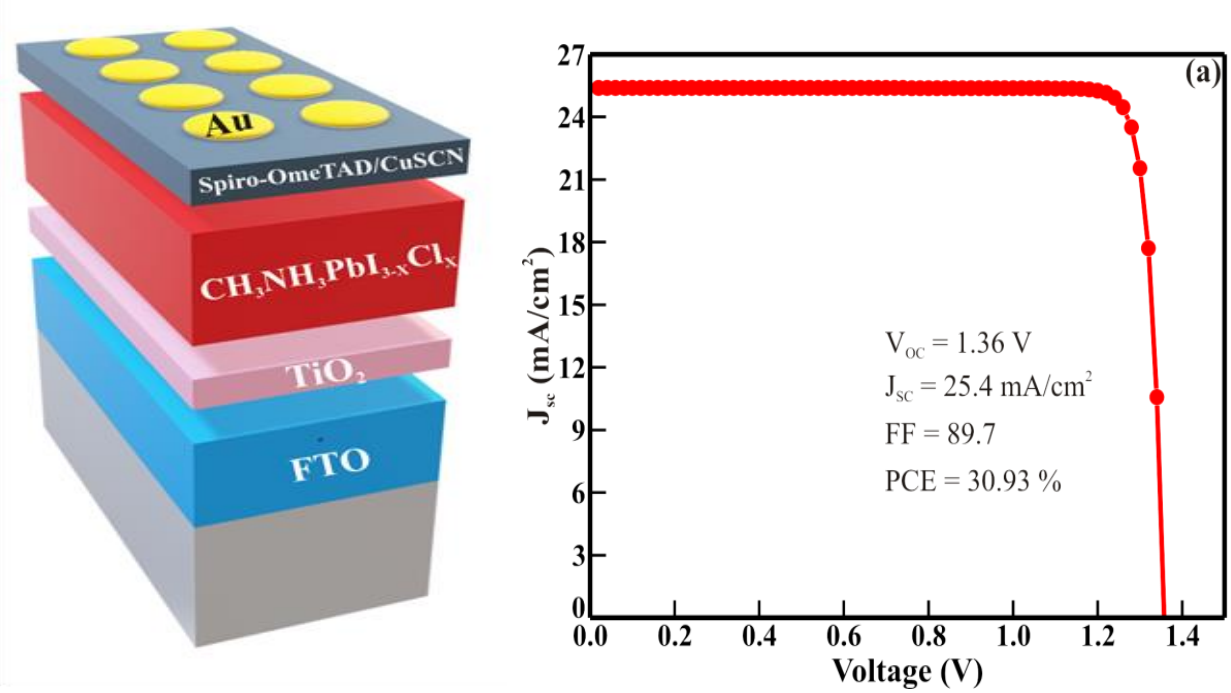

Figure 8.1 Theoretical optimization of the device structure based on $CH_3NH_3PbI_{3-X}Cl_X$ light harvesters and the associated *J-V* curve demonstrating PCE of ~30%.

Single junction solar cells with organic-inorganic perovskites have achieved efficiency > 25%, yet they suffer from long-term durability and toxicity. Additionally, all the best-performing perovskite light harvesters contain lead, hindering their real-time application. Herein, we report preliminary studies with the SCPAS-1D software package on three different perovskite light harvesters, namely $FAPbI_3$, $FASnI_3$, and $CsSnI_3$, considering an approach towards stable and environmentally benign perovskite light harvesters. Additionally, to extract the best performance, each perovskite light harvester is analyzed with four electron transport layers, namely TiO_2, SnO_2, $BaSnO_3$, and La doped $BaSnO_3$. The physical parameters such as thickness, doping, and defect density are optimized for the subsequent films to deliver high performance. Further, the operating temperature-dependent variation in power conversion efficiency and other solar cell parameters are also analyzed. In an attempt to replace the high-cost gold counter electrode, a comparative study on the performance of other possible counter electrodes is also comprehensively detailed.

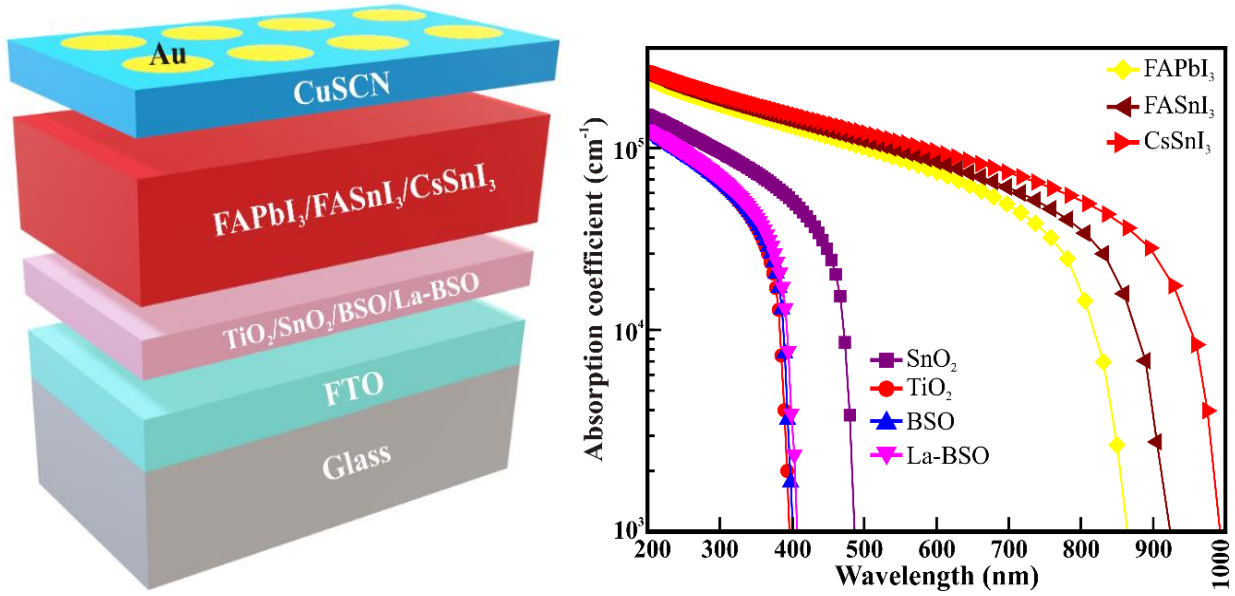

Figure 8.2 The schematics of the device considered for replacing the toxic lead ions with Sn ions and the corresponding absorption co-efficient subsequent layers.

Recently, the efficiency of single-junction perovskite solar cells has been competing with the crystalline Si solar cells. However, the perovskite absorbers are toxic and susceptible to moisture. Herein, the performance of an environmentally benign and durable Cs_2BiAgI_6 light harvester using the 1D Solar Cell Capacitance Simulator (SCAPS-1D) software package is evaluated. The primary physical parameters, namely, defect and doping densities and thickness of

the subsequent layers, are varied to achieve high efficiencies. The optimized Cs_2BiAgI_6-based double perovskite solar cells with three distinct hole-transporting layers (HTLs) (i.e., MoO_3, CuSCN, and spiro-OMeTAD) deliver a power conversion efficiency of ≈29% with AZnO as electron transport layer (ETL). Further, a variety of possible rear electrodes are explored, and their effect on the performance is estimated. For real-time examination of the Cs_2BiAgI_6-based double perovskite solar cells, the variation of power conversion efficiency (PCE) concerning the operating temperature is estimated. The thickness of the Cs_2BiAgI_6 light harvester layer and the bulk defect density are the key aspects in attaining high power conversion efficiencies in Cs_2BiAgI_6-based double perovskite solar cells.

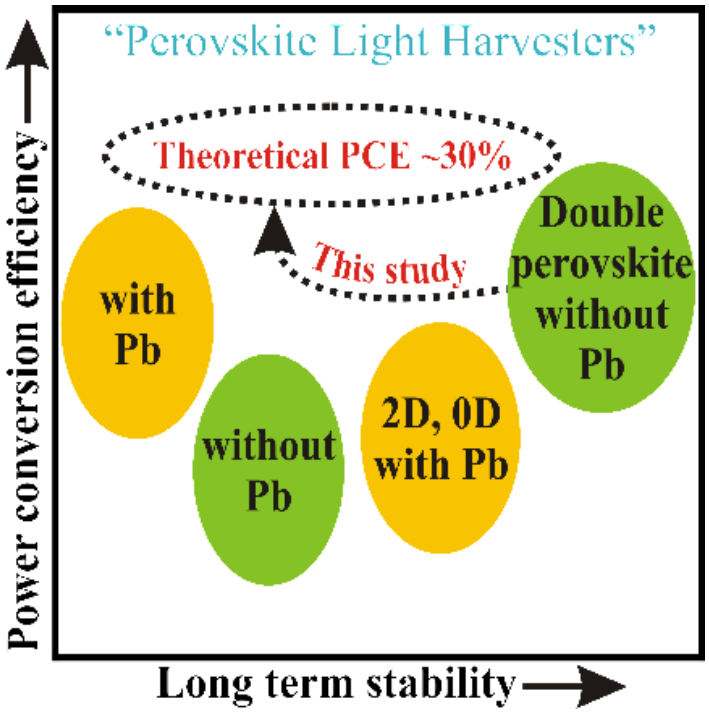

Figure 8.3 The possible PCE of PSCs based on a double perovskite light harvester dependent on the long-term stability and toxicity.

The main issues impeding the commercialization of perovskite solar cells are their toxicity and long-term stability. Thus, it is essential to find a robust and reliable alternative light absorber that is environmentally friendly and provides stability. Herein, we present stable and lead-free Cs_2CuSbX_6 (where X = Cl, Br, and I) double perovskite light harvesters as a substitute, which can render excellent efficiency and long-term stability. The double perovskite solar cells based on the Cs_2CuSbX_6 light harvester, the aluminium-doped ZnO electron transport layer, and the MoO_3 and

Cu_2O hole transport layers are critically evaluated using the SCAPS-1D software package. The densities of defects and dopants as well as the thickness of the succeeding layers of the double perovskite solar cells are altered to extract high efficiency. With aluminium-doped ZnO serving as the electron transport layer, the optimized Cs_2CuSbI_6-based double perovskite solar cells attain a power conversion efficiency (PCE) of about ~29% for both MoO_3 and Cu_2O hole transport layers. Several potential back electrodes are also investigated, and their impact on performance is assessed. The fluctuation in PCE concerning operating temperature is computed for authentic analysis of the double perovskite solar cells during real-time operation. Overall, in order to achieve high PCEs in Cs_2CuSbI_6-based double perovskite solar cells, it is crucial to consider both the thickness of the light harvester layer and the bulk defect density.

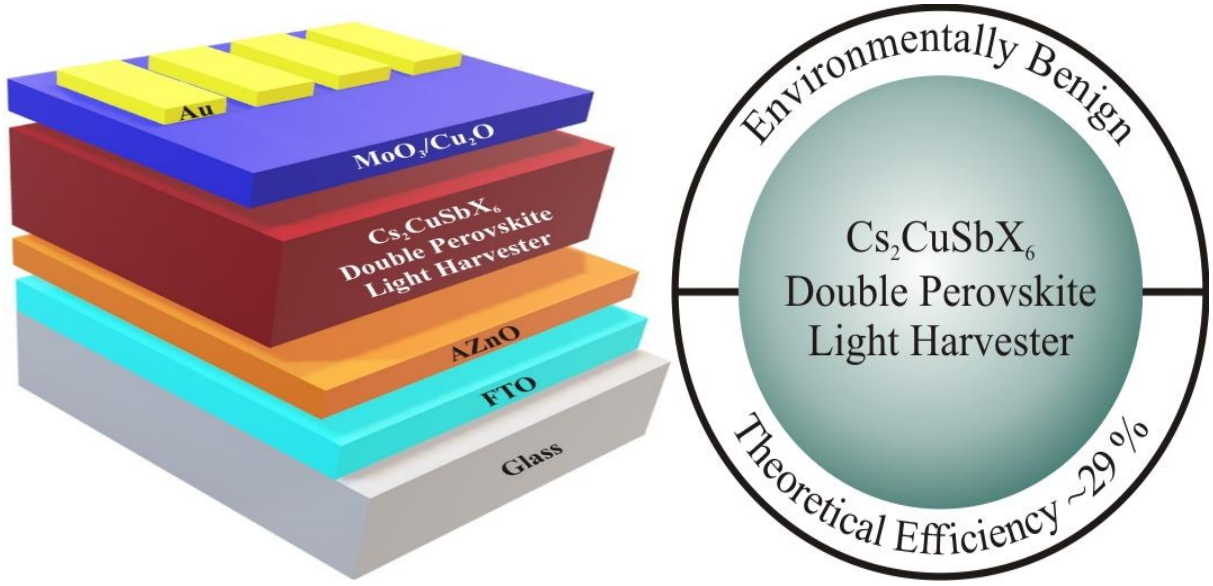

Figure 8.4 Schematics of the optimized and environmentally benign double perovskite solar cells yielding PCE of ~29%.

Owing to the low long-term stability and high toxicity, high-efficiency perovskite solar cells are yet to be commercialized. Therefore, it is imperative to find a reliable and environmentally benign alternative perovskite light harvester. Herein, we present a non-toxic double perovskite light harvester based on Cs_2AgSbX_6 (where X = Cl, Br, and I) as a substitute, which can render both high efficiency and long-term durability. The optoelectronic properties of the Cs_2AgSbX_6 double perovskite light harvesters were investigated with the CASTEP software package which is committed to density functional theory (DFT). The bandgap (indirect) tunability of Cs_2AgSbX_6

double perovskite light harvesters and associated changes in the density of states (DOS) were explored. The obtained results were further loaded as input to the SCAPS-1D software package to assess the potential of Cs_2AgSbX_6 double perovskite solar cells. With the FTO/AZnO/Cs_2AgSbX_6/MoO_3/rear contact device structure, the thickness and bulk defect density of the Cs_2AgSbX_6 light harvester had superior control over the performance of the double perovskite solar cells. The highest theoretical efficiency of ~29.9 % was estimated for the Cs_2AgSbI_6 light harvester. Additionally, the effectiveness of several prospective back electrodes was examined.

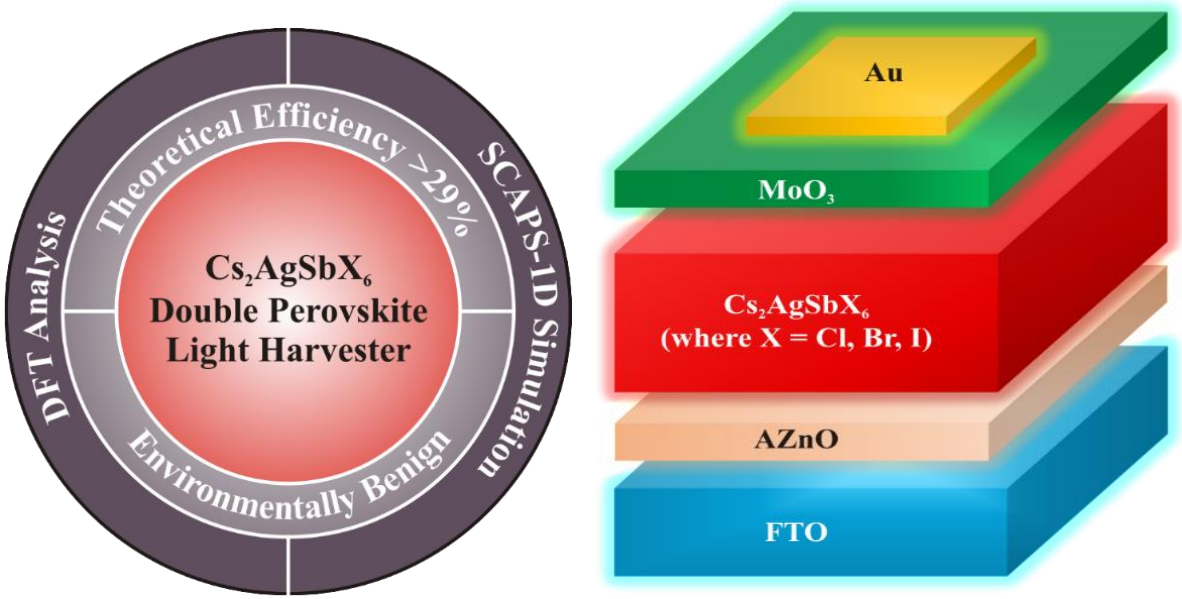

Figure 8.5 DFT calculations aided numerical estimation of Cs_2AgSbX_6 based double perovskite light harvester and the corresponding optimized solar cells.

8.2 Future scope

Although increasing energy consumption will boost economic growth, it will also result in greenhouse gas emissions and other concerns like pollution of the natural world, climate change, and other related difficulties. Thus, the only path to a greener future will involve the implementation of sustainable energy applications. Achieving zero carbon footprint will be greatly aided by sustainable energy applications like solar cells, photocatalysis, green hydrogen production, etc. Green hydrogen fuel can be produced and used effectively in industry, or it can be used to power internal combustion engines that emit no pollution and support modern transportation. Similarly, to reduce dependency on fossil fuels, PV panel output can operate as independent sources or be integrated into existing grids. When such applications are applied in tandem the output of the PV panel can be fed into the fuel cells to produce green hydrogen fuel by water splitting. Thus, for these sustainable energy applications, one ought to strive to boost the overall performance functional materials. The current work suggests that perovskite light harvesters can be tailored for solar energy conversion. Nonetheless, a few of the major conclusions offer guidelines for additional research, including:

1. Experimental investigation on the theoretically well-performing stable, non-toxic and perovskite solar cells with industrially feasible aiding transport layers and counter electrodes.
2. The comparison of the theoretical performance to the experimental output to comprehend the device and interfacial physics.
3. To use such theoretical optimization as guidelines for evaluating other optoelectronic devices like photodetectors, light emitting diodes, photo transistors, etc.
4. To compare the output of various other numerical estimations so as provide strategies for fabricating large area thin film solar cells.
5. Employing various software based on DFT to understand the properties other potential light harvesters which are not limited perovskite structures.